Photoelastic Studies of Damping, Crack Propagation, and Crack Arrest in Polymers and 4340 Steel

Prepared by
G. R. Irwin, D. B. Barker, R. J. Sanford, W. L. Fourney,
J. T. Metcalf, A. Shukla, R. Chona

Department of Mechanical Engineering
University of Maryland
College Park, Maryland 20742

8006020543

Abstract

This report describes the progress made during the fifth year on a research program dealing with the dynamic characterization of fracture. The significant findings during the past year include:

(1) The discovery that the drop in stress intensity from high K_Q levels to much lower dynamic values occurs in about 10 µs and is associated with very large crack tip accelerations ($\sim 10^7$ g's).

(2) The amount of energy attributed to damping in plate specimens of Homalite 100, Araldite B, and 4340 steel ranges from 25 to 45 percent of the initial strain energy. This loss seems to be about equally divided between the energy lost during propagation and that lost after arrest.

(3) The introduction of higher order terms seems to affect much more the shape of the isochromatic fringes than the isopachic fringes or caustics. In fact only the diameter of the caustic appears to change when higher order terms are introduced and this change cannot be separated from changes due to increased loading states.

(4) The K_a value and the K vs $\dot{a}$ relationship for 4340 steel are both dependent on the heat treatment given to the steel.

(5) The K-$\dot{a}$ relationship for 4340 steel displays increases in K with increases in crack velocity, with the rate of increase depending on the heat tint. No indication of a negative slope region is apparent.

(6) The two-dimensional, finite element computer code developed by the University of Maryland can be applied so as to predict quite well, stress intensity and crack growth as functions of time, when compared to laboratory results in CLWL-MCT specimens of Homalite 100. Predicted crack jump distances are, however, consistently greater than those observed experimentally, which is consistent with the computer code assumption of no damping energy losses.

(7) The two-dimensional finite difference code developed by BCL also gives similar results to (6) above, though the predicted crack jumps are somewhat larger than that obtained from the finite element computations, a..d crack propagation occurs at higher velocities than experimentally observed.

TABLE OF CONTENTS

TABLE OF CONTENTS
(continued)

LIST OF FIGURES

xi

LIST OF FIGURES
(continued)

LIST OF FIGURES

(continued)

LIST OF FIGURES
(continued)

Signature Page

This report entitled "Photoelastic Studies of Damping, Crack Propagation, and Crack Arrest in polymers and 4340 Steel" was prepared by the Department of Mechanical Engineering at the University of Maryland (College Park Campus) under Contract No. NRC-04-06-172 for the U. S. Nuclear Regulatory Commission. The research work described in this report was conducted from October 1, 1978 to September 30, 1979.

Messrs. C. Z. Serpan, Milt Vagins, and Pedro Albrecht of the Metallurgy and Materials Branch, Division of Reactor Safety Research, served as technical monitors. In addition to the listed authors, several other individuals were responsible for the research results. Prof. J. W. Dally was principal investigator until his departure to become Dean of Engineering at the University of Rhode Island in May of 1979. Dr. J. W. Phillips of the University of Illinois and Dr. Joachim Bienert of the Institut für Festkörpermechanik were involved in determining the effects on K of higher order terms using optical methods. Mr. M. Nutter assisted in performing many of the experiments and several students, F. Quigley, I. Sachs, M. Savell, and W. Schroeder assisted in data analysis and figure preparation.

In addition, partial support for the c   er time used was provided by the University of Maryland Computer Science C   er, whose facilities were extensively used.

Respectfully submitted,

G. R. Irwin, Visiting Professor

W. L. Fourney, Professor

D. B. Barker, Assistant Professor

J. T. Metcalf, Assistant Professor

R. J. Sanford, Visiting Professor

A. Shukla, Research Assistant

R. Chona, Undergraduate Research Assistant

1.0 Introduction

This is the fifth annual report and describes results from a research program dealing with characterization of several aspects of dynamic fracture. The program has several objectives as listed below:

. Determine the relationship between crack velocity, a, and stress intensity factor, K, for several different materials, including Homalite 100, Araldite B, other epoxies, and various heat treats of 4340 steel.

. Determine the amount of energy lost in damping during a run-arrest event in several different materials including Homalite 100, Araldite B and 4340 steel.

. Determine the manner in which the stress intensity decreases from the high static pre-initiation value to the lower dynamic value.

. Develop a 2D finite element computer code to predict crack propagation and arrest from a dynamic energy balance criterion.

. Compare the predicted crack growth from the BCL two dimensional finite difference code with experimental laboratory results in Homalite 100.

. Compare the crack growth predicted from the University of Maryland computer code with experimental laboratory results.

. Improve methods for determining the instantaneous stress intensity factor K from isochromatic and isopachic fringe patterns and from the method of caustics by investigating the influence of higher order terms.

. Provide consulting services for NRC.

This research program is part of a much larger co-ordinated effort involving BCL (Hahn, Kanninen and Hoagland), MRL (Ripling and Crosley), and the University of Illinois (Corten). The progress made in characterizing the dynamic aspects of fracture is due to the combined efforts of the four laboratories and the free exchange of ideas, data, codes and experience.

This report includes four chapters and an appendix in addition to the introduction.

Chapter 2 deals with:

a) The decrease in stress intensity with time from high initiation values (K_Q) to lower dynamic values $(K(t))$ associated with a running crack.

b) Damping losses in Araldite B, Homalite 100, and 4340 steel.

c) Damping losses associated with post arrest in Homalite 100.

It was prepared by Arun Shukla, J. T. Metcalf and W. L. Fourney.

Chapter 3 investigates the effect of higher order terms (up to 6) on K determination using optical techniques (isochromatic fringes, isopachic fringes, and caustics). It was prepared by R. J. Sanford (on sabbatical leave from NRL), J. W. Phillips (on sabbatical leave from the University of Illinois) and J. Beinert (visiting from Institut für Festkörpermechanik).

Chapter 4 describes a two dimensional, finite element, computer code developed by J. M. Etheridge of NSWC (who served as a consultant to the research program) that predicts dynamic crack propagation and arrest. Comparisons made of output from this code, the BCL 2-D finite difference code and laboratory experiments in Homalite 100 are also described. This chapter was prepared by R. Chona, W. L. Fourney, and G. R. Irwin.

Chapter 5 was written by D. B. Barker and presents results of tests conducted on different heat treats of 4340. K vs a curves were determined by using high speed photography in conjunction with photoelastic coatings.

The appendix contains the results obtained by the University of Maryland in the E24.01.06 ASTM cooperative test program and was prepared by D. B. Barker.

The research program was under the direction of J. W. Dally from October 1, 1978 to May 1, 1979. W. L. Fourney became principal investigator at that time and was responsible for the program through September 30, 1979.

G. R. Irwin has served as a consultant to NRC throughout the year, and in addition, has provided advice on the operation of the overall research program. In addition to those who participated in the report writing as previously mentioned, two other individuals contributed to the research results. These were H. P. Rossmanith from the Technical University of Vienna, Austria, and E. Gdoutos from the Democritus University of Thrace, Xanthi, Greece, who joined the research team for two months during the summer of 1979.

2.   Energy Loss in Homalite 100, Araldite B, and 4340 Steel During
      Crack Propagation and Arrest

2.1 Introduction

Most analytical studies of dynamic crack propagation [2.1, 2.2, 2.3]
use an energy balance between kinetic energy, T, strain energy, U, and the
energy required to extend the crack a unit distance, $\mathcal{G}$, with little or no
attention being paid to energy dissipation during crack propagation and
the initial arrest phase where re-initiation can occur.

It is possible to identify three major sources of energy dissipation
during crack propagation: (1) an inevitable loss of energy when the system
changes from a static to a dynamic configuration; (2) energy lost by high
frequency stress waves (generated during the drop in K at the crack tip from
a high K_Q to some lower value, K(t)) as they travel through the material; and
(3) energy absorbed by the impingement of rough fracture surfaces behind an
advancing crack front. The first possible source of energy loss stems from
the second law of thermodynamics, and would be important in polymers, where
static and dynamic elastic modulii can differ considerably. On the other hand,
the third source mentioned above would be especially important in metals, where
fracture surfaces with many late-breaking ligaments are well-known.

The sources of energy loss listed above are felt to be the most important
ones associated with crack propagation, though several additional sources of
energy loss do exist. For example, low amplitude stress waves are released
when microcracks form in the fracture process zone, and much of their energy
is lost due to internal friction as they reflect from the boundaries and return.
If vibrations occur in the specimen at the time of crack arrest, this kinetic
energy is also lost due to damping. These vibrations can be important, because
they can determine whether the crack reinitiates or stays arrested.

4

This chapter describes experimental methods used to determine the amount of energy dissipated during a run arrest event in fracture specimens made of Homalite 100, Araldite B, and 4340 Steel. Two different approaches were used to analyze the damping that occurred during the experiments. One utilized a balance of the energy in the system and the energy loss was evaluated as

$$E_d = U_i - U_a - E_f \qquad (2.1)$$

where

E_d is the total energy loss,

U_i is the initial strain energy in the system,

U_a is the final strain energy in the system after arrest and ring down, and

E_f is the fracture energy.

The use of eq. (2.1) implies that no energy is added or removed from the fracture specimen during the run arrest event by the loading system. Several experimental studies [2.4, 2.5, 2.6] have showed that such interactions do occur and because of this interaction, E_d could not be measured. To avoid this difficulty the loading system was carefully designed to give fixed grip conditions. In addition, the displacement of the loading members was monitored during the run arrest event to ensure that the fixed grip condition was actually achieved.

The model geometry used in conjunction with this approach was that of a Modified Compact Tension specimen. Specimens were loaded with fixed grip conditions and the initial strain energy, U_i, was determined. The crack was initiated and the isochromatic fringe

5

loops associated with the propagating or arrested crack were photo-graphed with a high-speed recording system to obtain the data neces-sary to determine E_f. After arrest and ring down, U_a was determined from the final crack length and load. Using this approach all of the data necessary to determine E_d was obtained. Considerable care was exercised to minimize error in each of the measurements so as to provide relatively accurate estimates of E_d.

The second approach is relatively simple and involved a compari-son of static and dynamic energy release rates $\mathcal{G}$ which were experi-mentally obtained as a function of crack length. Analytically, the energy balance equation in this case can be written as

$$E_d = h\left[\int_{a_0}^{a_f} \frac{K_s^2}{E_s}\,da - \int_{a_0}^{a_f} \frac{K_d^2}{E_{dyn}}\,da\right] \tag{2.2}$$

where

K_s is the static stress intensity factor

K_d is the dynamic stress intensity factor

E_s is the static elastic modulus

E_{dyn} is the dynamic elastic modulus

h is the specimen thickness

a is the crack length.

The motivation that led to developing this second method of analysis, eq. (2.2), was to make the study of damping simpler. Since photoelasticity is currently being used for fracture studies of opaque materials through the use of birefringent coating [2.7], this method should find wider applications. Moreover, the photoelastic method makes it possible to study damping in complicated geometries without

6

designing any special fixtures for the measurement of load or displacement (assuming that the load pins are fixed during the event).

The specimen used to demonstrate this second approach was a ring segment and was chosen to emphasize the fact that the method could be used with non-simple geometries. Moreover, the specimen is of interest since it simulates a thermally loaded thick walled cylinder as used for nuclear reactor vessels.

Both of the experimental procedures discussed give the total energy lost during propagation and after arrest. A series of experiments was performed to partition this energy into loss that occurred during propagation and loss after arrest. In these experiments, oscillations in stress intensity which occur in the post arrest period were studied to evaluate energy dissipation after arrest. With this information and knowing the total loss, it was possible to evaluate energy dissipation during propagation

To ensure accuracy in determining energy losses by either techniques it is necessary that all the quantities in equations (2.1) and (2.2) be measured as precisely as possible. The measurement of strain energy both prior to and after the run arrest event does not pose much difficulty since the measurements made are static ones and sensitive instruments are available for this purpose. Obtaining dynamic values of stress intensity which are extremely accurate is much more difficult to accomplish. Of particular concern is the manner in which the stress intensity changes from a relatively high static value (K_Q) to much lower dynamic values over extremely short periods of time. This information is not normally available from dynamic photoelastic tests as there is an inherent delay in the multiple spark

7

gap system used to record the dynamic fringe patterns. A series of experiments to be described in this chapter were conducted to determine the manner in which this transition from static to dynamic stress intensity occurs.

2.2 Dynamic Crack Behavior at Initiation

Recent studies in fracture mechanics have concentrated on the determination of the stress intensity which exists at the tip of a running crack. In particular it has been shown that crack velocity $\dot{a}$ depends upon the instantaneous stress intensity $K(t)$ and that the crack will branch when $K(t) \geq K_b$ and will arrest when $K(t) \leq K_m$ [2.8, 2.9, 2.10, 2.11]. The quantities K_b and K_m are the branching and arrest toughness, respectively.

Despite numerous experimental studies which characterize the dynamic behavior of crack propagation in materials, little is known about the transition from the static K to the dynamic K associated with a crack propagating at high velocity. The primary reason for the lack of data in this transition region is the excessive time (10 to 20 μs) required to initiate high speed photographic systems used to record the movement and stresses associated with the initiating crack.

This section describes an experimental approach used to examine the transition from a static crack to a crack propagating at high velocity. Measurements involve the rapid changes in $K(t)$ immediately after initiation and the average acceleration of the crack over the initiation period.

8

2.2.1 Experimental Procedure

The model employed in this study was a Modified Compact Tension specimen machined from 12.7 mm thick sheets of Homalite 100 as illustrated in Fig. 2.1. A near crack line load was applied with a split D type fixture which was inserted in the 3 in. (75 mm) diameter hole. The split D fixture was forced apart with a transverse wedge to give a specified value of K_Q (static stress intensity factor) at the first blunt crack tip. The crack was initiated at the first crack tip by drawing a sharp knife edge across the tip of the blunted crack.

The crack initiated and propagated across the ligament cutting through a strip of silver conducting paint before coming to arrest at the small hole which terminates the ligament. Cutting the silver conducting line provides an electrical pulse which is used to initiate the Cranz-Schardin camera [2.12] used to record the dynamic event.

After the crack arrests at the hole, the value of K at the tip of the second crack begins to increase until it becomes sufficiently large to produce reinitiation at the second crack tip. The bluntness of the second crack is controlled so that the crack remains at arrest for a relatively long time (approximately 200 μs) and reinitiation occurs at high values of K_Q.

The Cranz-Schardin camera was operated with an inter frame time of 5 μs (i.e., 200,000 frames/sec) and initiated so as to record the increase in K at the stationary crack prior to initiation and the dynamic value of K(t) immediately after initiation.

The value of K was determined from the isochromatic fringes which appear as loops at the crack tip as illustrated in Fig. 2.2.

2.2.2 Results

Five different experiments were conducted with K_Q ranging from 1.48 to 1.14 MPa$\sqrt{m}$. The instantaneous values of the stress intensity factor were determined from the dynamic isochromatic fringe loops by using the multiple-point over-deterministic method developed by Sanford and Dally [2.13]. A dynamic correction following the procedure developed by Irwin and Rossmanith [2.14] was made to account for the effect of velocity on K(t).

The results obtained for the five experiments are shown in Table 2.1. Typical results showing the variation in K with time and the position of the crack tip with time are shown in Fig. 2.3 and Fig. 2.4. These results show that K increases monotonically at the arrested crack until K_Q becomes large enough to produce initiation at the second crack tip. After initiation it is not possible to determine K from the isochromatic fringe loops until the shear stress wave has cleared the near field region (r = 5 mm and t = 4 μs). In the first frame after the shear wave has cleared the near field region (about 8 to 10 μs after initiation), the value of K(t) was determined. The decrease in K is quite rapid, for example K decreases from K_Q = 1.29 MPa$\sqrt{m}$ to K(t) = 0.81 MPa$\sqrt{m}$ in 8 μs.

The graph of crack position as a function of time (Fig. 2.3) indicates that the crack propagated at essentially constant velocity (342.9 m/s) after initiation. By extrapolating from the stationary crack and from the straight line with a slope of $\dot{a}$, a close estimate (i.e. ±0.2 μs) of the initiation time t_i = 34.7 μs can be made. The crack was observed at t = 36.5 μs at a position a = 0.62 mm propagating with velocity $\dot{a}$ = 342.9 m/s. If it is assumed that the acceleration of the crack is

10

uniform over the initiating time $\Delta t = 36.5 - 34.7 = 1.8$ μs, then the acceleration of the crack at initiation may be estimated from $\ddot{a} = \dot{a}/\Delta t = 2 \times 10^7$ g's. Since the initiating time Δt may be less than the 1.8 μs measured in this experiment, it is probable that crack tip acceleration in Homalite 100 is even higher.

It is interesting to note that initiation acceleration is of the same order as the crack tip deceleration in an abrupt arrest situation [2.15].

2.2.3 Conclusion

The experiments described above have revealed that the decrease in stress intensity from the high static value to the lower dynamic value is very rapid. As can be seen from Table 2.1, dynamic stress intensity values forty percent lower than the initiation values were reached in about 10 μs. This knowledge permits extrapolation of dynamic stress intensities towards crack initiation with greater confidence.

Table 2.1

Results from Five Test Specimens.

Test No.	K_Q (MPa√m)	t (μs)	K(t) (MPa√m)	$K(t)/K_Q$
1	1.48	15	0.69	0.47
2	1.35	10	0.81	0.60
3	1.29	8	0.81	0.63
4	1.18	10	0.81	0.69
5	1.14	10	0.71	0.62

2.3 Energy Loss During a Run Arrest Event.

2.3.1 Introduction

Damping losses for Modified Compact Tension samples made from Homalite 100, Araldite B, and 4340 steel were determined by computing the difference between strain energies and fracture energy. Eq. (2.1) from Section 2.1 was utilized, which gives the damping energy as the initial strain energy less the energy used to create the fracture surfaces and the strain energy remaining at the conclusion of the test. The geometry of this specimen is shown in Fig. 2.5 and was chosen since the crack path is easy to control and because arrest occurs even for high values of K_Q. Figure 2.6 shows the split D and transverse wedge used to load the sample. The split D's were fitted into the circular hole and a hydraulic cylinder was used to pull the wedge between them.

After the specimen was loaded to a specified value of K_Q (and U_i), the wedge was locked into a fixed position. In addition, two stops were placed along the load line on the outer edges of the specimen, to prevent any outward displacement during crack propagation and arrest. Displacement of the split D's was also monitored with an eddy current transducer to ensure that fixed grip conditions were achieved.

2.3.2 Strain Energy Determination

The initial strain energy U_i was determined from

$$U_i = \int_0^\Delta P d\Delta \qquad (2.3)$$

which is the area under the load displacement curves for the MCT specimen with a prescribed crack length a. To determine U_i, the relation between the load, P, and the split D displacement, Δ, was established with a

12

compliance calibration. The load P was measured with a quartz load cell positioned between the wedge and the split D fixture. The displacement was measured with an eddy current transducer which bridged the gap on the split D fixture. Accuracies of ± 0.025 mm and ± 4 N were achieved in the determination of Δ and P, respectively.

P vs Δ curves were obtained for the MCT specimen with about six different crack lengths as shown in Figs. 2.7 and 2.8. The results exhibit an initial nonlinearity which is probably due to the Hertzian contact displacements and is more pronounced in Homalite 100 as compared to Araldite B. Results for the compliance calibration were also displayed with the load as a function of crack length for a constant pin displacement as illustrated in Figs. 2.9 and 2.10. These results are of interest because the displacement of the split D is maintained at a constant value during the run-arrest event.

2.3.3 Material Properties

All polymeric photoelastic materials exhibit a change in the modulus of elasticity E with loading rate, Homalite 100 and Araldite B are no exception. Thus, it is important to determine an appropriate value of E which can be used to determine the fracture energy E_f from the data obtained for the instantaneous stress intensity factor $K(t)$. Two experiments were performed to bracket the value of E.

First, standard tensile tests were conducted to obtain a static modulus which corresponded to a loading time of about 10^3s. Second, a half-plane model was loaded with a small charge of lead azide, PbN_6, and a series of photoelastic patterns representing the propagation of the dilatational and shear waves were recorded. The wave velocities c_1 and c_2 were

13

determined and the dynamic modulus E_{dyn} was computed using c_1 and c_2. The loading time in this experiment was about 10^{-5}s.

As the loading time in a fracture experiment is between the static and dynamic loading times used in these two determinations of the modulus, an average value of E was used in the subsequent data analysis. Elastic moduli, as well as the photoelastic properties used in these experiments are listed in Table 2.2. The determination of the photoelastic properties is discussed in Reference [2.16].

2.3.4. Fracture Energy Determination

Dynamic photoelastic experiments were performed with M-CT specimens of Homalite 100 and Araldite B. The specimens were loaded to a preselected value of K_Q and the crack was initiated by pulling a sharp knife across the crack tip. As the crack began to propagate, it cut a line of silver conducting paint and initiated a multiple spark Cranz-Schardin camera. The camera was operated at a framing rate of 33,000 fps and provided sixteen isochromatic photographs at discrete times during the run-arrest event. Figure 2.11 presents nine frames showing the typical isochromatic patterns around a crack propagating at medium velocity in an M-CT specimen of Homalite 100.

2.3.5 Analysis and Results

The initial strain energy U_i in the specimen was determined by numerically integrating the area under the P vs Δ curves shown in Figs. 2.7 and 2.8, according to Eq. (2.3). The method employed was a trapezoidal rule of integration with a step size of 0.05 mm. The final strain energy in the specimen was determined in the same manner

14

Table 2.2

Elastic Modulii and Photoelastic Constants for
Homalite 100 and Araldite B

Material	Static E (GPa)	Dynamic E (GPa)	E_{avg} (GPa)	Static f_σ (MPa-m/fr)	Dynamic f_σ (MPa-m/fr)
Homalite 100	4.42	4.83	4.62	0.02207	0.02452
Araldite B	3.36	3.65	3.51	0.00982	0.00990

using a calibration curve from Figs. 2.7 and 2.8, corresponding to the final crack length, a_f, after arrest.

The energy required to produce fracture, E_f, was obtained from photoelastic data. This data was analyzed to obtain the stress intensity factor $K(t)$ and the velocity of the crack $\dot{a}$. The method of Sanford and Dally [2.13], modified to include dynamic effects [2.14], was used to determine K. The results of $K(t)$ as a function of crack tip position are shown in Fig. 2.12 to 2.23 for tests of both Homalite 100 and Araldite B. The results indicate that $K(t)$ for the propagating crack was close to K_{Im} for the material. The data also showed that K oscillated as the crack extended in dynamic propagation as shown in Fig. 2.24.

The amplitude of the oscillation of K is about 10 percent of the mean value and the frequency of oscillation is about 5,000 Hz. These oscillations are probably due to the dynamic vibratory behavior of the specimen during crack propagation. The scatter might be partly due to the experimental error. Crack tip position as a function of time was also plotted and the results are shown in Figs. 2.25 to 2.31 for tests D-1 to D-7 of H-100. The velocity of the crack in these experiments was about 250 m/s after initiation and decreased until arrest.

Curves showing K^2 as a function of a/w were also plotted for each experiment. Typical results for Homalite 100 and Araldite B are shown in Figs. 2.32 and 2.33. The energy E_f was determined from the K^2- a/w relation by:

$$E_f = \frac{h}{E_{av}} \int_{a_0}^{a_f} K^2(a)da \qquad (2.4)$$

16

where h is the specimen thickness

E_{av} is the average modulus

a_o is the initial crack length

and a_f is the final crack length.

Results for seven experiments conducted with two different sheets of Homalite 100 (Tests D-1 to D-7) are presented in Table 2.3 and Table 2.4. The initial strain energy in the experiments was varied from 0.111 to 0.182 J to cover the range of crack jump distances $(a_f - a_o)$ of interest. It was observed that the crack jump distance increased with U_i. A similar technique was used for Araldite B experiments, and the results are shown in Table 2.5.

The energy loss due to damping, E_d, ranged from 35% to 47% of the initial strain energy in Homalite 100. For Araldite B, this energy loss ranged from 22% to 38%. Although a specific relationship between E_d and U_i could not be developed it was observed that E_d increased with an increase in U_i. The ratio of E_f/E_d was slightly greater than 1 (about 1.2) for the second sheet of Homalite 100 and slightly smaller than 1 (about 0.75) for the first sheet of Homalite 100. For Araldite B, this ratio ranged from 1.1 to 2.5. The main point to be made here is that fracture and damping energies are comparable in all the experiments except Test 418 (Araldite B). This fact is illustrated in Figs. 2.34 and 2.35, which show E_f as a function of E_d for Homalite 100 and Araldite B, respectively.

2.3.6 Study of Energy Loss in 4340 Steel

The energy balance criterion given in eq. (2.1) was utilized to study energy loss in Modified-Compact-Tension specimens fabricated from 4340 steel. The geometry of the specimen is shown in Fig. 5.2.

17

Table 2.3

Summary of Results for Homalite 100 Sheet I

Expt. No.	U_i (Joules)	Crack Jump (mm)	Fracture Area ($m^2 \times 10^{-3}$)	E_f (Joules)	U_f (Joules)	E_d (Joules)	E_d/U_i
D-1	0.182	102	1.26	0.085	0.012	0.085	47%
D-2	0.139	69	0.87	0.057	0.022	0.060	43%
D-3	0.129	68	0.85	0.051	0.019	0.058	45%
D-4	0.126	64	0.81	0.050	0.019	0.058	46%

Table 2.4

Summary of Results for Homalite 100 Sheet II

Expt. No.	U_i (Joules)	Crack Jump (mm)	Fracture Area ($m^2 \times 10^{-3}$)	E_f (Joules)	U_f (Joules)	E_d (Joules)	E_d/U_i
D-5	0.162	86	1.08	0.078	0.013	0.071	44%
D-6	0.120	79	0.98	0.064	0.012	0.044	36%
D-7	0.111	60	0.76	0.048	0.024	0.039	35%

Table 2.5

Summary of Results for Araldite B

Model No.	Δa (m)	h (m)	U_i (Joules)	E_f (Joules)	U_f (Joules)	E_d (Joules)	E_d/U_i
412	7.19×10^{-2}	9.97×10^{-3}	0.1709	0.1023	0.0281	0.0405	23.7%
413	7.12	10.01	0.1807	0.0981	0.0334	0.0492	27.2%
414	7.22	9.90	0.2022	0.0952	0.0518	0.0552	27.3%
4.5	8.46	9.95	0.1968	0.1092	0.0276	0.0600	30.5%
416	7.29	10.02	0.1928	0.0983	0.0515	0.0430	22.3%
418	8.85	9.92	0.1597	0.1278	0.0185	0.0134	8.4%
419	9.66	9.80	0.3133	0.1420	0.0656	0.1057	33.4%
420	9.51	9.84	0.3064	0.1315	0.0579	0.1170	38.2%
421	5.85	9.87	0.1881	0.0717	0.0738	0.0426	22.6%

Strain energy in the specimen was measured using the compliance equations developed by BCL [2.17]. First, the displacement on the specimen was measured at $a/w = 0.25$ from the load line. This displacement was then converted to the load line displacement by the new relations of Kalthoff and BCL [2.17]. Knowing the displacement and the crack length it was possible to calculate the load from the compliance equations. The value of the elastic modulus used in this calculation was 230.60 GPa. Note that the effect of face grooves is neglected in this calculation as the effect is believed to be small. Finally, the strain energy was evaluated from eq. (2.3).

To evaluate energy loss in forming the fracture surface, dynamic experiments similar to the ones described above for Homalite 100 and Araldite B were performed. Values of dynamic stress intensity factor were evaluated by the procedure discussed in Chapter 5. K^2 was plotted as a function of crack length as shown in Fig. 2.36 and 2.37. Fracture energy was then evaluated from eq. (2.4).

The results from the analysis of two experiments are shown in Table 2.6. Some of this energy loss obviously occurs in the formation of ligaments on the fracture surface as shown in Fig. 2.38. In test S-2 there was some change in displacement of the split D's during the test which could explain the lower value obtained for energy loss. This data is preliminary and more extensive evaluations are presently underway.

2.4 Partitioning of Damping into Energy Loss During Propagation and After Arrest

2.4.1 Introduction

Numerical techniques using an energy balance criterion can predict

21

Table 2.6

Summary of Results for 4340 Steel

Test No.	U_i (Joules)	E_f (Joules)	U_f (Joules)	E_d (Joules)	E_d/U_i
S-1	120.78	49.03	24.97	46.78	39%
S-2	95.47	50.88	18.87	25.72	27%

crack jump distances and stress intensity factors with greater accuracy
if energy losses during propagation and after arrest are known separately.
The balance used in eq. (2.1) gives the total energy lost in damping but
does not give a separate estimate of the energy loss during propagation
as opposed to that after arrest. In this section, a method is developed
which uses oscillations in the stress intensity factor, K, in the post
arrest period to approximate energy losses after arrest. Knowing this and
the total energy loss it is possible to evaluate the energy loss during
propagation from

$$E_d = E_{dp} + T_a \qquad\qquad (2.5)$$

where E_{dp} is the energy loss during propagation,

and T_a is the kinetic energy available in the specimen at the arrest
        time t_a.

2.4.2 Analysis

The method of analysis utilizes oscillations in K in the post arrest
period to compute the total kinetic energy T_a available in the specimen at
the instant of arrest. This kinetic energy is continuously converted to
strain energy and back to kinetic energy until all the particles in the
specimen come to rest. As a consequence of this continuous conversion
of energy, the value of K oscillates. During this transition process,
energy is lost in the specimen in a manner analogous to a simple pendulum
which loses energy in overcoming the friction of air and comes to rest as
time goes to infinity. Analytically, T_a can be computed from

$$T_a = \frac{U_i}{K_Q^2} (K_p^2 - K_s^2) \qquad\qquad (2.6)$$

23

where U_i is the initial strain energy,

K_Q is the static stress intensity factor associated with the blunt starter crack of length $a_o/w = 0.4375$,

K_p is the stress intensity factor at the peak of oscillation,

and K_s is the static stress intensity factor after the ring down of oscillations.

Eq. (2.6) follows from the fact that in a quasi-static situation, all the strain energy available for fracture surface formation in a specimen appears at the crack tip as stress intensity factor, K_Q, and we can write

$$U_i \propto K_Q^2 \tag{2.7}$$

When the crack comes to a static configuration in a run arrest event, a similar situation occurs, and the strain energy corresponding to the arrested length of the crack, U_s is proportional to K_s^2.

$$U_s \propto K_s^2 \tag{2.8}$$

However, at the instant when the crack comes to arrest we have some additional kinetic energy present in the specimen. This kinetic energy undergoes a decaying cyclic transition and increases the value of U_s in cycles. At any peak of this cycle we assume that all of the energy in the specimen is in the form of potential strain energy and is thus proportional to K_p^2.

Then,

$$(U_s + T_a) \propto K_p^2 \tag{2.9}$$

and

$$T_a \propto K_p^2 - U_s \tag{2.10}$$

which can be rewritten, assuming $U_s \simeq K_s^2$, as

$$T_a \propto K_p^2 - K_s^2 \tag{2.11}$$

24

Assuming linear elastic properties for the material and dividing eq. (2.7)
by eq. (2.11) we get:

$$\frac{U_i}{T_a} = \frac{K_Q^2}{(K_p^2 - K_s^2)} \tag{2.12}$$

which can be rewritten to yield eq. (2.6):

$$T_a = \frac{U_i}{K_Q^2} (K_p^2 - K_s^2)$$

2.4.3 Calibration of the Specimen Used for Experiments

The loading system and specimen were calibrated to obtain a rela-
tion between the static stress intensity factor, K_Q, associated with a
blunt crack tip, and the displacement, Δ, between the two halves of the
split-D pin. A Modified-Compact-Tension specimen with an initial crack
length of $a_o/w = 0.4375$ was loaded while placed in a light field polari-
scope. The isochromatic fringe patterns obtained were used to evaluate
K_Q by using the multiple-point, over-deterministic method developed by
Sanford and Dally [2.13]. Eight different values of pin displacement,
Δ, were used and the values of K_Q determined. The crack was then extended
and the procedure repeated at the new crack length for the same eight
values of pin displacement. A family of curves of K_Q as a function of pin
displacement Δ was obtained for various crack lengths a_o/w, as shown in
Fig. 2.39. The non-linear segment of the curves may possibly be due to
Hertzian contact stresses between the pin and specimen. K_Q was also
plotted as a function of a_o/w for constant pin displacement, Δ, and the
curves are shown in Fig. 2.40.

2.4.4 Experimental Results

Four dynamic experiments, referred to here as P-1 to P-4, were performed with different values of U_i to study post arrest oscillations. The Cranz-Schardin camera was run at a framing rate of 33,000 fps with an initial delay of about 300 to 400 μs. The isochromatic photographs obtained were analyzed to obtain K, and K was plotted as a function of time. Plots of K versus time for Tests P-1 to P-4 are shown in Figs. 2.41 to 2.44. It is observed that K oscillates with a decaying amplitude and with a frequency of about 8,000 Hz. It is interesting to note that K does not oscillate about K_s in most of the experiments. This could be due to the fact that the modulus of elasticity also undergoes a change as the specimen reaches a static configuration. The results from all the four experiments were analyzed according to eq. (2.6) and are shown in Table 2.7. The results show that about 35-55 percent of the damping energy loss occurs in the post arrest period.

2.5 Comparison of Static and Dynamic Energy Release Rates in Homalite-100: A Study of Energy Losses

2.5.1 Introduction

Static and dynamic photoelastic experiments were conducted in a thick-walled ring specimen during a fracture event. The results of these experiments were used with eq. (2.13) to evaluate the energy lost during the dynamic event.

2.5.2 Analysis

The energy release rate $\mathcal{G}$ is defined as the energy that is released at the tip of a perfect crack, per unit of new separational area, in an

Table 2.7

Results from Post Arrest Experiments

Test No.	Initial Energy, U_i (Joules)	Total Damping Energy, E_d (Joules)	Energy Loss Prior to Arrest, E_{dp} (Joules)	Energy Loss After Arrest, T_a (Joules)	T_a/E_d
P-1	0.167	.067	.034	.033	49%
P-2	0.147	.059	.038	.021	36%
P-3	0.121	.045	.028	.017	38%
P-4	0.090	.036	.016	.020	56%

elastic solid, during an infinitesimal, virtual increment of forward
crack extension. Analytically, $\mathcal{G}$ is written as

$$\mathcal{G} = A \frac{K^2}{E} \tag{2.13}$$

where K is the stress intensity factor,

E is the elastic modulus, and

A is a factor which increases gradually from unity with increase
of crack speed.

In these experiments crack speed was small enough so that A can be taken to
be unity.

If the average value of $\mathcal{G}$ during crack propagation is multiplied
by the total surface area formed, one obtains the net energy absorbed
in forming that fracture surface. This is the basic concept used in this
damping analysis.

If the crack is extended in a quasi-static or static manner, then
all of the strain energy loss in the specimen appears in the form of energy
release rate at the crack tip. Thus, if the area beneath the static
curve of K^2/E versus crack length is evaluated, it gives the initial
strain energy in the specimen per unit thickness provided the crack is
extended from a_o to the outer boundary. Therefore, the first integral
on the right side of eq. (2.2) represents the portion of the initial strain
energy in the specimen released at the crack tip during quasi-static
crack growth. The second integral in eq. (2.2), by a similar argument,
represents the energy released at the crack tip in forming the fracture
surface during dynamic crack propagation. The difference between the two
integrals then gives the total energy loss during crack propagation and
after arrest, per unit thickness of the specimen. It is noteworthy that

28

eq. (2.2) does not contain, in explicit form, the final strain energy
left in the specimen at the instant of crack arrest.

2.5.3 Experimental Procedure

The specimen selected for the study was a ring with an inner
radius r_i = 101.6 mm and an outer radius r_o = 228.6 mm (r_o/r_i = 2.25).
The specimen was fabricated from a 12.7 mm thick sheet of Homalite 100
and is shown in Fig. 2.45.   The specimen geometry and loading prevent the
measurement of strain energies by the compliance calibration method, and
this emphasizes the effectiveness of the analysis outlined in the previous
section. Moreover, a crack propagates in pure opening mode in this
specimen, and crack arrests are obtained for a substantial range of values
of K_Q.

The specimen was loaded by a specially designed mechanical defor-
meter as shown in Fig. 2.46   The deformeter was massive and rigid as com-
pared to the relatively flexible photoelastic model.

First, the static stress intensity factor was determined as a
function of crack length in a manner similar to that described earlier
in Section 2.4.3 for the M-CT specimen. The crack length was increased
from test to test, and the fringe patterns recorded while the pins were
held fixed at the derived pin displacement by means of spacers. Three
different values of pin displacement were used, and curves of K_S vs a/w
obtained. These curves are shown in Fig. 2.47. It was observed that K_S
increased until a/w = 0.2, after which K_S decreased monotonically, tending
towards zero as the crack approached the outer boundary (a/w = 1.0).

The next step involved dynamic experiments which were performed to
investigate stress intensity during dynamic crack propagation, and to

29

determine what changes in displacement, if any, occurred at the pins.
Since any movement of the loading pins would result in energy entering
or leaving the system, it was necessary to lock the loading pins after
applying the initial displacement. This was accomplished by clamping the
two halves of the deformeter as shown in Fig. 2.46 with heavy metal plates.

The ring type fracture specimens were loaded to a specified value
of K_Q by applying a predetermined displacement to the pins of the mechan-
ical deformeter, and using the curves of K_s vs a/w obtained previously.
The ratio of K_Q/K_m used in the experiments conducted was 1.76, 1.96 and
2.15.

The starter crack was saw cut into the specimen and the crack tip
rounded to inhibit initiation prior to the desired value of K_Q. The crack
was then initiated by drawing a sharp blade across the tip after the load
was applied. As the crack propagated, it interrupted a silver conductive
paint line on the model and triggered the multiple spark Cranz-Schardin
camera. Typical high speed records of the dynamic isochromatic fringe pat-
terns showing the crack propagating in the ring specimen are shown in
Fig. 2.48. A cursory inspection of the size of the fringe loops at the
crack tip shows that K decreases monotonically throughout the propaga-
tion interval until the crack arrests in the initial compression zone.

2.5.4 Results from the Ring Specimen

Three static and three dynamic experiments, identified here as RS-1
through RS-3 and RD-1 through RD-3, were performed with the ring speci-
mens. The isochromatic fringe loops associated with the crack tip were ana-
lyzed to obtain the values of K_d [2.13, 2.14].

From the static photoelastic results, curves of K_s^2 vs a/w were prepared. The area below the three curves (one for each pin displacement value) was evaluated by using a trapezoidal integration technique with a step size of 0.05 a/w. From this, the static strain energy in the specimen was evaluated from

$$\text{Static Strain Energy} = h \int_{a_o}^{a_f} \frac{K_s^2}{E_s} \, da \qquad (2.14)$$

The results obtained are shown in Table 2.8 . As expected, the value of static strain energy increases as the value of K_Q/K_m is increased.

In experiment RD-1, the specimen was loaded until K_Q/K_m = 2.15. The fracture surface at the conclusion of the test indicated that the crack jumped to a/w = 0.82 before the first arrest occurred. The crack reinitiated and the final arrest of the crack was found to occur at a/w = 0.95. The displacement that occurred during crack propagation at the outer pins was 0.025 mm as shown in Fig. 2.49. This displacement was about 1 percent of the initial displacement given to the pins. If the load in the pins is assumed constant, the energy added to the system due to the above change in displacement would be 1.6 percent of the initial energy.

The load on the pins actually drops during the crack propagation but when the pin displacement is fixed no energy can enter or leave the specimen. For the case where a pin movement is observed an upper bound on the error in the energy calculation can be obtained by assuming a constant load value.

In experiment RD-2, the value of K_Q/K_m used was 1.96 and the crack first arrested at 0.756 a/w from the inner boundary. The final arrest of

Table 2.8

Summary of Results for the Ring Specimen

Test No.	K_Q/K_{Im}	Total Crack Jump $(a_f-a_o)/w$	U_i (Joules)	U_i-U_f (Joules)	E_f (Joules)	E_d (Joules)	E_d/U_i
RD-1	2.15	0.95	0.216	0.214	0.099	0.115	53%
RD-2	1.96	0.92	0.196	0.193	0.096	0.097	50%
RD-3	1.76	0.85	0.182	0.175	0.087	0.088	48%

$$U_i = h \int_{a_o}^{a_f} \frac{K_s^2}{E_s} da \quad \text{where } a_f/w = 1.0$$

$$U_i - U_f = h \int_{a_o}^{a_f} \frac{K_s^2}{E_s} da \quad \text{where } a_o/w < a_f/w < 1.0$$

$$E_f = h \int_{a_o}^{a_f} \frac{K_d^2}{E_{dyn}} da$$

the crack occurred at 0.92 a/w. The displacements in this experiment were monitored at the outer pins and across the starting crack. During the propagation period (about 500 μs), the displacement measured across the starter crack remained essentially constant. The displacement at the outer pins increased as the crack ran and was about 0.15 mm prior to crack arrest as shown in Fig. 2.49. This was about 6 percent of the initial displacement given to the pins.

In experiment RD-3, the specimen was loaded to K_Q/K_m = 1.76 and the crack first arrested at a/w = 0.66. The final arrest of the crack occurred at a/w = 0.85. The displacement in this experiment was monitored at the inner pins. It was observed that this displacement changed by only 0.0075 mm during the propagation period as shown in Fig. 2.49. This displacement was about 0.75 percent of the initial displacement given to the pins. Again, if the load is considered to be constant, an upper bound on the error in calculated energy is obtained. This calculation shows an energy increase of 1.5 percent of the initial energy.

The photoelastic data obtained from these tests were analyzed to determine K, a, and $\dot{a}$. The stress intensity factor, K, was plotted as a function of a/w and is shown in Fig. 2.50. The results show that K decreases monotonically with crack length. It is interesting to note that the dynamic value of K, is within the data scatter, independent of the initial value of K_Q.

A comparison of the K vs a/w relation for statically extended cracks and dynamically running cracks is shown in Fig. 2.51. It is evident from this comparison that a considerable difference exists between the stress intensity factor associated with a statically positioned crack and the crack which achieves the same position by dynamic propagation.

33

The area below the dynamic K^2-a/w curve was evaluated to determine the energy dissipated in forming the fracture surface from

$$E_{fracture} = h \int_{a_0}^{a_f} \frac{K_d^2}{E_{dyn}} \, da \qquad (2.15)$$

The results obtained are shown in Table 2.8.

2.5.5 Conclusions and Discussion

Static and dynamic photoelastic fracture experiments performed with ring specimens fabricated from Homalite 100 showed that a total of about 50 percent of the initial strain energy is lost due to damping during the crack propagation, crack arrest, and post arrest phases. This energy loss can probably be split into three parts. Firstly, energy is lost due to high frequency stress waves which are generated at the sudden burst of the crack at initiation. Secondly, energy is lost in the ringing down of the damped oscillations that occur after arrest. Finally, energy is lost during crack propagation due to internal friction of the material, heat, noise, etc. The total energy lost in damping is observed to be a function of the initial strain energy. As the initial strain increases the energy lost in damping increases. It is interesting to see that in these experiments also, the energy lost in forming the fracture surface is comparable to the energy lost in damping, as was the case for the M-CT samples discussed previously.

The measurement of displacement at the loading pins with a locked deformeter indicated that the pins were essentially stationary during crack propagation. This ensured that proper fixed grip conditions were maintained during the experiment and thus little work was done by the loading system during propagation. This condition is essential for the validity of eq. (2.2).

34

The pin movements observed in experiments RD-1 and RD-3 during propagation phase were less than one percent of the initial displacement. If the load in the pins is assumed to be constant this small pin movement corresponds to an energy increase of only 2 percent. Where the deformeter was not properly locked (RD-2), the displacement increased by about 6 percent which corresponds to an energy increase of 12 percent.

2.6   Conclusions and Discussion

The experiments performed with the Modified Compact Tension specimens indicate that a large percentage (35% to 47%) of the initial strain energy is lost in damping during the crack propagation, crack arrest, and post arrest phases. It was observed that this loss increases as the initial strain energy is increased. Moreover, the energy lost due to damping was found to be comparable to the energy required for new surface formation in all the experiments.

A large number of experiments were performed to minimize any errors caused by the experimental measurements. The results from all the experiments were in close agreement.

There are, however, certain points in the application of this experimental procedure which need further discussion. The displacements were measured on the loading pins and include Hertzian contact displacements that occur between the pins and the specimen. These contact displacements are not completely elastic and as such certain amounts of energy might be lost in plastic or viscoelastic deformations. To estimate the contact displacements, a load-displacement calibration was carried out with displacements being measured on the specimen as opposed to the splid D and the results are shown in Fig. 2.52. It was observed that the contact deformations are substantial as shown in the comparison presented in Fig. 2.53.

If it is assumed that all the contact displacements are plastic, then a lower bound on the energy loss can be established by using the compliance curves of Fig. 2.52. This was done, and the results are shown in Table 2.9. These results still indicate that a substantial amount of the initial strain energy is lost in damping. In some experiments it was observed that a part of the contact displacements were released during the fracture process. This was established by monitoring displacements on the specimen during the fracture process and observing that these displacements do increase during the fracture process even though the split D displacement remains fixed. An exact idea of the percentage of the contact deformations released and the time for complete release is not known at present and calls for further study.

In addition to the uncertainty regarding contact stresses, the average value of the elastic modulus used may not be justified and this might also give slightly different results. The effect of these two complexities is not believed to be large and although some changes might occur, the results are felt to be indicative of the amount of damping which occurs.

Table 2.9

Summary of Results for Homalite 100, Based
Upon Displacement Measurements in the Specimen

Test No.	U_i (Joules)	E_f (Joules)	U_f (Joules)	E_d (Joules)	E_d/U_i
D-1	0.136	0.085	0.004	0.047	35%
D-3	0.096	0.051	0.011	0.034	35%
D-4	0.093	0.050	0.011	0.032	34%
D-5	0.119	0.078	0.004	0.033	31%
D-6	0.088	0.064	0.005	0.019	22%
D-7	0.081	0.048	0.012	0.021	26%

References

2.1 Popelar, C.H. and Gehlen, P.C., "Modeling of Dynamic Crack Propagation: II. Validation of two-dimensional analysis." Int. J. of Fracture Vol. 15, No. 2, April 1979.

2.2 Hahn, et al, "Critical Experiments, Measurements and Analysis to Establish a Crack Arrest Methodology for Nuclear Pressure Vessel Steels." NUREG/CR-0824 BMI-2026, Dec. 78.*

2.3 Kanninen, M.R., Popelar, C. and Gehlen, P.C., "Dynamic Analysis of Crack Propagation and Arrest in DCB Test Specimens." Fast Fracture and Crack Arrest, ASTM STP 627(1977), pp. 19-38.

2.4 Fourney, W.L. and Kobayashi, T., "Influence of Loading System on Crack Propagation and Arrest Behavior in a DCB Specimen." Fracture Mechanics Applied to Brittle Materials, ASTM STP 678(1979), pp. 47-59.

2.5 Crosly, P.B., and Ripling, E.J., Third Annual Report for Electrical Power Research Institute, Project RP 303-1, "Crack Arrest Studies." MRL No. 752.

2.6 Gates, R.S., "Some effects of Specimen Geometry on Crack Propagation and Arrest." Presented at ASTM conference on Fast Fracture, Nov. 1978.

2.7 Zandman, F., Redner, S., and Dally, J.W., Photoelastic Coatings, SESA Monograph No.3, Iowa State University Press, 1977.

2.8 Bradley, W.B. and Kobayashi, A.S., "An Investigation of Propagating Cracks by Dynamic Photoelasticity", Expl. Mech., Vol. 10, No. 3, (1970) pp. 106-113.

2.9 Kobayashi, A.S., Wade, B.G. and Bradley, W.B., "Fracture Dynamics of Homalite 100", Deformation and Fracture of High Polymers, H.H. Kausch, J.A. Hassel, R.I. Jaffee eds, Plenum Press, New York, (1973), pp. 487-500.

2.10 Kobayashi, T. and Dally, J.W., "The Relation Between Crack Velocity and the Stress Intensity Factor in Birefringent Polymers", ASTM STP 627, (1977), pp. 257-273.

2.11 Irwin, G.R., Dally, J.W., Kobayashi, T., Fourney, W.L., Etheridge, M.J. and Rossmanith, H.P., "On the Determination of the à-K Relationship for Birefringent Polymers", Expl. Mech., Vol. 19, No. 4. (1979), pp. 27-33N.

2.12 Riley, W.F. and Dally, J.W., "Recording Dynamic Fringe Patterns with a Cranz Shardin Camera", Expl. Mech., Vol. 9, No. 8, (1969), pp. 27-33N.

---

*Available for purchase from the NRC/GPO Sales Program, U.S. Nuclear Regulatory Commission, Washington, D.C. 20555, and the National Technical Information Service, Springfield, Virginia 22161.

2.13 Sanford, R.J. and Dally, J.W., "A General Method for Determining Mixed-Mode Stress Intensity Factors from Isochromatic Fringe Patterns", Engr. Fract. Mech., Vol. 11, (1979), pp. 621-633.

2.14 Rossmanith, H.P. and Irwin, G.R., "Analysis of Dynamic Isochromatic Crack-Tip Stress Patterns", Univ. of Maryland Report, 1979.

2.15 Dally, J.W. and Kobayashi, T., "Crack Arrest in Duplex Specimens", Intl. J. Solids and Structures, Vol. 14, (1978), pp. 121-129.

2.16 Irwin, G.R. et al., "Photoelastic Studies of Crack Propagation and Crack Arrest", U.S. NRC-Report NUREG-0342, University of Maryland, 1977.*

2.17 Rosenfield, A.R., et al., "Critical Experiments, Measurements and Analysis to Establish a Crack Arrest Methodology for Nuclear Pressure Vessel Steels", Battelle Columbus Laboratories Progress Report, January-June 1979, NUREG/CRO991, BMI-2036.*

---

*Available for purchase from the NRC/GPO Sales Program, U.S. Nuclear Regulatory Commission, Washington, D.C. 20555, and the National Technical Information Service, Springfield, Virginia 22161.
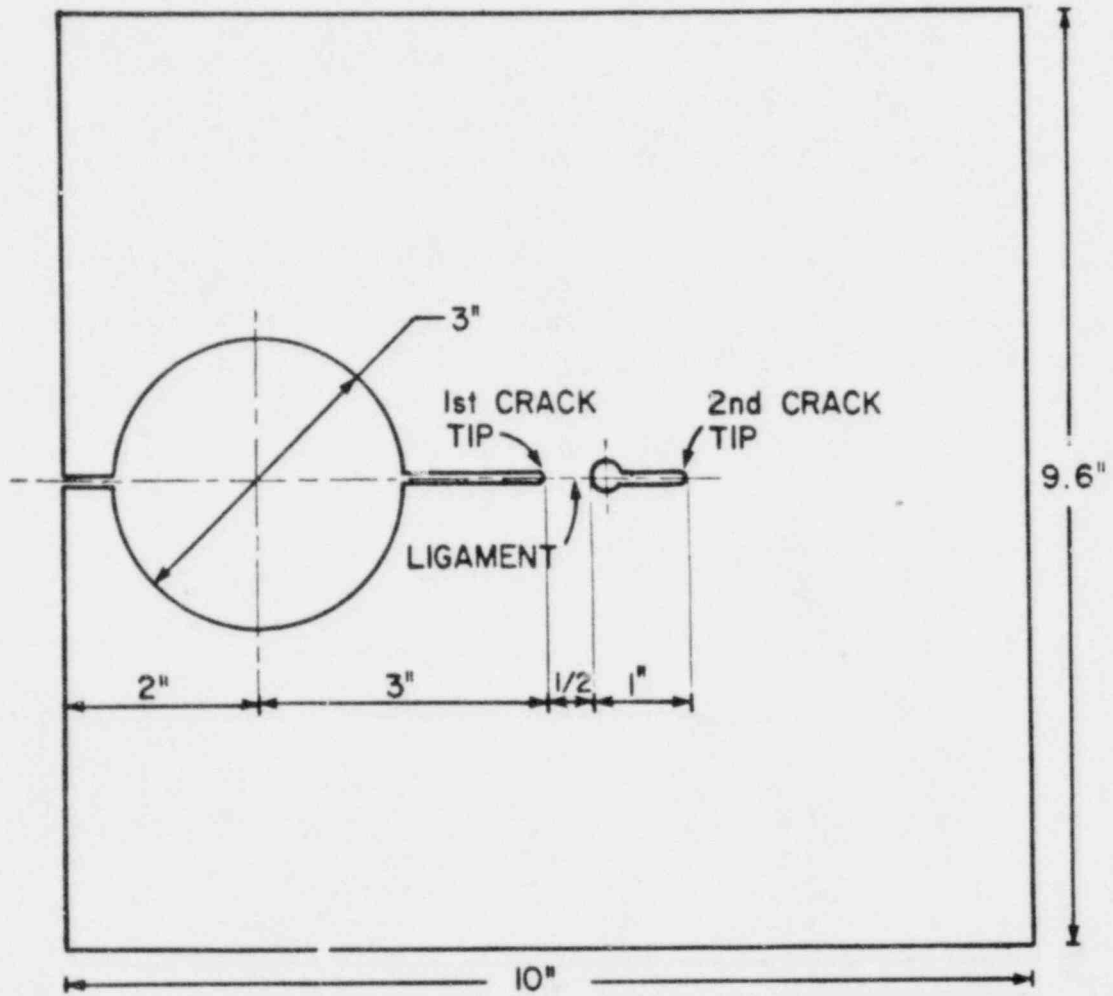
Fig. 2.1   Geometry of the Modified-Compact-Tension Specimen Used to
            Study Crack Initiation Behaviours.
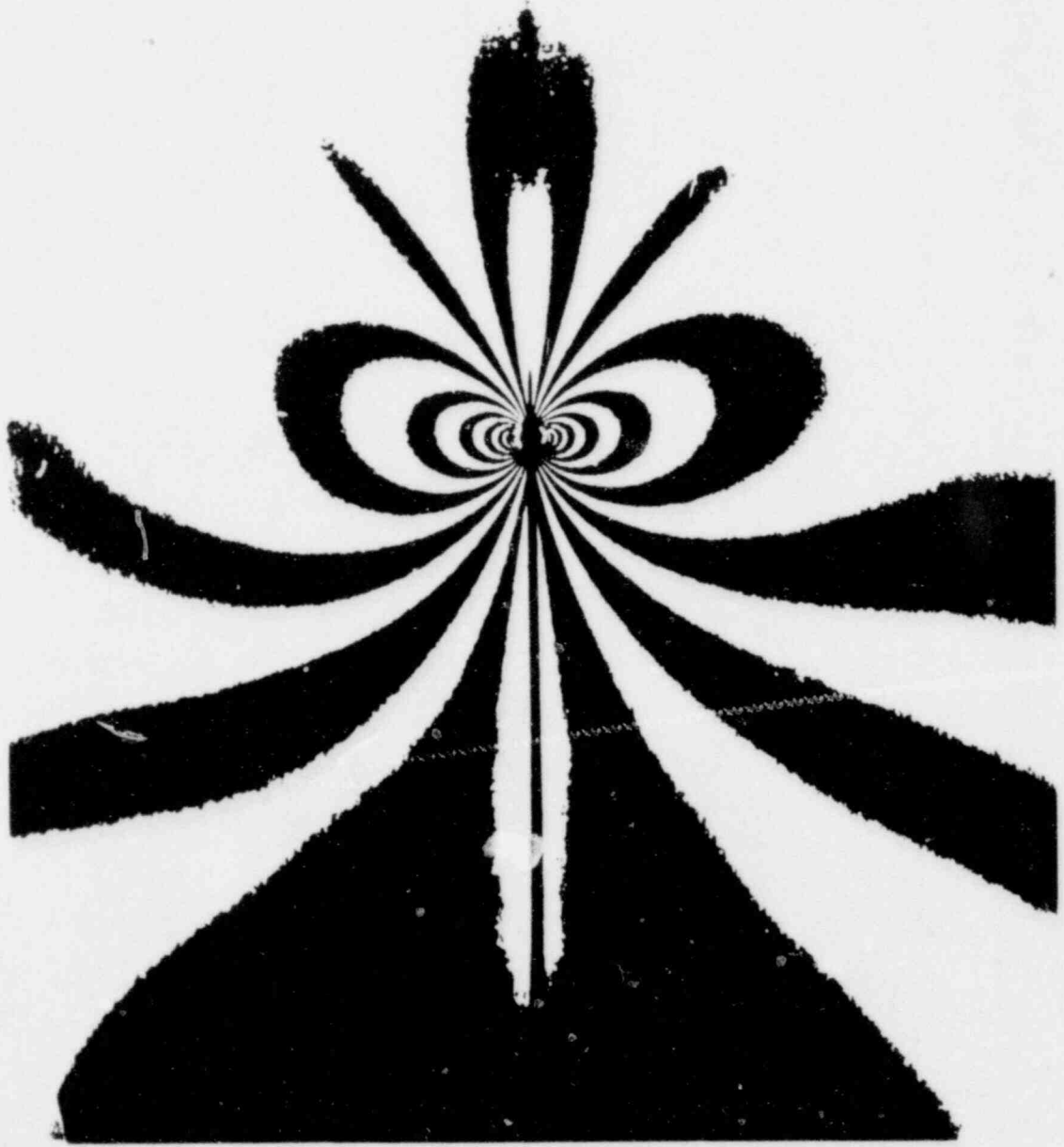
Fig. 2.2 Isochromatic Fringe Loops at the Tip of a Propagating Crack.

41
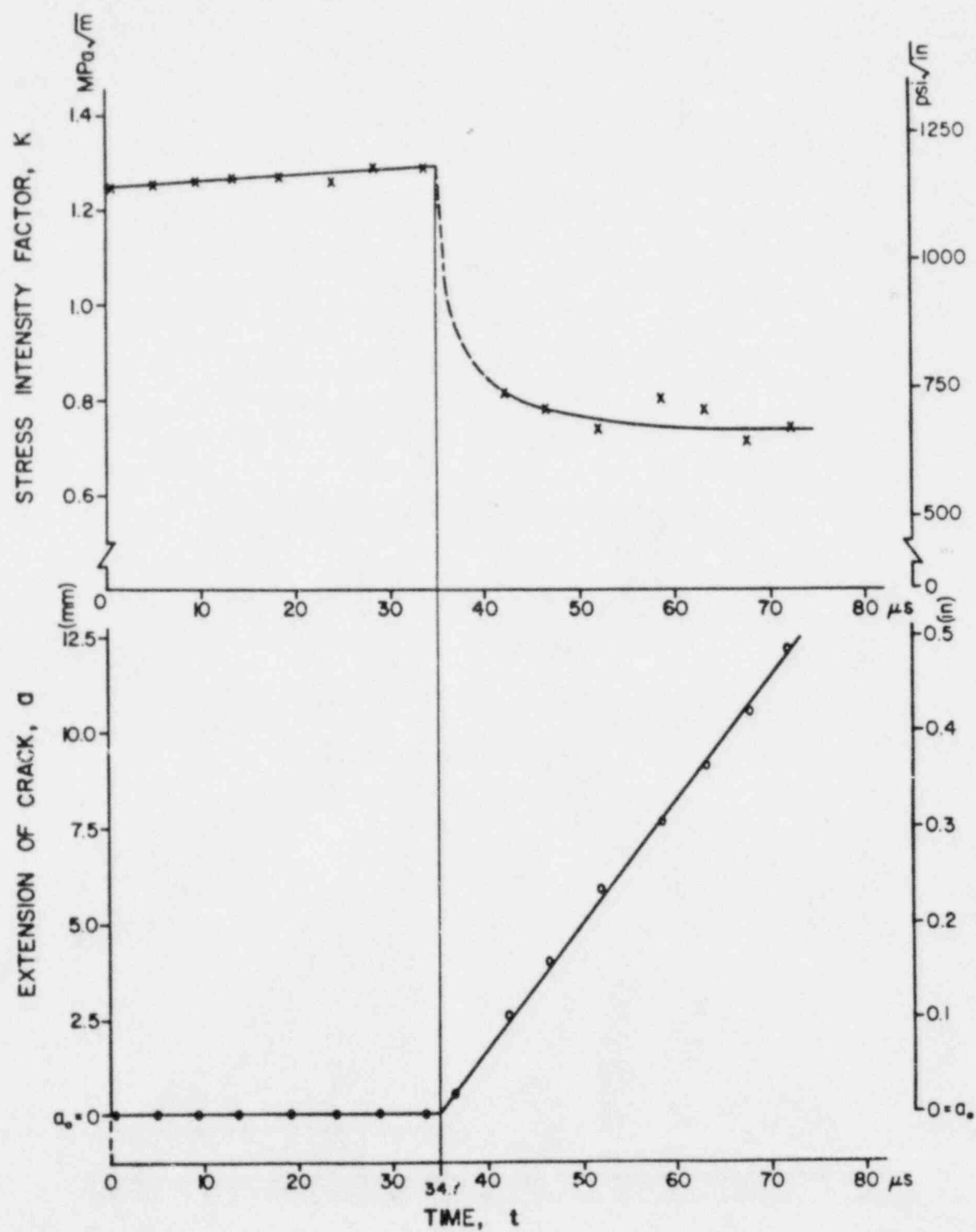
Fig. 2.3 Stress Intensity Factor and Crack Tip Position as a Function of Time for Test 3.

42
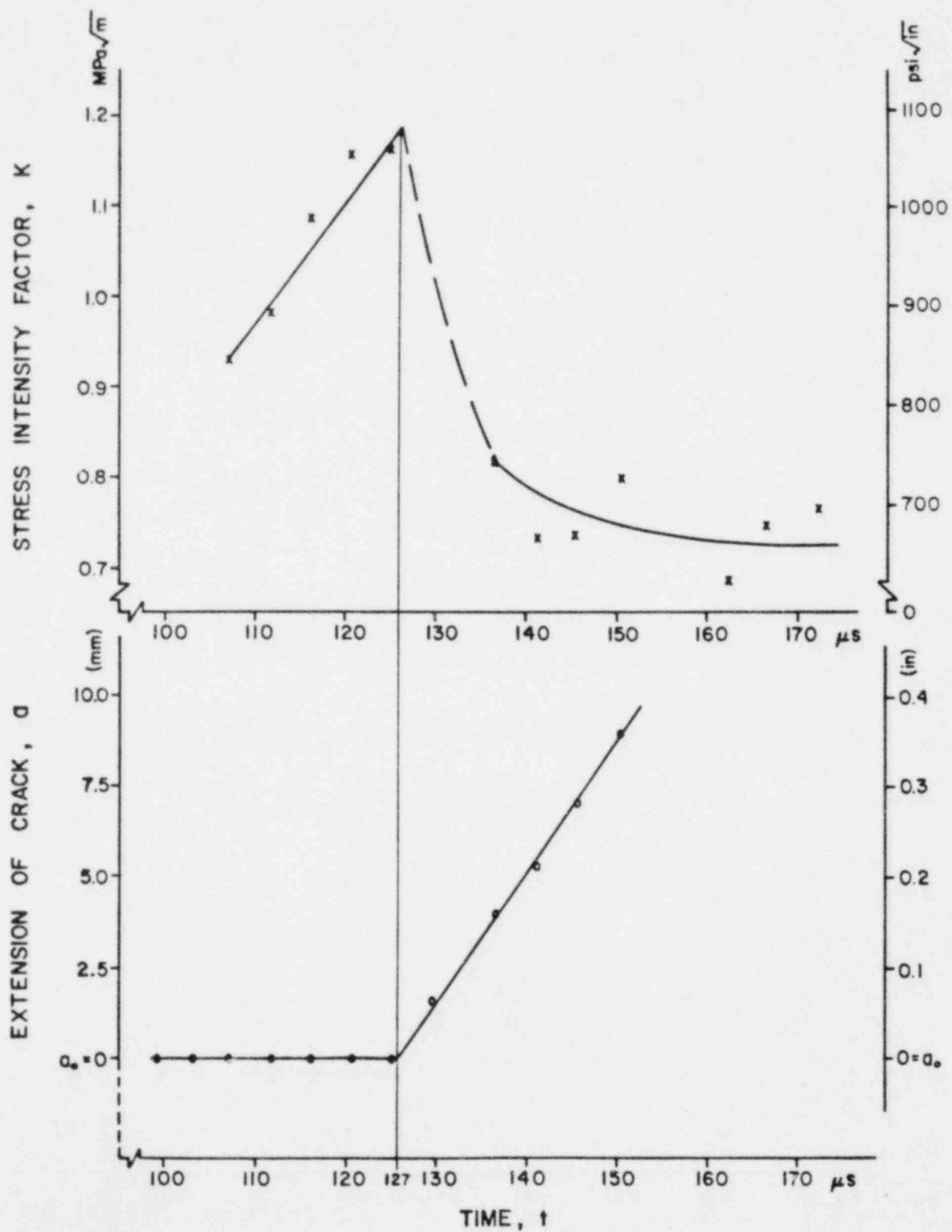
Fig. 2.4   Stress Intensity Factor and Crack Tip Position as a Function
           of Time for Test 4.
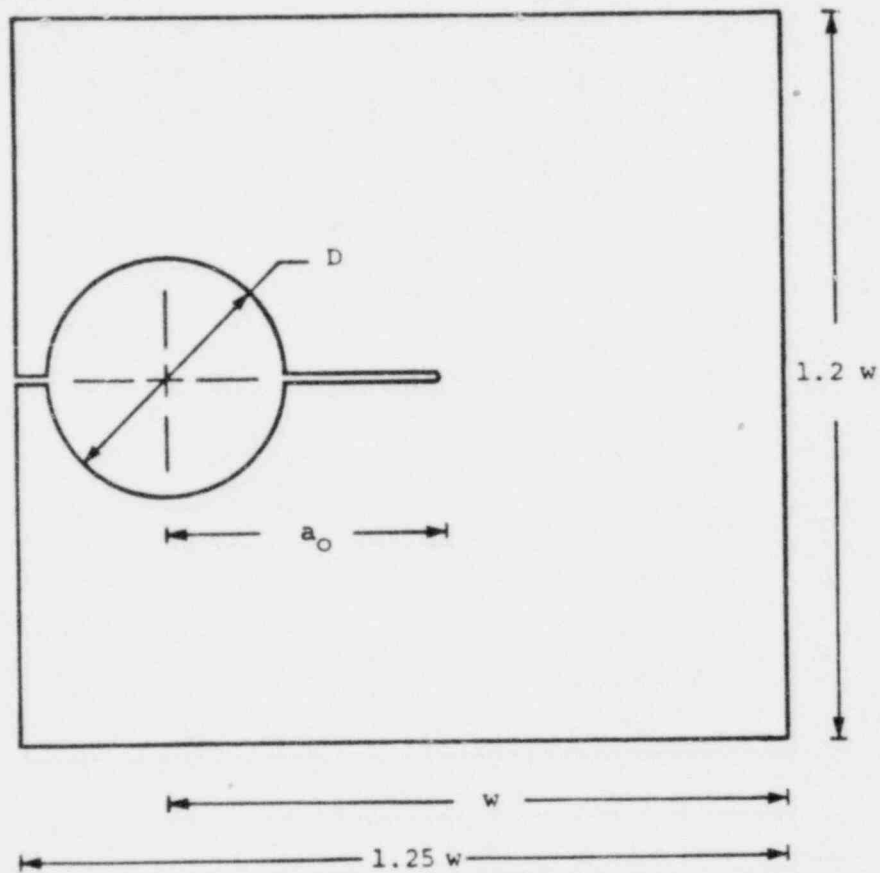
w = 203.2 mm (8.0 inches)

D = 76.2 mm (3.0 inches)

a_O = 88.9 mm (3.5 inches)

Fig. 2.5   Geometry and Dimensions of the Modified-Compact-Tension Specimen.
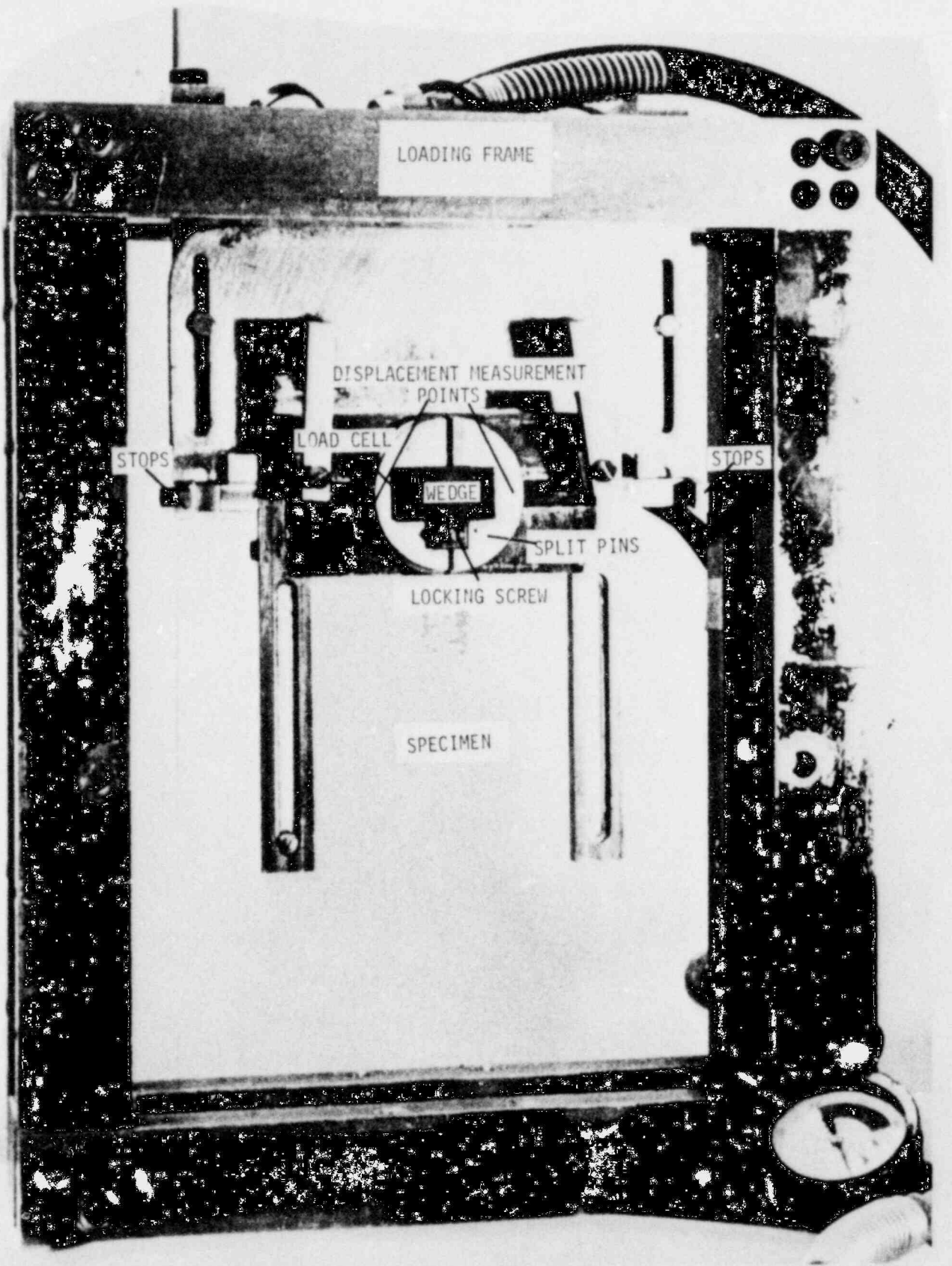
Fig. 2.6   The Modified-Compact-Tension Specimen with the Loading Fixture
Used.
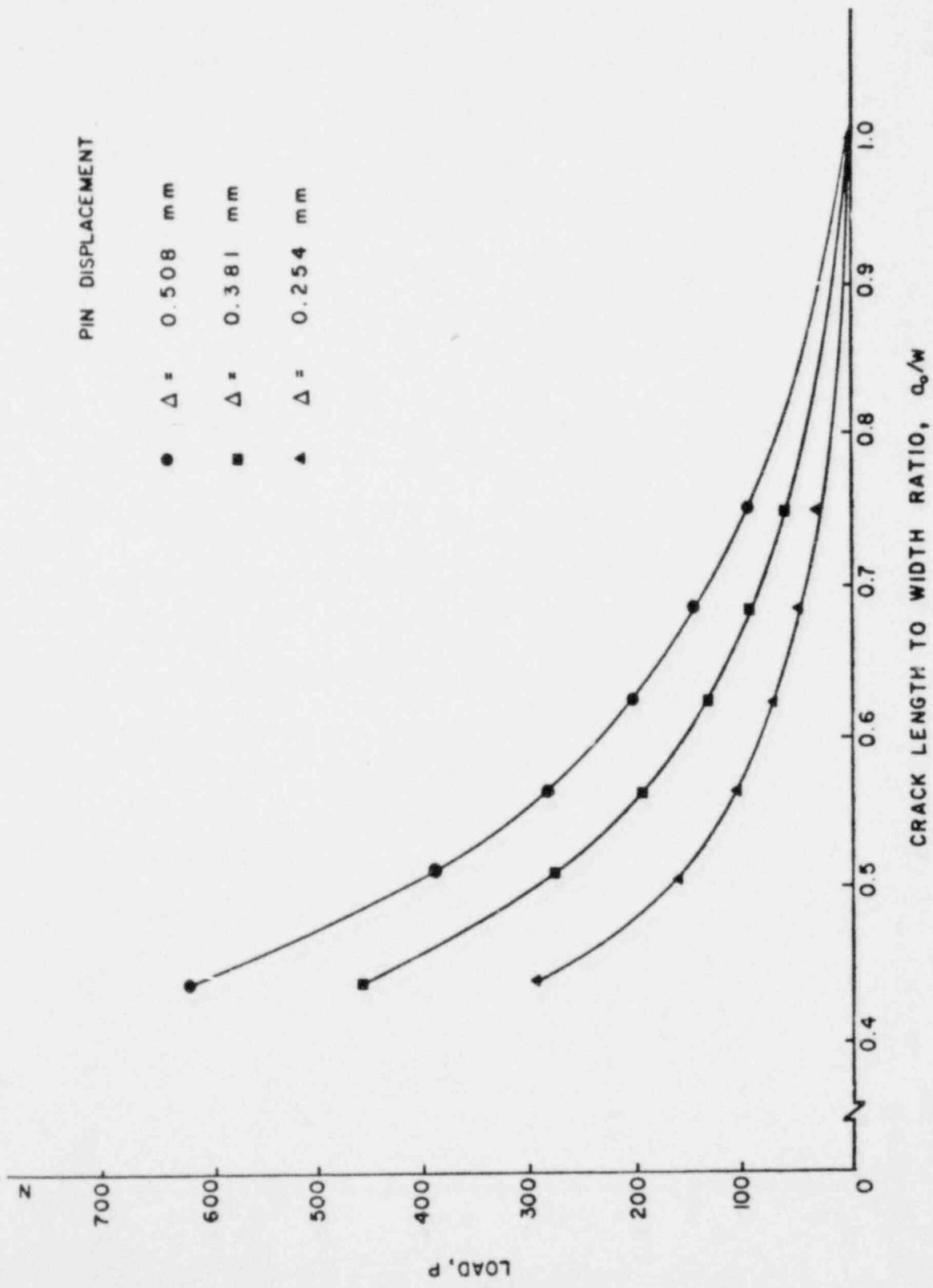
Fig. 2.9 Load as a Function of a/w for Constant Pin Displacement for Homalite 100.

48
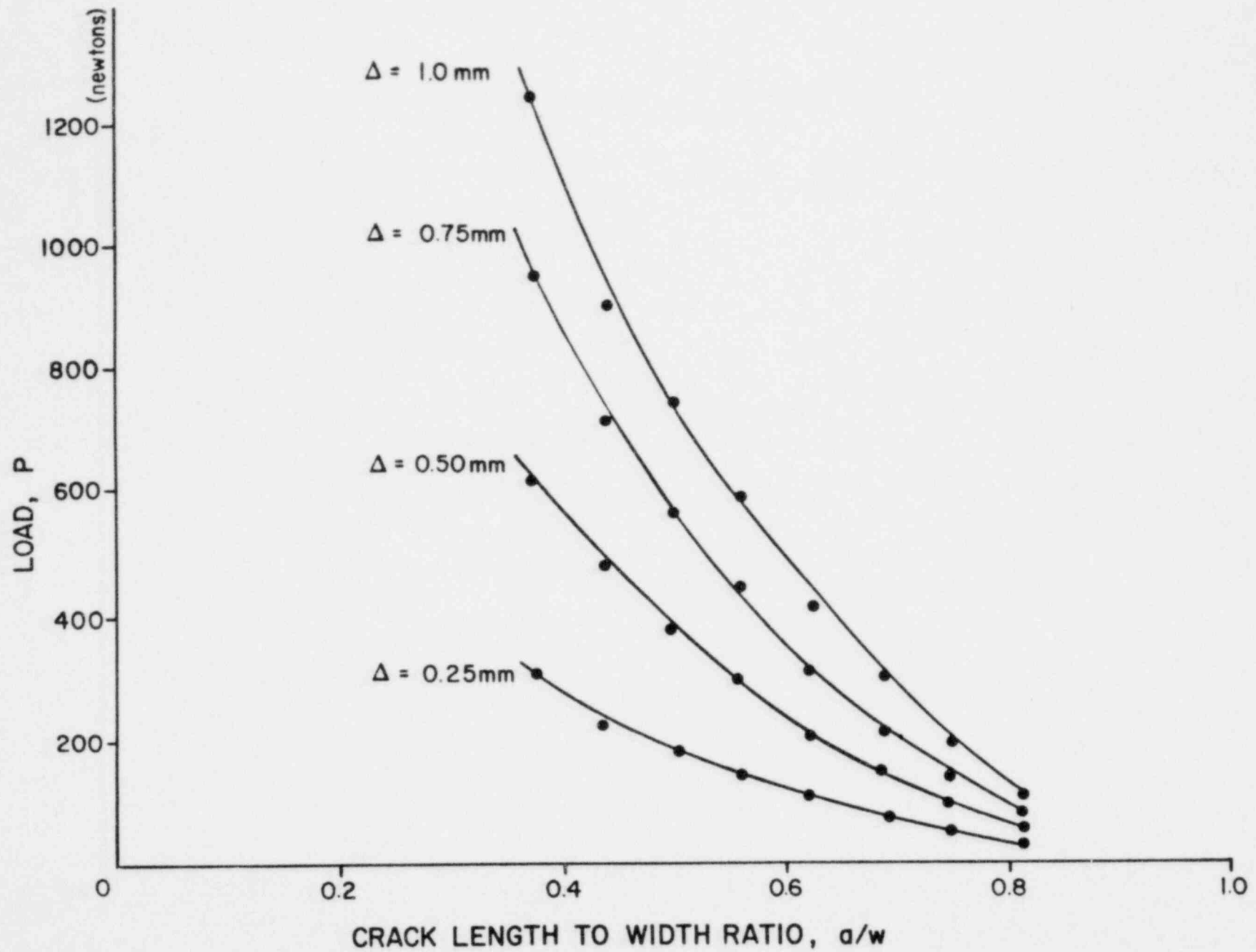
Fig. 2.10 Load as a Function of a/w for Constant Pin Displacement for Araldite B.
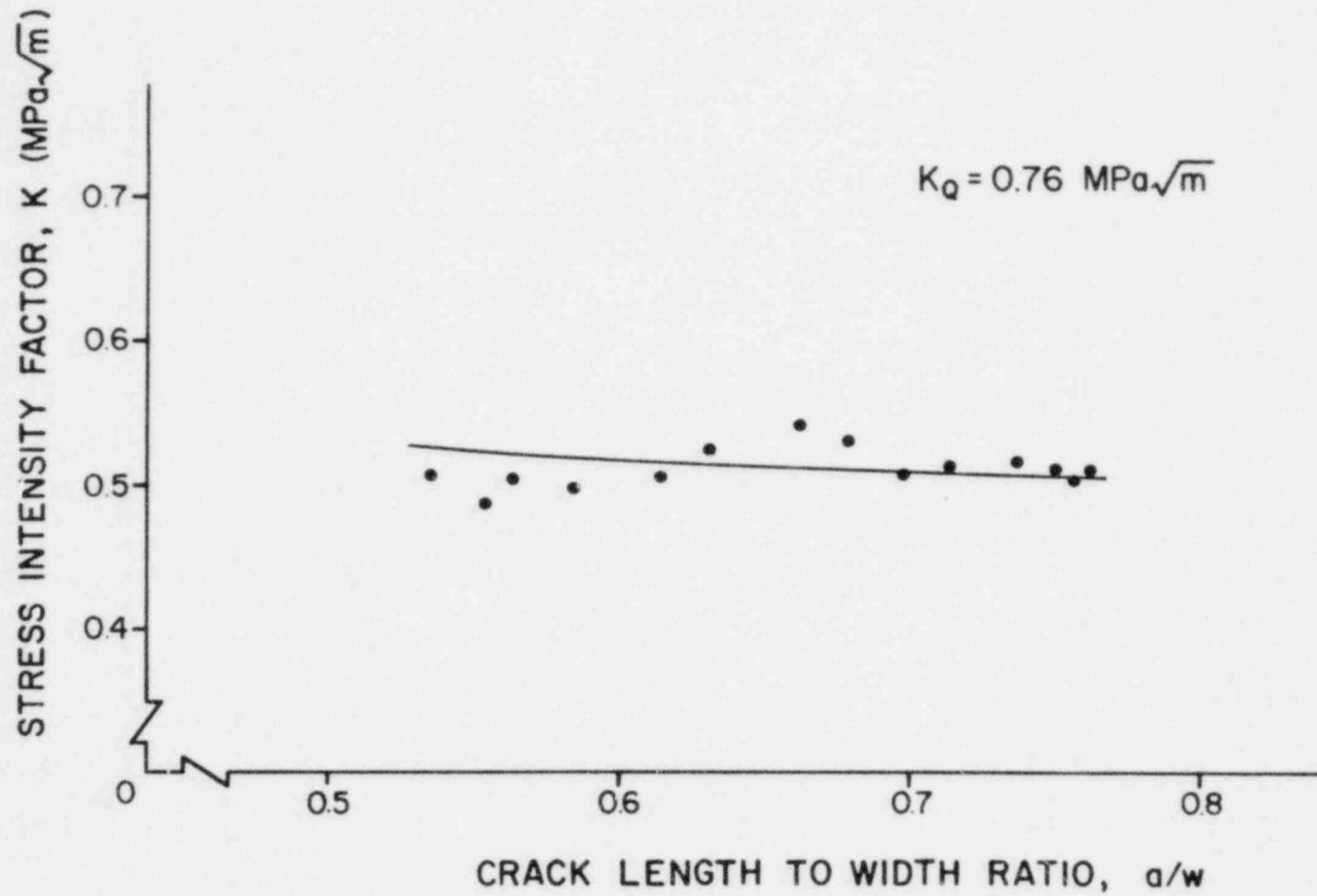
Fig. 2.13 Stress Intensity Factor, K, as a Function of a/w for Test D-2 (Homalite 100).

$K_Q = 0.82$ MPa$\sqrt{m}$

CRACK LENGTH TO WIDTH RATIO, a/w
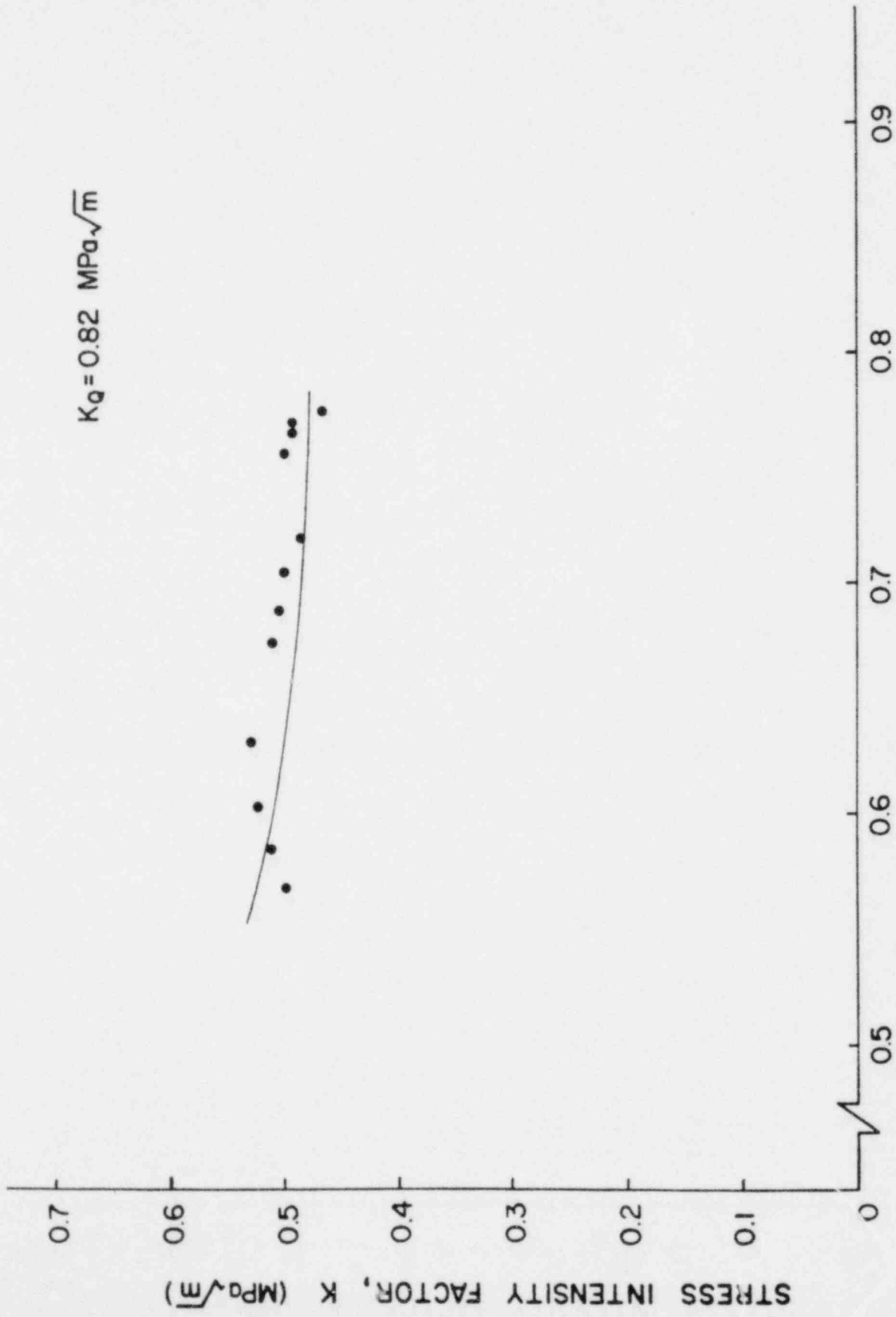
STRESS INTENSITY FACTOR, K (MPa$\sqrt{m}$)

Fig. 2.14 Stress Intensity Factor, K, as a Function of a/w for Test D-3 (Homalite 100).

$$K_Q = 0.79 \text{ MPa}\sqrt{m}$$
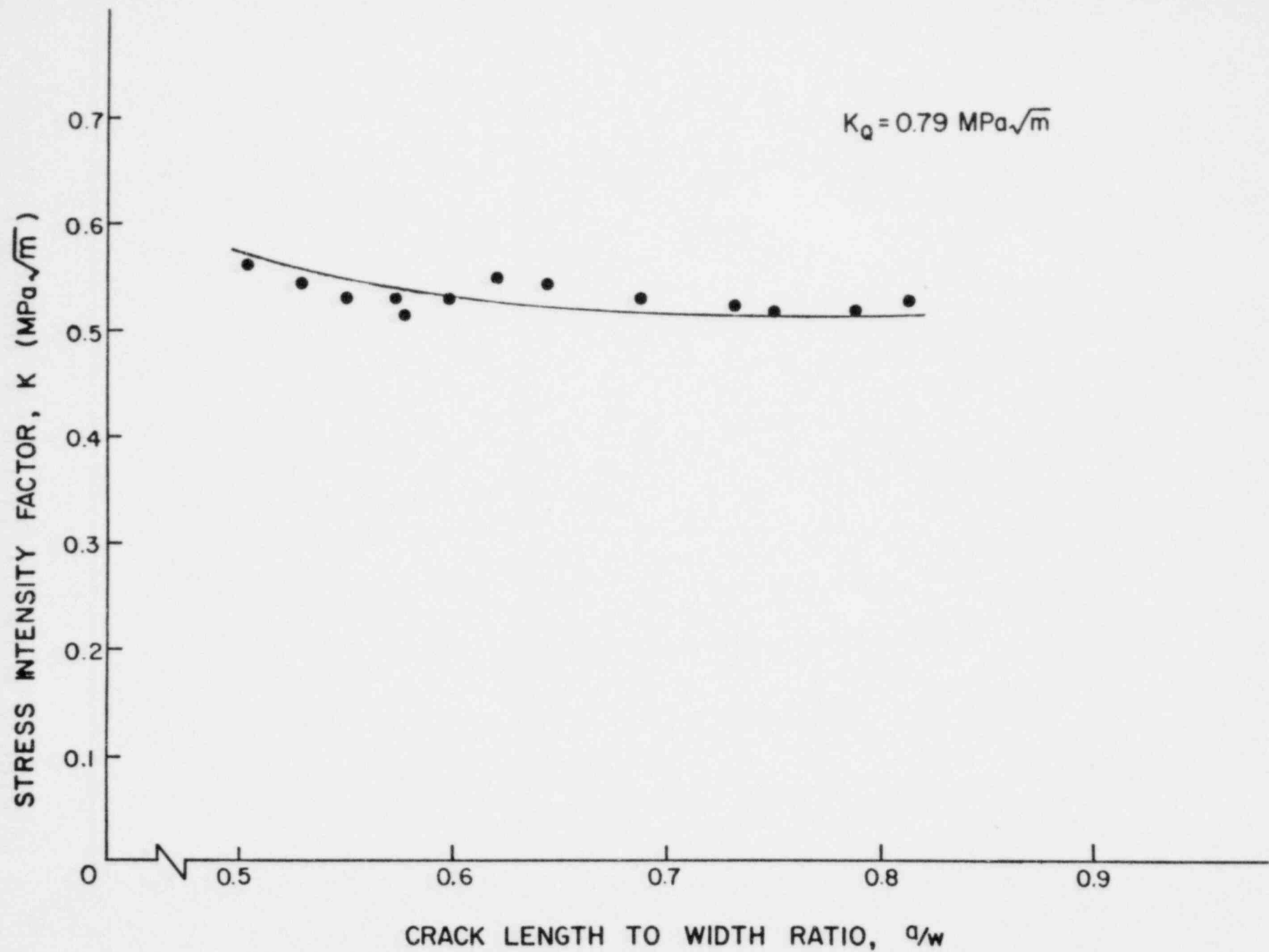
Fig. 2.17 Stress Intensity Factor, K, as a Function of a/w for Test D-6 (Homalite 100).
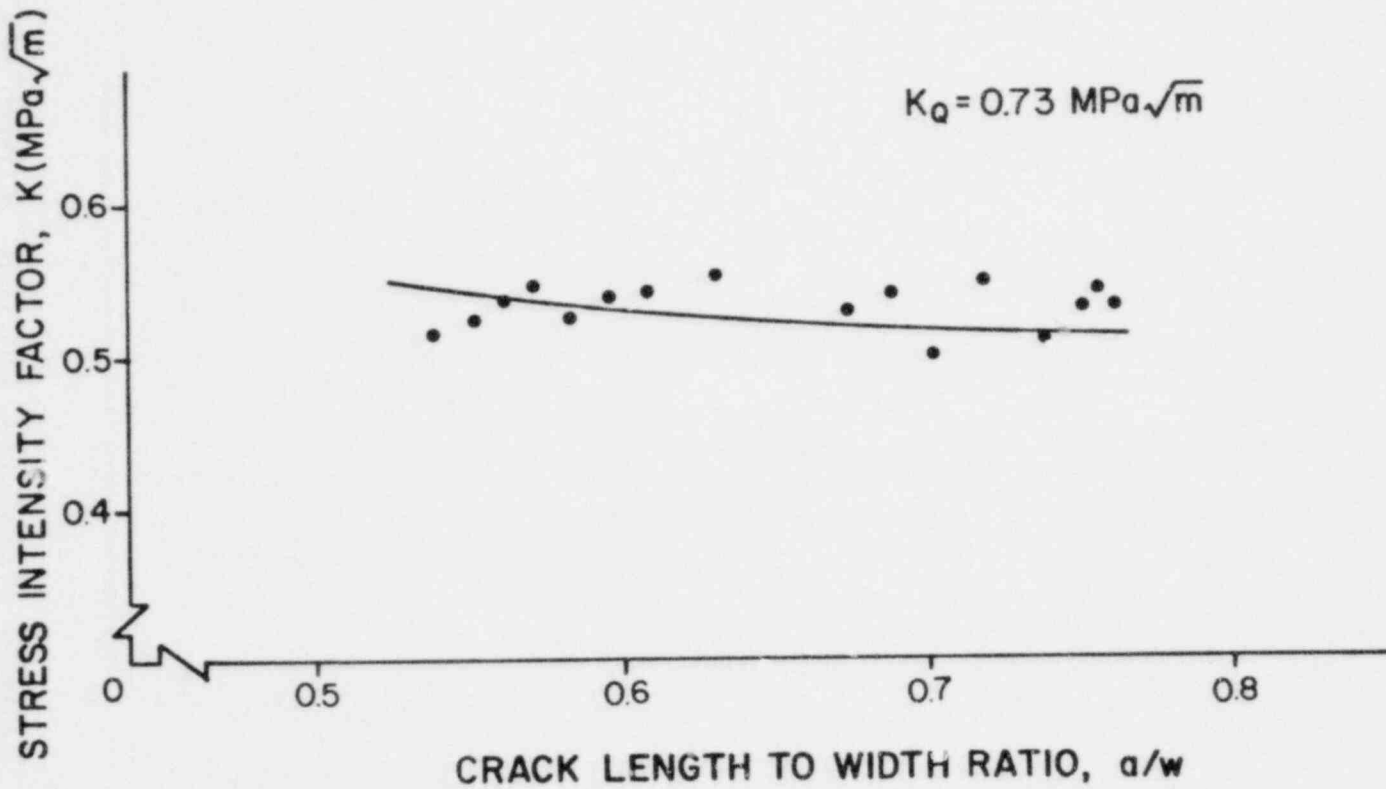
Fig. 2.18 Stress Intensity Factor, K, as a Function of a/w for Test D-7 (Homalite 100).

ARALDITE B
DISPLACEMENT = 0.58 mm
● 414 DYNAMIC
○ 419 DYNAMIC
$K_Q = 1.29 \ MPa\sqrt{m}$

STRESS INTENSITY FACTOR RATIO, K/K_Q

CRACK LENGTH TO WIDTH RATIO, a/w

Fig. 2.21   Stress Intensity Factor, K, as a Function of a/w for Tests
No. 414 and 419 (Araldite B).

60

ARALDITE B
DISPLACEMENT = 0.55 mm
● 415 DYNAMIC
○ 416 DYNAMIC
$K_Q = 1.22 \text{ MPa}\sqrt{m}$

CRACK LENGTH TO WIDTH RATIO, a/w

STRESS INTENSITY FACTOR RATIO, K/K_Q
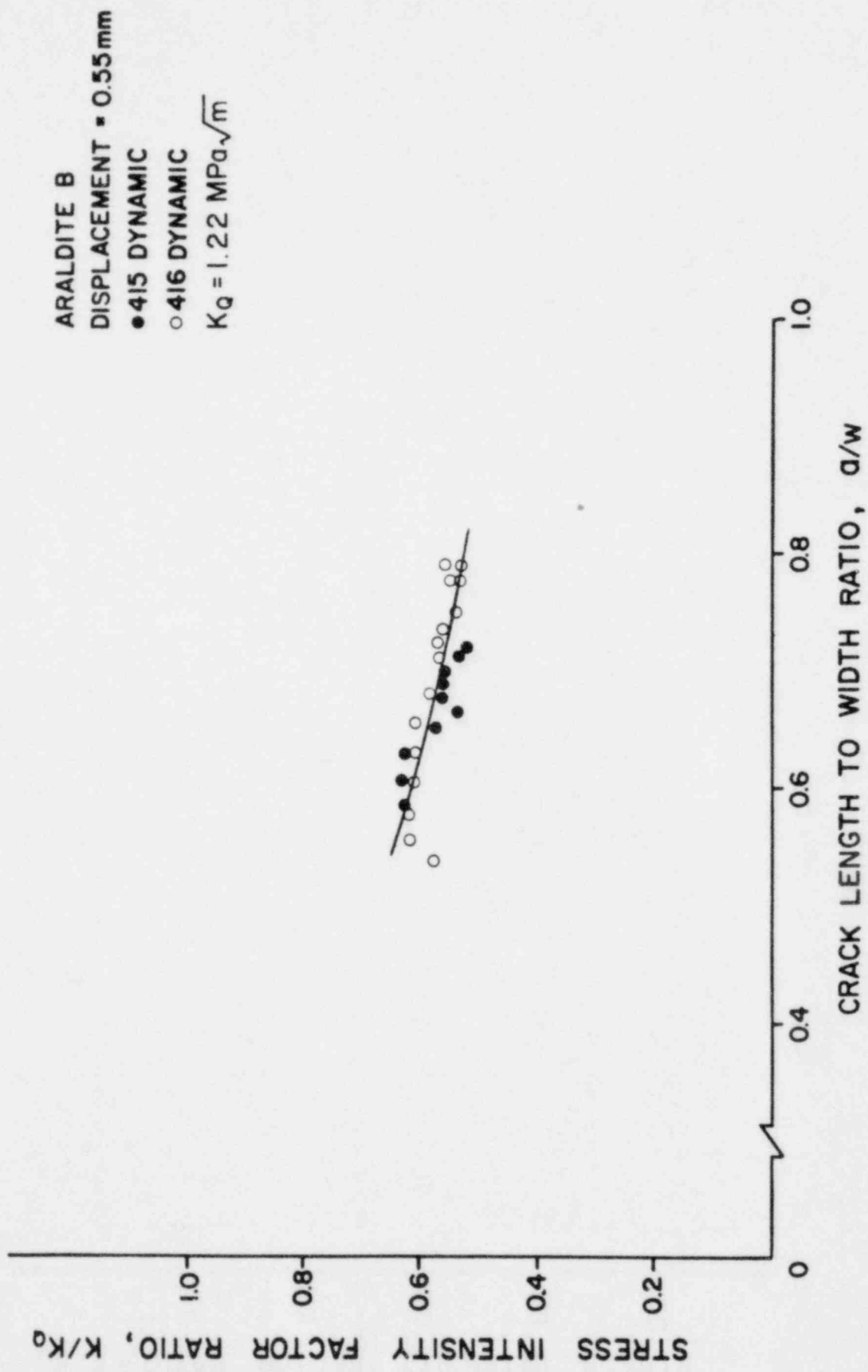
Fig. 2.22 Stress Intensity Factor, K, as a Function of a/w for Tests No. 415 and 416 (Araldite B).

61

ARALDITE B
DISPLACEMENT = 0.47 mm
● 418 DYNAMIC
○ 421 DYNAMIC
$K_Q = 1.05$ MPa$\sqrt{m}$

STRESS INTENSITY FACTOR RATIO, K/K_Q

CRACK LENGTH TO WIDTH RATIO, a/w
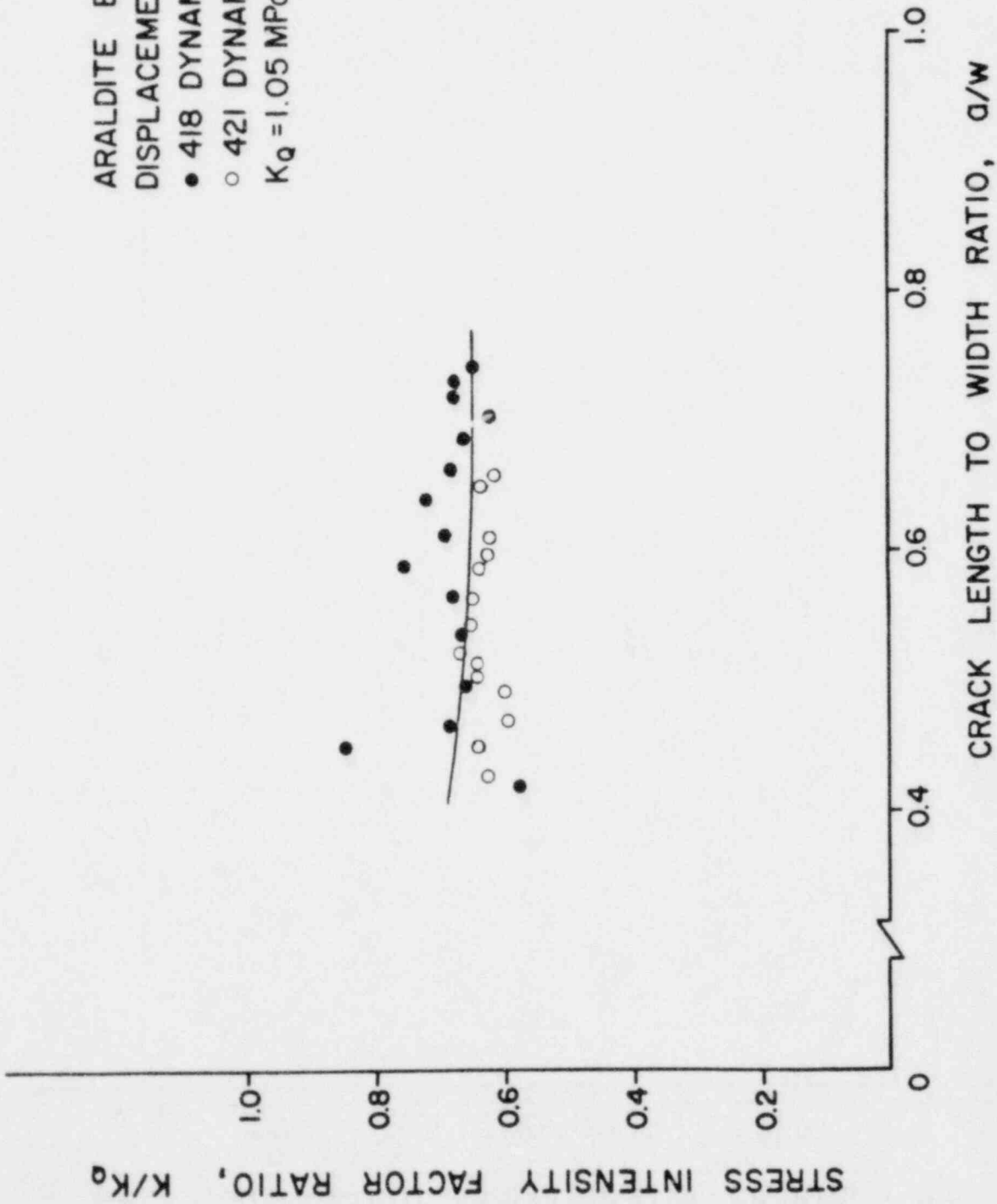
Fig. 2.23 Stress Intensity Factor, K, as a Function of a/w for Tests
No. 418 and 421 (Araldite B).
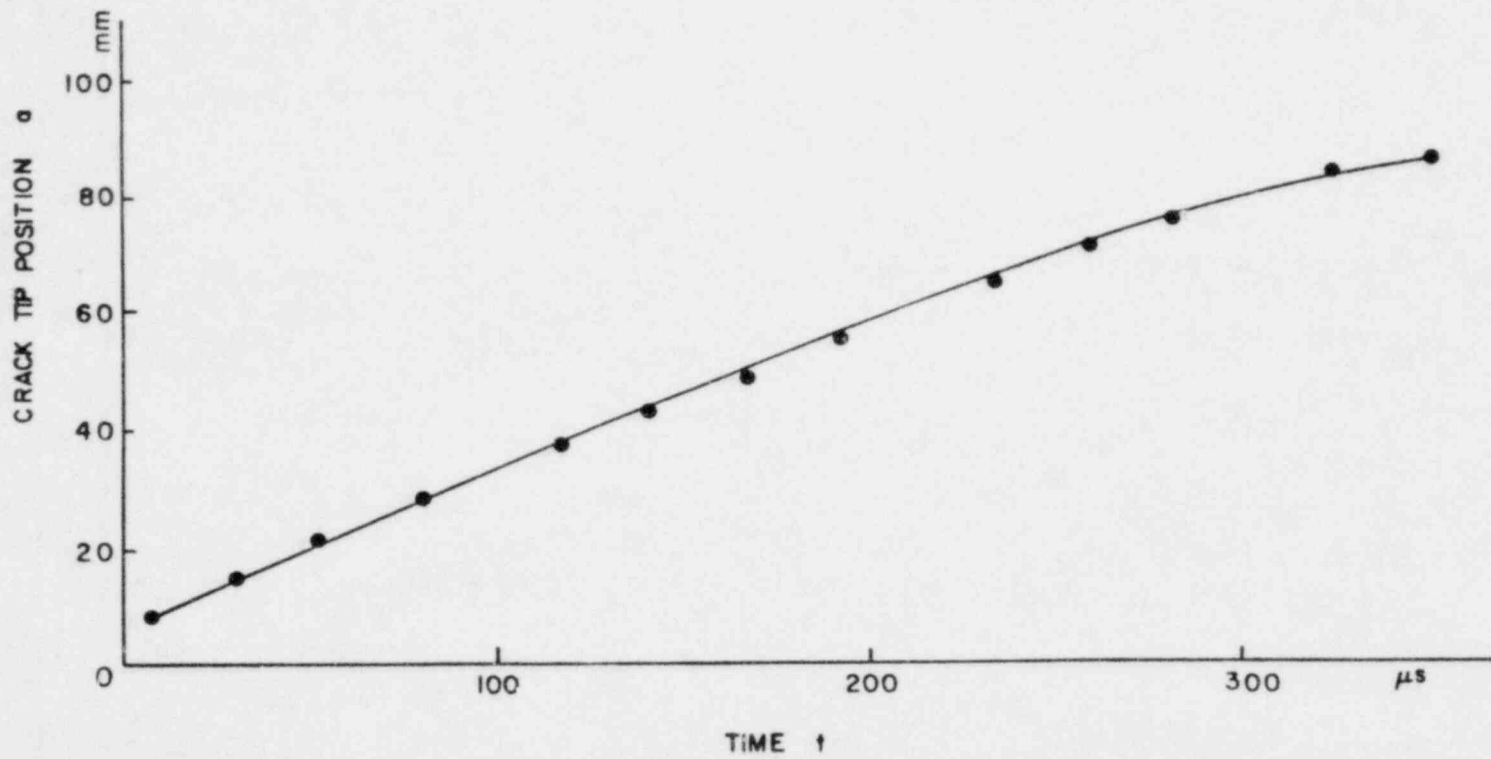
Fig. 2.25 Crack Tip Position as a Function of Time for Test D-1
(Homalite 100).
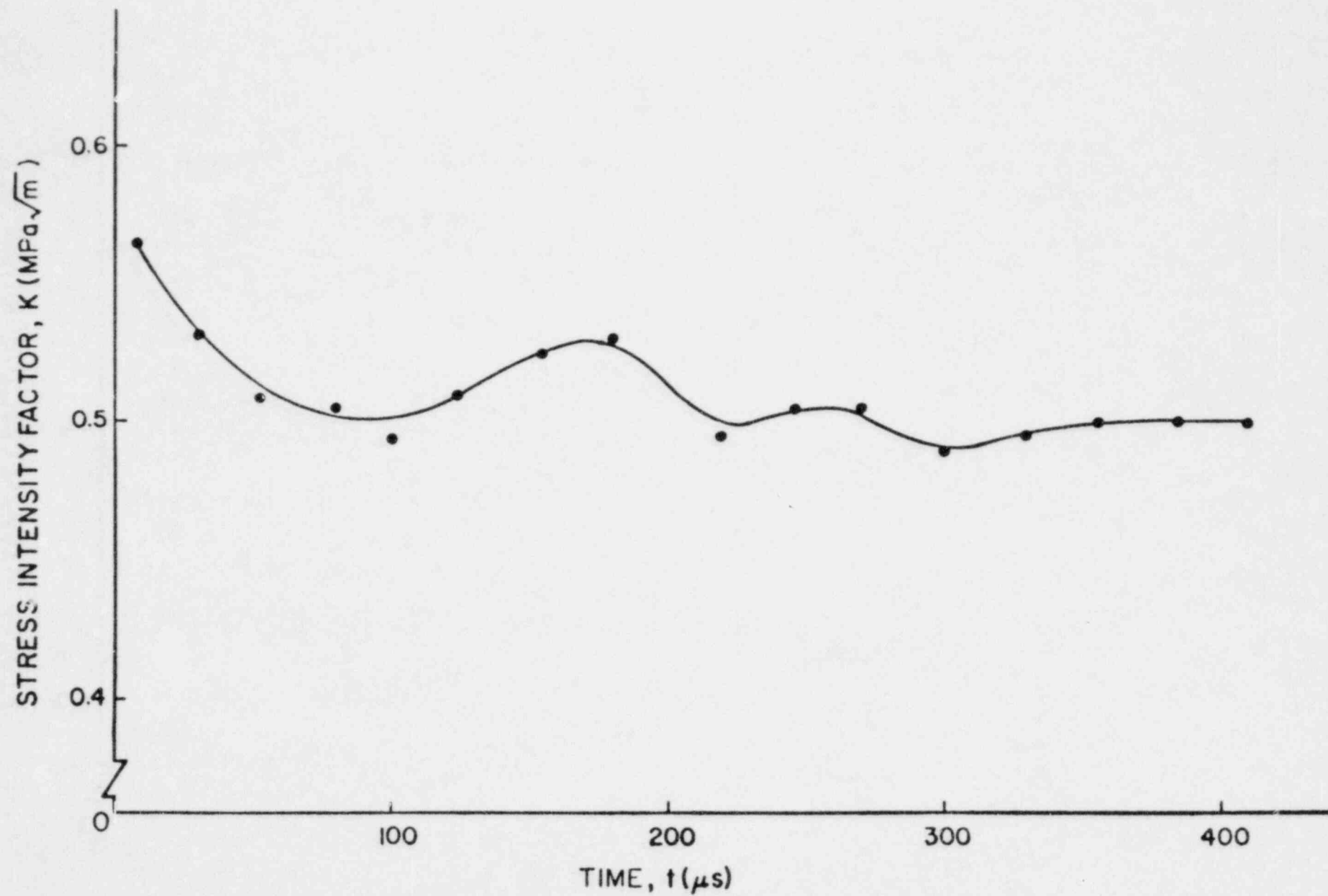
Fig. 2.24 Stress Intensity Factor, K, as a Function of Time for Test D-3 (Homalite 100).
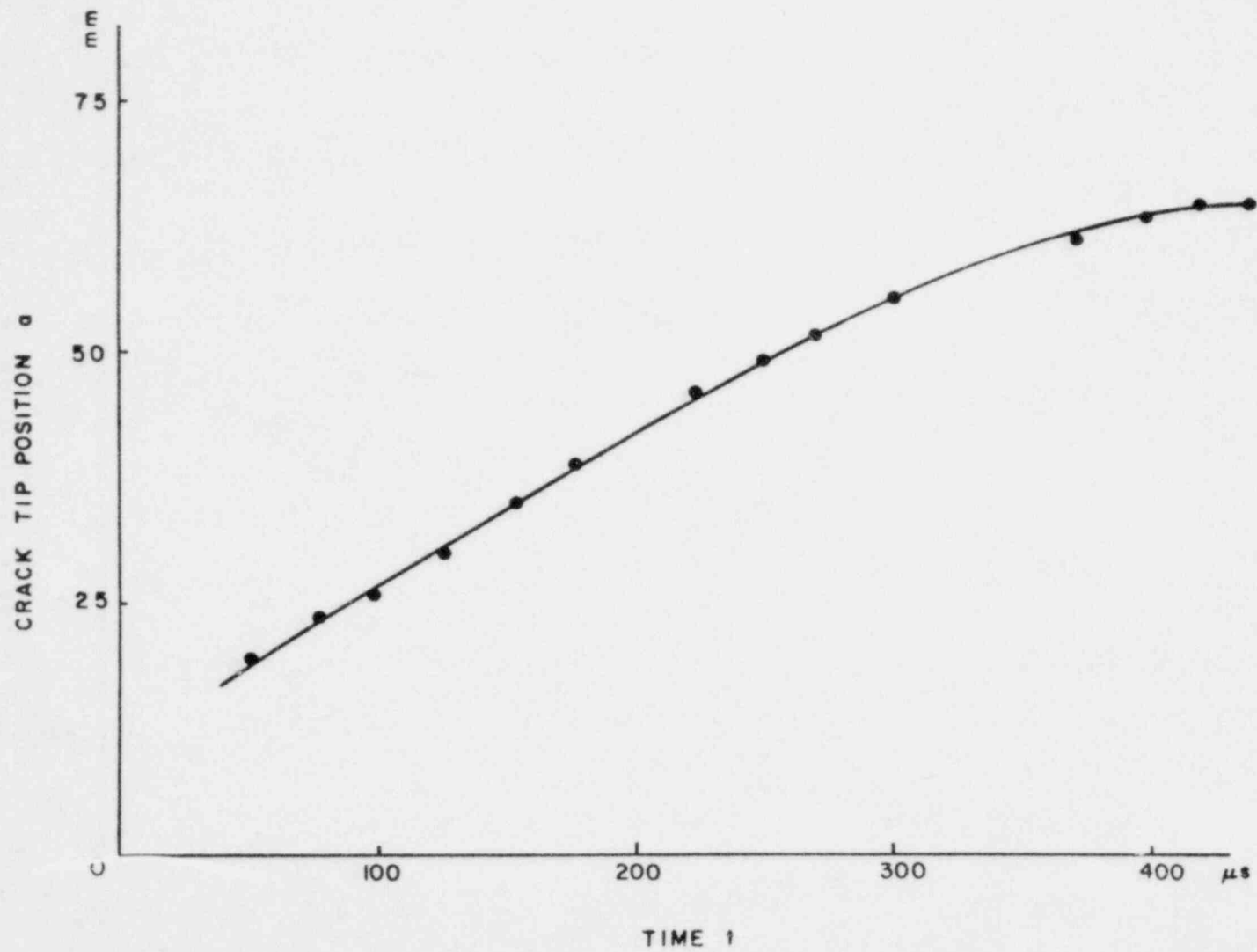
Fig. 2.26 Crack Tip Position as a Function of Time for Test D-2 (Homalite 100).
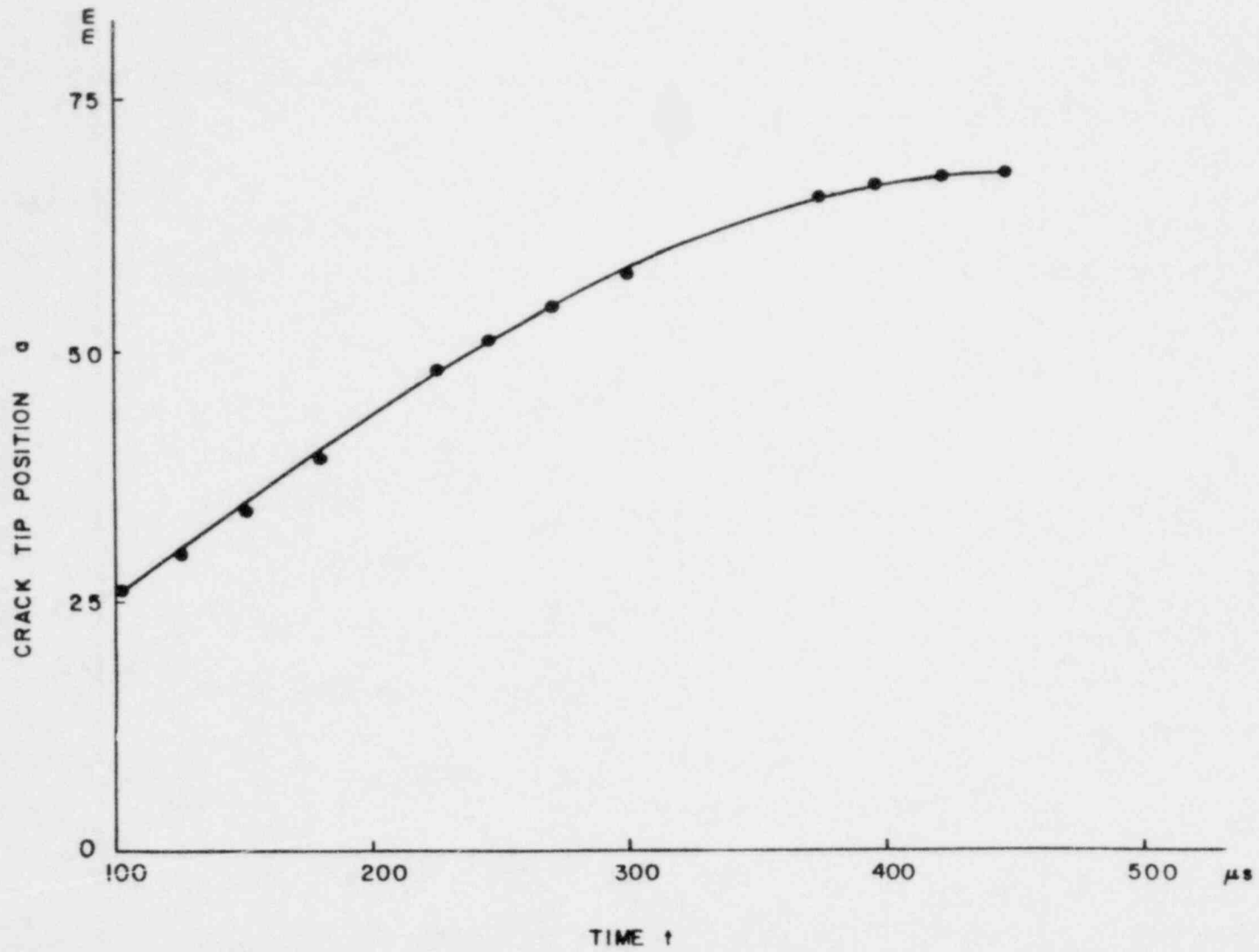
Fig. 2.27 Crack Tip Position as a Function of Time for Test D-3
(Homalite 100).
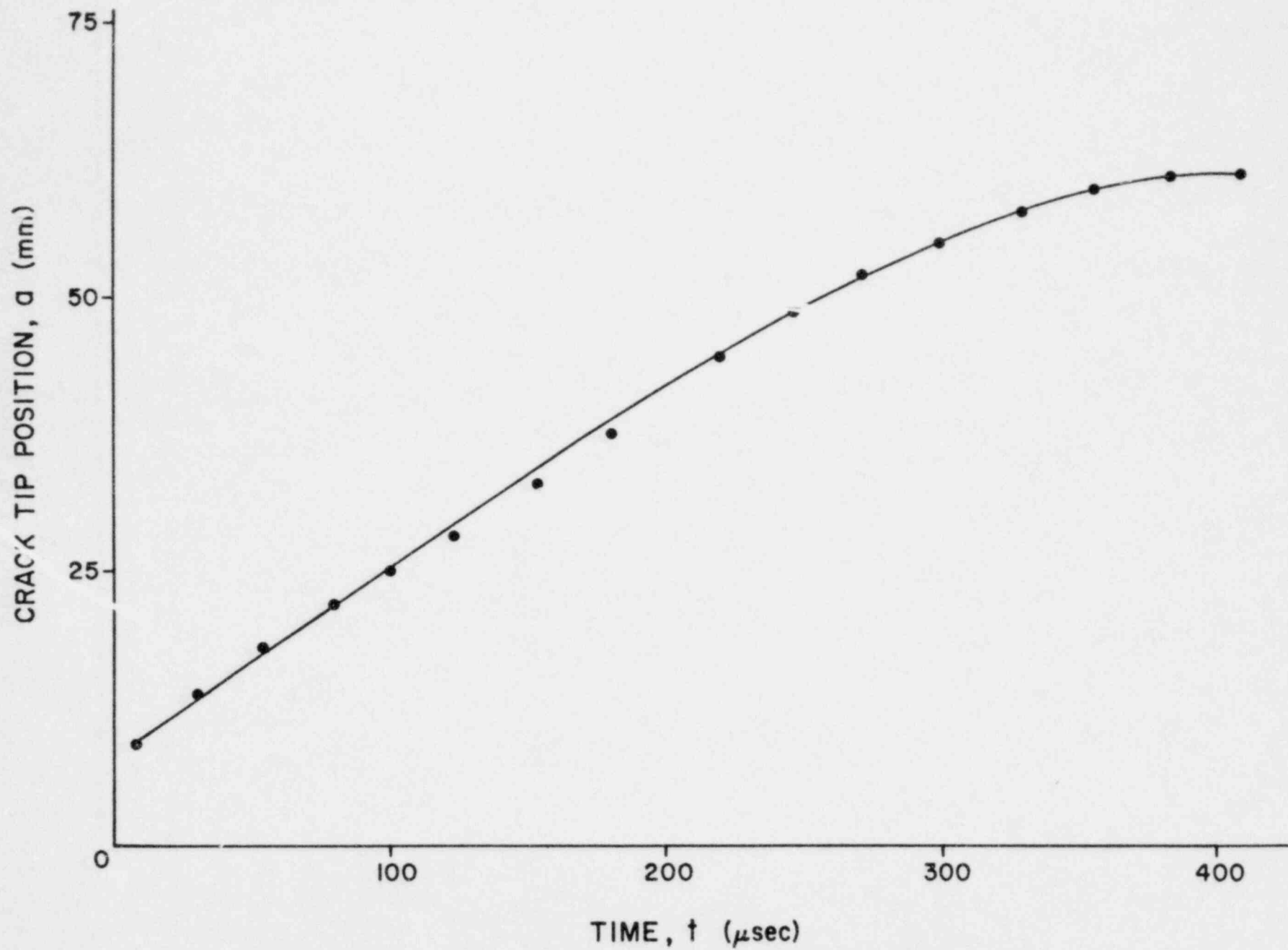
Fig. 2.28 Crack Tip Position as a Function of Time for Test D-4
(Homalite 100).

CRACK TIP POSITION

mm

75

50

25

0   100   200   300   400   μs

TIME t
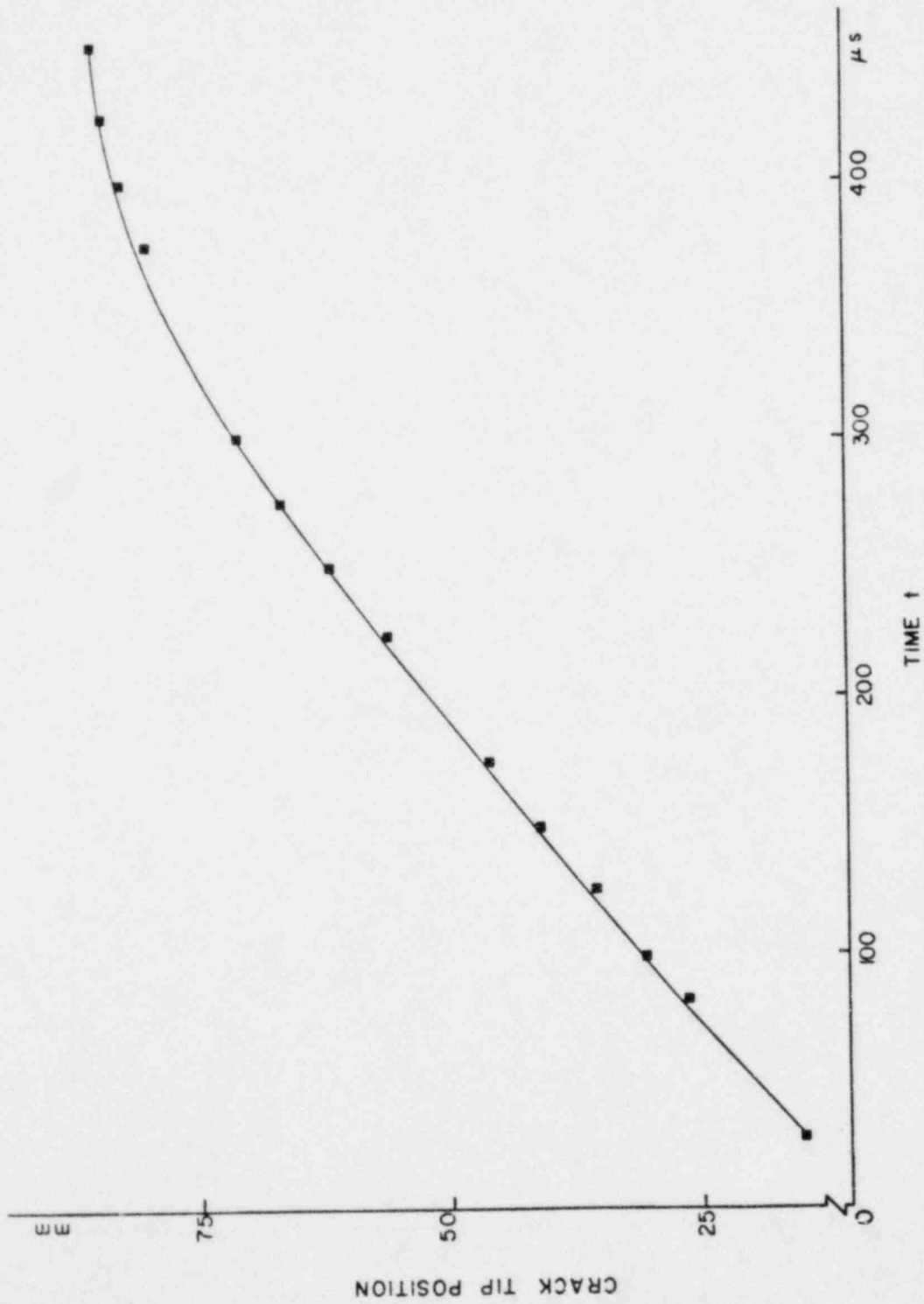
Fig. 2.29 Crack Tip Position as a Function of Time for Test D-5 (Homalite 100).

68
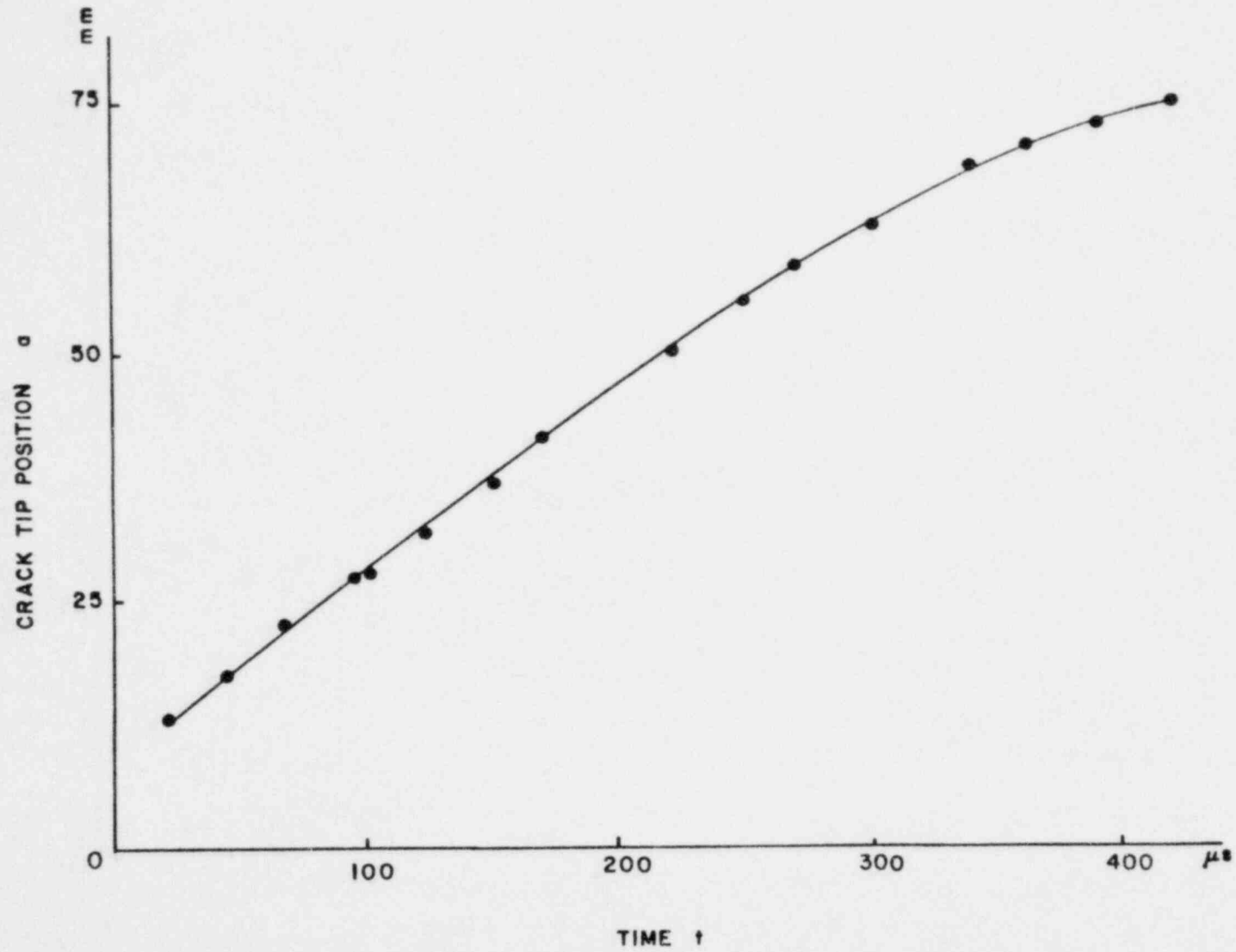
Fig. 2.30   Crack Tip Position as a Function of Time for Test D-6
(Homalite 100).

CRACK TIP POSITION a

TIME t
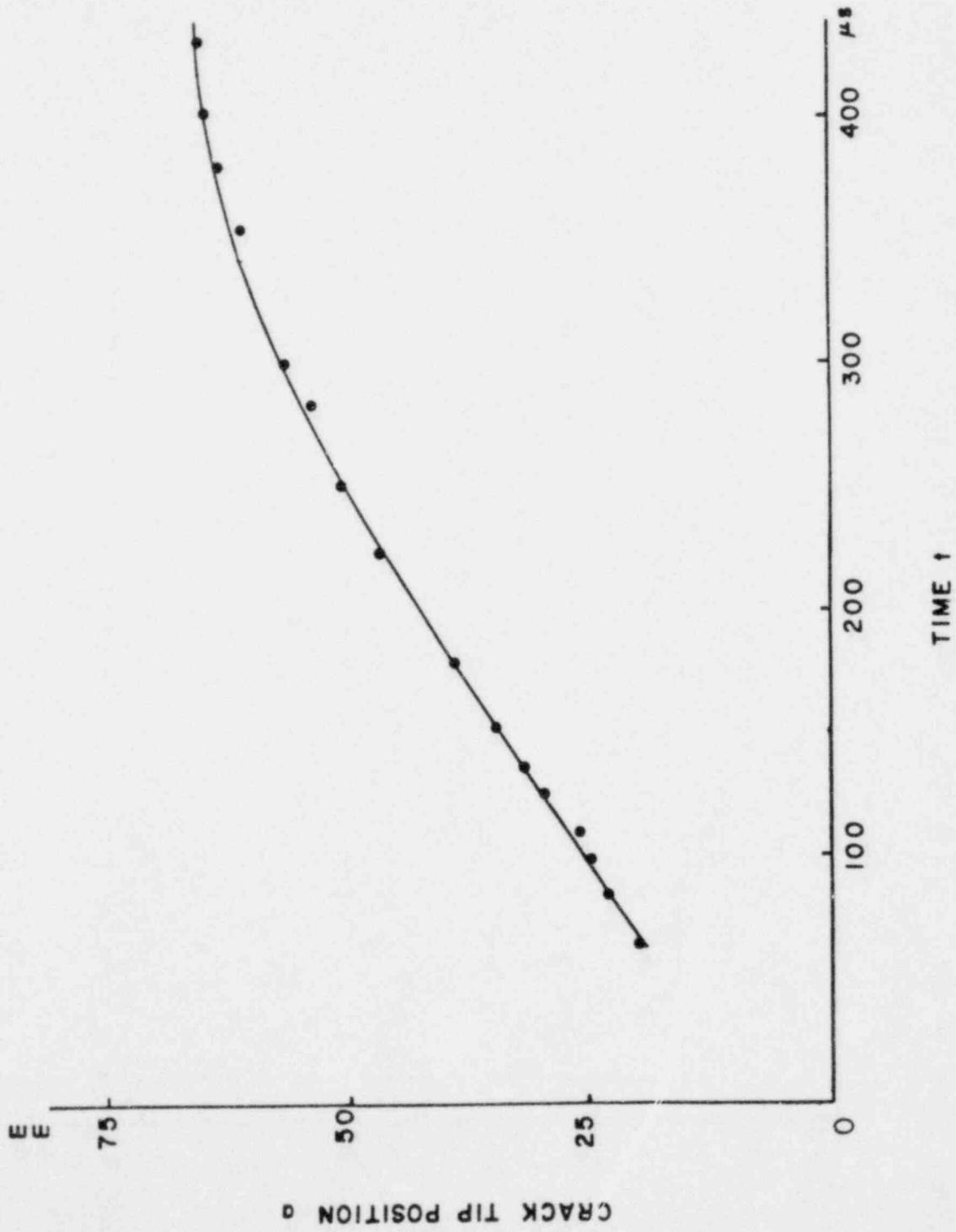
Fig. 2.31 Crack Tip Position as a Function of Time for Test D-7
(Homalite 100).

70
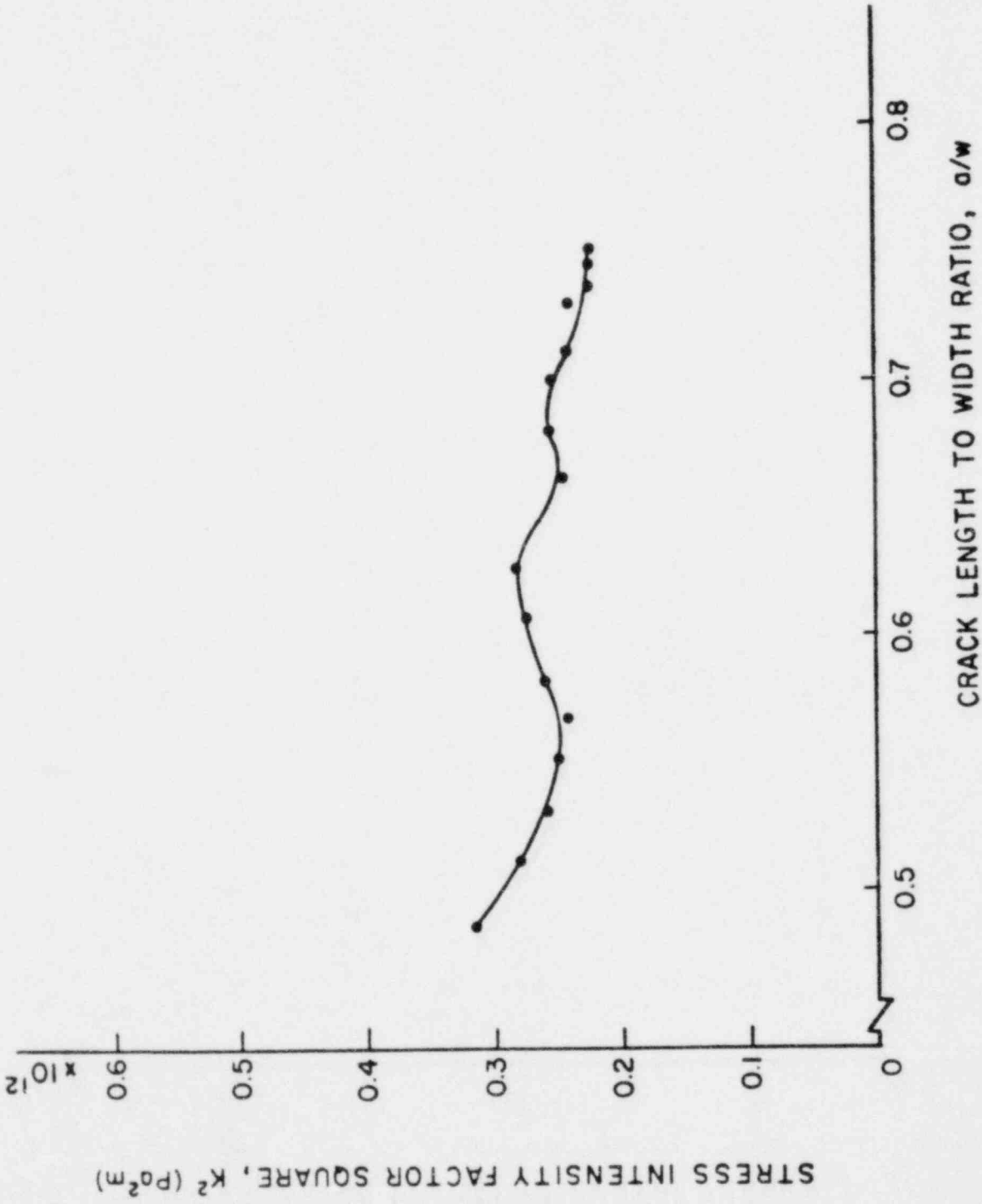
Fig. 2.32 K^2 as a Function of a/w for Test D-3 (Homalite 100).

STRESS INTENSITY FACTOR SQUARE, K^2 (Pa²m)

CRACK LENGTH TO WIDTH RATIO, a/w
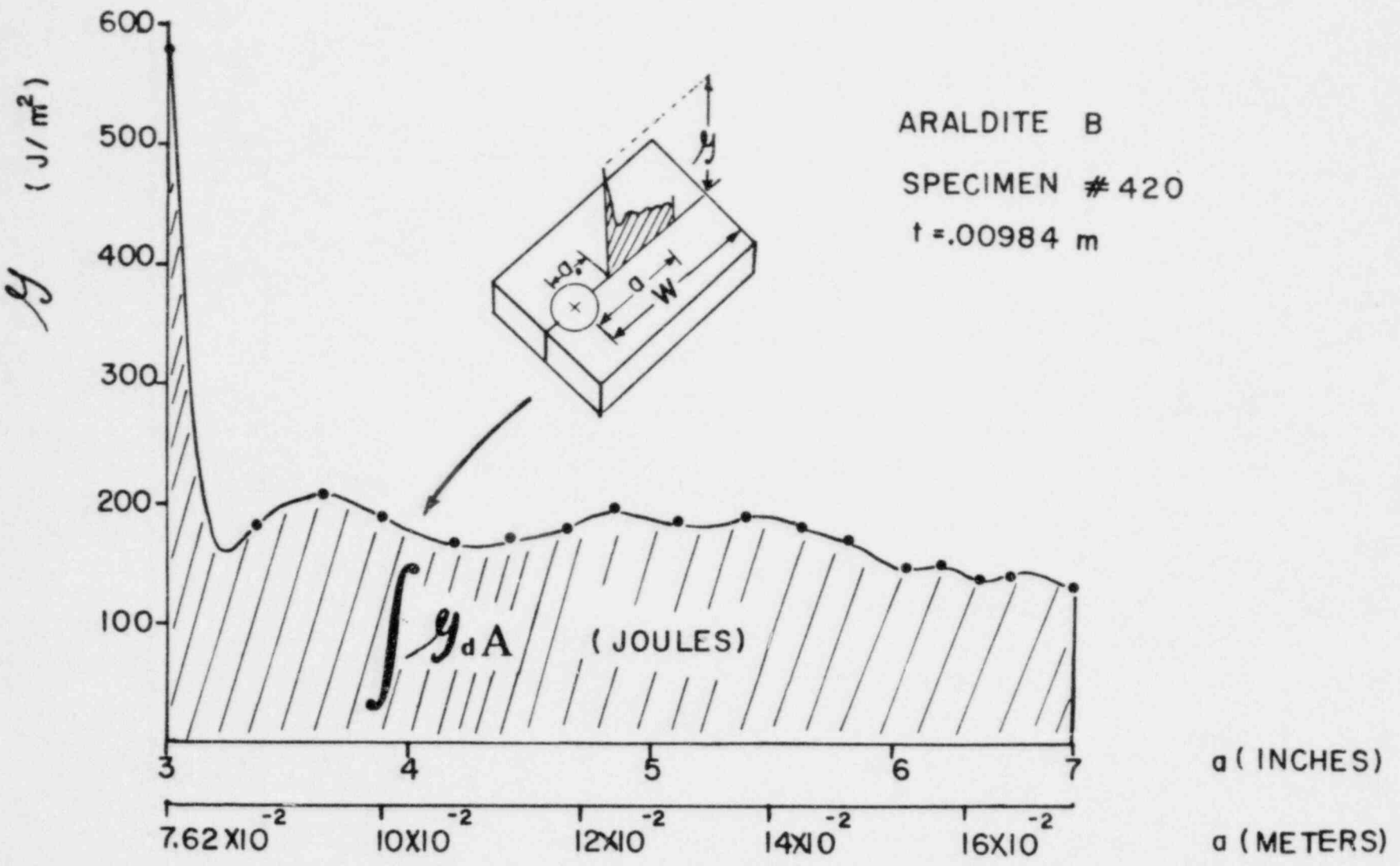
Fig. 2.33 Energy Release Rate, $\mathcal{G}$, as a Function of a/w for Test 420 (Araldite B).
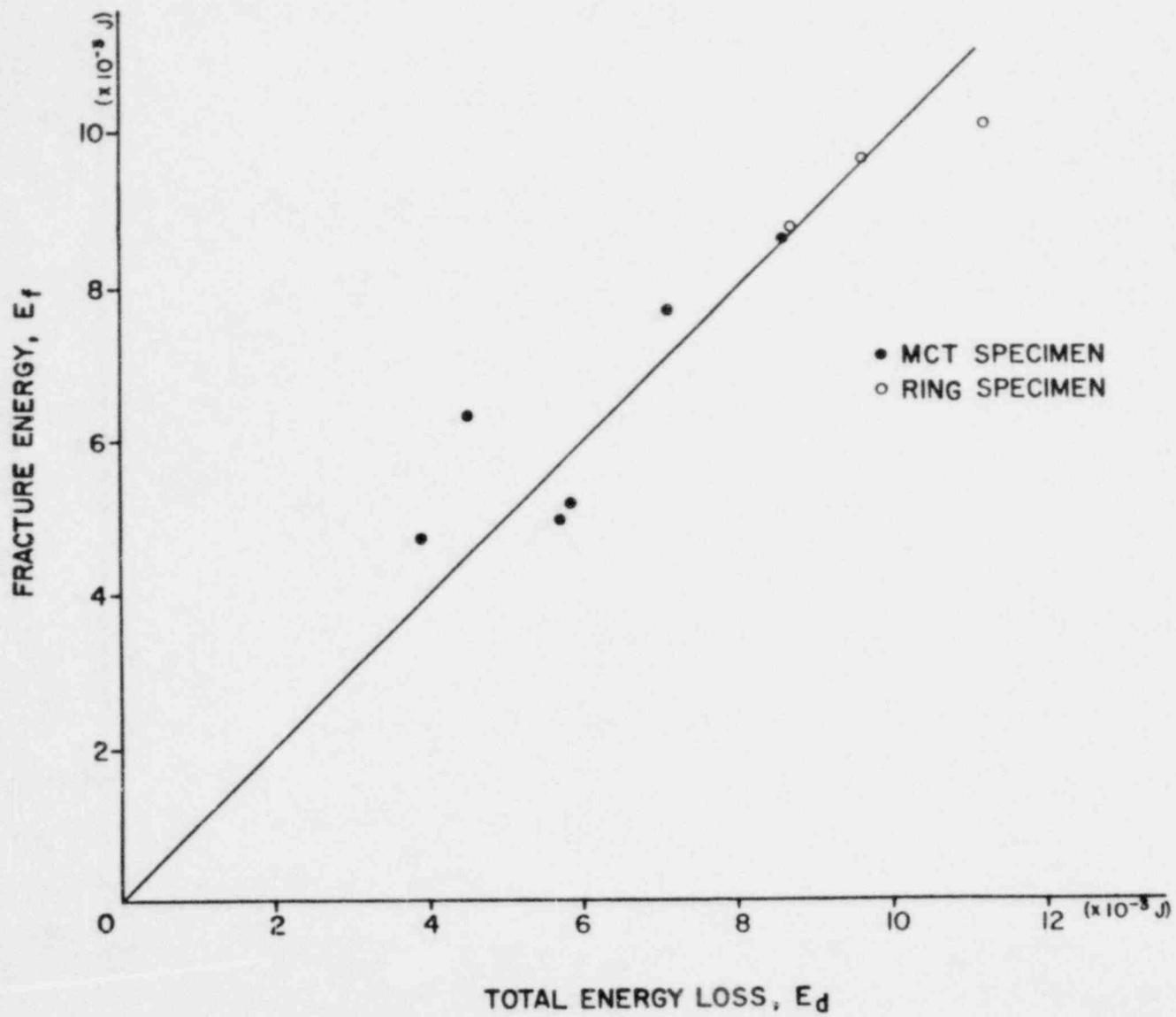
Fig. 2.34 Fracture Energy, E_f, as a Function of Damping Energy, E_d, for Homalite 100.

73
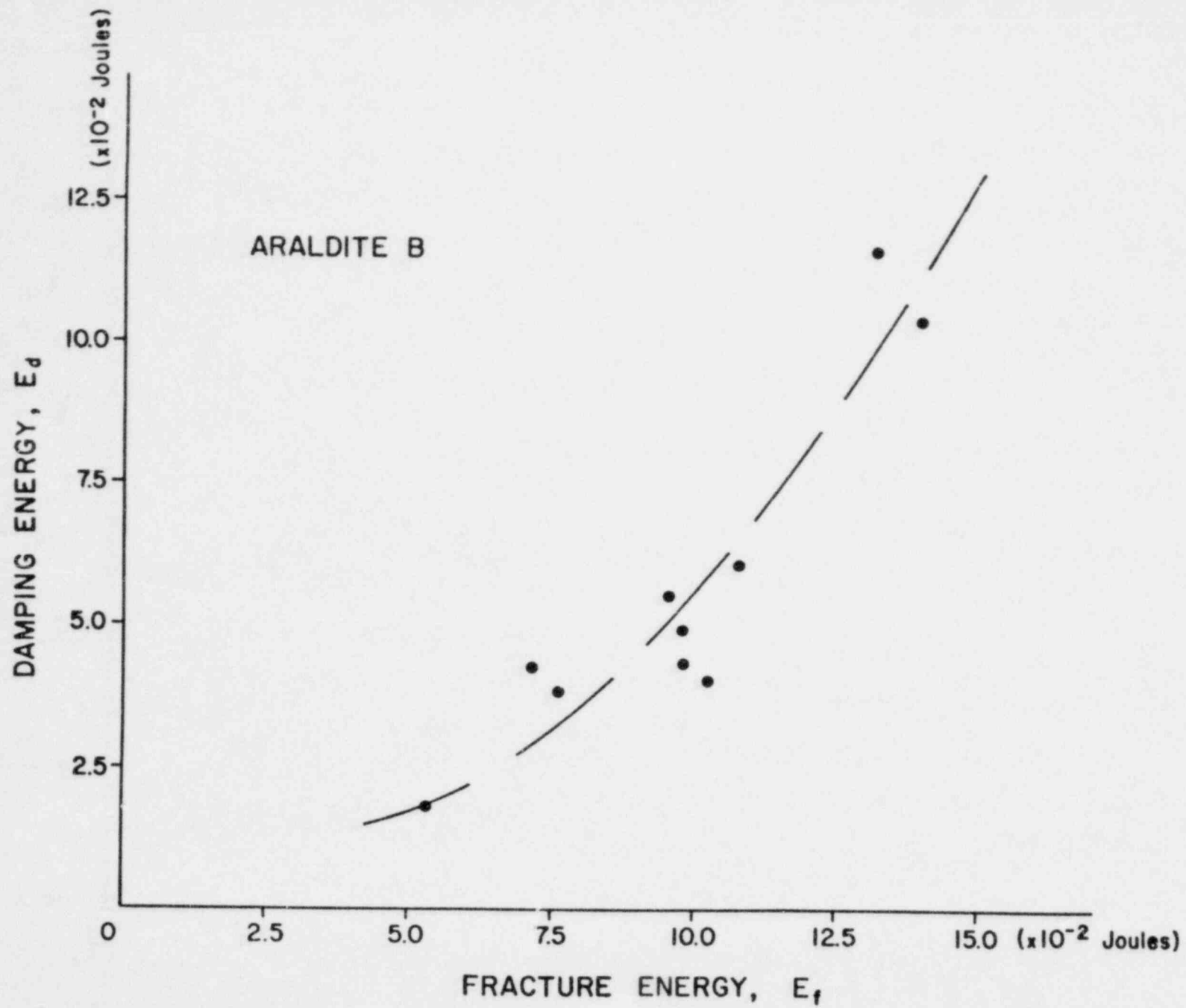
Fig. 2.35   Fracture Energy, E_f, as a Function of Damping Energy, E_d, for Araldite B.
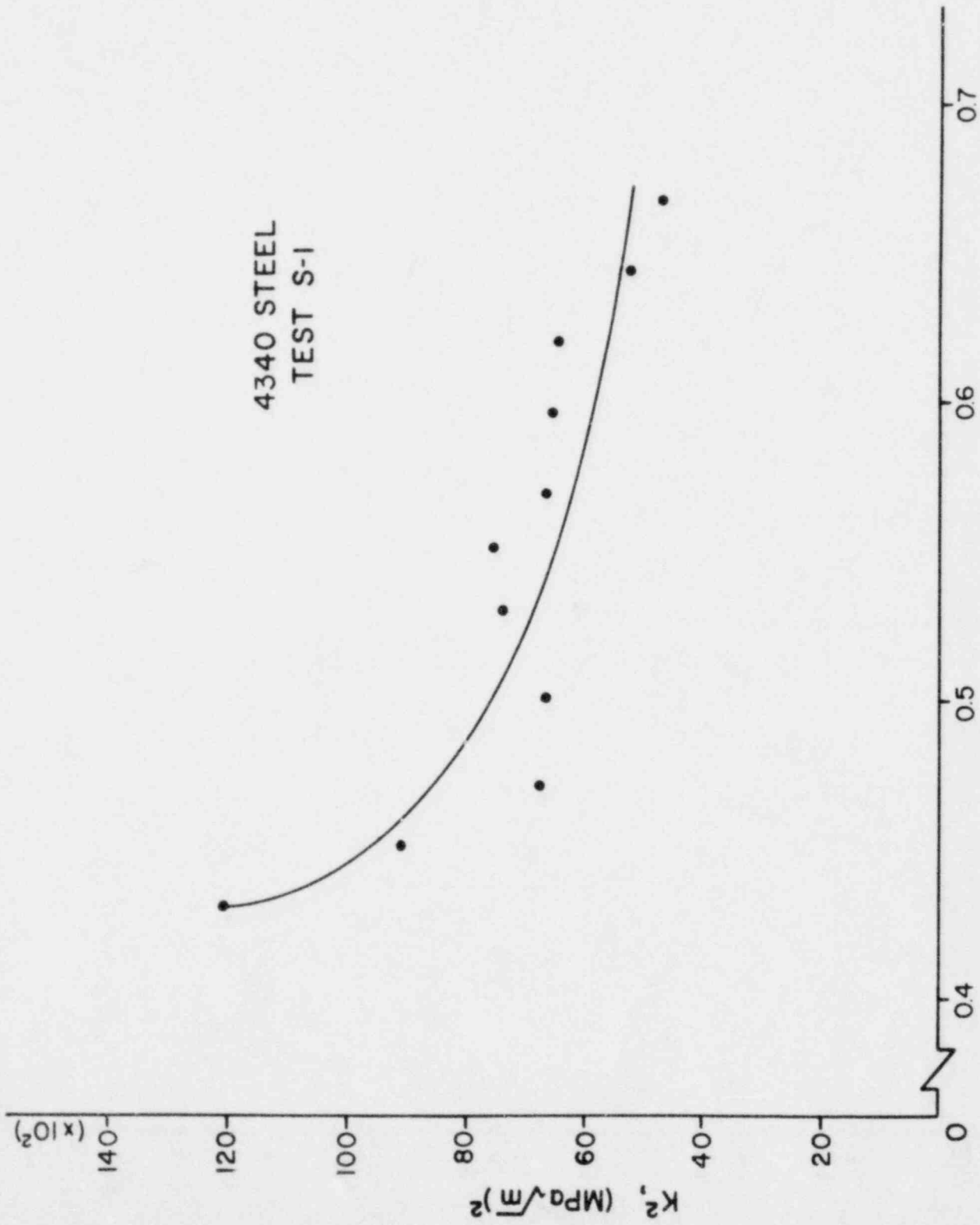
Fig. 2.36 K^2 as a Function of a/w for Test S-1 (4340 Steel).
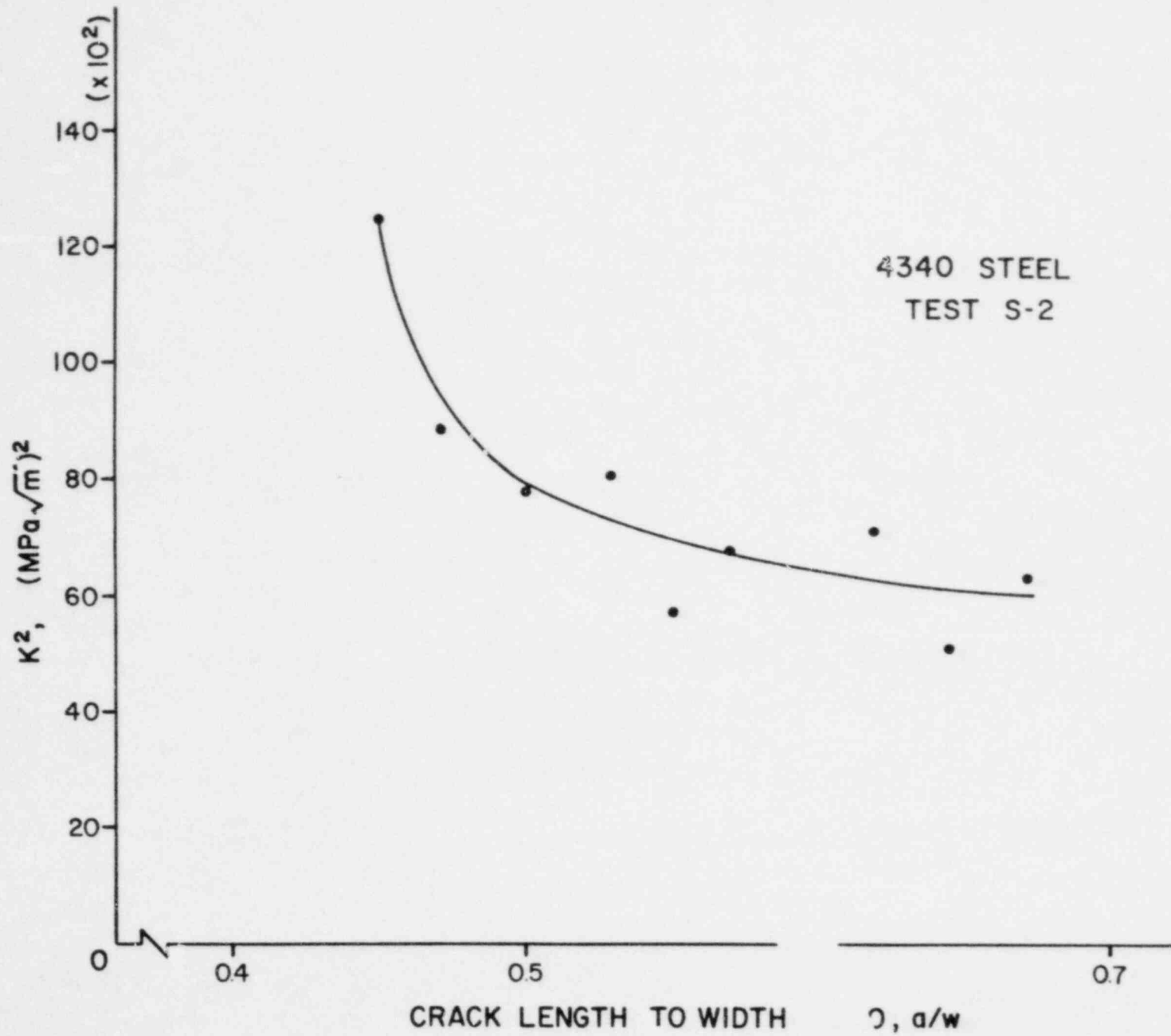
Fig. 2.37 K^2 as a Function of a/w for Test S-2 (4340 Steel).

TOP VIEW

Fig. 2.38 Fracture Surface of a 4340 Steel Specimen, Showing Late-Breaking Ligaments.
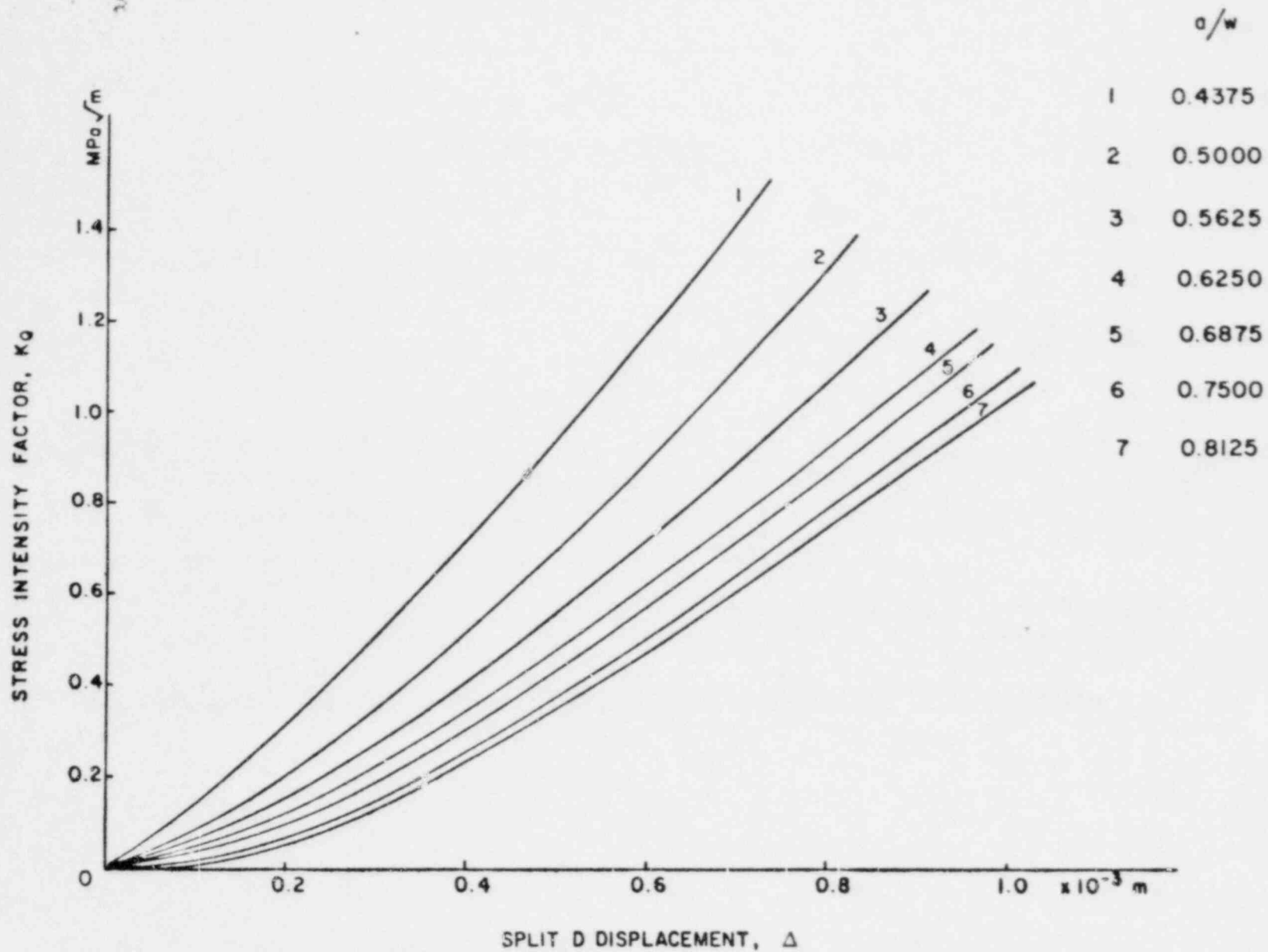
Fig. 2.39 Static Stress Intensity Factor, K_Q as a Function of Pin
Displacement for the Homalite 100 M-CT Specimen.
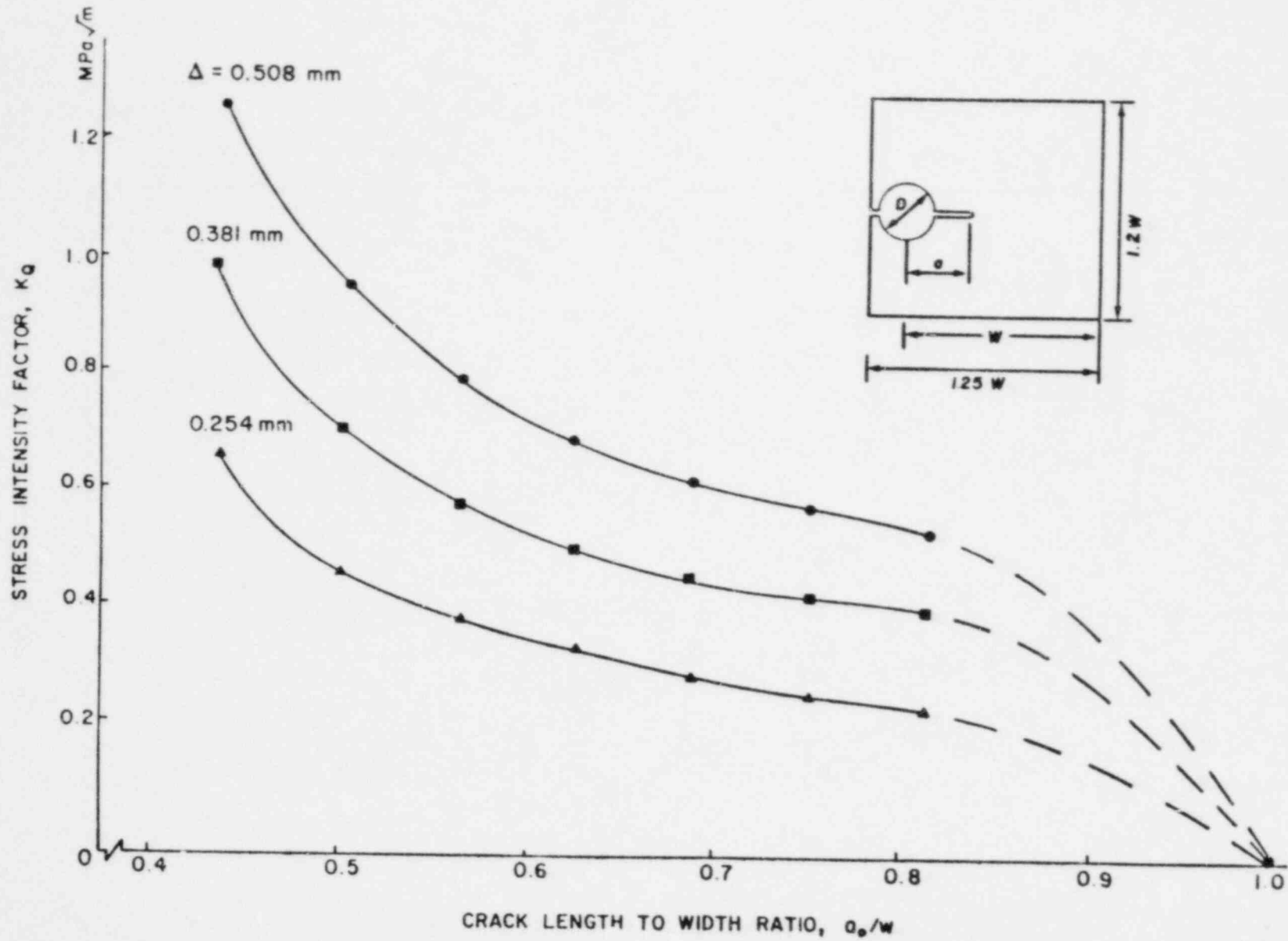
Fig. 2.40   Static Stress Intensity Factor, K_Q, as a Function of a/w
for the Homalite 100 M-CT Specimen.
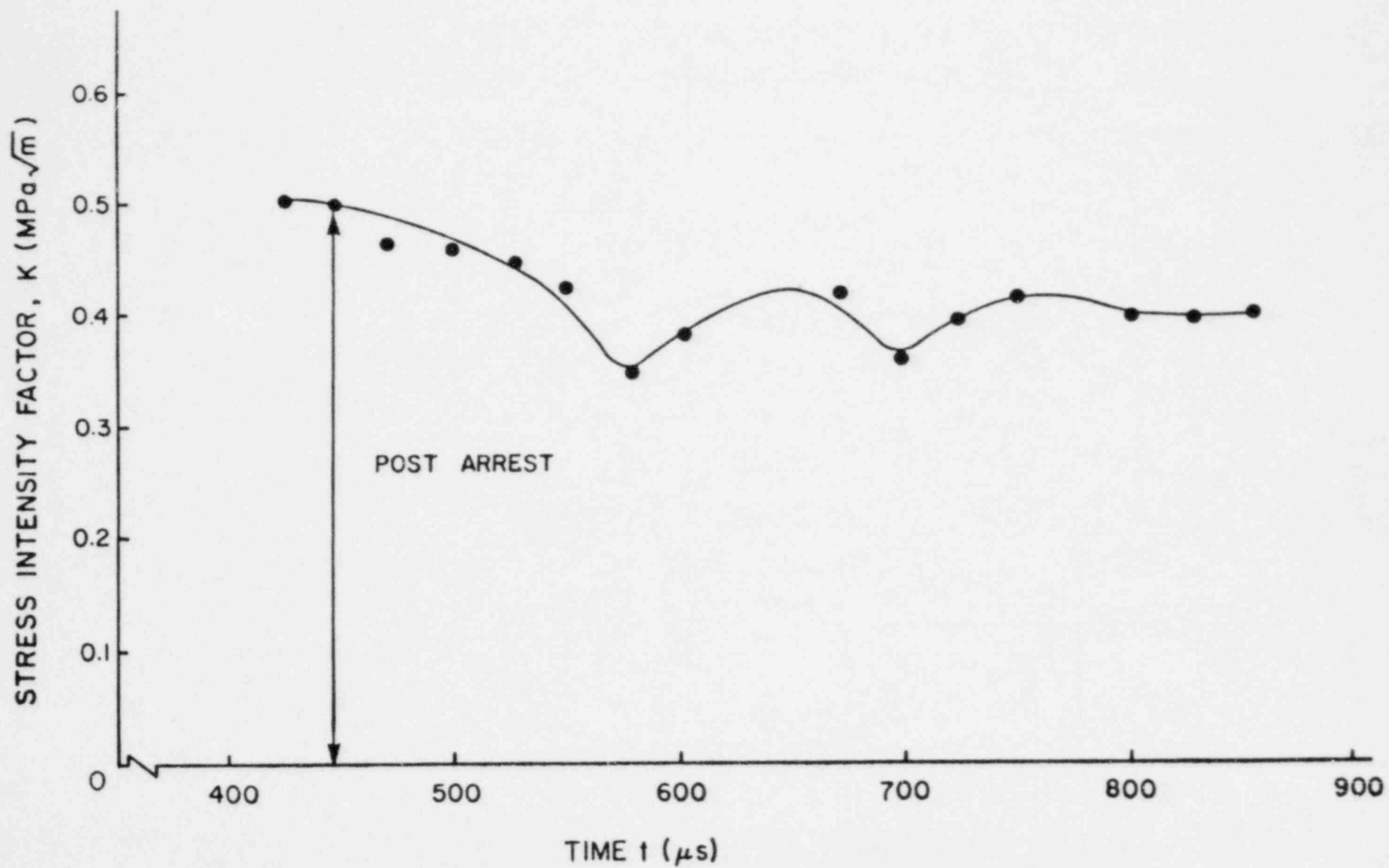
Fig. 2.41   Stress Intensity Factor, K, as a Function of Time for Test P-1 (Homalite 100).
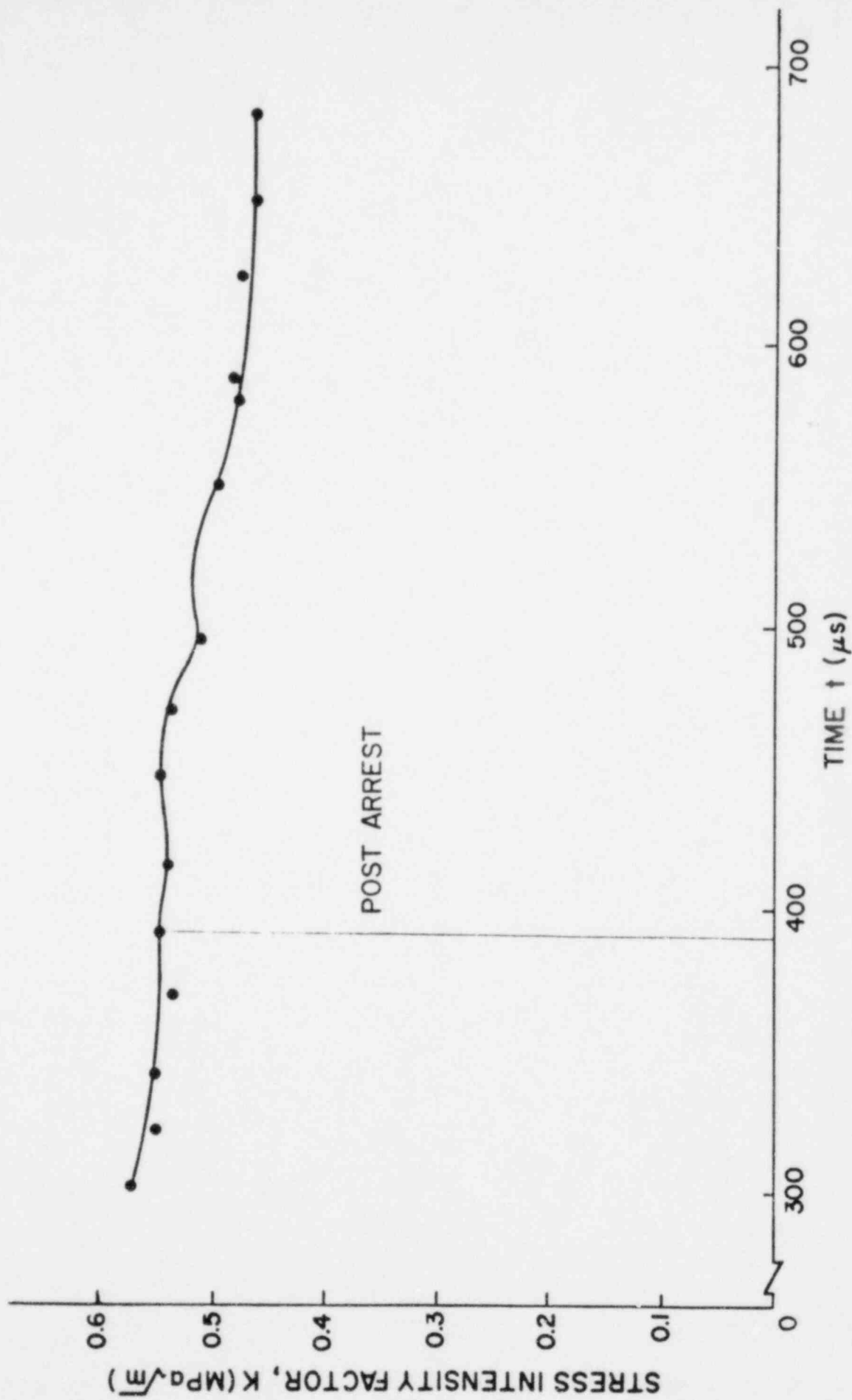
Fig. 2.42 Stress Intensity Factor, K, as a Function of Time for Test P-2 (Homalite 100).
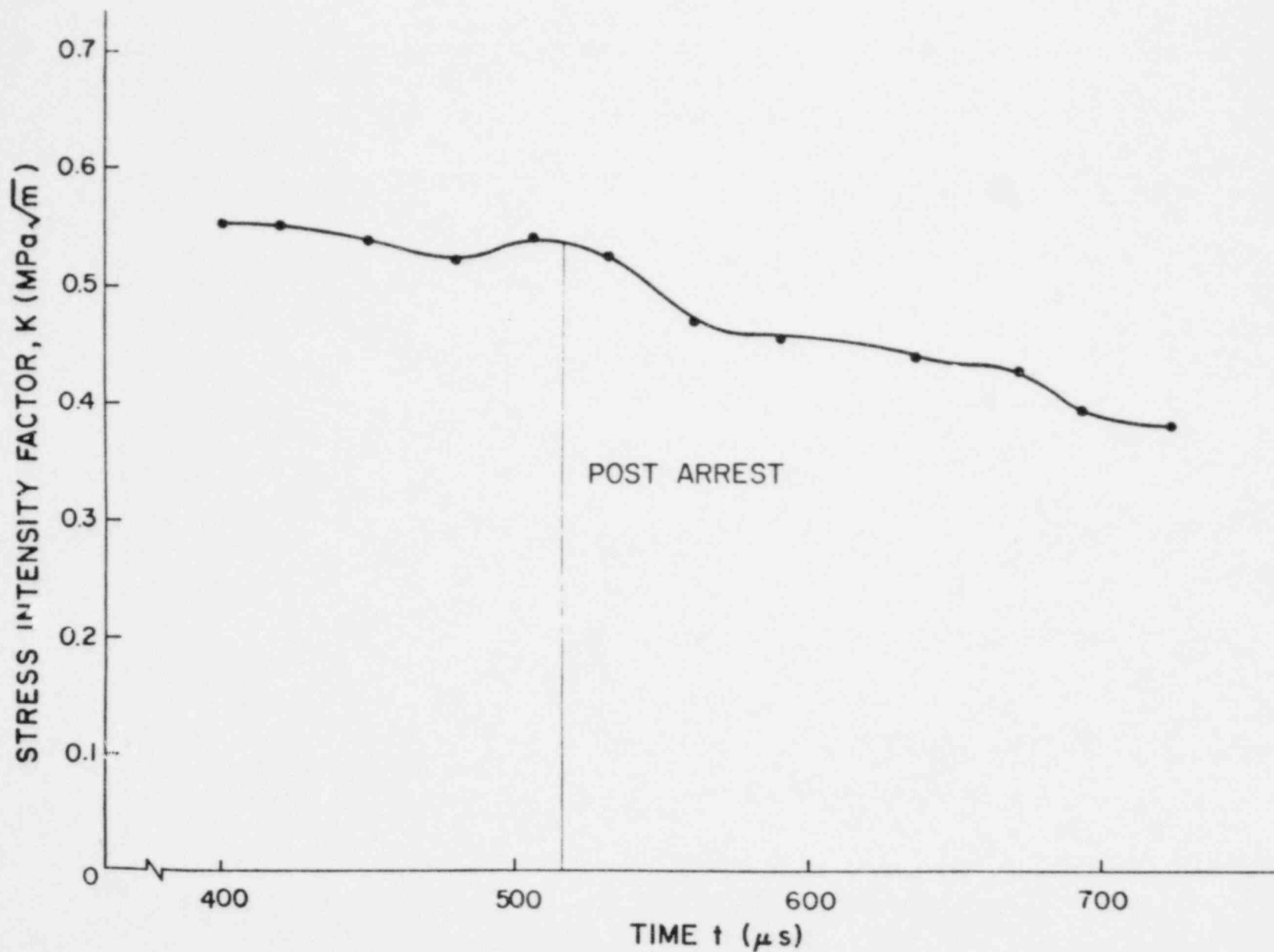
Fig. 2.43 Stress Intensity Factor, K, as a Function of Time for Test P-3
(Homalite 100).
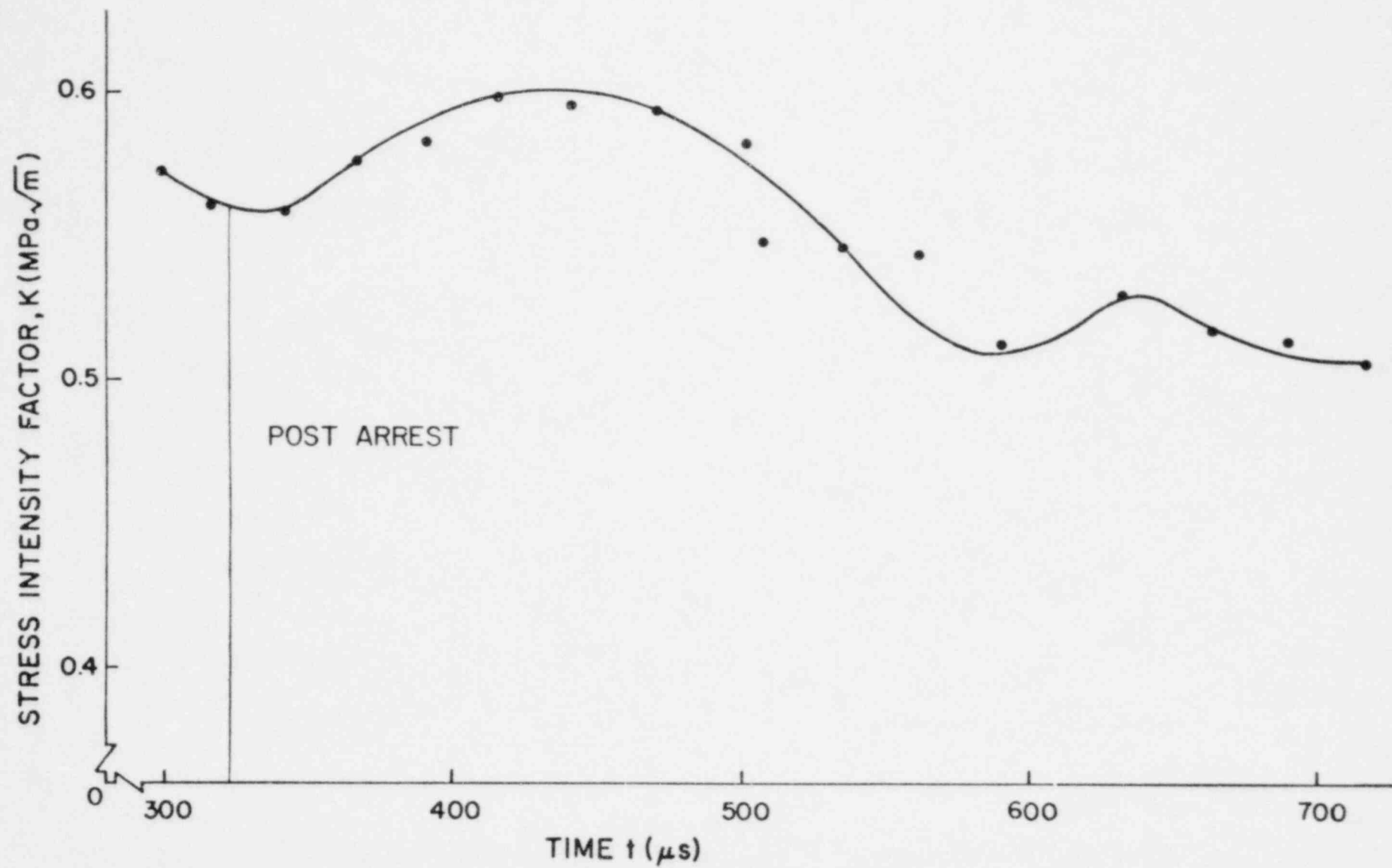
Fig. 2.44   Stress Intensity Factor, K, as a Function of Time for Test P-4
(Homalite 100).
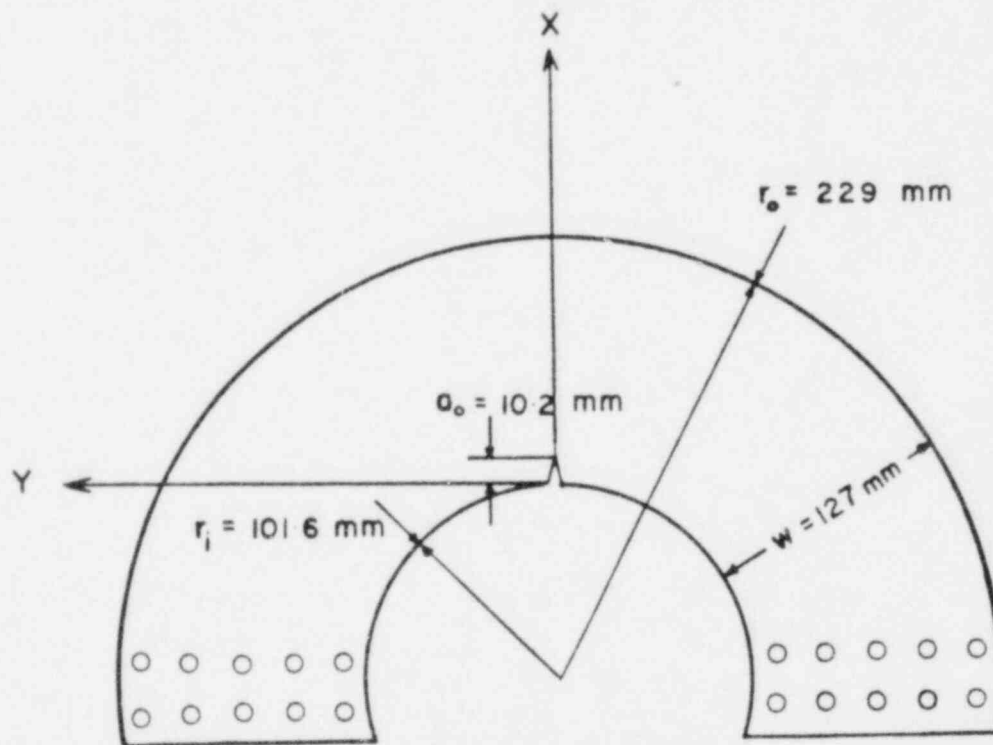
Fig. 2.45 Geometry and Dimensions of the Ring Specimen.
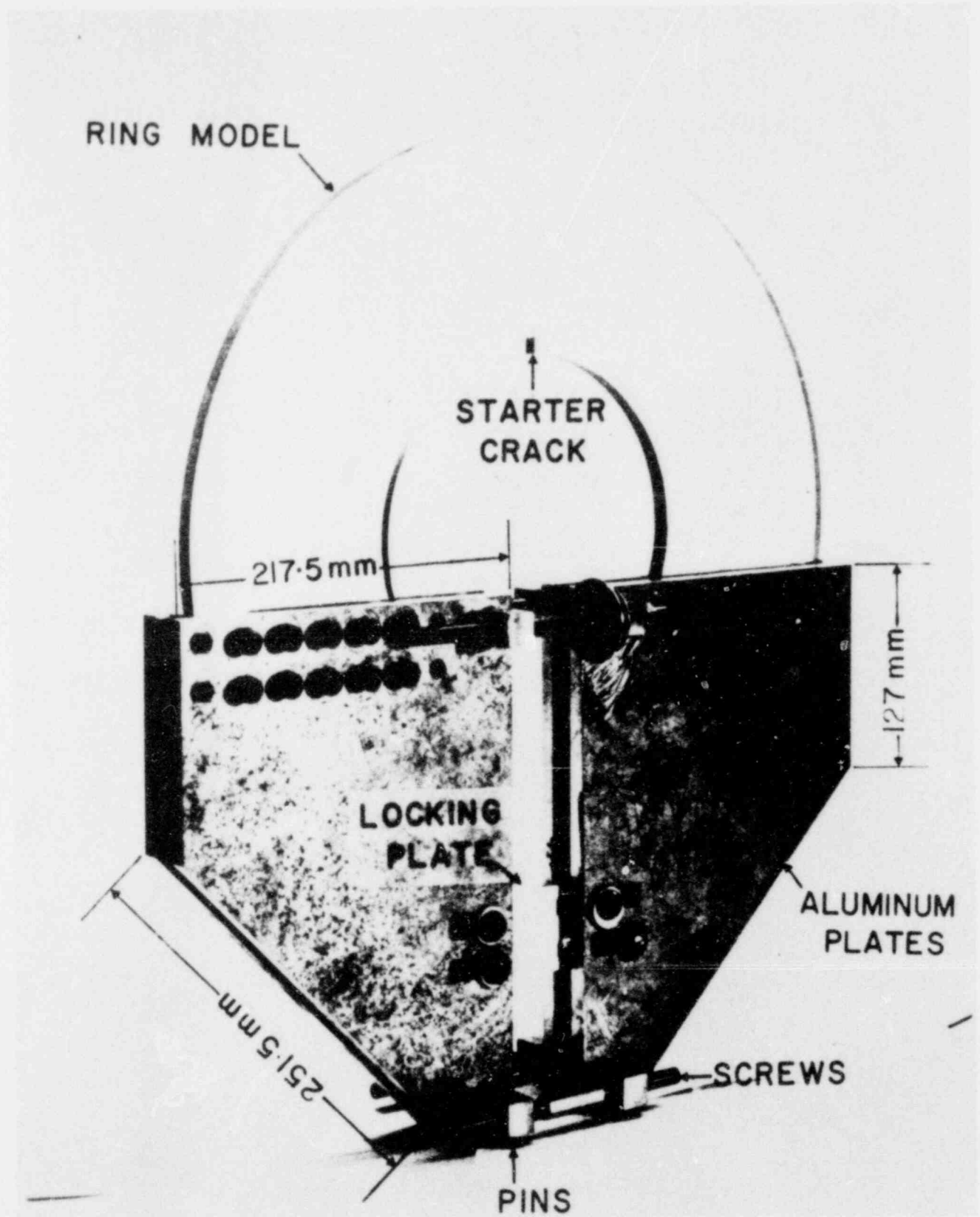
Fig. 2.46 The Ring Specimen Attached to the Loading Fixture Used.
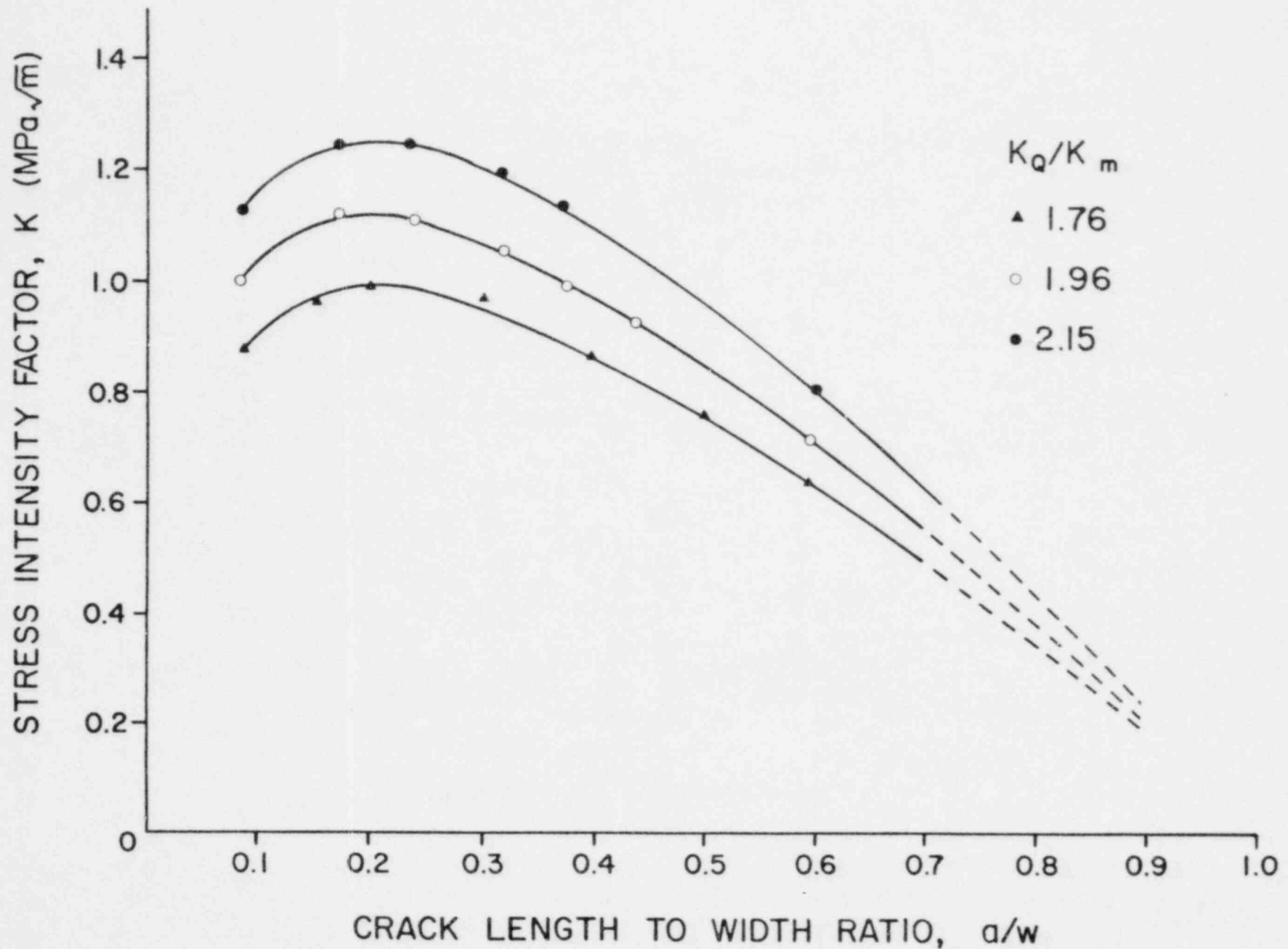
Fig. 2.47 Static Stress Intensity Factor, K_s, as a Function of Starter Crack Length to Width Ratio, a_o/w, for the Ring Specimen.

FRAME 1, 22 μs   FRAME 2, 45 μs   FRAME 3, 68 μs   FRAME 4, 98 μs

FRAME 5, 147 μs   FRAME 6, 170 μs   FRAME 7, 200 μs   FRAME 8, 233 μs

FRAME 9, 256 μs   FRAME 10, 285 μs   FRAME 11, 317 μs   FRAME 12, 352 μs

FRAME 13, 358 μs   FRAME 14, 380 μs   FRAME 15, 410 μs   FRAME 16, 442 μs
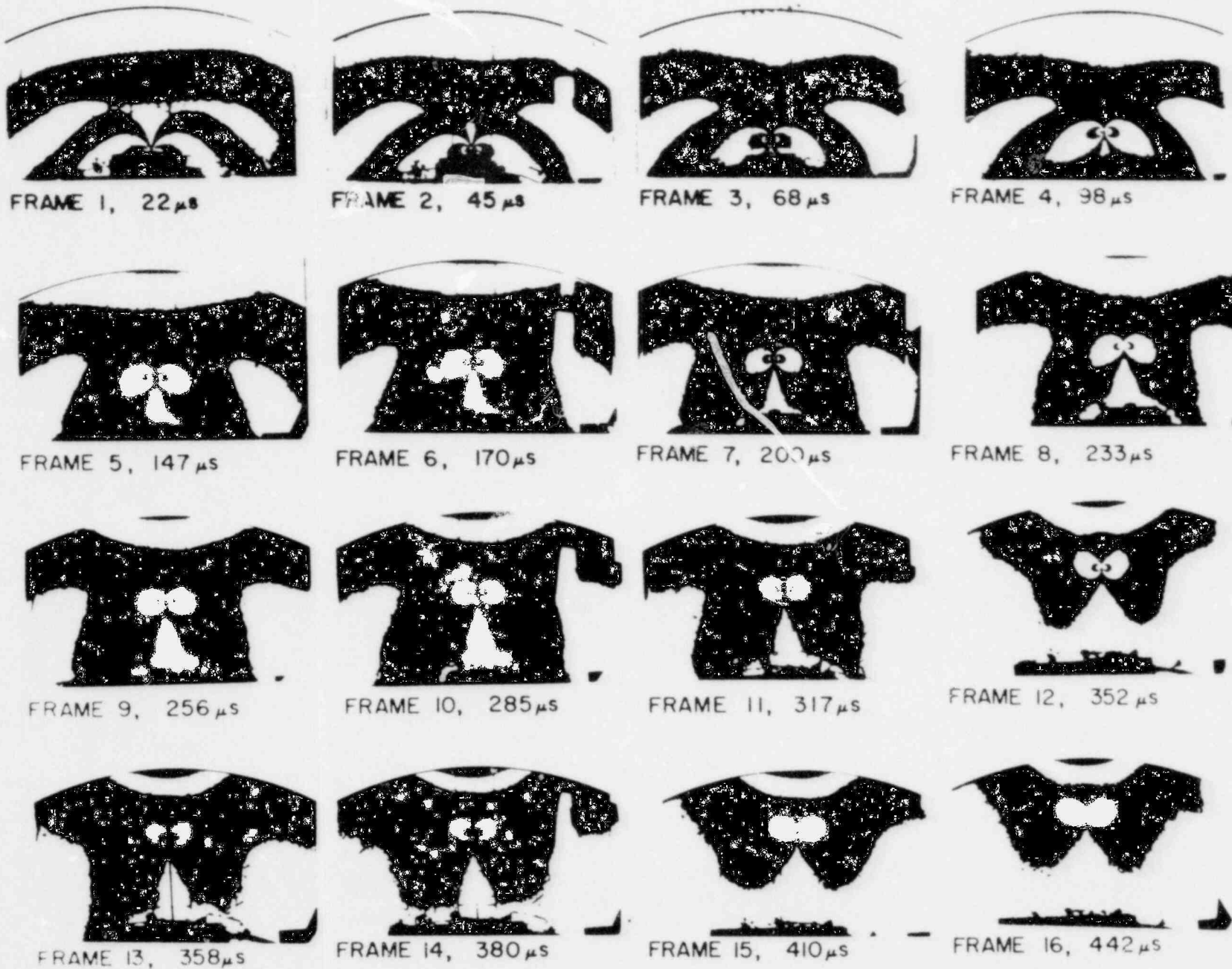
Fig. 2.48   Typical Dynamic Isochromatic Fringe Patterns Showing a Crack
Propagating in a Ring Specimen.
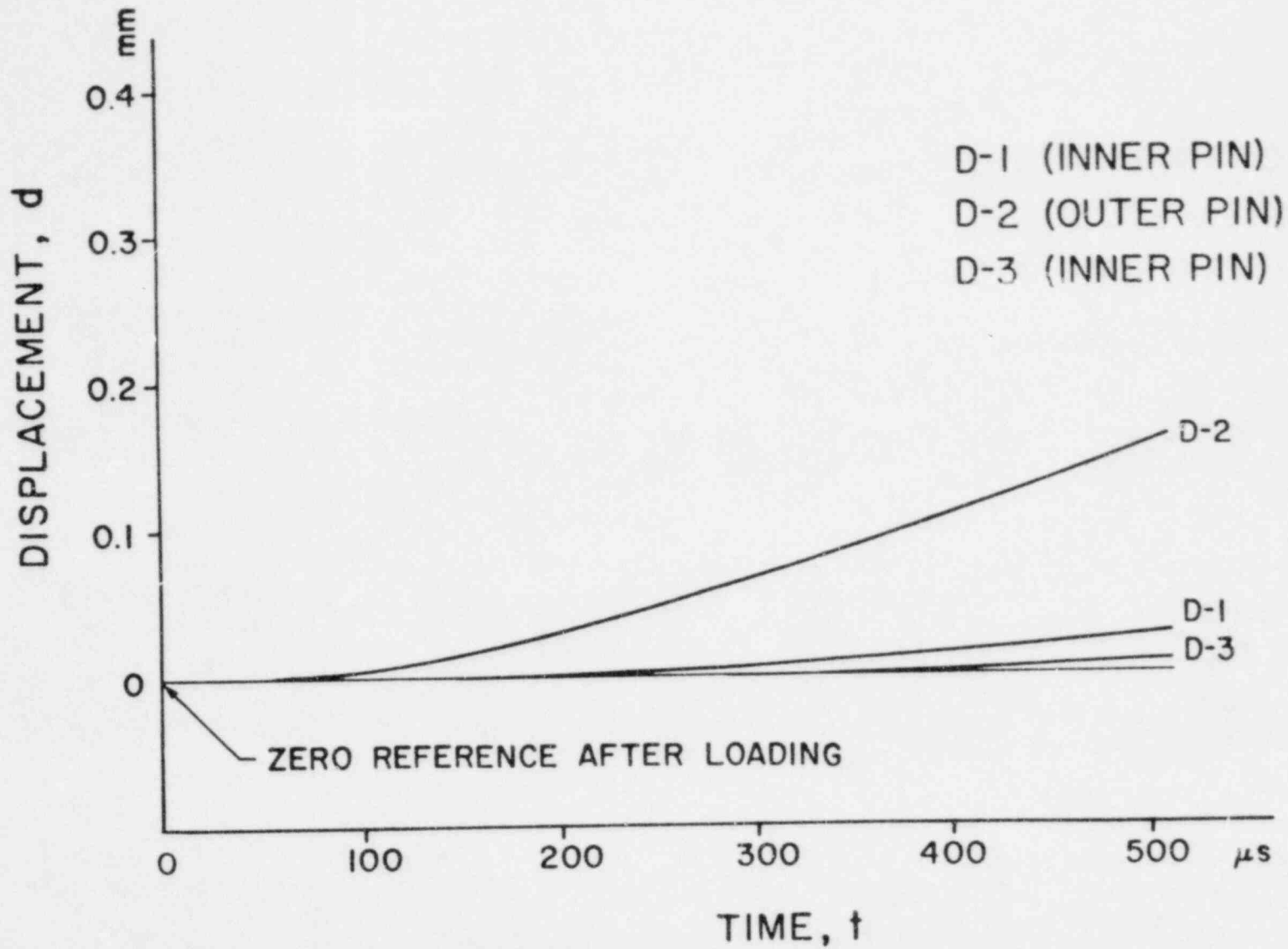
Fig. 2.49 Loading Pin Displacements as a Function of Time During Crack
Propagation and Arrest.
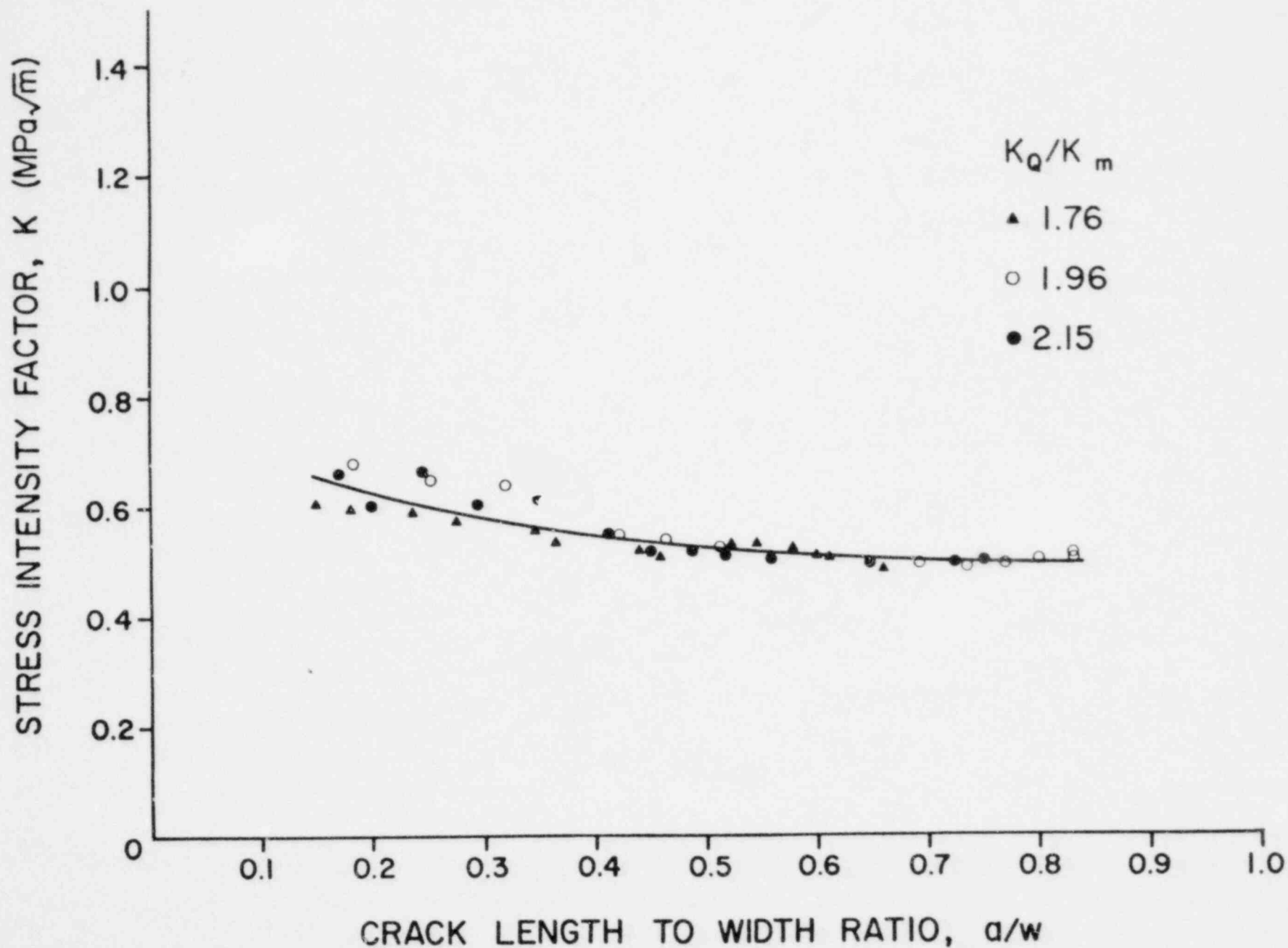
Fig. 2.50 Stress Intensity Factor, K, as a Function of a/w for the Ring
Specimen.
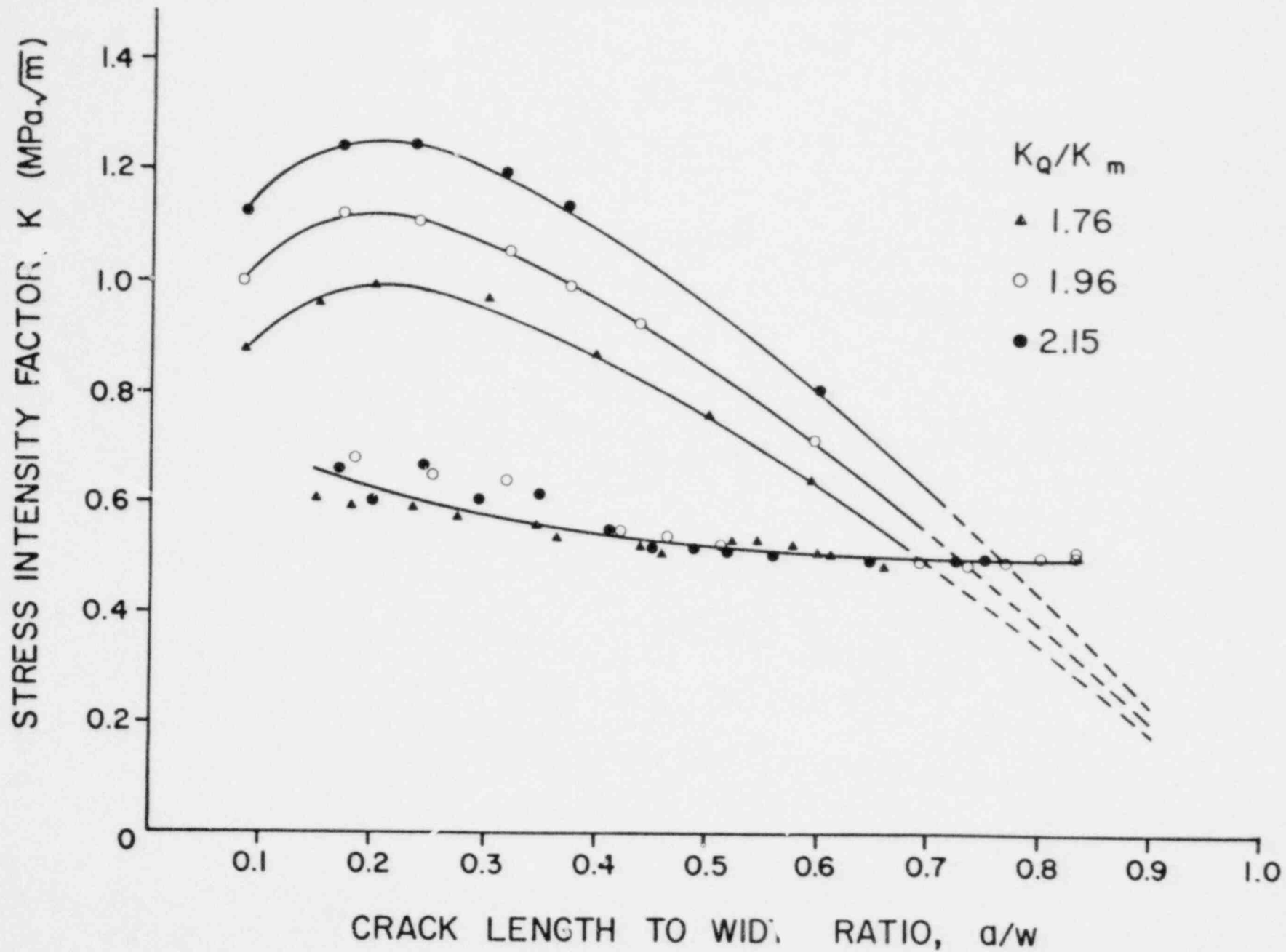
Fig. 2.51 Static and Dynamic Stress Intensity Factor, K, as a Function of a/w for the Ring Specimen.

CURVE	a/w
1	0.4375
2	0.5000
3	0.5625
4	0.6250
5	0.6875
6	0.7500
7	0.8125

DISPLACEMENT, Δ

LOAD, P (N)
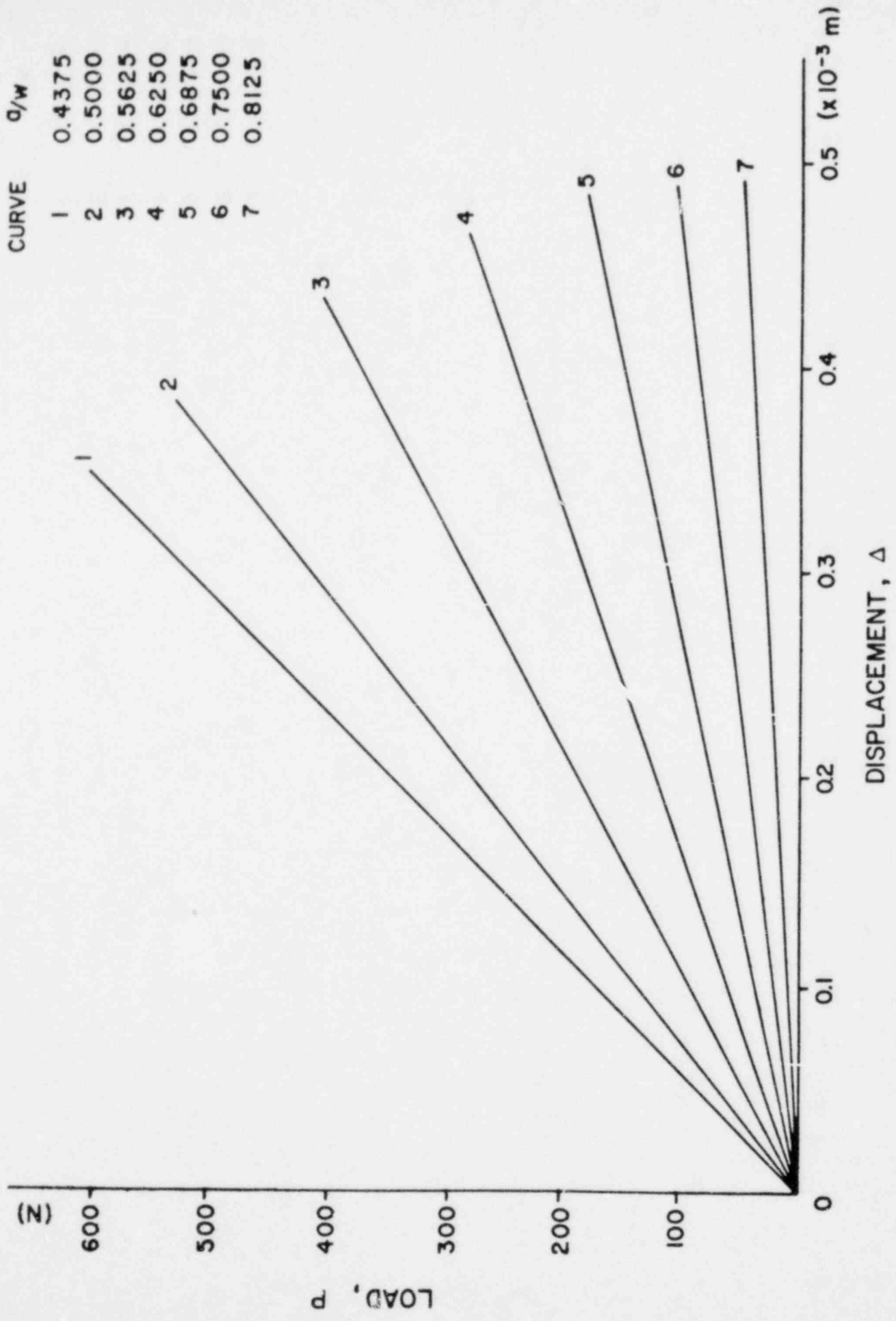
Fig. 2.52 Load as a Function of Displacements Measured on the Homalite 100 M-CT Specimen.
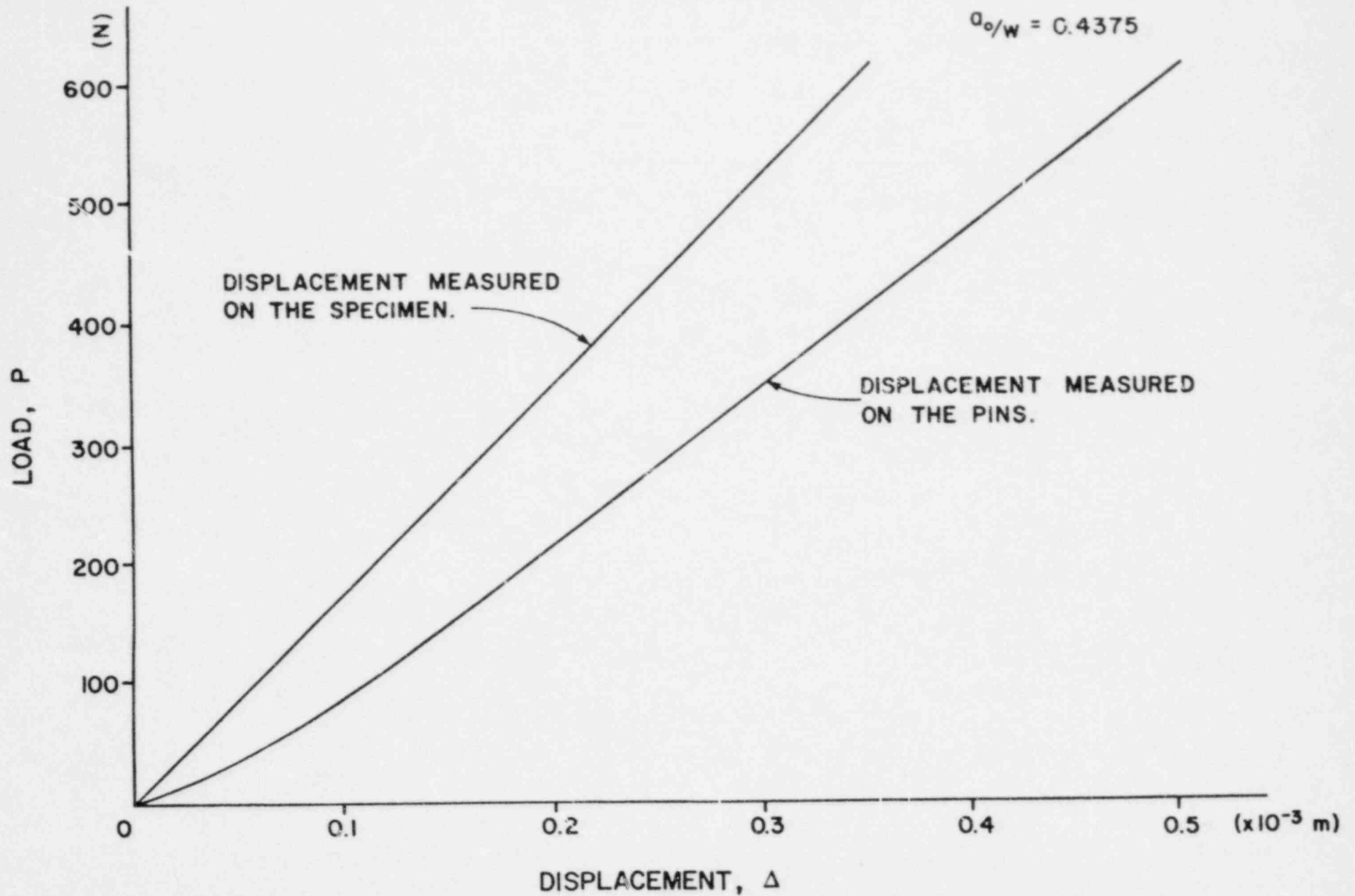
Fig. 2.53 Comparison of Compliance Curves for the Homalite 100 M-CT
Specimen Obtained Using Displacements Measured on the Pins
and on the Specimen.

3. Effect of Higher Order Terms on K-Determination Using Optical Methods

3.1 Introduction

It is generally recognized that the Irwin near-field equations adequately describe the state of stress in the immediate neighborhood of a stationary crack tip, excluding a very small region around the crack tip itself. For the opening mode of crack extension these equations are of the form [3.1]:

$$\sigma_x = \frac{K}{\sqrt{2\pi r}} \cos \frac{\theta}{2} \left(1 - \sin \frac{\theta}{2} \sin \frac{3\theta}{2}\right) - \sigma_{ox}$$

$$\sigma_y = \frac{K}{\sqrt{2\pi r}} \cos \frac{\theta}{2} \left(1 + \sin \frac{\theta}{2} \sin \frac{3\theta}{2}\right) \tag{3.0}$$

$$\tau_{xy} = \frac{K}{\sqrt{2\pi r}} \cos \frac{\theta}{2} \sin \frac{\theta}{2} \cos \frac{3\theta}{2}$$

where r and θ are polar coordinates with the origin located at the crack tip.

The region of validity of these equations is however quite restricted (r/a<<1). The problem is further complicated by the fact that in the local neighborhood of the crack tip there is a gradual transition from a state of plane strain to generalized plane stress, even in thin specimens. To avoid this region of uncertainty the experimental stress analyst is constrained to take measurements outside of the transition region. The size of this region for purely elastic specimens is of the order of one-half the plate thickness.

On the other hand, measurements taken outside of this region border on the validity of the near-field equations. Accordingly, it

93

is appropriate to investigate the influence of higher order terms on the stress field around but not immediately adjacent to the crack tip. In this chapter the effect of these higher order (i.e. non-singular) terms on the correct interpretation of fringe patterns obtained from photoelasticity, optical interferometry and the method of caustics will be examined. The optical equations, including the higher order effects, in their most general form for each of these alternate experimental techniques for determining the stress intensity factor will be derived in sections 3.4, 3.5 and 3.6, respectively. In each case the significance of the non-singular terms will be discussed in relation to the interpretation of the observed fringe pattern.

Prior to the derivation of these equations a brief review of the Westergaard method for solving opening mode crack problems will be presented. The modified Westergaard equations which have, to date, formed the basis for most linear elastic fracture mechanics analysis, will be shown to be inadequate to describe some of the effects observed in experiments. Fortunately, there is a generalization of the Westergaard procedure which does possess the flexibility to explain the experimental observations. This generalization of the Westergaard method is developed in detail in section 3.3 and forms the basis for the derivation of the optical equations which follow.

3.2 History of the Westergaard Method

In his original paper, Westergaard demonstrated that "in a restricted but important group of cases the normal stresses and the shearing stress in the directions x and y can be stated in the form" [3.2]:

94

$$\sigma_x = \text{Re}Z(z) - y\text{Im}Z'(z) \tag{3.1}$$

$$\sigma_y = \text{Re}Z(z) + y\text{Im}Z'(z) \tag{3.2}$$

$$\tau_{xy} = -y\text{Re}Z'(z) \tag{3.3}$$

where

$$Z = Z(z) = Z(x+iy) = \text{Re}Z + i\text{Im}Z \tag{3.4}$$

and

$$Z'(z) = \frac{dZ}{dz} = \text{Re}Z' + i\text{Im}Z' \tag{3.5}$$

For traction-free cracks located along the x-axis and subjected to symmetric loads, the stress function, Z, is chosen such that:

$$\text{Re}Z(z) = 0 \tag{3.6}$$

over the domain of the crack (to ensure that $\sigma_y = 0$). Note that the other boundary condition, $\tau_{xy} = 0$, along the entire x-axis is automatically satisfied from the form of eq. (3.3).

In 1958, Irwin in a discussion [3.1] of the experimental work of Wells and Post [3.3] noted that the equations of Westergaard could be modified to include an arbitrary uniform stress in the x-direction, σ_{ox}; thus, the modified Westergaard equations became

$$\sigma_x = \text{Re}Z - y\text{Im}Z' - \sigma_{ox} \tag{3.7}$$

$$\sigma_y = \text{Re}Z + y\text{Im}Z' \tag{3.8}$$

$$\tau_{xy} = -y\text{Re}Z' \tag{3.9}$$

The inclusion of the non-singular stress, σ_{ox}, was necessary to explain the tilt of the isochromatic fringe loops away from the normal in the work of Wells and Post. The Irwin modification, in conjunction with the near field stress equations, has formed the basis for the analysis of photoelastic fringe patterns in the neighborhood of a crack tip from which the stress intensity factor has been obtained for a variety of geometries. A review of these methods can be found in references [3.4, 3.5, 3.6].

Tada, Paris and Irwin [3.7] suggest that a mode I stress function of the form

$$Z(z) = \frac{K}{\sqrt{2\pi z}} + \sum_{n=1}^{N} \bar{A}_n z^{n-\frac{1}{2}} \tag{3.10}$$

be used in conjunction with the boundary collocation method to solve opening mode crack problems with finite boundaries. At this point it is instructive to pose the following question: is the stress function, eq. (3.10), in conjunction with the modified Westergaard equations, eq. (3.7-3.9), sufficiently general to solve a broad class of problems of current interest? To answer this question examine the form of the maximum shearing stress in Westergaard notation. Recall that

$$(\tau_m)^2 = \left(\frac{\sigma_x - \sigma_y}{2}\right)^2 + (\tau_{xy})^2 \tag{3.11}$$

thus

$$(\tau_m)^2 = y^2 Z' \cdot \bar{Z}' + y\sigma_{ox} \text{Im} Z' + \left(\frac{\sigma_{ox}}{2}\right)^2 \tag{3.12}$$

where $\bar{Z}$ = complex conjugate of Z. In particular, along the axis of symmetry, $y = 0$, eq. (3.12) reduces to:

$$2\tau_m = |\sigma_{ox}| \tag{3.13}$$

96

Thus, if the modified Westergaard eqs. are valid, the photoelastic fringe order (proportional to $2\tau_m$) ahead of the crack is constant FOR ANY STRESS FUNCTION Z. Clearly, this is not always the case. For example, for cracks approaching a boundary, as in Fig. 3.1, of a Modified-Compact-Tension specimen, isochromatic fringe loops typically form ahead of the crack. This counter-example raises questions about the validity of the modified Westergaard equations in general, and on the use of the series stress function (eq. 3.10) in particular, for solving problems in which the boundary or stress gradient ahead of the crack can be expected to play a significant role.

3.3 The Generalized Westergaard Equations [3.8]

From the conclusions of the previous section it is clear that the modified Westergaard formulation does not provide the most general formulation for an opening mode crack problem in the plane. Fortunately, there is a generalization of the Westergaard equations which does provide the required versatility. To derive these equations it is useful to follow Sih's procedure [3.9] of using the Goursat-Kolosov complex representation of the plane problem and the potential functions, ϕ and ψ, i.e.

$$\sigma_x + \sigma_y = 4\text{Re}[\phi'(z)] \tag{3.14}$$

$$\sigma_y - \sigma_x + 2i\tau_{xy} = 2[\bar{z}\phi''(z) + \psi'(z)] \tag{3.15}$$

Separating eq. (3.15) into real and imaginary parts yields:

$$\tau_{xy} = x\text{Im}\phi'' - y\text{Re}\phi'' + \text{Im}\psi' \tag{3.16}$$

97

Imposing the symmetry condition $\tau_{xy} = 0$ on $y = 0$ results in the following relation which must be satisfied:

$$x\,\mathrm{Im}\phi'' + \mathrm{Im}\psi' = 0 \qquad \text{on } y = 0 \tag{3.17}$$

Define a function, $\eta(z)$, such that

$$\eta(z) = z\phi''(z) + \psi'(z) \tag{3.18}$$

Then, the symmetry condition of eq. (3.17) is equivalent to:

$$\mathrm{Im}\eta(z) = 0 \text{ on } y = 0 \tag{3.19}$$

Combining eq. (3.18) and eq. (3.15) yields

$$\sigma_y - \sigma_x + 2i\tau_{xy} = 2[(\bar{z}-z)\phi''(z) + \eta(z)] \tag{3.20}$$

and

$$\sigma_x = 2\mathrm{Re}\phi' - 2y\,\mathrm{Im}\phi'' - \mathrm{Re}\eta \tag{3.21}$$

$$\sigma_y = 2\mathrm{Re}\phi' + 2y\,\mathrm{Im}\phi'' + \mathrm{Re}\eta \tag{3.22}$$

$$\tau_{xy} = -2y\,\mathrm{Re}\phi'' + \mathrm{Im}\eta \tag{3.23}$$

The symmetry condition of eq. (3.19) can be satisfied by any one of three conditions dependent upon the degree of constraint placed on $\eta(z)$. Each case will be examined individually in order of increasing generality and the results transformed into the familiar Westergaard notation.

98

Case 1: $\eta(z) = 0$ for all z (3.24)

Setting $2\phi' = Z(z)$ yields:

$$\sigma_x = \text{Re}Z - y\text{Im}Z'$$

$$\sigma_y = \text{Re}Z + y\text{Im}Z'$$

$$\tau_{xy} = -y\text{Re}Z'$$

These are the original Westergaard equations, eq. (3.1 - 3.3).

Case 2: $\eta(z) = A$, a real constant for all z (3.25)

Setting $2\phi' = Z(z) - A$, yields

$$\sigma_x = \text{Re}Z - y\text{Im}Z' - 2A$$

$$\sigma_y = \text{Re}Z + y\text{Im}Z'$$

$$\tau_{xy} = -y\text{Re}Z'$$

which can be recognized as Irwin's modified Westergaard equations,
eq. (3.7-3.9), with $\sigma_{ox} = 2A$. Note that this case is equivalent to the
condition: $\text{Im}\eta(z) = 0$ for all z.

Case 3: $\text{Im}\eta(z) = 0$ only on $y = 0$ (3.26)

Setting $2\phi' = Z(z) - \eta(z)$ yields

$$\sigma_x = \text{Re}Z - y\text{Im}Z' + y\text{Im}\eta' - 2\text{Re}\eta \qquad (3.27)$$

$$\sigma_y = \text{Re}Z + y\text{Im}Z' - y\text{Im}\eta' \qquad (3.28)$$

$$\tau_{xy} = -y\text{Re}Z' + y\text{Re}\eta' + \text{Im}\eta \qquad (3.29)$$

For each of the above cases, the stress function $Z(z)$ is the familiar
Westergaard stress function for the geometry under consideration and must
satisfy the condition of eq. (3.6). Similarly, $\eta(z)$ must satisfy eq.
(3.19). As a complement to the series stress function, eq. (3.10), a
suitable function for $\eta(z)$ is:

$$\eta(z) = \sum_{m=0}^{M} \alpha_m z^m \tag{3.30}$$

With this choice of $\eta(z)$, the photoelastic fringe order ahead of the crack is of the form:

$$2\tau_m = 2 \left| \sum_{m=0}^{M} \alpha_m x^m \right| \tag{3.31}$$

Clearly, of the three possible constraint conditions, only the "generalized" Westergaard eqs.(3.27-3.29) can provide the flexibility to solve plane crack problems such as that shown in Fig. 3.1 in which the photoelastic fringe order varies ahead of the crack.

It should be noted that the same type of generalization can be applied to the forward shear mode (Mode II) Westergaard equations; however, these equations are of no interest in the present study and will not be developed in this report.

In the following sections the application of the generalized Westergaard equations, eqs.(3.27-3.29), to each of the three major types of optical methods used in fracture mechanics, i.e. isochromatics, isopachics, and the method of caustics,will be developed and the effect of the higher order non-singular terms on the shape of the optical pattern will be demonstrated.

3.4 Application to Isochromatics

In the previous section it was demonstrated that, if the overly restrictive constraints imposed by Westergaard are removed, the state of stress in a plane body containing a crack subjected to opening mode forces only can be expressed as:

$$\sigma_x = \text{Re}Z - y\text{Im}Z' + y\text{Im}\eta' - 2\text{Re}\eta$$

$$\sigma_y = \text{Re}Z + y\text{Im}Z' - y\text{Im}\eta'$$

$$\tau_{xy} = -y\text{Re}Z' + y\text{Re}\eta' + \text{Im}\eta$$

where the complex functions $Z(z)$ and $\eta(z)$ are chosen such that:

$\text{Re}Z = 0$ on the crack boundary

and $\quad\quad\quad$ $\text{Im}\eta = 0$ on $y = 0$.

Consider the problem depicted in Fig. 3.2, i.e. a single-ended, traction-free crack with infinite or finite boundaries subjected to symmetric forces in the plane. Let the origin of the complex coordinate, z, be located at the crack tip. Then, the Westergaard stress function, Z, can be expressed as:

$$Z(z) = \sum_{n=0}^{N} \frac{A_n}{(n-\frac{1}{2})} z^{n-\frac{1}{2}} \tag{3.32}$$

where, the stress intensity factor, K, is given by:

$$K = -2\sqrt{2\pi}\, A_0 \tag{3.33}$$

Recall that, the η function is of the form (eq. 3.30):

$$\eta(z) = \sum_{m=0}^{M} \alpha_m z^m$$

From eq. (3.11), the photoelastic fringe order, N, can be expressed in the form:

$$\left(\frac{Nf_\sigma}{2t}\right)^2 = D^2 + T^2 \tag{3.34}$$

where, from (3.27 - 3.29)

$$D = y\text{Im}Z' - y\text{Im}\eta' + \text{Re}\eta \tag{3.35}$$

$$T = -y\text{Re}Z' + y\text{Re}\eta' + \text{Im}\eta$$

101

f_σ = the photoelastic fringe constant

and t = model thickness.

In terms of the crack tip coordinates, (r, θ), the functions D and T become:

$$D = \sum_{n=0}^{N} A_n r^{n-\frac{1}{2}} \sin \theta \sin (n-\tfrac{1}{2})\theta$$

$$+ \sum_{m=0}^{M} \alpha_m r^m [\cos (m\theta) - m \sin \theta \sin (m-1)\theta] \qquad (3.37)$$

and

$$T = \sum_{n=0}^{N} (-A_n) r^{n-\frac{1}{2}} \sin \theta \cos (n-3/2)\theta$$

$$+ \sum_{m=0}^{M} \alpha_m r^m [\sin (m\theta) + m \sin \theta \cos (m-1)\theta] \qquad (3.38)$$

Eqs. (3.37) and (3.38) when substituted into eq. (3.34) represent the general solution for the isochromatic fringe pattern around a crack tip for any size region. The size of the region and the degree of precision desired determines the number of terms in the series expansions which must be retained in order to adequately describe the stress state. The constants, A_0, A_1, ..., α_0, α_1, ..., in these series can be determined from the experimentally obtained fringe pattern for any geometry by employing the non-linear least-squares method developed by Sanford and Dally [3.10] and Sanford [3.11]. This method utilizes an iterative procedure based on the Newton-Raphson method. Consider a set of functions of the form:

102

$$g_k(A_0, A_1, \ldots, A_N, \alpha_0, \alpha_1, \ldots, \alpha_M) = 0 \qquad (3.39)$$

where $k = 1, 2, \ldots, L$ $(L>N+M)$.

Taking the Taylor's series expansion of eq. (3.39) yields:

$$(g_k)_{i+1} = (g_k)_i + \left[\frac{\partial g_k}{\partial A_0}\right]_i \Delta A_0 + \left[\frac{\partial g_k}{\partial A_1}\right]_i \Delta A_1 + \ldots + \left[\frac{\partial g_k}{\partial A_N}\right]_i \Delta A_N$$

$$+ \left[\frac{\partial g_k}{\partial \alpha_0}\right]_i \Delta \alpha_0 + \left[\frac{\partial g}{\partial \alpha_1}\right]_i \Delta \alpha_1 + \ldots + \left[\frac{\partial g_k}{\partial \alpha_M}\right]_i \Delta \alpha_M \qquad (3.40)$$

where i refers to the ith iteration step, and ΔA_0, ΔA_1, $\ldots \Delta A_N$, $\Delta \alpha_1$, $\ldots \Delta \alpha_M$ are corrections to the previous estimates of A_0, A_1, $\ldots A_N$, α_0, α_1, $\ldots \alpha_M$, respectively.

Recognizing that from eq. (3.39), the desired result is $(g_k)_{i+1} = 0$, yields an iterative equation of the form:

$$\left[\frac{\partial g_k}{\partial A_0}\right] \Delta A_0 + \left[\frac{\partial g_k}{\partial A_1}\right] \Delta A_1 + \ldots + \left[\frac{\partial g_k}{\partial A_N}\right] \Delta A_N +$$

$$\left[\frac{\partial g_k}{\partial \alpha_0}\right] \Delta \alpha_0 + \left[\frac{\partial g_k}{\partial \alpha_1}\right] \Delta \alpha_1 + \ldots + \left[\frac{\partial g_k}{\partial \alpha_M}\right] \Delta \alpha_M = -(g_k) \qquad (3.41)$$

In matrix notation eq. (3.41) becomes:

$$[g] = [c] [\delta] \qquad (3.42)$$

where:

$$[g] = \begin{bmatrix} -g_1 \\ -g_2 \\ . \\ . \\ . \\ -g_L \end{bmatrix} ;$$

103

$$[c] = \begin{bmatrix} \dfrac{\partial g_1}{\partial A_0} & \cdots & \dfrac{\partial g_1}{\partial A_N} & \dfrac{\partial g_1}{\partial \alpha_0} & \cdots & \dfrac{\partial g_1}{\partial \alpha_M} \\ \vdots & & \vdots & \vdots & & \vdots \\ \dfrac{\partial g_L}{\partial A_0} & \cdots & \dfrac{\partial g_L}{\partial A_N} & \dfrac{\partial g_L}{\partial \alpha_0} & \cdots & \dfrac{\partial g_L}{\partial \alpha_M} \end{bmatrix} ;$$

$$[\delta] = \begin{bmatrix} \Delta A_0 \\ \vdots \\ \Delta A_N \\ \Delta \alpha_0 \\ \vdots \\ \Delta \alpha_M \end{bmatrix}$$

Since matrix $[c]$ is not square (L>M+N) eq. (3.42) has no unique solution. However, it can be shown that a solution in the least squares sense can be obtained from an auxiliary equation of the form [3.11]:

$$[\delta] = [d]^{-1}[c]^T[g] \tag{3.43}$$

where:

$$[d] = [c]^T[c]$$

and $\qquad [c]^T$ = transpose of $[c]$

To apply this solution scheme to the isochromatic equation, eq. (3.34) is recast in the form:

$$g_k = D_k^2 + T_k^2 - \left(\frac{N_k f_\sigma}{2t} \right)^2 = 0 \tag{3.44}$$

where k refers to the value of the function evaluated at a point in the field (r_k, θ_k) at which the fringe order is N_k.

Note that the column elements of the matrix [c] are of the form:

$$\frac{\partial g_k}{\partial A_0} = 2D_k\left(\frac{\partial D}{\partial A_0}\right)_k + 2T_k\left(\frac{\partial T}{\partial A_0}\right)_k$$

$$\vdots \qquad \qquad \vdots$$

$$\frac{\partial g_k}{\partial \alpha_0} = 2D_k\left(\frac{\partial D}{\partial \alpha_0}\right)_k + 2T_k\left(\frac{\partial T}{\partial \alpha_0}\right)_k$$

$$\vdots \qquad \qquad \vdots$$

Thus, the procedure for determining the best fit values of the constants consists of the following steps:

(a) from the fringe pattern select a sufficiently large set of data points (r_k, θ_k, N_k) over the region to be characterized,

(b) assume initial values for A_0, A_1, ... A_N, α_0, α_1, ...α_M,

(c) compute the elements of the matrices [g] and [c] for each data point,

(d) compute [δ] from eq. (3.43),

(e) .evise the estimates of the unknowns, i.e.

$$(A_0)_{i+1} = (A_0)_i + \Delta A_0$$

$$(A_1)_{i+1} = (A_1)_i + \Delta A_1$$

$$\vdots \qquad \qquad \vdots$$

$$(\alpha_M)_{i+1} = (\alpha_M)_i + \Delta \alpha_M \quad ,$$

(f) repeat steps (c), (d), and (e) until [δ] becomes acceptably small.

As an example of the application of the method developed above, consider the fringe pattern shown in Fig. 3.1. It was previously demonstrated that, since the isochromatic fringe order in this pattern is not

105

constant along the symmetry axis, the generalized Westergaard equations
must be used to describe the stress state in the region beyond the K-
dominated zone. From this pattern 60 data points were selected and
used with the least-squares method to compute the best fit values of
the first three terms of the series representation of each of the func-
tions Z and η, i.e. a six-parameter isochromatic model. The computed
values of these constants are given in Table 3.1. Using the values
from this Table, the theoretical isochromatic pattern was plotted as
shown in Fig. 3.3. For comparison the experimental fringe pattern over
the sub-region of Fig. 3.1 from which the 60 data points were selected
is also shown in Fig. 3.3.

Table 3.1

Coefficients of Six-parameter Model

A_0	-303.7 psi-$\sqrt{in}$
A_1	-382.4 psi/$\sqrt{in}$
A_2	-870.0 psi-$(in)^{-3/2}$
α_0	-33.0 psi
α_1	-211.1 psi/in
α_2	-114.3 psi/in^2
$f_\sigma = 134$ psi-in/Fringe $t = 0.5$ in	

3.5 Application to Isopachics

With the advent of holographic interferometry the observation
of the isopachic field (contours of constant sum of the principal
stresses) can be accomplished with relative ease. An example of such
a field in a Plexiglas model with a natural crack is shown in Fig.3.4.
To date, the application of holographic interferometry to the deter-
mination of the stress intensity factor has received only minimal attention.
In this regard, the research of Dudderar and O'Regan [3.12] and Dudderar
and Gorman [3.13] serve as examples of the current state of the art. In
these studies the analysis of the fringe pattern was based on the near-
field equations. Because of the inherent sensitivity of the method,
i.e. the large number of fringes available for analysis, and the ability
to enlarge the region near the crack tip using the magnifying property
of the holographic real image [3.14], there is a temptation to assume
that it is always possible to restrict measurements to the K-dominated
region. However, as was previously described, this assumption is in
conflict with the requirement to take measurements only outside the
plane strain to plane stress transition region. Therefore, it is
appropriate to examine the effect of the higher order terms on the
interpretation of isopachic fringe patterns around a crack tip from
the viewpoint of the generalized Westergaard equations.

The governing equation for an isopachic fringe pattern is given by:

$$\frac{Nf_p}{t} = \sigma_1 + \sigma_2 = \sigma_x + \sigma_y \qquad (3.45)$$

107

Therefore, from eq. (3.27-3.28)

$$\frac{Nf_p}{2t} = ReZ - Re\eta \qquad (3.46)$$

Substituting the series representations of the stress functions Z (eq. 3.32) and η (eq. 3.30) into the above equation yields the general solution for the isopachic fringe pattern around a crack tip for any size region, i.e.:

$$\frac{Nf_p}{2t} = \sum_{n=0}^{N} \frac{A_n}{(n-\frac{1}{2})} r^{n-\frac{1}{2}} \cos (n-\frac{1}{2})\theta \qquad (3.47)$$

$$- \sum_{m=0}^{M} \alpha_m r^m \cos m\theta$$

For an arbitrary point in the field (r_k, θ_k) eq. (3.47) has the form:

$$\frac{N_k f_p}{2t} = \frac{-2A_0}{\sqrt{r_k}} \cos \frac{\theta_k}{2} - \alpha_0 + 2A_1\sqrt{r_k} \cos \frac{\theta_k}{2}$$

$$- \alpha_1 r_k \cos \theta_k + \frac{2A_2}{3} r_k^{3/2} \cos \frac{3\theta_k}{2}$$

$$- \alpha_2 r_k^2 \cos 2\theta_k + \ldots \qquad (3.48)$$

Notice that, in marked contrast to the isochromatic equation (eq. 3.44), the above equation is linear in the unknown coefficients, A_n, α_m. In concept, the coefficients which provide the best match to a given experimental pattern could be obtained by direct application of the linear least squares algorithm developed by Sanford [3.11]. Since no iterative procedure

108

is required, the coefficients would be obtained from the solution of the auxiliary equation (similar to eq. 3.43) corresponding to a redundant set of equations of the form given by eq. (3.48). In practice, however, this procedure has not yielded satisfactory results. Preliminary studies indicate that, although the diameter of a given fringe changes, the basic shape of the fringe is only mildly affected by the higher order terms (except in extreme cases). To illustrate this effect the theoretical isopachic fringe pattern corresponding to the six parameters listed in Table 3.1 is shown on the right side of Fig. 3.5. For comparison the near-field solution at the same K level is shown on the left.

Although fundamentally different in origin, the shape of the caustic curve around a crack tip is similar to that of an isopachic and suffers from the same problem, i.e. the shape of the pattern is not strongly influenced by the higher order terms. This is not to say that the higher order terms do not influence the pattern. On the contrary, the effect may be large, but the ability of available analysis procedures to discriminate between the contribution due to the singular term versus the non-singular terms is poor and a possibility of an error in the determination of the stress intensity factor exists. Because of the similarity between isopachics and caustics, a discussion of the effect of neglecting higher order terms will be deferred until after the general theory of caustics is developed in the next section.

3.6 Application to Caustics

The method of shadow patterns, more commonly referred to as the method of caustics, has received considerable attention in European

109

laboratories as a method for determining the stress intensity factor. This optical method utilizes the refraction of light caused by changes in the optical properties of the material in the vicinity of a crack tip. The method was first introduced by Manogg [3.15] in 1964 and since that time has been applied to a variety of fracture-related problems by Beinert, Kalthoff, et al, at the Institut für Festkörpermechanik (IFKM) in Freiburg, Germany, and by Theocaris and co-workers at the Athens National Technical University in Greece. The method is applicable to both transparent and non-transparent materials. However, for purposes of this report, only the application to transparent materials (in particular photoelastic materials) will be discussed. A detailed description of the method is given in [3.16].

The physical principle underlying the method of shadow patterns is illustrated in Fig. 3.6 [3.17]. An initially plane parallel specimen containing a crack is loaded by a tensile stress, σ. In the upper part of the figure a transparent specimen is considered. The stress intensification in the region surrounding the crack tip causes a reduction of the thickness of the specimen and a change in the refractive index of the material. As a consequence, the area surrounding the crack tip behaves like a divergent lens and light transmitted through the specimen is deflected outward. Therefore, on a plane at a distance, z_0, behind the specimen the shadow image of the crack tip is obscured by a dark spot. This spot is bounded by a bright light concentration, i.e. an optical caustic. The shadow pattern is shown schematically on the right side of Fig. 3.6. In the lower part of the figure a similar effect is illustrated for a non-transparent material with a mirrored

110

surface except that in this case the caustic appears on a virtual image plane. Since the magnitude of the light deflection is related to the stress-strain distribution around the crack tip, the shadow pattern contains information about the stress intensification at the crack tip. Manogg [3.15] derived the governing relations for the light deflections and resulting shape and size of the shadow pattern for a given stress distribution. His procedure will be utilized in the following analysis.

In Fig. 3.7 [3.18], a light beam is considered which traverses the specimen at a point $P(r, \theta)$ in the object (specimen) plane, E. The undeflected beam would intercept the image plane E', (also called the reference plane) at a point P_m, defining a vector, $\vec{r}_m$. Due to the light deflection at point P, the beam is displaced to a point $P'(x', y')$ with a position vector, $\vec{r}'$, relative to the crack tip. The unrefracted and refracted position vectors, $\vec{r}_m$ and $\vec{r}'$ are related by a displacement vector, $\vec{w}$, such that:

$$\vec{r}' = \vec{r}_m + \vec{w} \tag{3.49}$$

where $\vec{w}$ is a function of the coordinates (r,θ) of the point,P, in the object plane and the stress state in the neighborhood of the point, P.

The shadow optical image is completely described by eq. (3.49) which is called the "Image Equation". For every point $P(r,\theta)$ in the object plane there is a corresponding point, $P'(x',y')$ in the image plane, into which the light through P is imaged. The converse is not true, since the image plane contains a shadow zone in which no light appears, bounded by a caustic envelope. This caustic is a singular curve of the image equation, eq. (3.49). Since the image equation represents a coordinate transformation from (r, θ) to (x', y'), a

111

necessary condition for the existence of such a singularity is that the Jacobian functional determinant, J, of the transformation vanishes, i.e.

$$J = \frac{\partial x'}{\partial r} \frac{\partial y'}{\partial \theta} - \frac{\partial x'}{\partial \theta} \frac{\partial y'}{\partial r} = 0 \tag{3.50}$$

Those points P whose coordinates (r, θ), satisfy eq. (3.50) are imaged onto the caustic. The locus of these points in the object plane is called the "Generating Curve" and can be physically interpreted as being the region of the specimen which is sampled in making the caustic measurement. The size of the generating curve can be controlled within relatively narrow bounds by the optical set-up parameters and the magnitude of the applied load [3.16]. The caustic curve itself is obtained by substituting the coordinates of the generating curve into the image equation, eq. (3.49). In many cases the determinant equation eq. (3.50) cannot be solved analytically. In a later section of this chapter two numerical procedures for determining the generating curve(s) and the corresponding caustic(s) will be described.

The first step in calculating the caustic curve is to establish the image equation, eq. (3.49), for the given problem. From elementary optics the vector $\vec{r}_m$ is given by:

$$\vec{r}_m = \mu \vec{r} \tag{3.51}$$

where μ is the magnification factor for the projected shadowgram. For parallel incident light, $\mu = 1$. For convergent (divergent) incident light, $\mu < 1 (\mu > 1)$.

112

The vector, $\vec{w}$, from the theory of the eikonal, is given by:

$$\vec{w}(r,\theta) = z_0 \text{ grad } \Delta s(r,\theta) \tag{3.52}$$

where Δs is the change in the optical path length of the light passing through the point (r,θ) of the object and z_0 is the distance between the object plane, E, and the image (reference) plane, E', (refer to Fig. 3.7). For a linear photoelastic specimen viewed in normal incidence the optical path length change, Δs, is related to the stresses by the Maxwell-Neumann stress-optic law:

$$\Delta s_1 = (a\sigma_1 + b\sigma_2)d$$

$$\tag{3.53}$$

$$\Delta s_2 = (a\sigma_2 + b\sigma_1)d$$

where Δs_1 and Δs_2 are the path length changes for light polarized parallel to the principal stresses, σ_1 and σ_2, respectively, a and b are the elasto-optical constants of the material and d is the specimen thickness.

Equations (3.53) can also be written in terms of the principal stress sum and difference:

$$\Delta s_{1,2} = cd[\sigma_1 + \sigma_2 \pm \lambda(\sigma_1 - \sigma_2)] \tag{3.54}$$

where the positive (negative) sign of λ refers to $\Delta s_1 (\Delta s_2)$ and:

$$c = \frac{a+b}{2}$$

$$\tag{3.55}$$

$$\lambda = \frac{a-b}{a+b}$$

The value of λ describes the amount of optical anistropy. For optically isotropic materials, a = b and $\lambda = 0$. The functional form of eq. (3.54) is the same for both plane stress and plane strain, only the numerical values of the constants, c and λ, vary. Values of these constants for typical materials in transmitted light are given in Table 3.2.

113

Table 3.2

Elasto-optic Constants for Several Materials [ref. 3.16]

Material	Plane Stress		Plane Strain	
	$c\,(m^2/N)$	$|\lambda|$	$c\,(m^2/N)$	$|\lambda|$
Araldite B	-0.97×10^{-10}	0.288	-0.58×10^{-10}	0.482
Homalite 100	-0.92×10^{-10}	0.121	-0.77×10^{-10}	0.149
PMMA	-1.08×10^{-10}	~0	-0.75×10^{-10}	~0

Using eqs. (3.51), (3.52) and (3.54), the image equation (3.49) for a photoelastic material in transmitted light has the form:

$$\vec{r}' = \mu\vec{r} + cdz_0 \ \text{grad} \ [\sigma_1 + \sigma_2 \pm \lambda(\sigma_1 - \sigma_2)] \tag{3.56}$$

For practical reasons eq. (3.56) may be separated into two terms:

$$\vec{r}' = \vec{r}'_{iso} \pm \lambda\vec{r}'_{aniso} \tag{3.57}$$

where

$$\vec{r}'_{iso} = \mu\vec{r} + cdz_0 \ \text{grad} \ (\sigma_1 + \sigma_2) \tag{3.58}$$

and

$$\vec{r}'_{aniso} = cdz_0 \ \text{grad} \ (\sigma_1 - \sigma_2) \tag{3.59}$$

By separating the image equation (eq. 3.57) into these two terms, the role of the isopachic and isochromatic gradients in the formation of the caustic is more clearly evident and the results of the previous sections can be applied directly. Recall that, from eq.(3.46), the sum of the principal stresses can be expressed in terms of the stress functions, Z and n, as:

$$\sigma_1 + \sigma_2 = 2ReZ - 2Re\,\eta \tag{3.60}$$

114

and, from eq. (3.34), the difference of the principal stresses is:

$$\sigma_1 - \sigma_2 = [(2D)^2 + (2T)^2]^{\frac{1}{2}} \qquad (3.61)$$

where D and T are given by eqs. (3.35) and 3.36), respectively.

Before proceeding to substitute the above expressions into the image equations, it will prove to be convenient to introduce certain dimensionless variables. Following Manogg, the radius, r, can be written in the normalized form:

$$\bar{r} = \frac{r}{r_o} \qquad (3.62)$$

where:

$$(r_o)^5 = (\frac{3}{2} \frac{K}{\sqrt{2\pi}} \frac{1}{\mu} cdz_o)^2 \qquad (3.63)$$

The normalizing factor, r_o, has a physical interpretation. Namely, it represents the radius of the generating curve in an isotropic material

which corresponds to the caustic for the case in which only the crack tip singularity contributes to the stress field, i.e. under these conditions the generating curve is a circle. Using the same normalization factor, the components x' and y' of the vector $\vec{r}'$ in the reference plane can be written as:

$$\bar{x}' = \frac{x'}{r_o} \qquad \text{and} \qquad \bar{y}' = \frac{y'}{r_o} \qquad (3.64)$$

Following the procedure suggested by Irwin of factoring out $K/\sqrt{2\pi z}$, the stress functions, Z and η can be expressed in an alternate form with dimensionless coefficients, Y_n and δ_m, respectively:

$$Z = \frac{K}{\sqrt{2\pi z}} \sum_{n=0}^{N} Y_n \left(\frac{z}{r_o}\right)^n \qquad (3.65)$$

and

$$\eta = \frac{K}{\sqrt{2\pi z}} \sum_{m=0}^{M} \delta_m \left(\frac{z}{r_o}\right)^{m+\frac{1}{2}} \qquad (3.66)$$

115

where in terms of the previously defined constants A_n, α_m:

$$\gamma_n = \frac{A_n \sqrt{2\pi}}{(n-\frac{1}{2})K} r_0^n \tag{3.67}$$

and

$$\delta_m = \frac{\alpha_m \sqrt{2\pi}}{K} r_0^{m-\frac{1}{2}} \tag{3.68}$$

Note that, from eq. (3.33),

$$\gamma_0 \equiv 1 \tag{3.69}$$

Using the normalized stress functions, eqs. (3.65) and (3.66) in eq. (3.60) and taking the gradient as required in eq. (3.58), the normalized Cartesian components of the isotropic image equation (3.58) become:

$$\frac{1}{\mu} \bar{x}'_{iso} = \bar{r}\cos\theta - \frac{4}{3} \sum_{n=0}^{N} (n-\tfrac{1}{2})\gamma_n \bar{r}^{-(n-3/2)} \cos(n-3/2)\theta$$

$$+ \frac{4}{3} \sum_{m=0}^{M} m\delta_m \bar{r}^{-(m-1)} \cos(m-1)\theta \tag{3.70}$$

and

$$\frac{1}{\mu} \bar{y}'_{iso} = \bar{r}\sin\theta + \frac{4}{3} \sum_{n=0}^{N} (n-\tfrac{1}{2})\gamma_n \bar{r}^{-(n-3/2)} \sin(n-3/2)\theta$$

$$- \frac{4}{3} \sum_{m=0}^{M} m\delta_m \bar{r}^{-(m-1)} \sin(m-1)\theta \tag{3.71}$$

In deriving the above equations, the following transformations and identity were employed:

$$\text{grad}_x(\sigma_1 \pm \sigma_2) = \cos\theta \, \text{grad}_r(\sigma_1 \pm \sigma_2) - \sin\theta \, \text{grad}_\theta(\sigma_1 \pm \sigma_2) \tag{3.72}$$

$$\text{grad}_y(\sigma_1 \pm \sigma_2) = \sin\theta \, \text{grad}_r(\sigma_1 \pm \sigma_2) + \cos\theta \, \text{grad}_\theta(\sigma_1 \pm \sigma_2) \tag{3.73}$$

116

and, from (3.63)

$$|cd\,z_o| = \frac{2}{3}\frac{\sqrt{2\pi}}{K}\mu r_o^{5/2} \tag{3.74}$$

where subscripts, x, y, r, θ denote differentiation with respect to the indicated variable.

Before deriving the corresponding image equations for the anisotropic contribution, it is necessary to express the functions, D and T, (eq. 3.35 and 3.36) in terms of the dimensionless variables, γ_n, δ_m. The results are:

$$D = \frac{K}{\sqrt{2\pi}r_o}\left[-\sum_{n=0}^{N}(n-\tfrac{1}{2})\gamma_n\,\overline{r}^{-(n-\tfrac{1}{2})}\sin\theta\sin(n-3/2)\theta\right.$$

$$+\sum_{m=0}^{M}m\delta_m\overline{r}^{-m}\sin\theta\sin(m-1)\theta$$

$$\left.-\sum_{m=0}^{M}\delta_m\overline{r}^{-m}\cos m\theta\right] \tag{3.75}$$

and

$$T = \frac{K}{\sqrt{2\pi}r_o}\left[-\sum_{n=0}^{N}(n-\tfrac{1}{2})\gamma_n\,\overline{r}^{-(n-\tfrac{1}{2})}\sin\theta\cos(n-3/2)\theta\right.$$

$$+\sum_{m=0}^{M}m\delta_m\overline{r}^{-m}\sin\theta\cos(m-1)\theta$$

$$\left.+\sum_{m=0}^{M}\delta_m\overline{r}^{-m}\sin m\theta\right] \tag{3.76}$$

In terms of the above quantities, the gradients of $(\sigma_1 - \sigma_2)$ are:

$$\mathrm{grad}_r(\sigma_1 - \sigma_2) = \frac{1}{r_o}[(2D)^2 + (2T)^2]^{-\tfrac{1}{2}}\left(4D\frac{\partial D}{\partial\overline{r}} + 4T\frac{\partial T}{\partial\overline{r}}\right) = G_r \tag{3.77}$$

117

and
$$\text{grad}_\theta(\sigma_1 - \sigma_2) = \frac{1}{r_o} [(2D)^2 + (2T)^2]^{-\frac{1}{2}} \left(\frac{4D}{r} \frac{\partial D}{\partial \theta} + \frac{4T}{r} \frac{\partial T}{\partial \theta} \right) = G_\theta \qquad (3.78)$$

Finally, from eqs.(3.72) and (3.73), the normalized Cartesian components of the anisotropic image equation (3.59) become:

$$\bar{x}'_{aniso} = \frac{-2}{3} \frac{\sqrt{2\pi}}{K} \mu r_o^{5/2} (G_r \cos\theta - G_\theta \sin\theta) \qquad (3.79)$$

$$\bar{y}'_{aniso} = \frac{-2}{3} \frac{\sqrt{2\pi}}{K} \mu r_o^{5/2} (G_r \sin\theta + G_\theta \cos\theta) \qquad (3.80)$$

where the minus sign on the right hand side of each expression is included to account for the fact that the material constant, c, is negative (see Table 3.2).

Combining the results for the isotropic and anisotropic contributions, the normalized Cartesian components of the image equation for transmitted light through a specimen of photoelastic material are:

$$\bar{x}' = \bar{x}'_{iso} \pm \lambda \bar{x}'_{aniso} \qquad (3.81)$$

$$\bar{y}' = \bar{y}'_{iso} \pm \lambda \bar{y}'_{aniso} \qquad (3.82)$$

where the isotropic and anisotropic terms are given by eqs. (3.70), (3.71) and (3.79), (3.80), respectively.

Clearly, solving equation (3.50) analytically to determine the shape of the caustic(s) is, in all but the simplest of cases, impossible. Instead, numerical techniques have been developed and used to illustrate the effects of the higher order terms on the shape of the caustic(s).

Two procedures have been developed for constructing theoretical caustics and displaying them graphically. The simpler method involves a direct

118

mapping of a polar grid, centered at the crack tip in the object plane, into its counterpart in the reference plane. This procedure is useful for visualizing the formation of a given caustic, but it does not actually locate the caustic line(s) deterministically. The more involved method actually locates points on the caustic line(s) by satisfying the vanishing-Jacobian condition of eq. (3.50). It is this second method which proves to be of most value for the numerical comparison of various caustic patterns. The two methods will now be discussed.

In the polar grid method, equally spaced values of the angle θ in the object plane are selected, and for each value of θ, equally spaced values of the normalized radius $\bar{r}$ are selected; this establishes a grid of points in the object plane which can be individually mapped into corresponding points in the image plane by means of the image equations (3.81) and (3.82). A computer program which accomplishes this task has been written. For each value of θ, the program determines various functions of θ and then computes, for a sequence of values of $\bar{r}$ (in the neighborhood of $\bar{r} = 1$), the corresponding points $(\bar{x}', \bar{y}')$ in the normalized image plane. The graphical mapping of radial and circumferential lines is achieved by selective plotting of the stored transformed image points.

As an example of this method of plotting, consider the classical solution for an optically isotropic material ($\lambda = 0$) retaining only the near-field stress distribution, i.e.

$$\gamma_0 = 1 \qquad \text{(all other } \gamma_n, \delta_m = 0)$$

The result for points mapped from the upper half of the object plane is shown in Fig. 3.8. Here, θ has assumed values of $2°$, $9°$, $16°$, ..., $177°$, and $\bar{r}$ has assumed values of 0.50, 0.55, 0.60, ..., 1.50. Only one caustic

119

pattern is generated since the material is optically isotropic, and the
pattern is symmetric with respect to the $\bar{x}'$-axis since the stress state
is symmetric with respect to the $\bar{x}$-axis.

When the material is optically anisotropic ($\lambda \neq 0$), two distinct caustic
patterns are produced. Examples will be given later in this chapter. One
of the caustics, called caustic #1, is produced in accordance with the
plus (+) sign in the image equation (3.57); the other, called caustic #2, is
produced when the minus (-) sign is employed. Since both caustics are
symmetric with respect to the $\bar{x}'$-axis, plotting only the upper halves of the
two caustics gives complete information about the caustic patterns in the
anisotropic case.

In the vanishing Jacobian method, equally spaced values of the angle
θ are selected, and for each value of θ, the value of $\bar{r}$ satisfying
eq. (3.50) is found numerically by a Newton iteration procedure. Com-
putationally, this method involves more work than does the polar grid
method. The benefits are that (a) only the points defining the caustic
line itself are stored, so that plotting proceeds quickly, and that (b)
the comparison of caustics for different loading cases is made easier
(both visually and computationally). One drawback which becomes important
when significant higher-order stress terms are considered is that the Newton
procedure for finding $\bar{r}$ can break down in the vicinity of a kink in the
caustic, if a kink exists. Normally, such kinks do not arise when the
singular term:

$$\frac{K}{\sqrt{2\pi z}}$$

120

in the stress function, Z, is sufficiently strong, or when the material is only weakly birefringent, or both.

A computer program for locating and plotting the caustic lines using this method has also been written. In addition to determining the values of $\bar{r}$ which satisfy eq. (3.50) and computing the corresponding points in the reference plane, the program also scans the values of $\bar{y}'$ as they are calculated to determine the maximum value of $\bar{y}'$, called $\bar{y}'_{max}$, for each of the two caustics for each loading case. In addition, it calculates two correction factors, f, when various higher-order stress terms are present, according to the relation

$$ f = \left(\frac{(\bar{y}'_{max})_{ref}}{\bar{y}'_{max}} \right)^{5/2} \quad , \tag{3.83} $$

where the subscript "ref" denotes the reference case (the near-field solution) for the same value of the anisotropy parameter λ. If $\lambda \neq 0$, two values of f are generated, one for the outer caustic and one for the inner caustic. It is not generally known, before a calculation is made, what the relation between caustic number (#1 or #2) and caustic type (outer or inner) is, so a test is made to determine which caustic number has the largest value of $\bar{y}'_{max}$. Equation (3.83) is then used to compare only outer caustics or inner caustics. The correction factors given by eq. (3.83) are defined in such a way that, if the vertical diameter of a caustic is measured experimentally and a provisional value of K, say K*, is computed by ignoring higher-order stress terms, then the correct value of K is given by

$$ K = f K^* \tag{3.84} $$

121

Since the ratio of caustic diameters is raised to the 2.5 power, seemingly small variations in the caustic diameter caused by the presence of higher-order stress terms can give rise to significant variations in the calculations of K.

A systematic study of the influence of the first few higher-order stress terms on the size and shape of caustics for a birefringent material has been initiated, and some of the more interesting results will be reported here. The anisotropy parameter λ was assumed to have the value 0.288, which corresponds to the strongly birefringent material Araldite-B under plane-stress conditions (see Table 3.2).

The first parameter considered was δ_0, which governs the strength of the constant stress field

$$\sigma_x (x,y) = \sigma_{0x}$$

previously introduced by Irwin [3.1] in connection with the interpretation of photoelastic fringe patterns. It should be pointed out that for a non-birefringent material ($\lambda = 0$), the single caustic that is produced is unaffected by the value of δ_0. For a birefringent material, however, the (double) caustics are found to depend upon the value of δ_0. To see that this is the case, consider the results in Figs. 3.9 and 3.10. For both sets of figures, λ has the value 0.288. Figs. 3.9(a,b) are polar-grid caustic mappings for the near-field solution, i.e. the one in which

$$\gamma_0 = 1, \delta_0 = 0 \quad \text{(all other } \gamma_n, \delta_m = 0).$$

Figs. 3.10(a,b) are corresponding mappings for the case

$$\gamma_0 = 1, \delta_0 = -0.4 \quad \text{(all other } \gamma_n, \delta_m = 0).$$

Note that for the value of δ_0 selected, a noticeable kink in the caustic line for caustic #1 is predicted in the vicinity of the image angle $\theta' = 70°$.

122

In roughly the same vicinity, caustic #2 is "stretched". This result suggests that for sufficiently large (negative) values of δ_0, the anisotropic contribution $\vec{r}'_{aniso}$ to the image position vector $\vec{r}'$ undergoes a large and rapid change with respect to points in the object plane in the neighborhood of $\theta = 60°$. It is possible that a kink like the one depicted in Fig. 3.10(a) would be difficult to produce experimentally, since preliminary calculation based on photoelastic data indicate that $|\delta_0|$ is usually of the order of 0.1 or less, except in extreme loading cases. In all probability, a kink like the one seen in Fig. 3.10(a) would manifest itself as a bright spot on an experimentally produced caustic; it would be interesting to pursue the possibility.

At this point, it may be instructive to illustrate how the theoretical correction factors for the caustics are computed and employed. For the case in question ($\lambda = 0.288$ and $\delta_0 = -0.4$), the pertinent data can be obtained graphically from Figs. 3.9(a,b) and 3.10(a,b) by noting, first, that the outer caustic for the near field solution is caustic #1 (Fig. 3.9(a)). For this caustic, $\bar{y}'_{max} = 1.658$. The inner caustic for the near field solution is caustic #2 (Fig. 3.9(b)), and for this caustic, $\bar{y}'_{max} = 1.524$. Comparison must be made between these values of $\bar{y}'_{max}$ and the corresponding values for the outer and inner caustics shown in Figs. 3.10(a,b). The outer caustic now turns out to be caustic #2, with a $\bar{y}'$ equal to 1.619 whereas the inner caustic, caustic #1, has a $\bar{y}'_{max}$ equal to 1.574. The two correction factors are therefore, from eq. (3.83),

$$f_{outer} = \left(\frac{1.658}{1.619}\right)^{5/2} = 1.061, \text{ and}$$

$$f_{inner} = \left(\frac{1.524}{1.575}\right)^{5/2} = 0.922.$$

Suppose that the vertical diameter, $2\,\bar{y}'_{max}$, has been measured experimentally for the outer caustic produced by a Mode-I-loaded Araldite-B specimen, and that a provisional value of stress-intensity-factor, K^*, has been calculated from eq. (3.63),

$$K^* = \frac{2}{3}\sqrt{2\pi}\,\frac{\mu}{c\,d\,z_0}\,(r_0)^{5/2}$$

where r_0 is deduced from the experimental observation by

$$\mu r_0 = \frac{y'_{max}}{1.658}\ ,$$

the factor 1.658 being the theoretical value of $\bar{y}'_{max}$ for $\delta_0 = 0$ ($\lambda = 0.288$, $\mu = 1$, outer caustic). The correct value of K would then be given by

$$K = f_{outer}\,K^* = 1.061\,K^*.$$

Note that the correction factor in this example is about 6%. It is interesting to compare this correction, due to the presence of δ_0 alone, with the correction which would be required to account for anisotropy alone. To this end, consider the isotropic case ($\lambda = 0$) and note from eq. (3.71) that in the near-field solution, [3.15]

$$\bar{y}' = \sin\theta + \frac{2}{3}\sin\frac{3}{2}\theta \qquad (3.85)$$

since it is known that the generating curve for the classical solution is a circle with radius $\bar{r} = 1$. Differentiating eq. (3.85) once with respect to θ and setting the derivative equal to zero yields

$$\cos\theta + \cos\frac{3}{2}\theta = 0,$$

which has the solution, $\theta = 72°$ (exact). Hence,

$$\begin{aligned}\bar{y}'_{max} &= \sin 72° + \frac{2}{3}\sin 108°\\ &= 1.585.\end{aligned}$$

124

The correction due to anisotropy alone is therefore

$$\left(\frac{1.585}{1.658}\right)^{5/2} = 0.894$$

which is about 11%. It is concluded that the effect of higher-order stress terms can be of the same order as the effect of aniso-tropy.

The effects of some of the other higher-order stress terms (γ_1, δ_1, γ_2, δ_2, ...) have been investigated in a similar manner, but numerical results will not be presented here. Briefly, γ_1 was found to play a minor role in determining the shape of the caustics, although it does affect the size; δ_1, if negative, tends to make the outer caustic pear-shaped, while blunting the inner caustic, so that the two caustics can cross in two places in the first quadrant in the image plane.

As was done for the cases of isochromatics and isopachics, an example of the combined effects of higher order terms on caustic patterns is presented for the Compact Tension specimen shown in Fig. 3.1. Using the data of Table 3.1 and the conversion eqs. (3.67, 3.68) the dimensionless coefficients become (for $r_0 = 0.2"$):

$$\gamma_0 \equiv 1 \qquad \gamma_1 = -0.252 \qquad \gamma_2 = -0.038$$
$$\delta_0 = -0.024 \qquad \delta_1 = -0.031 \qquad \delta_2 = -0.003$$

The normalized caustics which would be produced in a Homalite 100 specimen are shown in Fig. 3.11, where they are compared with the caustics that would be produced if all of the higher order terms were zero. These caustics were plotted using the vanishing Jacobian method previously described. As shown in the Figure, the correction factors for this case are:

125

$$f_{outer} = 0.905 \qquad f_{inner} = 0.914.$$

Thus, it can be concluded that a systematic error of about 9% in the calculation in K would have occurred if the higher order terms had been neglected. Notice however, that, other than a shift to the right, the basic shape of the caustics provides no clues to the influence of higher order terms.

3.7 Summary

Traditionally, optical methods for determining the stress intensity factor have used as their basis the near-field equations, eq. (3.0), developed by Irwin some twenty years ago. However, the region of validity of these equations is quite restricted and, accordingly, measurements must be taken very close to the crack tip. On the other hand, it has been demonstrated [3.12] that the transition from plane strain at the crack tip to generalized plane stress in the surrounding field adversely influences optical measurements close to the crack tip. Thus, to properly interpret optical patterns in the neighborhood of a crack (but beyond the transition region) the effects of non-singular terms on the governing optical equations must be considered.

In this chapter, it was first demonstrated that the modified Westergaard equations, eqs. (3.7-3.9), were inadequate to describe some of the effects observed in experiments and that a more general set of equations would be required. These equations were obtained by relaxing the constraint on the symmetry condition imposed by Westergaard. The resulting equations, termed the "generalized Westergaard equations", contain two stress functions, Z and η, each of which can be expressed

126

in series form so as to satisfy the boundary conditions on the axis
of symmetry. These series representations of the stresses then form
the basis for the development of the governing optical equations for
the analysis of isochromatic, isopachic, and caustic patterns to obtain
the stress intensification around an opening mode crack for a region
of arbitrary size.

The analysis of isochromatic patterns, incorporating an arbitrary
number of higher order terms, was reduced to the problem of deter-
mining the coefficients of the two series which produced the best
match to the experimental fringe pattern over a chosen region. A
non-linear, least squares algorithm for determining these coefficients
was developed in matrix notation, and its application demonstrated.
To date, numerical procedures for matching experimental fringe patterns
to the series representation of the stresses with up to six terms
(i.e. a six-parameter isochromatic model) have been developed. There
appears to be little justificaton for extending the analysis beyond
six terms, unless very large regions are being considered. On the
other hand, all six terms were needed to adequately describe the iso-
chromatic field shown in Fig. 3.1. The number of terms necessary
can, quite possibly, be estimated from an examination of the maximum
shear stress distribution ahead of the crack, using eq. (3.31) as a
guide.

In contrast to the governing equation for isochromatics, the iso-
pachic equations including higher order terms are linear in the unknown
coefficients. Conceptually, this should make the determination of the
coefficients from an experimental isopachic fringe pattern easier to

127

perform. In practice, however, this is not the case. The reason for this is that the influence of the higher order terms on the shape and size of the isopachic fringes is not as pronounced as in the case of isochromatics.

The third major type of optical method used to determine the stress intensity factor is the method of caustics, first introduced by Manogg. As with the two other methods, the general governing equations for the optical pattern (in this case, the caustic shape) have been developed so as to include the effects of optical anisotropy and an arbitrary number of higher order terms. It was demonstrated that, except in extreme cases, the shape of the caustic is virtually unaffected by the presence of higher order terms and consequently there is no practical method available for determining these terms from an experimental caustic pattern. On the other hand, ignoring the higher order terms can result in significant errors in the determination of the stress intensity factor as illustrated in Fig. 3.11 for the case of a crack approaching the boundary (a/w = 0 .813) in a Modified Compact Tension specimen. If the magnitude of the higher order terms were known _a priori_ or could be estimated, the numerical procedures developed in this chapter could be used to compute correction factors to be applied to the caustic diameter measurement based on elementary theory.

The results reported in this Chapter represent an initial effort in the study of the effects of higher order terms on static patterns. The emphasis has been placed on the development of the governing equations in their most general form. Further study will be required to define

128

the conditions under which the higher order terms need to be included in order to improve the accuracy of stress intensity factor measurements. Specifically, the effects of the following factors on the number and relative magnitude of the higher order terms required to adequately describe the stress state need detailed and systematic study:

1) Crack length as a ratio of specimen width;

2) Stress gradients in the neighborhood of the crack (as it approaches a boundary for example);

3) The size of the region of data acquisition.

In addition, efficient computational methods for implementing the algorithms developed in this Chapter for determining the coefficients of the Z and η functions will be required.

References

3.1 Irwin, G.R., "Discussion of: The Dynamic Stress Distribution Surrounding a Running Crack--A Photoelastic Analysis", Proc. SESA, Vol. 16, 1958 (93-96).

3.2 Westergaard, H.M., "Bearing Pressures and Cracks", Trans. ASME, Vol. 61, 1939 (A49-A53).

3.3 Wells, A.A. and Post, D., "The Dynamic Stress Distribution Surrounding a Running Crack--A Photoelastic Analysis, Proc. SESA, Vol. 16, 1958 (69-93).

3.4 Kobayashi, A.S., Experimental Techniques in Fracture Mechanics, Monograph #1, SESA, Westport, Conn., 1973.

3.5 Redner, A.S., "Experimental Determination of Stress Intensity Factors--A Review of Photoelastic Approaches", Fracture Mechanics and Technology, Noordhoff Int., 1978 (607-622).

3.6 Etheridge, J.M. and Dally, J.W., "A Critical Review of Methods for Determining Stress Intensity Factors from Isochromatic Fringes", Experimental Mechanics, Vol. 17, 1977 (248-254).

3.7 Tada, H., Paris, P., and Irwin, G.R., The Stress Analysis of Cracks Handbook, Del. Research Corp., Hellertown, PA, 1973 (127).

3.8 Sanford, R.J., "A Critical Re-examination of the Westergaard Method for Solving Opening Mode Crack Problems", Mechanics Research Communications, Vol. 6, 1979 (289-294).

3.9 Sih, G.C., "On the Westergaard Method of Crack Analysis", Intl. J. Fracture Mechanics, Vol. 2, 1966 (628-631).

3.10 Sanford, R.J., and Dally, J.W., "A General Method for Determining Mixed-Mode Stress Intensity Factors from Isochromatic Fringe Patterns", Eng. Fracture Mechanics, Vol. 11, 1979 (621-633).

3.11 Sanford, R.J., "Application of the Least Squares Method to Photoelastic Analysis", to appear in Experimental Mechanics.

3.12 Dudderar, T.D., and O'Regan, R., "Measurement of the Strain Field Near a Crack Tip in Polymethylmethacrylate by Holographic Interferometry", Experimental Mechanics, Vol. 11, 1971 (49-56).

3.13 Dudderar, T.D., and Gorman, H.J., "The Determination of Mode I Stress-intensity Factors by Holographic Interferometry", Experimental Mechanics, Vol. 13, 1973 (145-150).

3.14 Holloway, D.C., and Johnson, R.H., "Advancements in Holographic Photoelasticity", Experimental Mechanics, Vol. 11, 1971 (57-63).

3.15   Mannog, P., Anwendung der Schattenoptik zur Untersuchung des
       Zerreißvorgangs von Platten, Dissertation, Freiburg, Germany,
       1964.

3.16   Beinert, J., and Kalthoff, J.F., "Experimental Determination of
       Dynamic Stress Intensity Factors by the Method of Shadow Patterns,
       Mechanics of Fracture, Vol. VII, Noordhoff Int. (in press).

3.17   Kalthoff, J.F., Beinert, J., Winkler, S., and Klemm, W.,
       "Experimental Analysis of Dynamic Effects in Different Crack
       Arrest Test Specimens", Symposium on Crack Arrest Methodology
       and Applications, ASTM, Philadelphia, PA., 1978.

3.18   Beinert, J., Kalthoff, J.F., and Maier, M., "Neuere Ergebrisse
       zur Anwendung des Schattenfleckverfahrens auf stehende und
       schnell-laufende Brüche", 6th International Conference on
       Experimental Stress Analysis, VDI--Berichte Nr 313, Dusseldorf,
       Germany, 1978 (791-798).
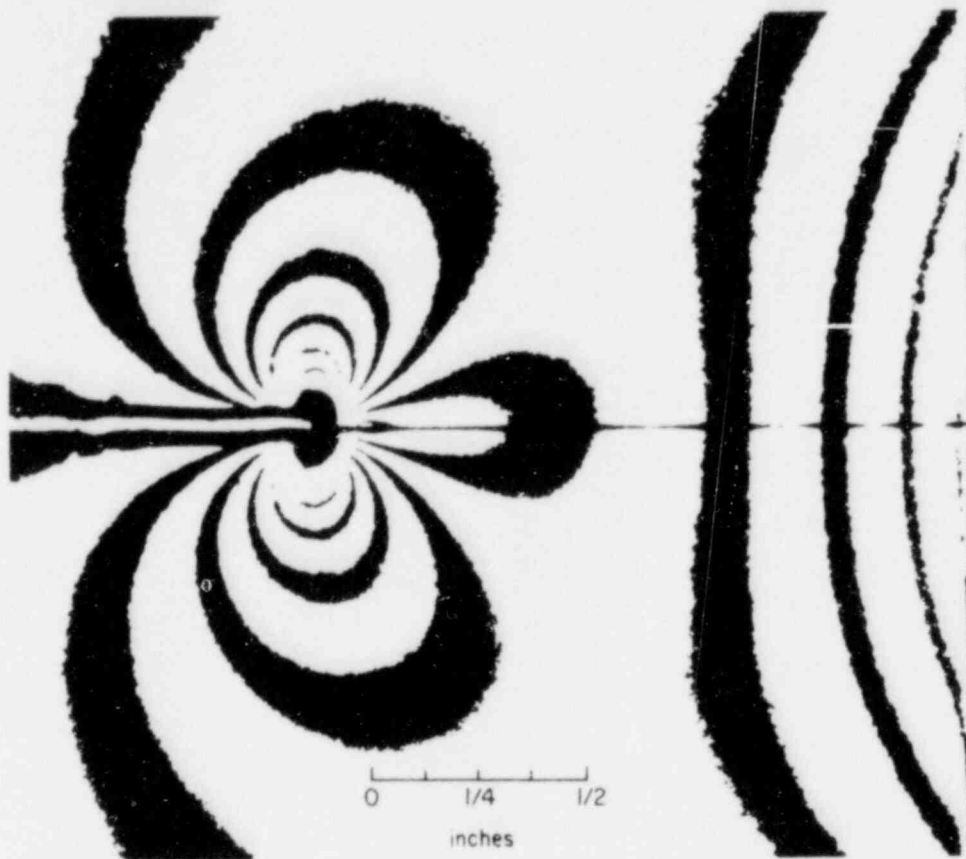
Fig. 3.1 Light-Field Isochromatic Pattern Showing a Crack Close to the Boundary of a Modified-Compact-Tension Specimen (a/w = 0.813).
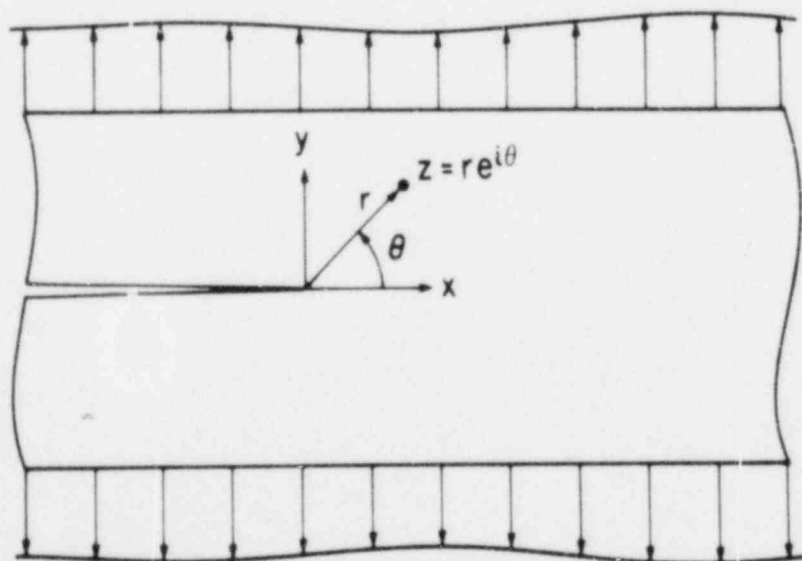
Fig. 3.2 Crack Tip Coordinate Systems for a Single-Ended Crack Geometry Under Opening Mode Loading.

132

a) EXPERIMENTAL PATTERN
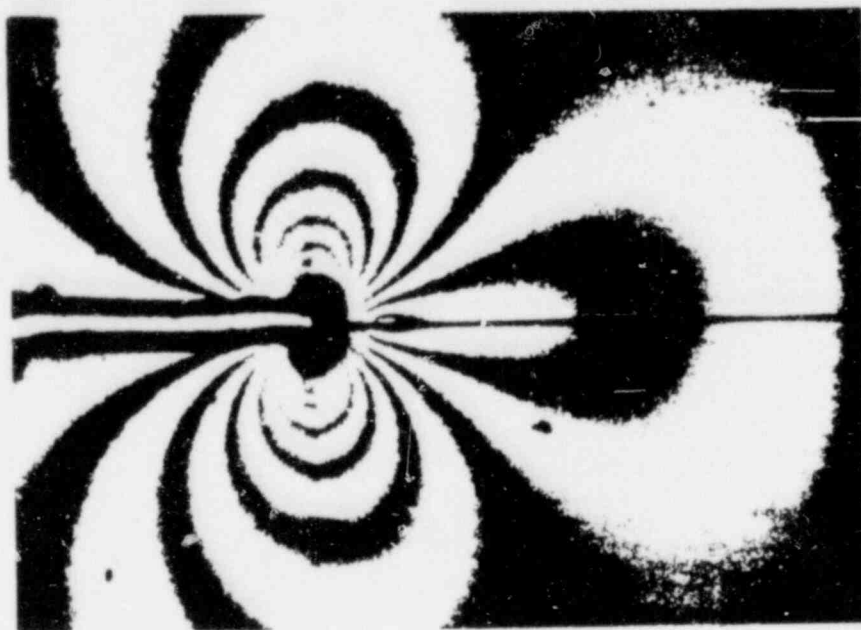
b) THEORETICAL PATTERN

0   1/4   1/2

inches
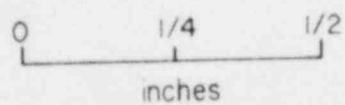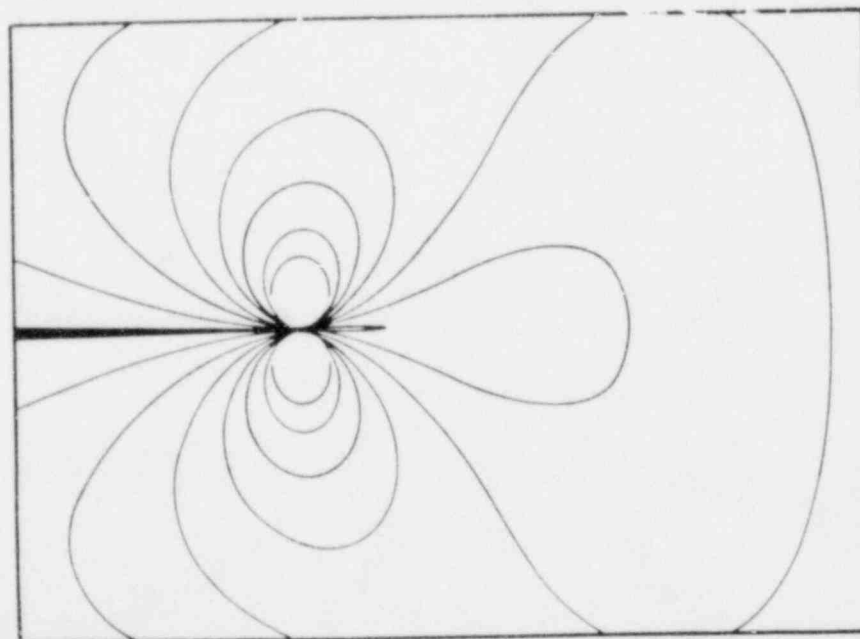
Fig. 3.3 Comparison of Experimental and Best-Fit, Six-Parameter,
Theoretical Fringe Patterns for a Sub-Region of Fig. 3.1.

133
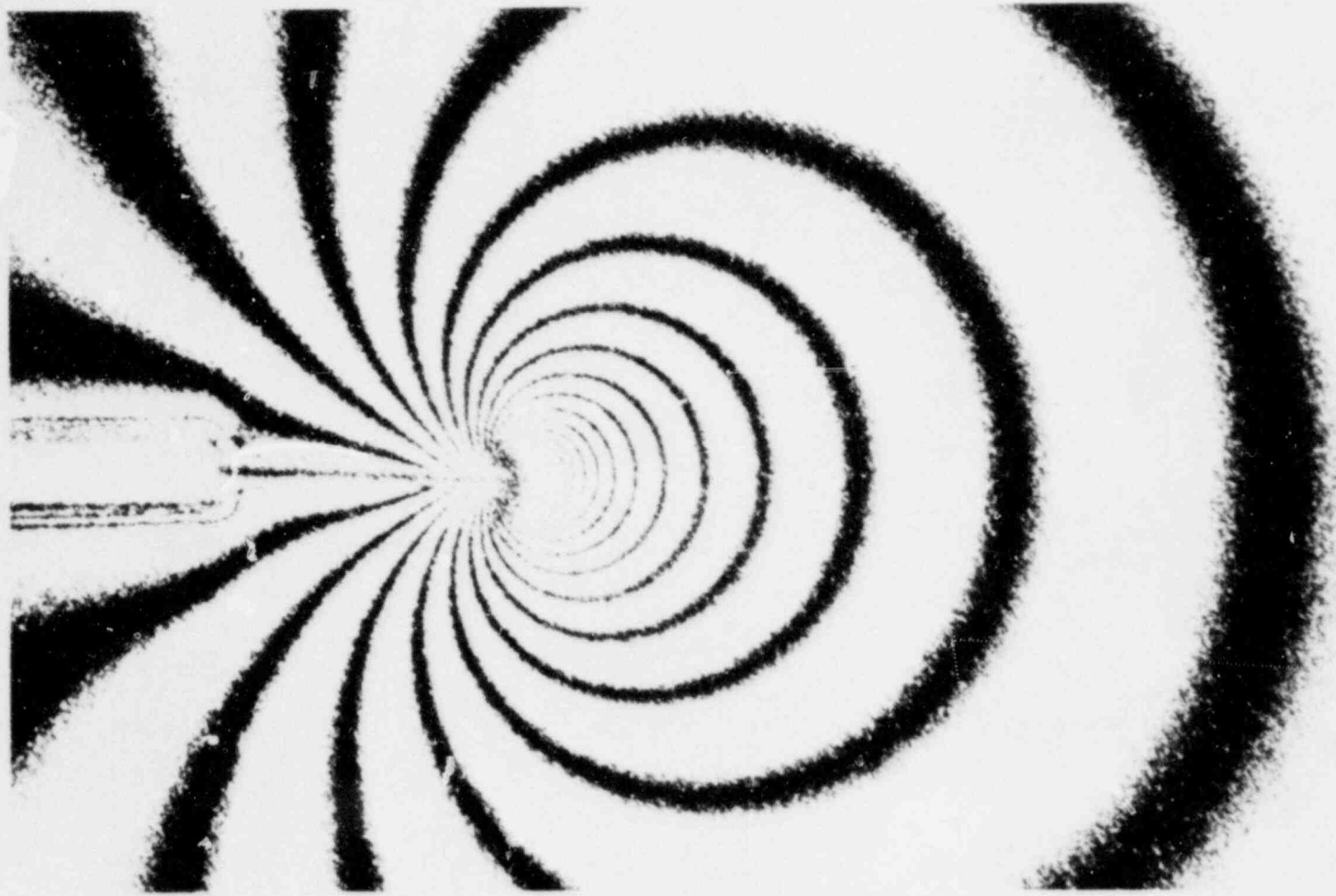
Fig. 3.4 A Typical Holographic Interference (Isopachic) Pattern Around a Crack Tip in Plexiglas.

134

a) NEAR-FIELD SOLUTION
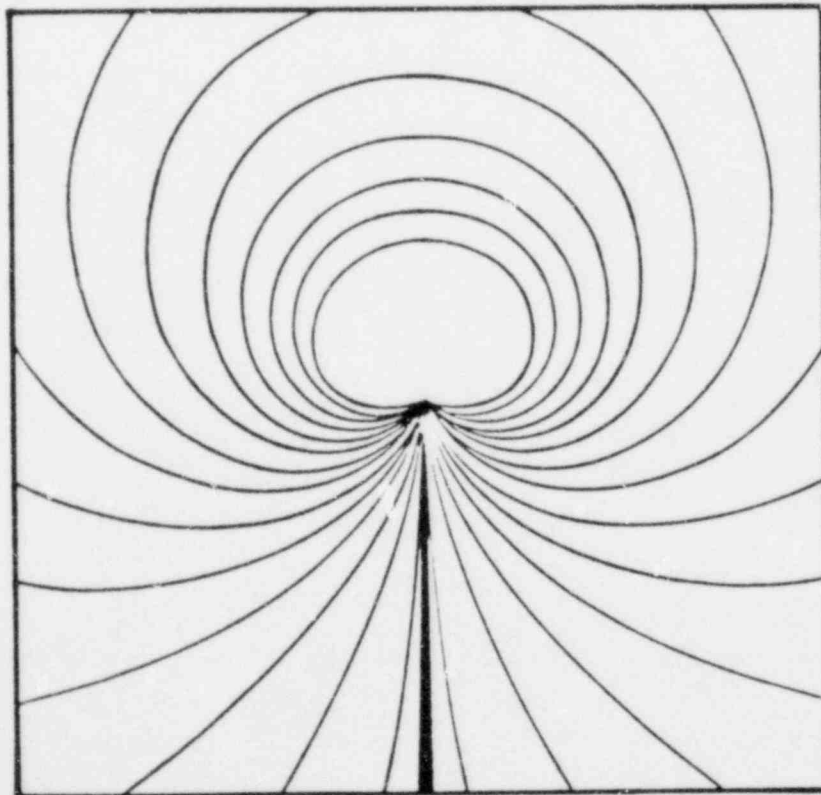
b) SIX-PARAMETER SOLUTION
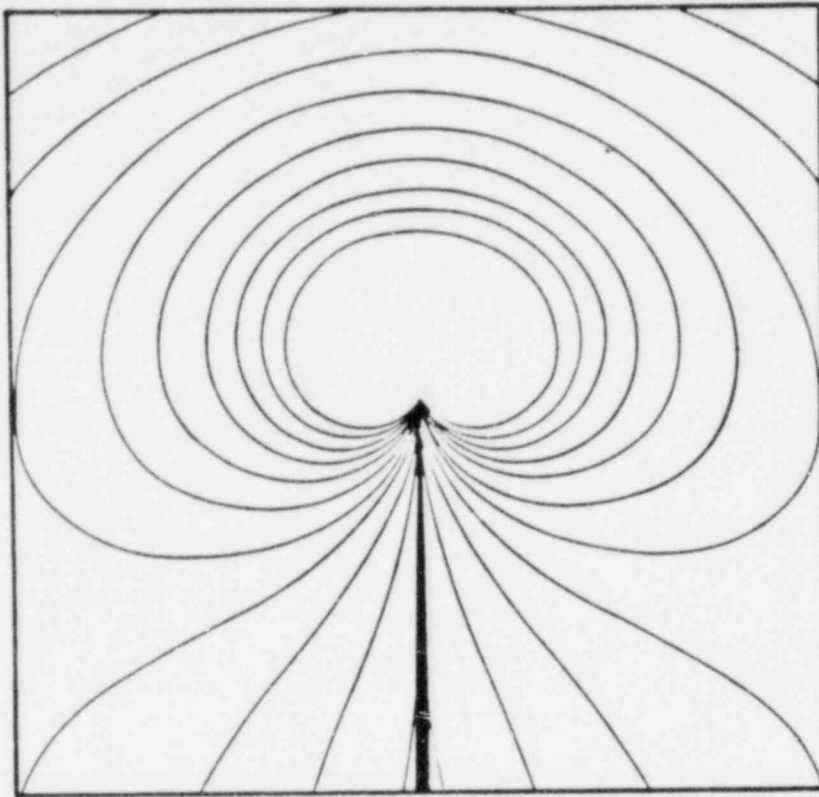
Fig. 3.5 Comparison of Near-Field and Six-Parameter Isopachic Patterns Around a Crack Tip Using the Parameter Values in Table 3.1.

135

TRANSMISSION

CAUSTIC

CRACK

D

σ

CRACK

z₀

TRANSMITTED
LIGHT

σ

SPECIMEN

REAL
IMAGE PLANE

THE CAUSTIC IN
THE IMAGE PLANE

REFLECTION

σ

CRACK

z₀

REFLECTED
LIGHT

σ

SPECIMEN

VIRTUAL
IMAGE PLANE

CAUSTIC

CRACK

D
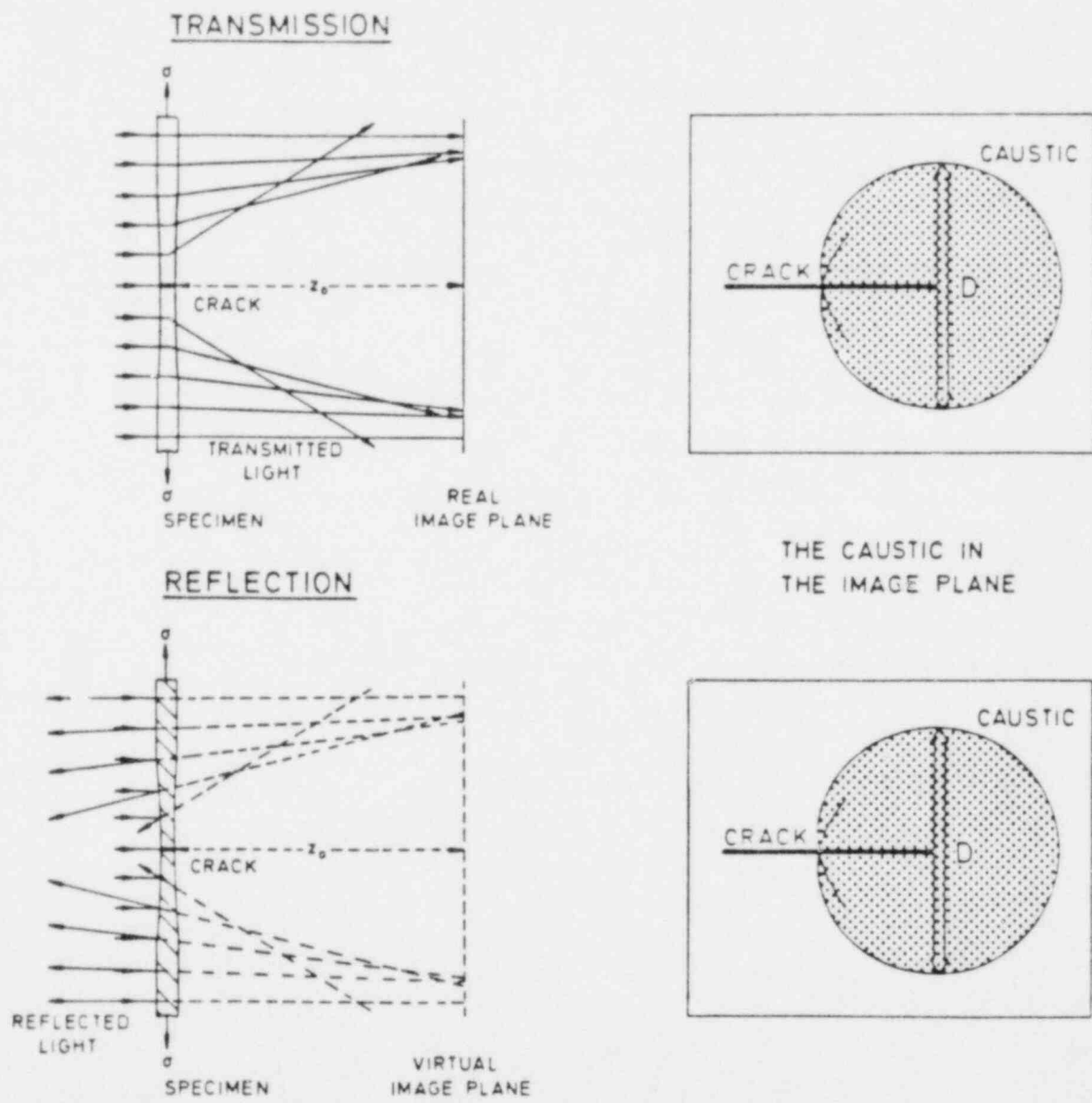
Fig. 3.6 Principle of the Formation of the Caustic in Transmission and
Reflection [3.17].
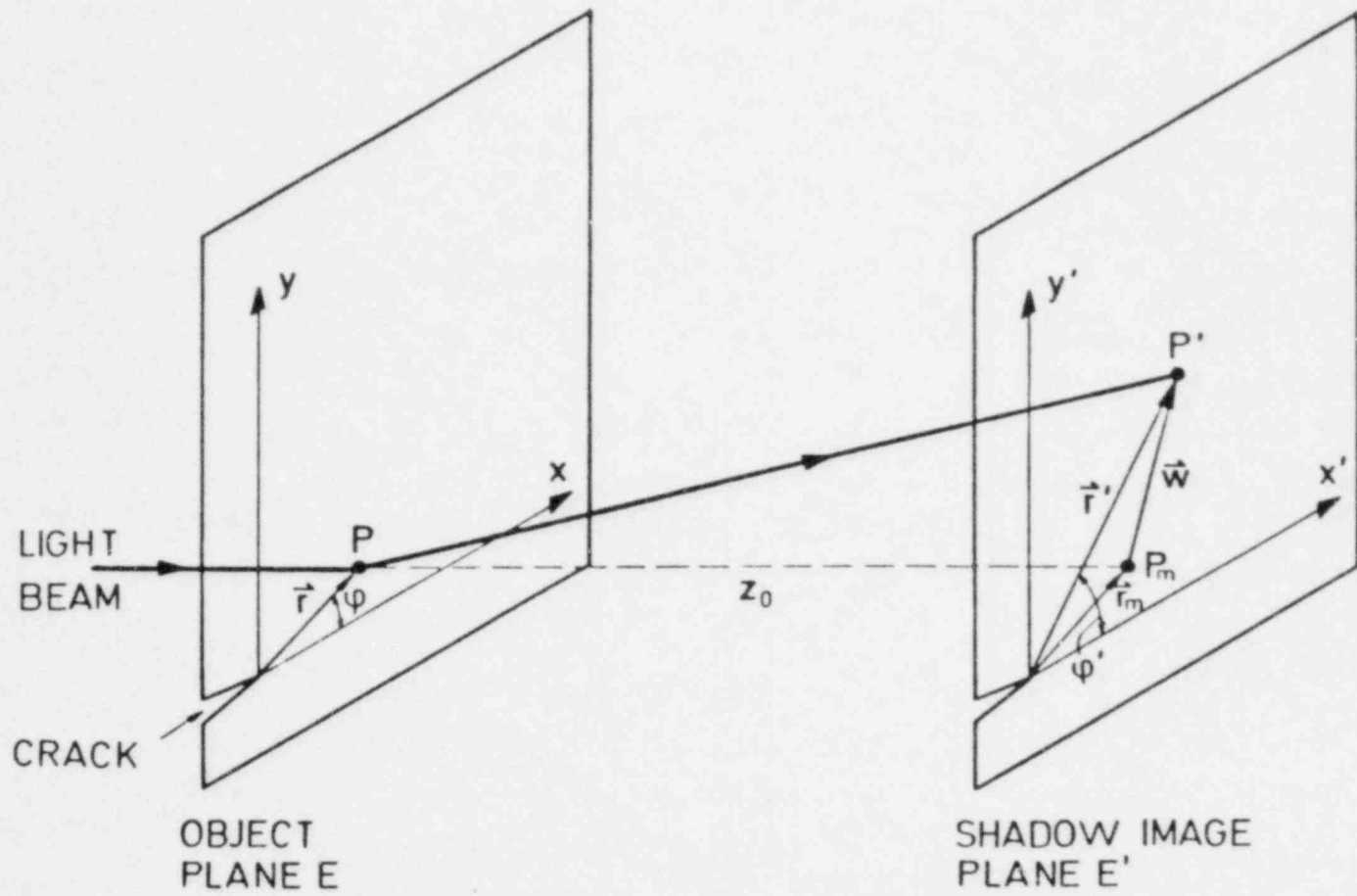
Fig. 3.7 Geometrical Relationships for Shadow Optical Analysis [3.18].
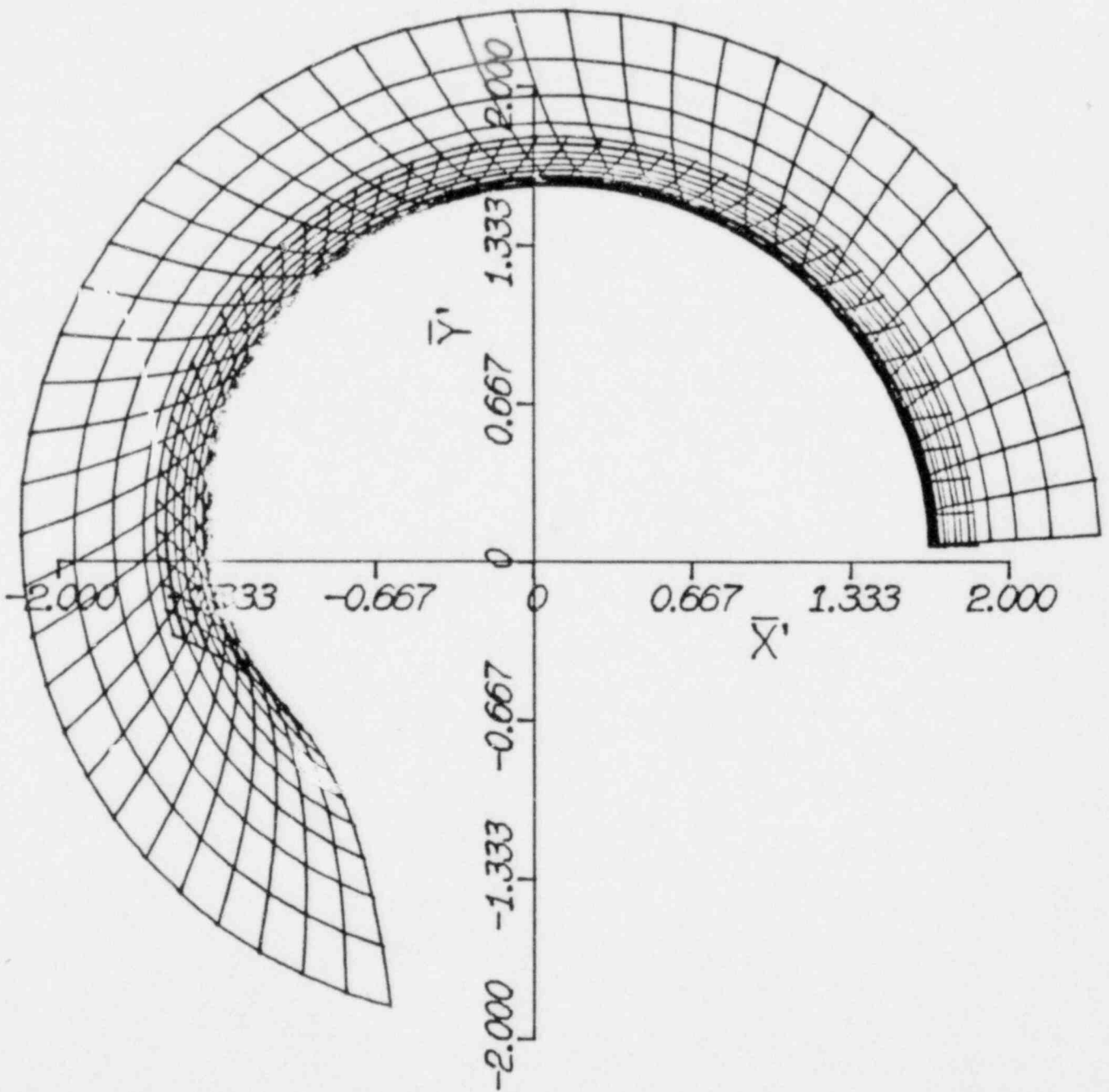
Fig. 3.8 Polar Grid Map of the Caustic Pattern for an Isotropic Material (λ=0) Due to the Stress Singularity Term (Near-Field Solution).
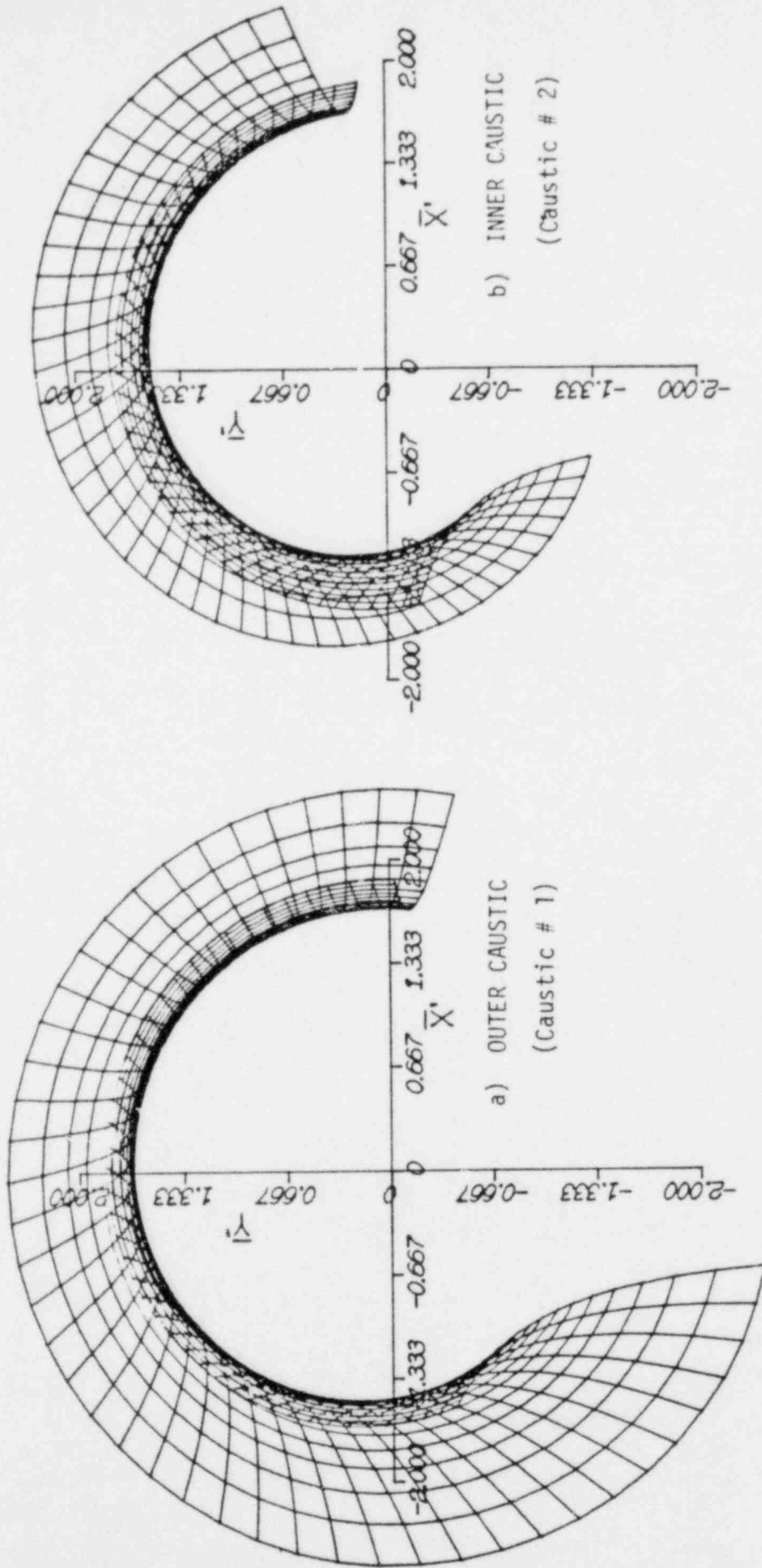
Fig. 3.9 Polar Grid Map of the (a) Outer and (b) Inner Caustics for an Anisotropic Material (Araldite B, $\lambda = 0.288$) Due to the Stress Singularity Term (Near-Field Solution).

a) OUTER CAUSTIC

(Caustic # 2)

b) INNER CAUSTIC

(Caustic # 1)

CORRECTION FACTORS

$f_{outer} = 1.061$

$f_{inner} = 0.922$
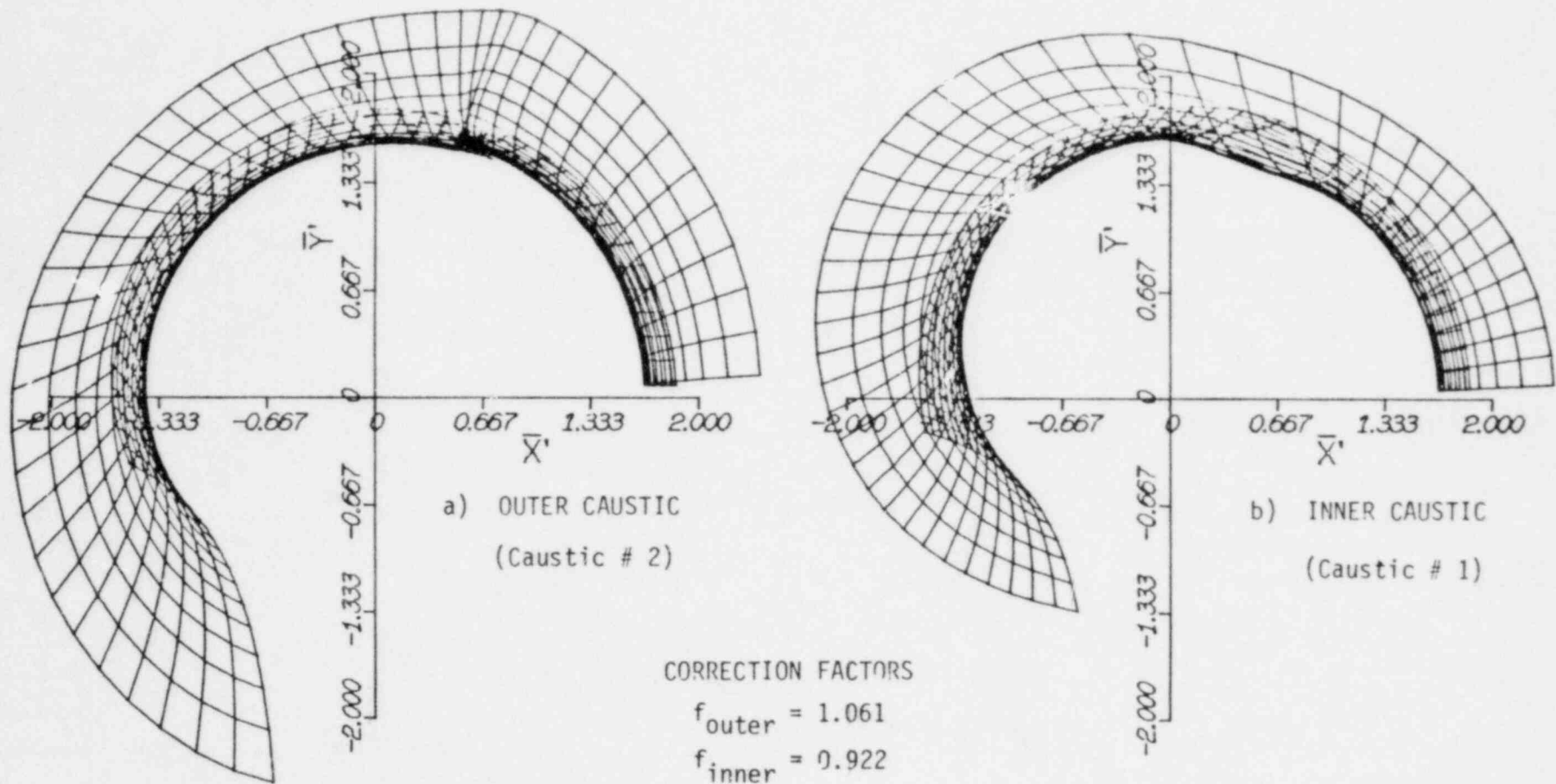
Fig. 3.10 Effect of the Introduction of a Moderately Large Constant Stress ($\delta_o = -0.4$) on the Shape of the (a) Outer and (b) Inner Caustics for an Anisotropic Material (Araldite B, $\lambda = 0.288$).
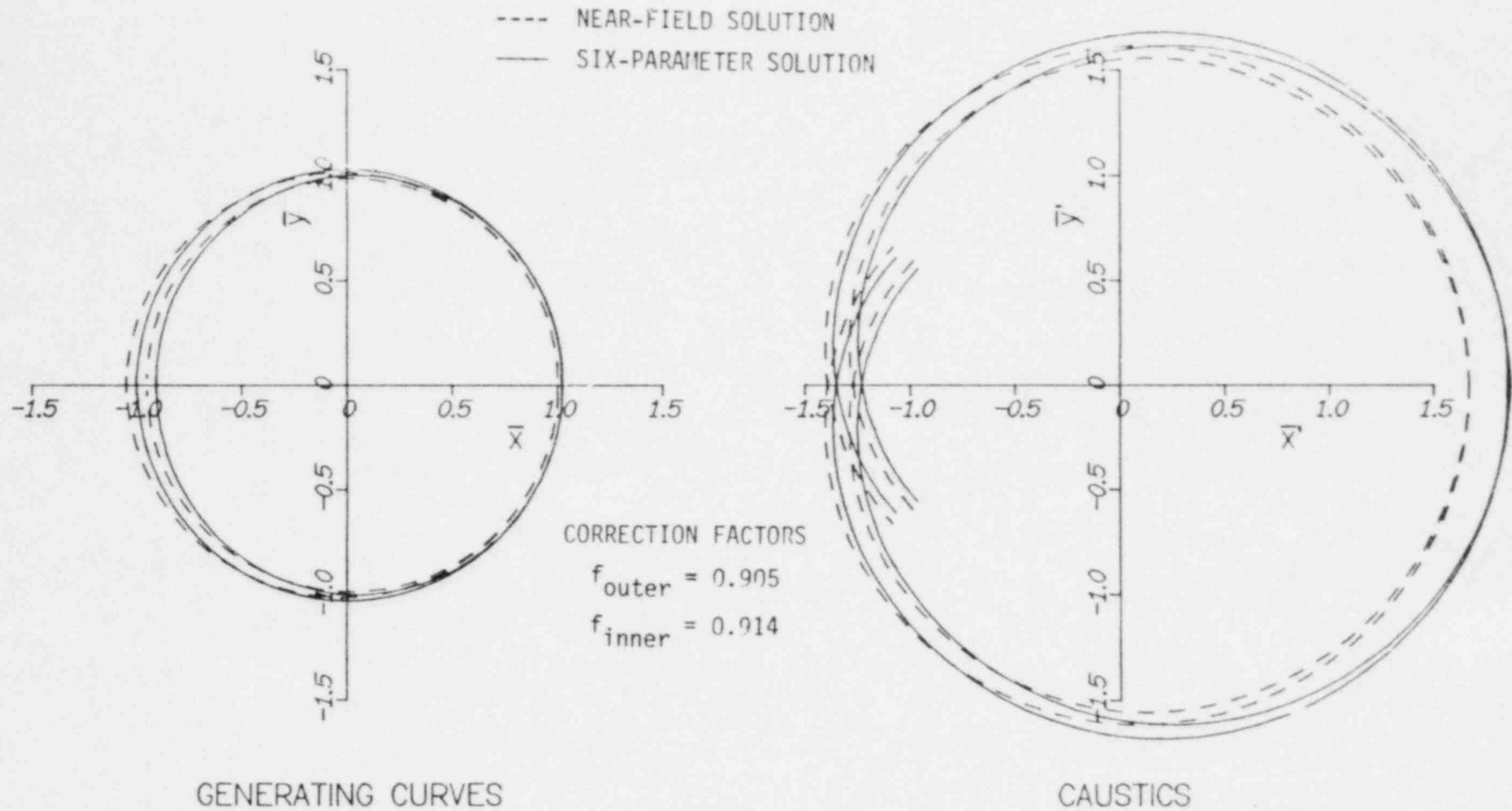
Fig. 3.11 Comparison of the (a) Generating Curves and (b) Caustics Using Near-Field and Six-Parameter Solutions (Table 3.1), for the Stress State Shown in Fig. 3.1, for a Homalite 100 M-CT Specimen.

141

4.   Two Dimensional Computer Codes for the Analysis of Running Cracks

4.1   Introduction

Two-dimensional dynamic computer codes for predicting crack propaga-
tion have been developed both by the University of Maryland and by Battelle
Columbus Laboratories. These two codes have the common feature of utilizing
the changes in the displacement field in the specimen to compute the stress
field energy as the crack propagates. The University of Maryland program
is a finite element code, whereas the BCL code is based on finite difference
techniques.

The detailed structure of the University of Maryland code will not
be discussed in this report, but only a brief outline of its functioning
will be given. A separate User's Manual that covers the details of the
code has been prepared and is available. The methodology of the BCL
code has already been extensively reported [4.1, 4.2]. Both codes were
programmed into the University of Maryland's Univac Computer System,
and have been executed for several different problems. The problems
investigated correspond to 12.7 mm (0.5 inch) thick, Modified-Compact-
Tension, fracture test specimens of Homalite 100, for which experimentally
obtained photoelastic data was available. The results from the two com-
puter codes and the experimental observations have been compared, and
the comparisons are presented in this report. In addition, some in-
depth evaluations of the University of Maryland code are also provided.

These preliminary comparisons show that both the University of
Maryland finite element code (SAMCR) and the BCL finite difference code
(TWOD2) predict, to a fair degree of accuracy, the behavior of a running crack

142

in a crack-line-loaded fracture test specimen. The evaluation of the University of Maryland code is not complete at the time of this writing, and some details of planned future work will be given in the last section of this chapter.

4.2   The University of Maryland Finite Element Code

The University of Maryland's Finite Element Code was developed by Dr. J.M. Etheridge of the Naval Surface Weapons Center, White Oak, Maryland, who served as a consultant to the Photomechanics Laboratory on this project. The details of the mathematical models used for the code, as well as comprehensive information regarding program structure, input and output, etc., are contained in a User's Manual and only a brief overview of the code structure will be given here.

Essentially, the code consists of three separate groups of programs. The first step in a problem solution is to generate the finite element mesh for the given specimen geometry. Considerable latitude exists with regard to the problem being considered, with the code having the ability to accomodate the geometry of rectangular, contoured, and C-shaped specimens, of both monolithic and duplex varieties. In addition, the code can also take into account the presence o. a loading apparatus that is made of a material different to the specimen material. The program used here for mesh generation is program 'MESHGN', which is available from Weiler Research Inc., Mountain View, California. The finite element mesh geometry (nodal point locations, element node numbers, etc.) and the initial loading data are then used as input to the second group of

programs, which compute the initial displacement field. Once again, the programs used here are available from Weiler Research, Inc., and are termed 'DOASIS'.

The displacement field generated by DOASIS is computed on a unit-load, unit-thickness basis and has to be scaled to the actual level of the experiment prior to being input to SAMCR. This displacement field is used to obtain the initial stresses and strains within the specimen, which are, in turn, used to compute the initial value of the stress intensity factor at the crack tip, K_Q. SAMCR itself is a dynamic, finite-element-type code in which a straight moving crack is modelled by the controlled release of nodal forces perpendicular to the crack face. The displacement field is calculated at the end of each time step, and a J-integral computation carried out along a contour that moves with the crack tip. The mode I stress intensity factor, K, is then calculated from the numerical value of the J-integral, and the crack tip velocity, $\dot{a}$, computed from an $\dot{a}$ - K relationship that has to be specified.

Output from SAMCR may be taken in both printed and plotted form and can consist of combinations of the following: time, crack-tip position, stress intensity factor, crack tip velocity, nodal point displacements, nodal stresses, and nodal strains, with data being extracted at the end of each time step or after a specified number of time steps. A summary of these three sets of programs is given in Table 4.1.

The break up of the code into three related but basically independent parts is especially convenient from the point of view of repeated calculations for the same test specimen geometry, but with different load levels.

144

Table 4.1 Summary of Programs Used For Running-Crack Analysis

Program Name	Function	Number of Fortran Source Statements	Core Requirements	Typical Execution Time on UNIVAC 1108
MESHGN	Generate Grid	3000	Moderate	3 mins.
DOASIS	Compute Initial Displacements	9000	Large	10 mins.
SAMCR	Model Propagating Crack	2000	Moderate	10-60 mins.*

*-dependent upon time step size and total run time desired.

The output of DOASIS for a given specimen geometry, if stored, need not be re-computed each time, and can simply be read in prio. to the execution of SAMCR. This considerably speeds up the execution of multiple runs and results in large savings of computer time and costs.

4.2.1 Application of SAMCR to a M-CT Specimen

The Modified-Compact-Tension specimen has been used extensively for mode I fracture studies. The standard geometry of this specimen is shown in Fig. 4.1. For purposes of analysis, the axis of symmetry of the specimen may be taken as the x-axis, and only the portion of the specimen corresponding to $y \geq 0$ used, with the conditions that $\tau_{xy} = 0$ and $v = 0$ on $y = 0$, ahead of the crack tip. In addition, in the finite element analysis, one must also specify the x-direction displacement component, u, at some point in the specimen, so as to prevent rigid body motion.

A finite element grid that can be used to analyze the crack-line-loaded M-CT specimen is shown in Fig. 4.2. The semi-circular inclusion on the left side of the model is one-half of the split-D pin that is used in the experiment to apply loads to the specimen. The material properties of the pin usually differ from those of the specimen, with steel pins being used in a Honalite 100 specimen. Experimental values of Young's Modulus, E, and Poisson's Ratio, v, used were

$$E_{steel} = 2.07 \times 10^5 \text{ MPa} = E_{static}; \ v_{steel} = 0.30$$

$$E_{H-100} = 3.86 \times 10^3 \text{ MPa} = E_{static}; \ v_{H-100} = 0.31$$

An important consideration that arises in the comparison of theoretically predicted and experimental results is the modelling of the interface between pin and model. In the computer code, the two materials are assumed to be perfectly bonded, so that u and v displacements of nodal points along the junction are the same as those of corresponding nodal points in the specimen. In the actual experimental situation, distortions of the loading surfaces lead to a rather complicated Hertzian-type contact stress at the pin-model interface. This would in turn, give rise to differences between the load-line y-displacement measured on the two halves of the split-D and load-line y-direction displacements measured in the specimen (see Fig. 2.53). For this reason, it was chosen to scale the displacement field from DOASIS in terms of the off-pin displacements, rather than the displacement of the pin halves, since both quantities had been measured experimentally.

Other factors that can affect the computed results are the time step size, the specified value of K_a, the manner of nodal force decay, and the value of E used in converting a calculated J-integral value into Stress Intensity Factor, K. Computations based on finite element or finite difference techniques employ discrete time steps in the modelling of a propagating crack. The actual physical phenomenon is a continuous one and would be most closely approximated if extremely small time steps were used. However, stability considerations and operational costs combine to preclude the use of a very small time step size. Some preliminary calculations showed that a time step of 10^{-2} μs was the minimum required for stability in so far as SAMCR is concerned. A typical run-arrest time for the specimen being studied is 500 μs, and it becomes clear that such a small time

147

step size would result in astronomically high computer costs and would, therefore, be impractical. On the basis of the nodal spacing ahead of the crack tip and the wave speed in the material, a critical maximum time step size was calculated and the actual time step used was selected to be 90% of the critical value, which gave $\Delta t = 0.8496$ μs. A similar calculation for the BCL code gave $\Delta t = 0.513$ μs.

The $\dot{a}$-K relationship for polymeric materials such as Homalite 100 has been shown to be a Γ-shaped curve [4.3]. The experimentally determined relationship exhibits a nearly vertical stem in the low velocity region and a flat plateau at some terminal velocity, which is typically about 1/3 of the shear wave speed. For Homalite 100, this terminal velocity is about 400 m/s (16,000 in/s). This curve cannot be easily characterized by a mathematical relationship between $\dot{a}$ and K, and it has been decided, in this computer code, to approximate the curve with a number of straight line segments. The curve for the shipment of material used for the experimental comparisons is shown in Fig. 4.3, which also shows the line-segment approximation adopted.

It has also been observed that the value of K_a changes from one batch of material to another [4.4] and sometimes, variations can even be observed from one sheet to the next. However, the shape of the $\dot{a}$-K curve does not show any significant changes and a change in K_a can be viewed as the translation of the curve along the K-axis. Since the stress intensity existing at the crack tip, when compared to K_a, is a measure of the driving force moving the crack, the value of K_a needs to be rather carefully determined and should be specified in a computer code as accurately as possible

148

for the particular material being used.

It was stated earlier that SAMCR models a straight moving crack by the controlled release of nodal forces perpendicular to the crack face. The boundary conditions that prescribe $\tau_{xy} = 0$ and $v = 0$ ahead of the crack tip lead to the existence, in the computer model, of a force distribution as shown in Fig. 4.4. Once the K-value is calculated by the J contour method, the $\dot{a}$-K relationship is used to determine whether the crack will propagate, and if so, at what velocity. The product of this velocity and the time step provides information as to the distance, Δa, which the crack advances in the next time step. If the nodal spacing is defined as b, and the magnitude of the nodal force as F_0 when the crack tip is located at the node, the new magnitude of this nodal force, F, can be taken as a function of F_0, Δa, and b. Two obvious possibilities that come to mind are

$$\frac{F}{F_0} = \left(1 - \frac{\Delta a}{b} \right)^m \qquad (4.1a)$$

and

$$\frac{F}{F_0} = \cos^m \left(\frac{\pi \Delta a}{2b} \right) \qquad (4.1b)$$

where m is an additional parameter that can be varied. With this formulation, the force at the node immediately behind the crack tip becomes zero when the crack reaches the next node, at which point the whole process is repeated again. It is essential that the crack tip should not overshoot a node in its travel, and this is achieved by

149

checking to see if overshoot will occur, in which case the time step-size is reduced for that one calculation. Possible values of the ratio F/F_0 are shown as a function of $\Delta a/b$ in Figs. 4.5a and 4.5b, which correspond to the two possibilities discussed here. The series of computer runs used for comparison used eqn (4-1a) with $m = 1/3$. It is proposed during the coming year to evaluate the effects of using either of eqns (4.1a) or (4.1b), with different values of m.

Lastly, there is some degree of ambiguity as to the most appropriate value of Young's Modulus, E, to use in finite element or finite difference computations. The modulus is certainly a strain-rate dependent quantity for a polymeric material [4.3], and the ideal solution would be to compute the strain rate at each point and let the code pick off the appropriate value of E from a specified modulus vs. strain rate relationship. This method would become so complex and time-consuming, that it is in fact not feasible. Some kind of compromise has then to be made between using a static value of E(which is 3.86×10^3 MPa for Homalite 100) and a dynamic value which can be as high as 4.86×10^3 MPa for the bar wave speed. Schirrer for example [4.5], has concluded that variations in the elastic modulus do not change the stress distribution appreciably, but do in fact alter the strain distribution around the crack tip. As a compromise, it was decided to use a value of $E_{static} = 3.86 \times 10^3$ MPa for all computations except in the conversion of the J-integral value to K at the crack tip, where a value of $E_{dynamic} = 4.86 \times 10^3$ MPa has been used.

150

4.3 The BCL Finite Difference Code

4.3.1 The Structure of the BCL Code

The given specimen geometry and dimensions are first used to compute a uniform grid covering the entire plane of the specimen and the initial positions of the nodal points determined for zero load. The grid is usually formulated so that the nodal density in the direction of crack propagation is at least one order of magnitude higher than the nodal density perpendicular to the crack line. In the case where the specimen is symmetric about the crack line, only half of the specimen is used in the actual computation, so as to cut down on the computation time required [4.1, 4.2].

The displacement field is then computed for a given initial value of the static crack tip stress intensity factor, K_Q. There is a problem here, which arises due to the fact that K_Q is higher than K_{Ic}, the stress intensity factor necessary for initiation of a mathematically sharp crack. This is circumvented by employing an "energy-quench technique" [4.2] to calculate the initial strain energy in the specimen. This procedure, and the establishment of a grid, are both performed by the set of programs named TWOD.

The static displacement field output by program TWOD serves as input to the programs under TWOD2, which compute the various parameters required to describe the behavior of the crack as it propagates. The initial K_Q value (or an experimentally measured displacement) is input and used to scale the static displacement field to the correct value prior to the

151

start of the dynamic calculation. The changes in the displacement field as the crack propagates are then used to compute the specimen strain energy and the other parameters necessary to describe the crack extension process.

The finite difference code uses a grid that is rather different to that used in the finite element scheme. Figure 4.6 shows the specimen grid corresponding to the BCL code. In this grid, nodes in the pinhole are assigned an "effective density factor", thus avoiding the bi-material formulation of DOASIS and SAMCR. Note also, that the grid has a uniform nodal density in the x-direction, and a different, though still uniform, nodal density in the y-direction. Crack tip velocities are determined by taking energy levels available at the crack tip and computing how many time steps are required to propagate the crack to the next grid line. The ratio of the nodal separation and the number of time steps computed in the above manner can be used to obtain the crack tip velocity. The $\dot{a}$-K relationship to be used also has to be specified.

4.3.2 Modifications of the BCL Code

The BCL TWOD and TWOD2 codes were provided to the University of Maryland in late 1977 in the form of card decks, accompanied by a program listing and a sample output from the BCL computer pertaining to a pin-loaded compact specimen of steel.

Since the original programs were written for a CDC-5500 series computer system, they were not immediately compatible with the UNIVAC 1108 or 1100/42 series computers available at the University of Maryland.

152

Substantial changes had to be made and considerable reprogramming carried out before the programs were working on the computer system here. Some of the changes, such as variable name length, input and output statements, etc., were necessary from a purely compilation aspect, while others, such as the use of mass storage files rather than tapes for data storage, and the elimination of plotted output, were made from the point of view of computer efficiency, and with the intention of reducing run times and computer costs. Considerable care was, however, taken to ensure that the code was not altered in any way, insofar as the methodology or order of computation was concerned.

The successfully compiled and de-bugged programs were first checked by inputting the same set of data that BCL had used to produce the sample output provided with the programs. The results matched those obtained earlier, and at this stage, it was felt that the code was ready to be run for input data pertaining to fracture test specimens for which photoelastic results had already been obtained.

The specimen type that has commonly been used in photoelastic studies of energy loss during crack propagation is a Modified-Compact-Tension specimen, with crack-line-wedge-loading by means of a split-D pin [4.6]. It was felt that these experiments had the most carefully monitored data for initial pin load and displacement, and this, coupled with the fact that the M-CT specimen is being adopted by ASTM as a standard specimen [4.7], was the basis for the choice of specimen with which to test the code. Introducing data for the crack-line-loading situation proved to have a detrimental effect on the TWOD programs, which failed to

153

generate a static displacement field without persistent errors in the form of storage overflows and underflows for no readily apparent reason.

Consultation with Dr. Gehlen of BCL revealed that additional modifications to the programs had been made since 1977, which were required to permit crack line loading to be accomplished. After these modifications were made and some internally located material constant changes identified, the BCL code executed successfully on the University of Maryland computer system.

This was accomplished by mid-July of 1979. The results obtained showed that some errors still existed in our version of the programs and it was decided, after discussions with Dr. Kanninen of BCL, that the greatest efficiency would result from our furnishing the necessary input data to him and having the BCL code run on the Battelle computer system. Hence the (TWOD2) results to be discussed in the next section were obtained from BCL.

4.4 Results from the Computer Codes

4.4.1 Comparison of Results from SAMCR, the BCL Code, and Experiments

Three experiments from a series of run-arrest studies in M-CT specimens of Homalite 100 were chosen for the purpose of evaluating the computer codes. Crack arrest occurred in all of the experiments in this series, and the three particular tests selected corresponded to a low, intermediate, and high value of K_Q. Three quantities were available from the experimental data for purposes of initializing the computer codes. These were the y-displacement of the split-D pins, the y-displacement on the load line measured at the edge of the specimen, and the load on the

154

split-D pins.

The pin displacement measurement was believed to be influenced by Hertzian indentations at the pin-model interface, while the pin load could not be used as the primary input in the BCL code. It was felt that a fair comparison of the results from the codes and experiment required as close a match-up in starting configuration as possible, and it was therefore decided to use the displacements measured at the edge of the specimen as the scaling quantity. Table 4.2 summarizes the data for the three experiments and also shows the K_Q values predicted by the SAMCR and BCL codes. The same modulus formulation and å-K relationship was adopted for both codes.

Computer results for the dynamic run-arrest event can be adequately evaluated by examining:

a) crack extension as a function of time;

b) instantaneous stress intensity factor as a function of time; and

c) instantaneous stress intensity factor as a function of crack extension.

All of the above information was also available from photoelastic experiments for comparison purposes. These plots were prepared from the results obtained from the computer codes for all three initial conditions, and are shown in Figs. 4.7a - 4.7c, 4.10, 4.11, and 4.12.   In each case, experimental results and computer code predictions have been presented on the same figure for easier comparison.

The use of a multi-flash Cranz-Schardin camera in dynamic photoelastic studies provides a total of 16 pictures of the propagating crack, taken over some interval of time (in this case, of the order of 450 µs).

155

Table 4.2 Summary of Load, Displacement, and K_Q Data

| Test Number | Pin Load | Experimental Data | | K_Q Predicted by SAMCR* | K_Q Predicted by the BCL Code |
		Pin Displacement	Off-Pin Displacement		
P-9	115 lbs.	16.3 mils	11.5 mils	696 psi-in$^{\frac{1}{2}}$	632 psi-in$^{\frac{1}{2}}$
		0.414 mm	0.292 mm	0.765 MPa-m$^{\frac{1}{2}}$	0.695 MPa-m$^{\frac{1}{2}}$
P-7	125 lbs.	18.6 mils	12.5 mils	759 psi-in$^{\frac{1}{2}}$	686 psi-in$^{\frac{1}{2}}$
		0.472 mm	0.318 mm	0.834 MPa-m$^{\frac{1}{2}}$	0.754 MPa-m$^{\frac{1}{2}}$
P-10	145 lbs.	20.8 mils	14.5 mils	878 psi-in$^{\frac{1}{2}}$	796 psi-in$^{\frac{1}{2}}$
		0.528 mm	0.368 mm	0.965 MPa-m$^{\frac{1}{2}}$	0.875 MPa-m$^{\frac{1}{2}}$

*-Using $E_{Static} = 3.86 \times 10^3$ MPa

156

Data is thus available only at preset intervals of time, Δt, during which the crack has moved through some finite distance, Δa. Results from the computer codes, on the other hand, are available after each time step, and may be regarded as being very nearly continuous.

4.4.2 Crack Extension as a Function of Time

Figures 4.7a, 4.7b, and 4.7c show crack extension as a function of time from experimental observations and from the two computer codes. Experimental data points appear as solid circles (●) and have been connected by solid lines for clarity. Results from SAMCR are denoted by open squares (□) and have been extracted from the computer outputs at every tenth time step (approximately every 8.5 μs). Data from the BCL code was available each time that the crack jumped from one node to the next and is shown by crosses (+).

Both computer codes predict a larger crack jump than is observed experimentally, with SAMCR overpredicting by 10% - 20% and the BCL code by 15% - 25%. A small problem arose with respect to Test P-10, for which the BCL code did not show a final arrest. The computation was halted at t = 490 μs after a crack extension of 108.4 mm because the crack tip was regarded as being too close to the edge of the specimen. An examination of the BCL Δa vs. t data for this test showed that the crack slowed considerably between 338 μs and 417 μs, at which point, the crack velocity was down to about 35 m/s and Δa was equal to 101.6 mm. Following this, the crack speeded up again and continued propagating until the computation was halted. In Tests P-9 and P-7, a similar slowing down of the crack was

157

followed by a final arrest which occurred approximately 95 μs later, with an additional extension equal to about 2.5 mm. The speeding up observed in P-10 was fe c to quite possibly be an artificial phenomenon caused by the closeness to the specimen boundary. It was therefore decided in the subsequent discussion, to regard the BCL predicted arrest length for P-10 as being equal to 101.6 + 2.5 = 104.1 mm at a time given by 417 + 95 = 512 μs.

The predicted and actual crack jump distances are tabulated in Table 4.3, which also shows the predicted crack jump as a percentage of the experimental value. Notice that the experimental data in Figs 4.7a, 4.7b, and 4.7c do not show the final arrest point, since the last flash photograph was prior to final arrest. The experimental crack jump distances shown in Table 4.3 were obtained from measurements made on the actual test specimen after the test was completed.

Table 4.3   Summary of Crack Jump Distances from
            Experiment and the Computer Codes

Test Number	Experimental Crack Jump	SAMCR Prediction	BCL Code Prediction
P-9	65.0 mm	77.5 mm (119.4%)	82.97 mm (125.0%)
P-7	79.5 mm	87.4 mm (109.8%)	91.44 mm (115.0%)
P-10	86.1 mm	100.6 mm (117.0%)	104.1 mm (121.9%)

158

4.4.3 Stress Intensity Factor as a Function of Time and Crack Extension

Dynamic photoelastic experiments provide the initial starting configuration and up to 16 data sets recorded during the course of the run-arrest event at preset intervals of time. Information regarding crack tip positions and the stress intensity at the crack tip can be extracted from this data. The output structure of the BCL code, in its present form, provides complete information regarding time, crack tip position, crack velocity, and the crack tip stress intensity factor at every time step that the crack moves from one nodal point to the next. Results from SAMCR include the same information as that provided by the BCL code but display it at the end of every time step, irrespective of the crack position and velocity.

Plots of K vs. t and K vs. Δa from SAMCR show that the predicted K-values are oscillatory in nature. This can be seen in Figs. 4.8a-4.8c and Figs. 4.9a-4.9c, which show SAMCR results for K vs. t and K vs. Δa, respectively, for Tests P-9, P-7, and P-10. For purposes of comparison with experimental results and the BCL code predictions, average curves faired through this data were used, since curves such as those shown in Figs. 4.8 and 4.9 led to plots that were difficult to examine and comprehend. The average curves used are also shown in Figs. 4.8 and 4.9.

A comparison of observed and predicted K vs. t and K vs. Δa behaviors is shown in Figs. 4.10, 4.11, and 4.12, for Tests P-9, P-7, and P-10 (in that order). Solid circles (●) connected by solid lines have been used to indicate experimental data and crosses (+) have been used to show the BCL code results. The average curves from the SAMCR results are shown as dashed lines (———). The experimentally observed rapid initial drop from a high

preinitiation K_Q value to a much lower K_D (see Chapter 2) is indicated by dotted lines (----) in all six figures.

Other than the oscillatory nature of the computer code results, the major point to be noted here is the computer predicted nature of the drop from K_Q to K_D. SAMCR results show this occurring over about 25-40 μs, while results from the BCL code show a substantially higher K-value being present for 100 μs or more. This becomes especially important if an integral of the form

$$E_f = \frac{h}{E} \int_{a_0}^{a_f} K_D^2 \, da \qquad (4.2)$$

is used to compute fracture energies. This is clearly evident from the plots of K vs. Δa, in which the area under the K-curves (and hence under curves of K^2 vs. Δa) is much larger for the BCL code than for SAMCR or the experiments. The problem is compounded by the fact that a major part of the crack extension occurs during the very period when the BCL code predicts a K-value much higher than the experimental K_D. Notice also that the BCL code uniformly predicts a starting K_Q value that is somewhat lower than both photoelastic observations and the SAMCR predictions.

4.4.4 Crack Jump as a Function of K_Q

Figure 4.13 shows the total crack jump, a_f-a_o, as a function of the initial experimental K_Q value for both of the codes and the experiments. It is possible to pass the same curve through each of the three sets of data points by a simple translation up or down. This further reinforces the possibility discussed earlier, of the failure of the BCL code to predict

160

arrest in Test P-10, being due to the closeness of the specimen boundary and hence an artifact. The systematic overprediction in crack jump that is displayed by both codes also suggests that energy dissipation in the experimental situation is occurring by means other than fracture surface formation.

4.5 Conclusions and Discussion

The results of a comparison between experiments, the University of Maryland Code, and the BCL Code show that both codes overpredict the total crack jump distance to be expected for a given initial energy level. This is consistent with the findings reported in Chapter 2 of this report, where it has been shown that substantial energy can be dissipated by means other than fracture surface formation. (The computer codes assume that the only mechanism of energy dissipation is fracture surface formation.) The results also show that SAMCR appears to predict the overall crack extension behavior more closely than does the BCL code.

Preliminary results of another series of computer runs have shown that the crack jump distance and crack extension behavior is rather closely connected to the value of K_a that has been specified as a part of the input to the code. This would seem to suggest that the results from SAMCR can be used to predict the arrest toughness for a material for which a complete crack extension history has been established experimentally. The comparison should, however, be based on predicted and observed crack extension behavior over say 80-85% of the total observed crack jump rather than on the final crack jump distance.

161

As discussed earlier, the manner in which nodal forces are released can be varied with ease. It would be informative to perform runs with different values of m for both eqns (4.1a) and (4.1b) to determine if there is an optimum value of m, or an optimum form of the force decay function. Controlled release of nodal forces was adopted when it was found that sudden release of the force at a node gave rise to severe perturbations in the K-value. It is therefore possible that a study such as that suggested above will also shed some light on the oscillatory nature of the SAMCR predicted K-values.

In its present form, SAMCR uses the $\dot{a}$-K relationship to determine the crack tip velocity and hence the amount of force decay occurring behind the crack tip. It is unfortunate that the specimens tested show values of K and $\dot{a}$ that lie on the near-vertical stem of the relationship. As a consequence, a drop in K from 0.505 MPa$\sqrt{m}$ to 0.500 MPa$\sqrt{m}$ results in a velocity-drop from 228.6 m/s to zero. Some form of averaging of crack tip velocities and/or the computed K-values may be reasonable and should have a discernible effect on the oscillations in K that are seen in Figs. 4.8 and 4.9. Another possibility would be the use of a velocity threshold, where the crack tip would be given some small finite velocity unless the instantaneous velocity had remained at zero for a specified interval of time. Some support for such a mechanism comes from our observations in photoelastic experiments where velocities below 100 m/s have not been seen in M-CT specimens of Homalite 100. The effects on the results of time step size and the specified J-contour are also items that would

merit further investigation.

In conclusion, it can be said, that a number of factors remain to be studied in detail before the evaluation of the SAMCR code can be considered to be comp e. The performance of the code as reported here certainly seems encouraging. The approach and modelling mechanisms used in SAMCR do seem to predict overall behavior to a somewhat better degree than the BCL code. In addition, the finite element formulation seems to have greater potential for studying features such as late breaking ligaments and the diffused crack tip region that are encountered in tough steels.

4.6   Future Work

Based on the points raised in the previous sections, the following program for complete code evaluation is planned to be carried out over the course of the coming year. Some of the areas of investigation listed have already been pursued to some extent, but conclusive results are not yet available.

The planned approach consists of:

1) altering time step size to study the effect of this variable on oscillations in K, and to establish an optimum time step size from the point of view of accuracy and computer costs;

2) changing the manner of nodal force decay in an independent attempt, from (1) above, towards decreasing oscillations in K;

3) studying the possibilities of using different values of K_a and comparing predictions of crack extension histories with experimental

163

results in steel specimens to establish the arrest toughness of the material;

4)   incorporating averaging schemes for crack tip velocities and/or K-values and studying the effects on the code results;

5)   using the concept of a velocity threshold in support of and separate from (4) above; and

6)   incorporating material damping as a source of energy dissipation in addition to the energy released during fracture surface formation.

References

4.1 Hahn, G.T., et al., "Critical Experiments, Measurements and Analyses to Establish a Crack Arrest Methodology for Nuclear Pressure Vessel Steels", 1st Annual Progress Report to NRC, BMI-1937, Battelle Report, August 1975.

4.2 Hahn, G.T., et al., "Critical Experiments, Measurements and Analyses to Establish a Crack Arrest Methodology for Nuclear Pressure Vessel Steels", 2nd Annual Progress Report to NRC, BMI-NUREG-1959, Battelle Report, October 1976.

4.3 Kobayashi, T., and Dally, J.W., "The Relation Between Crack Velocity and the Stress Intensity Factor in Birefringent Polymers", ASTM STP 627, (1977), pp. 257-273.

4.4 Dally, J.W., "Dynamic Photoelastic Studies of Fracture", Experimental Mechanics, Vol. 19, (10), (1979), pp. 349-367.

4.5 Schirrer, R., "The Effects of a Strain Rate-Dependent Young's Modulus Upon the Stress and Strain Fields Around the Running Crack Tip", Intl. Jnl. of Fracture, Vol. 14, No. 3, (June 1978), pp. 265-279.

4.6 Irwin, G.R., et al., "Photoelastic Studies of Crack Propagation and Crack Arrest", U.S. NRC - Report NUREG-0342, University of Maryland, 1977.*

4.7 ASTM STP 632 (1977), E561-76T, "Tentative Recommended Practice for R-Curve Determination".

---

*Available for purchase from the NRC/GPO Sales Program, U.S. Nuclear Regulatory Commission, Washington, D.C. 20555, and the National Technical Information Service, Springfield, Virginia 22161.
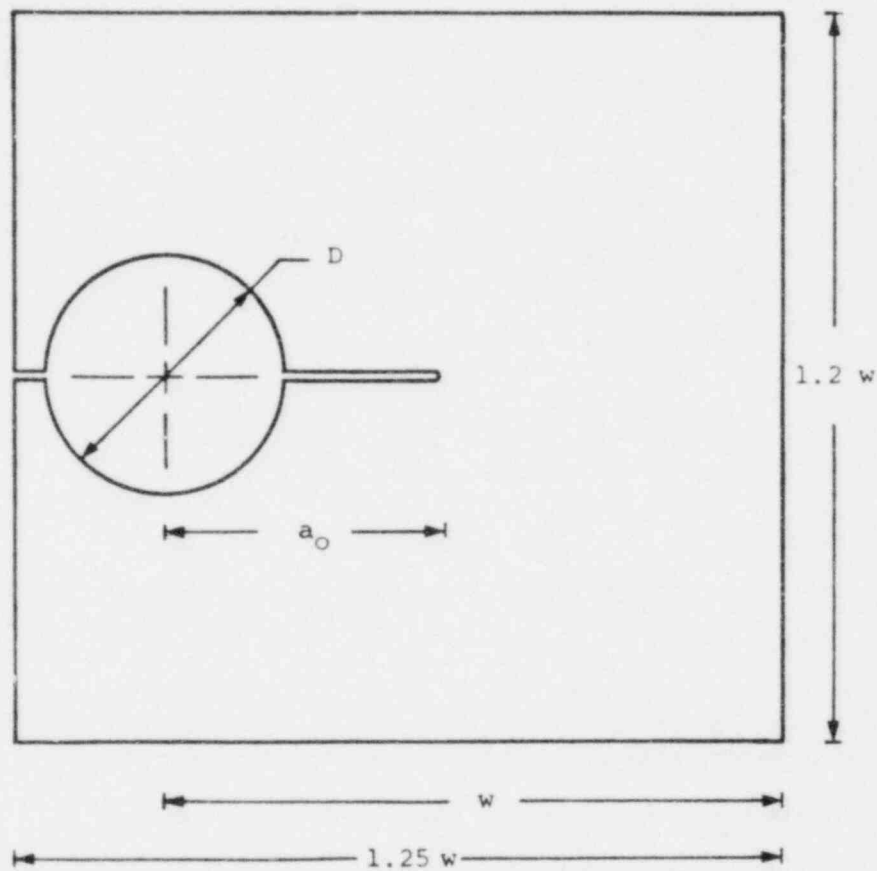
w = 203.2 mm (8.0 inches)

D = 76.2 mm (3.0 inches)

a_0= 88.9 mm (3.5 inches)

Fig. 4.1   Geometry and Dimensions of the Standard 12.7 mm Thick
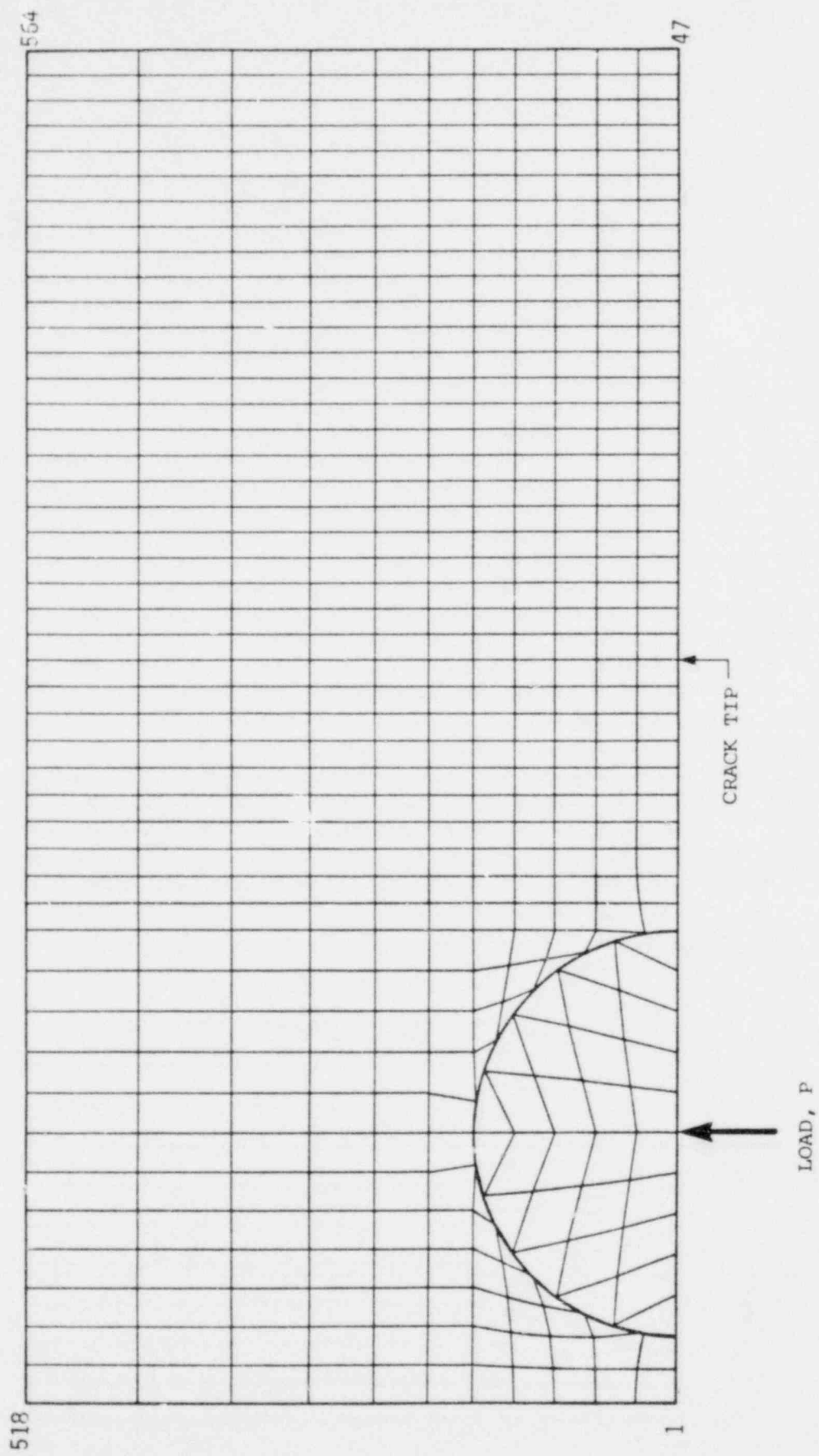Modified-Compact-Tension Specimen.

166

Fig. 4.2   Symmetric (Upper) Half of the M-CTSpecimen showing the
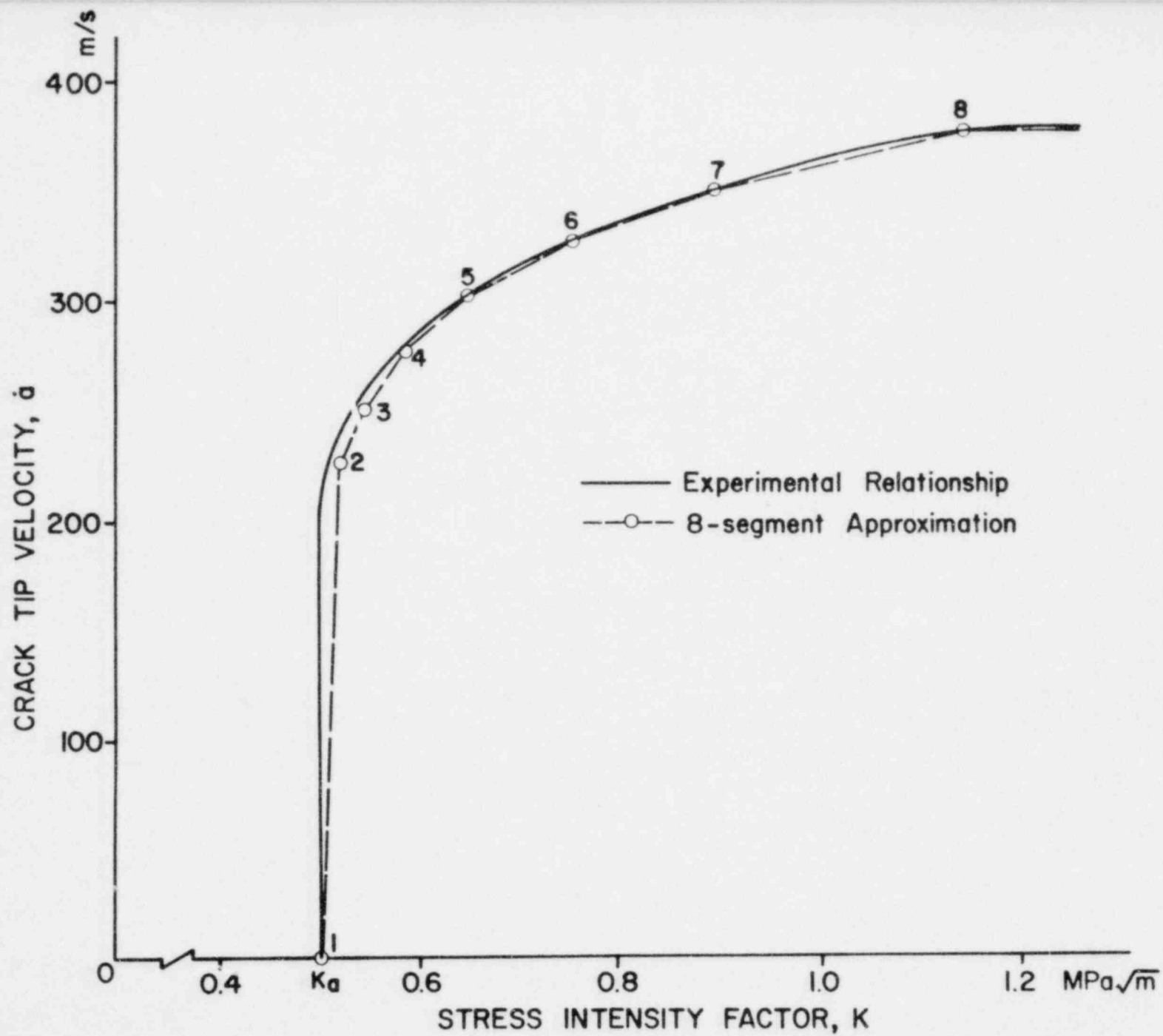Finite Element Mesh Used by SAMCR.

167

Fig. 4.3 The Experimental à-K Relationship and the Approximation Used in SAMCR and the BCL Code.
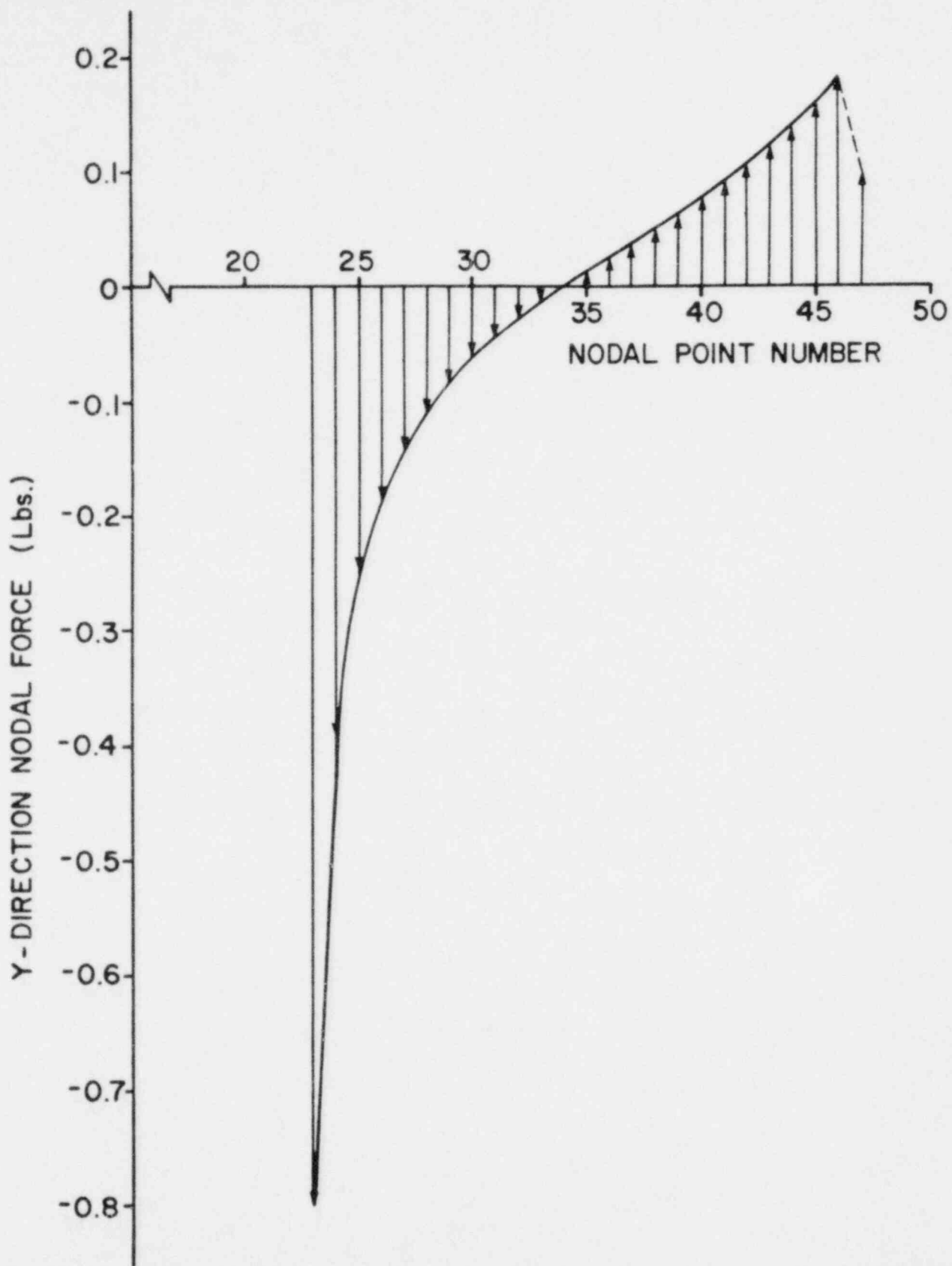
Fig. 4.4   The Vertical Nodal Force Distribution Ahead of the Starter
Crack Tip Resulting from the Prescribed Boundary Conditions,
for a Unit Load Applied at Node 8 to a Specimen of Unit Thickness.
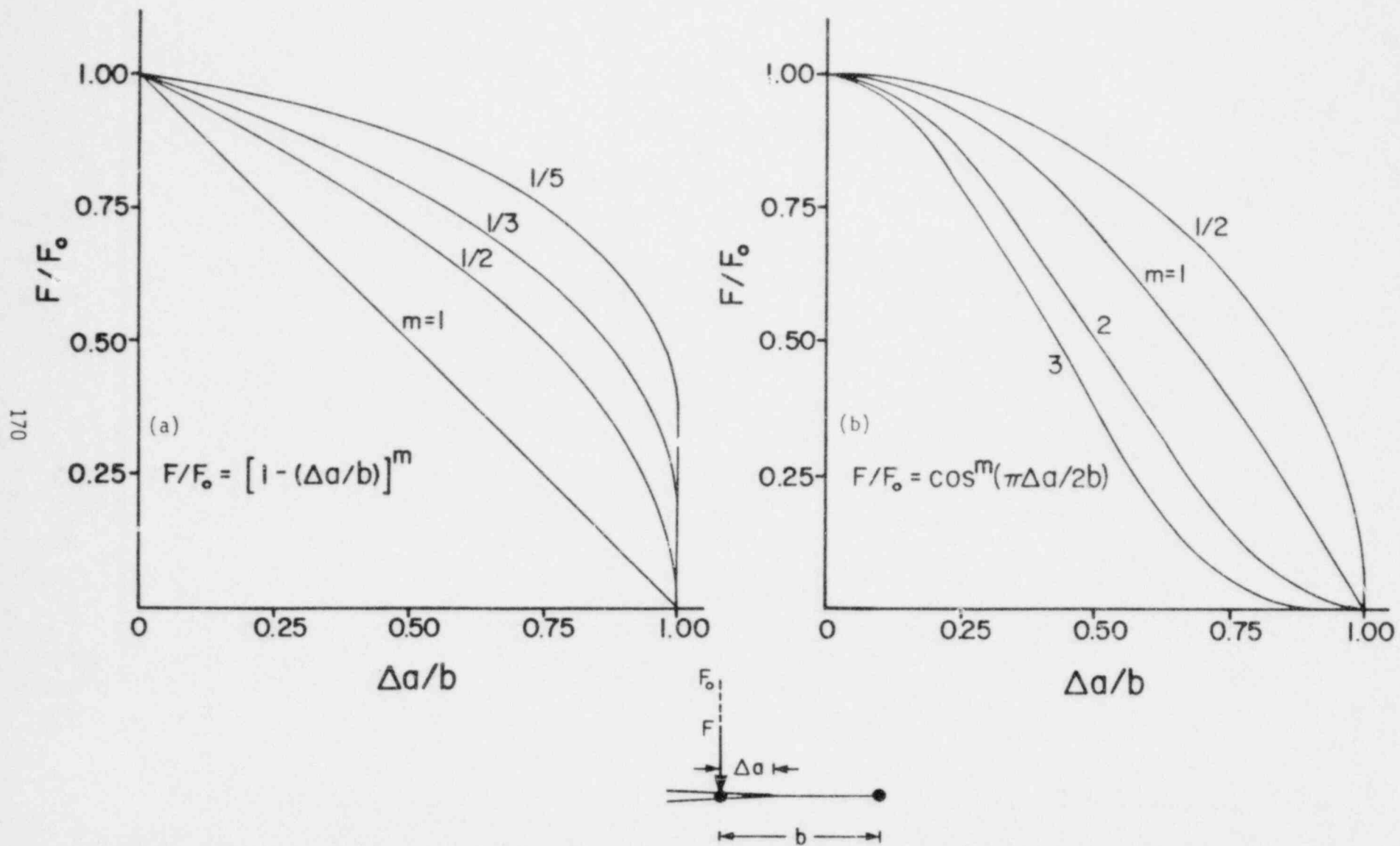
169

Fig. 4.5 Two Possible Forms of the Nodal Force Decay Function Employed by SAMCR.
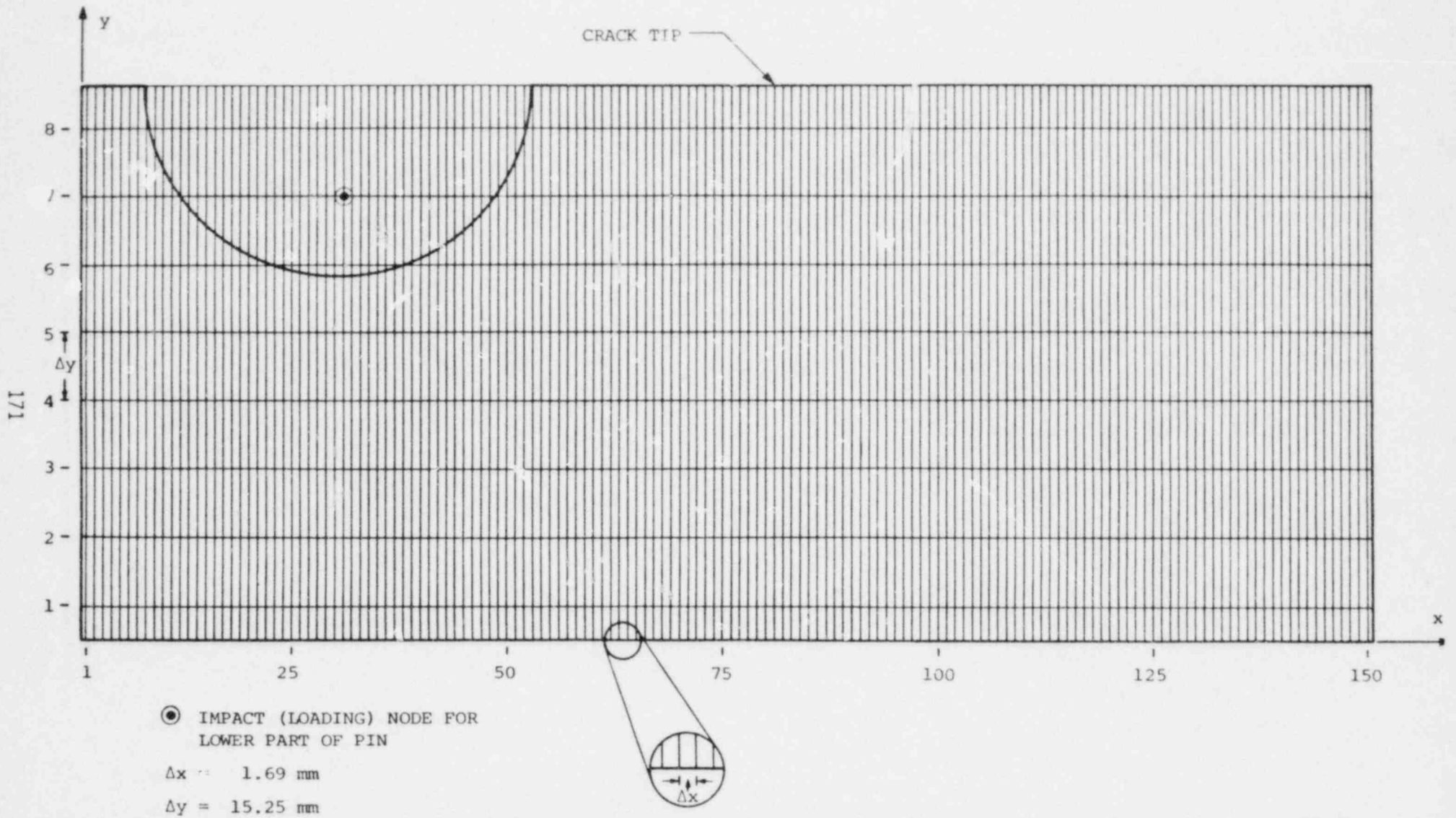
Fig. 4.6 Symmetric (lower) Half of the M-CT Specimen with a Super-imposed Finite Difference Grid such as that Used by the BCL Code.
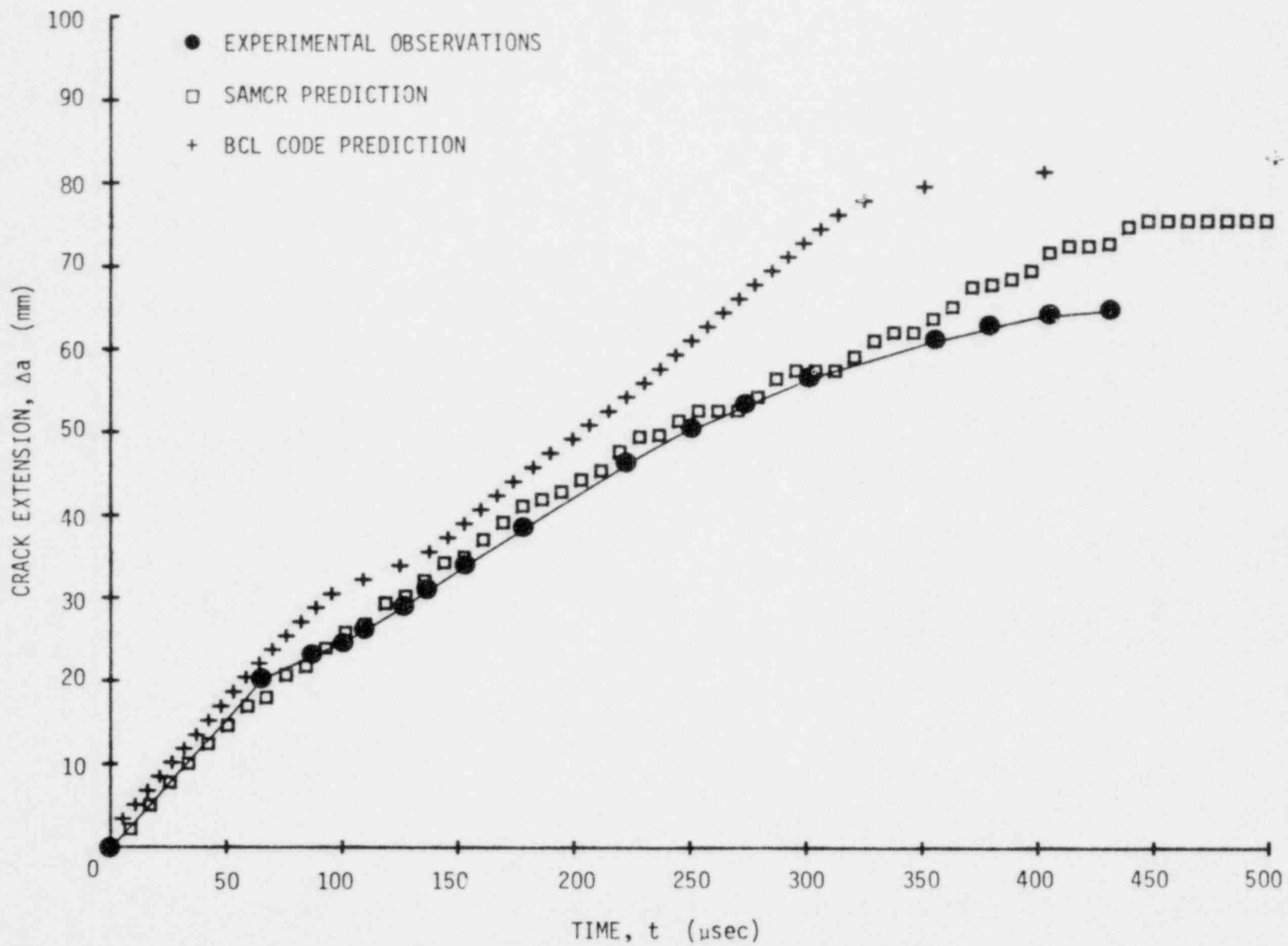
Fig. 4.7a Observed and Predicted Crack Extension as a Function of Time for Test P-9

172
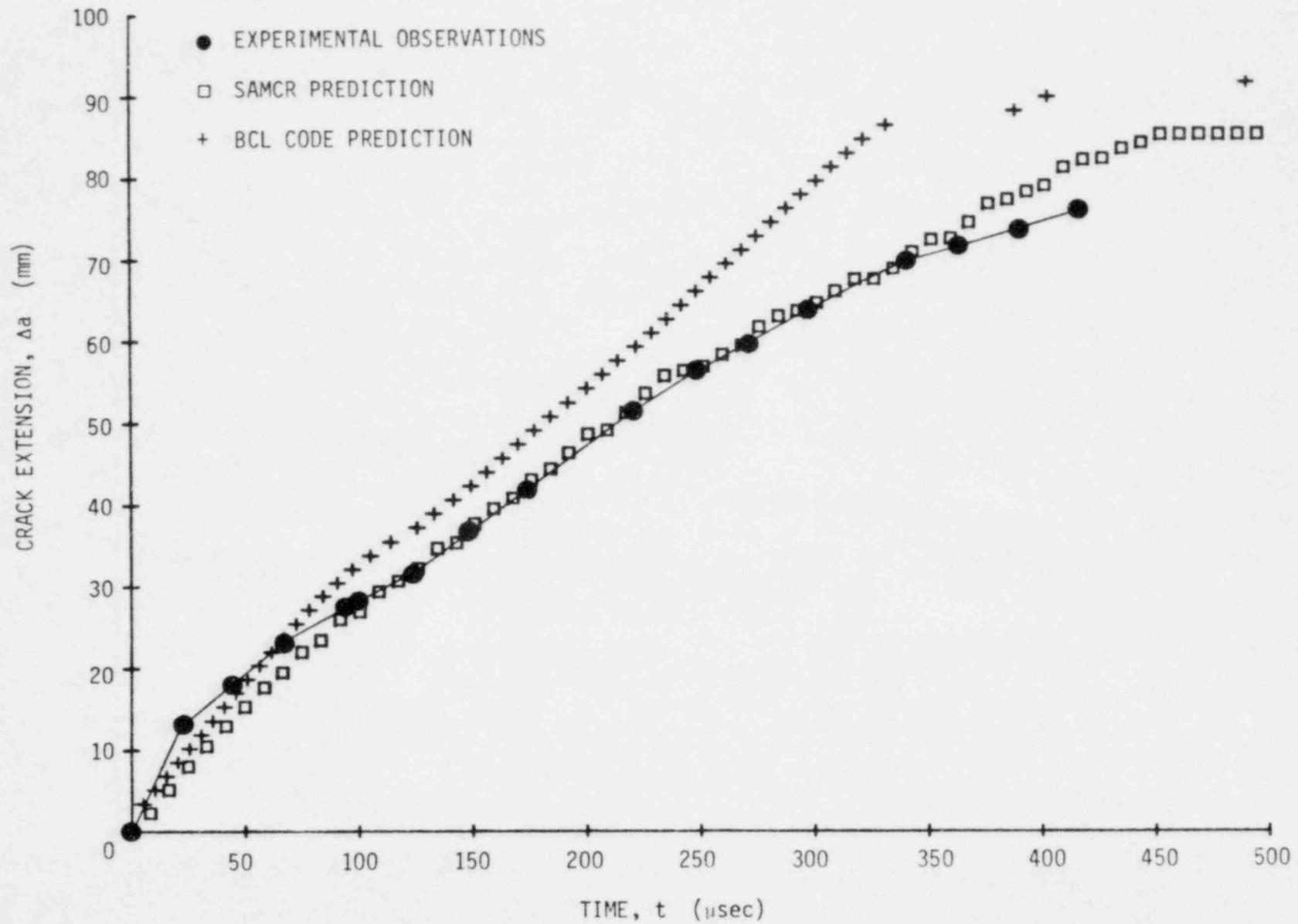
Fig. 4.7b Observed and Predicted Crack Extension as a Function of Time for Test P-7

173
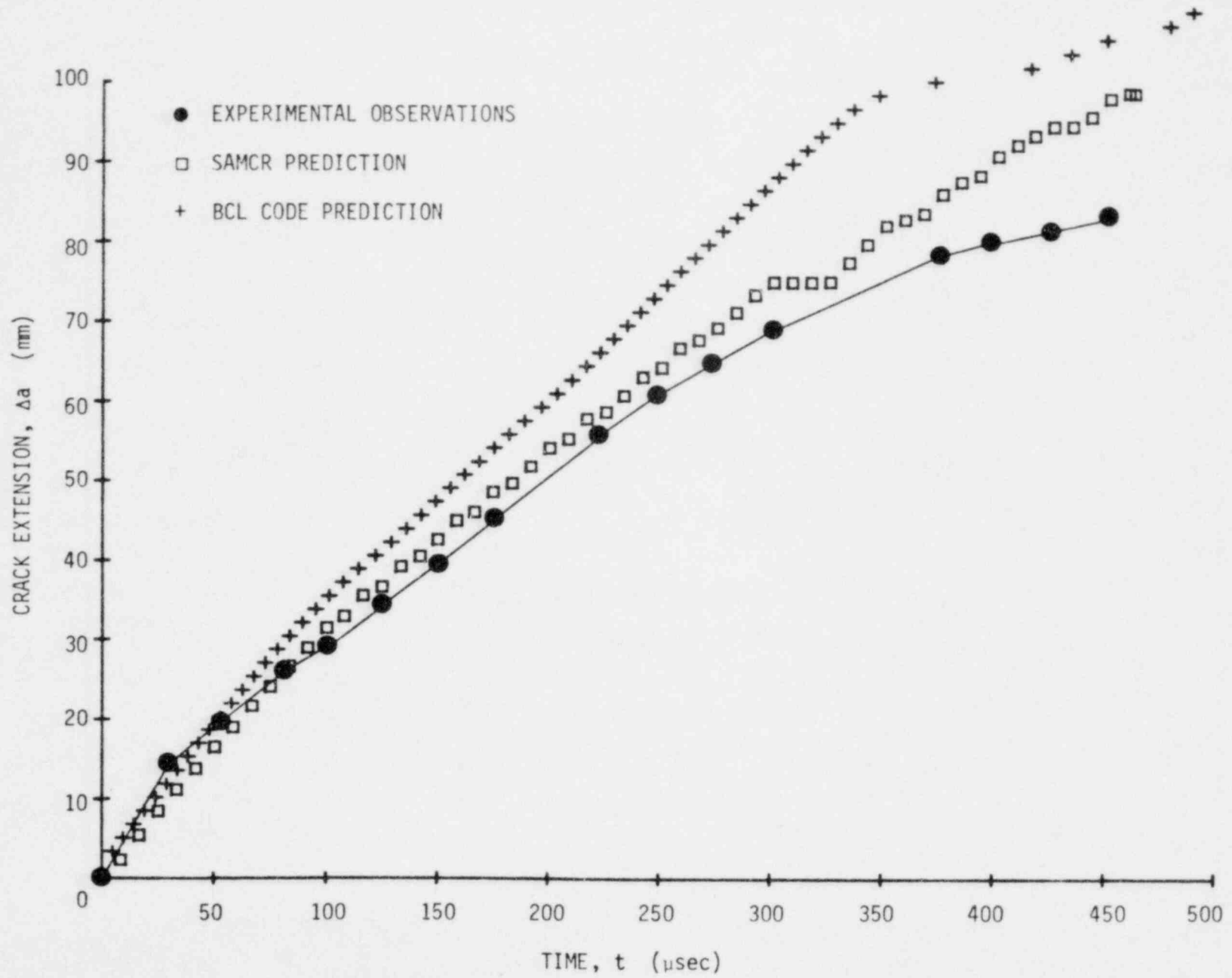
Fig. 4.7c Observed and Predicted Crack Extension as a Function of Time for Test P-10
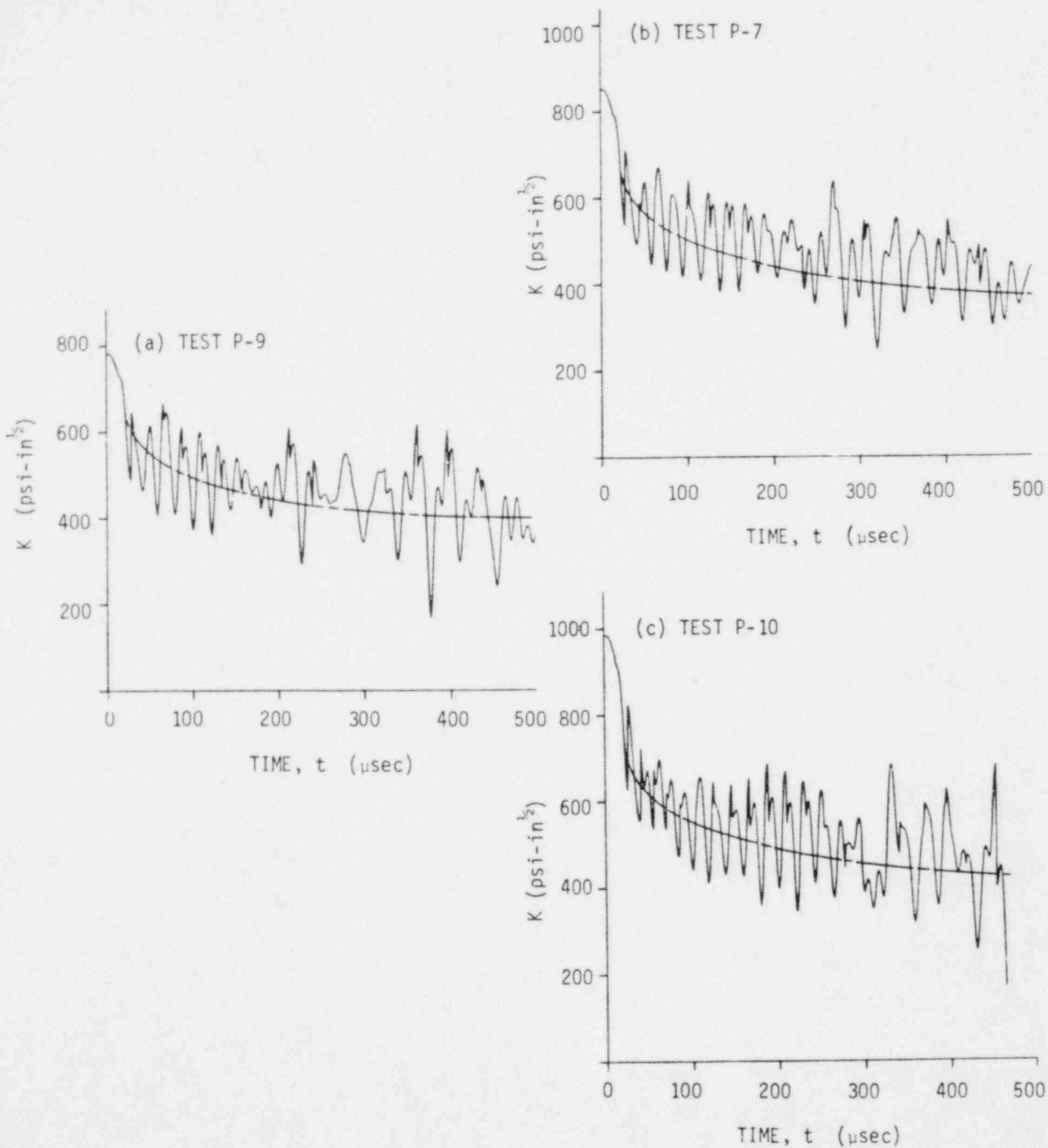
Fig. 4.8 SAMCR Results for Stress Intensity as a Function of Time for
Tests P-9, P-7, and P-10

175
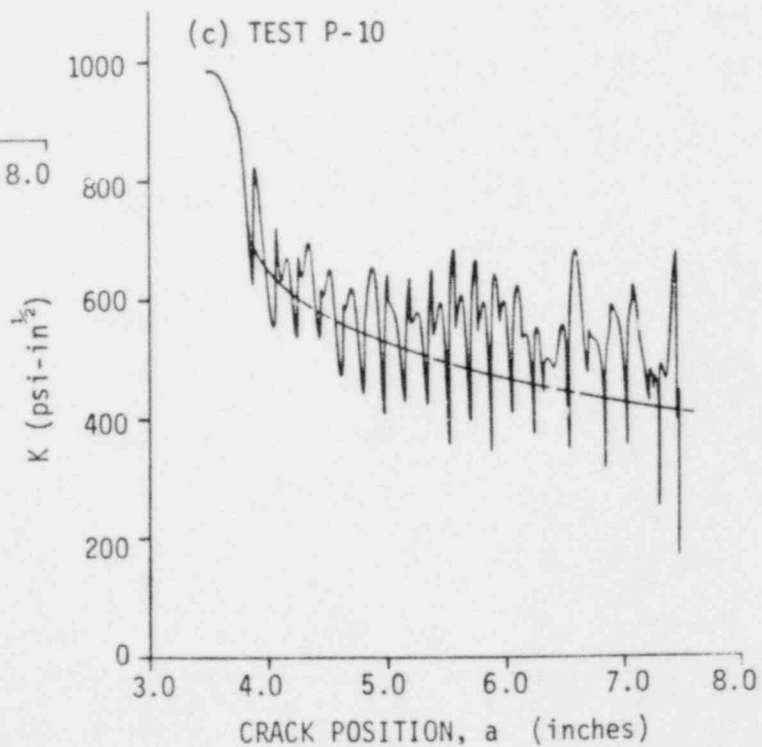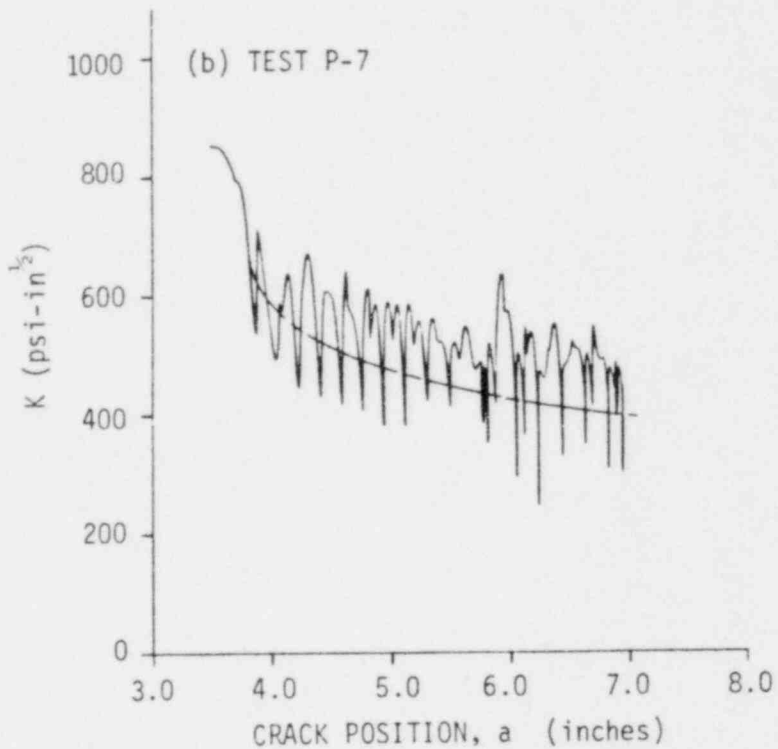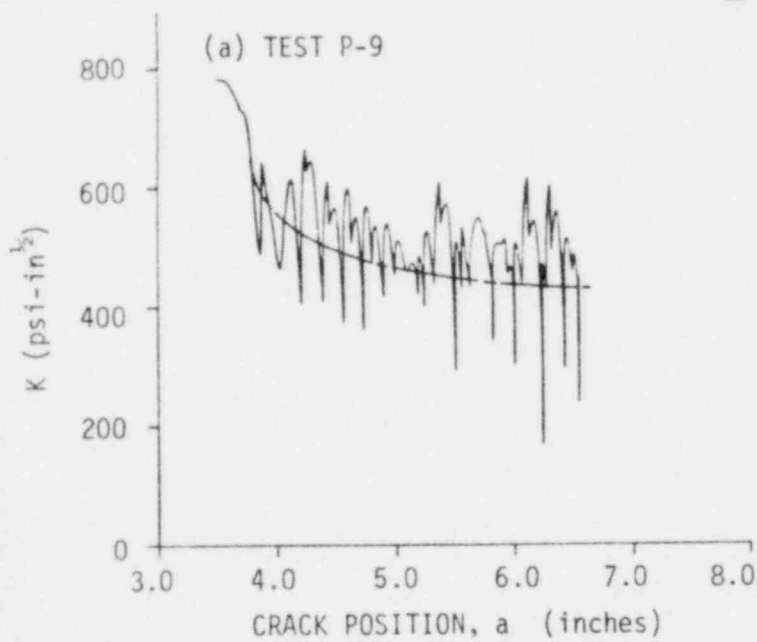
Fig. 4.9 SAMCR Results for Stress Intensity as a Function of Crack
Position for Tests P-9, P-7, and P-10
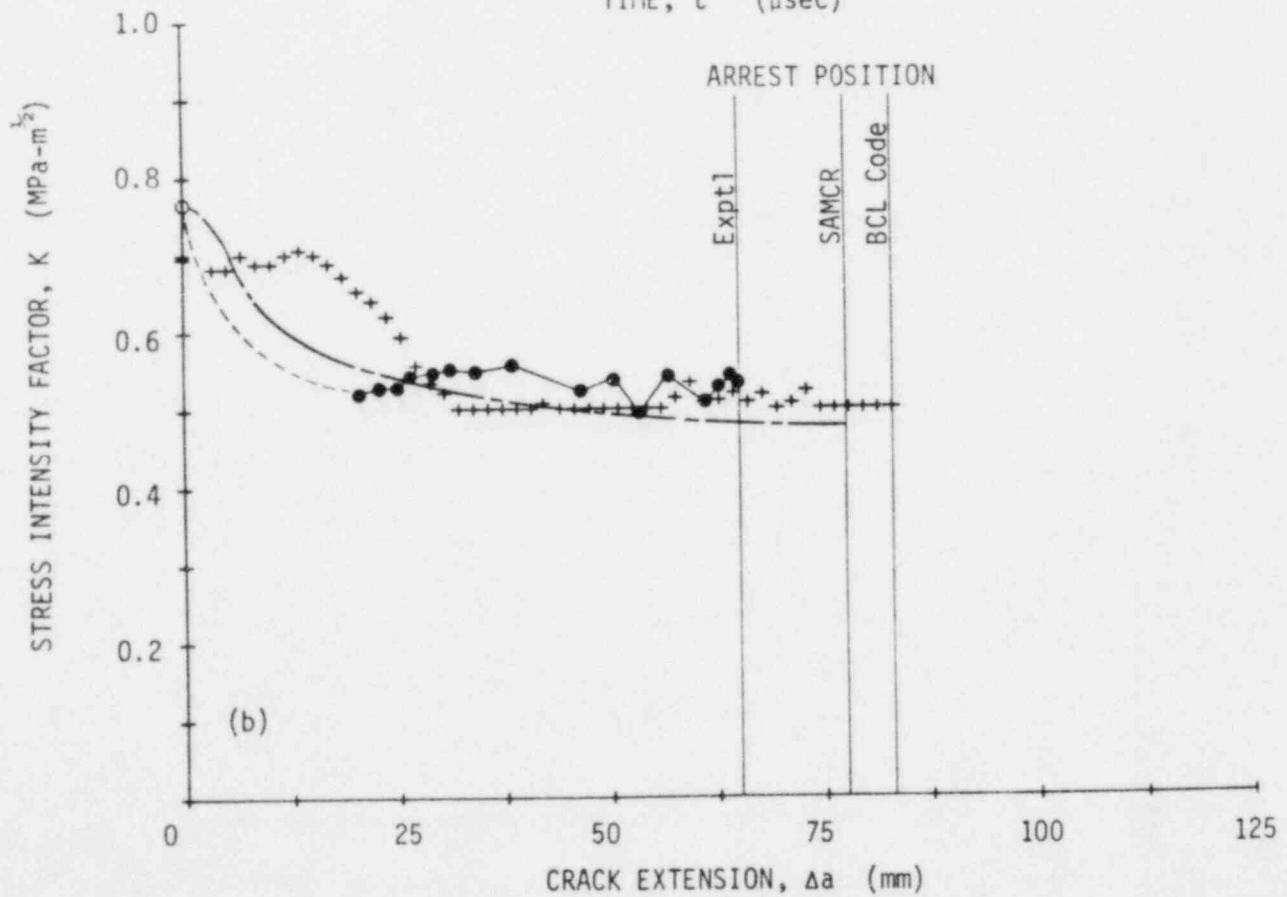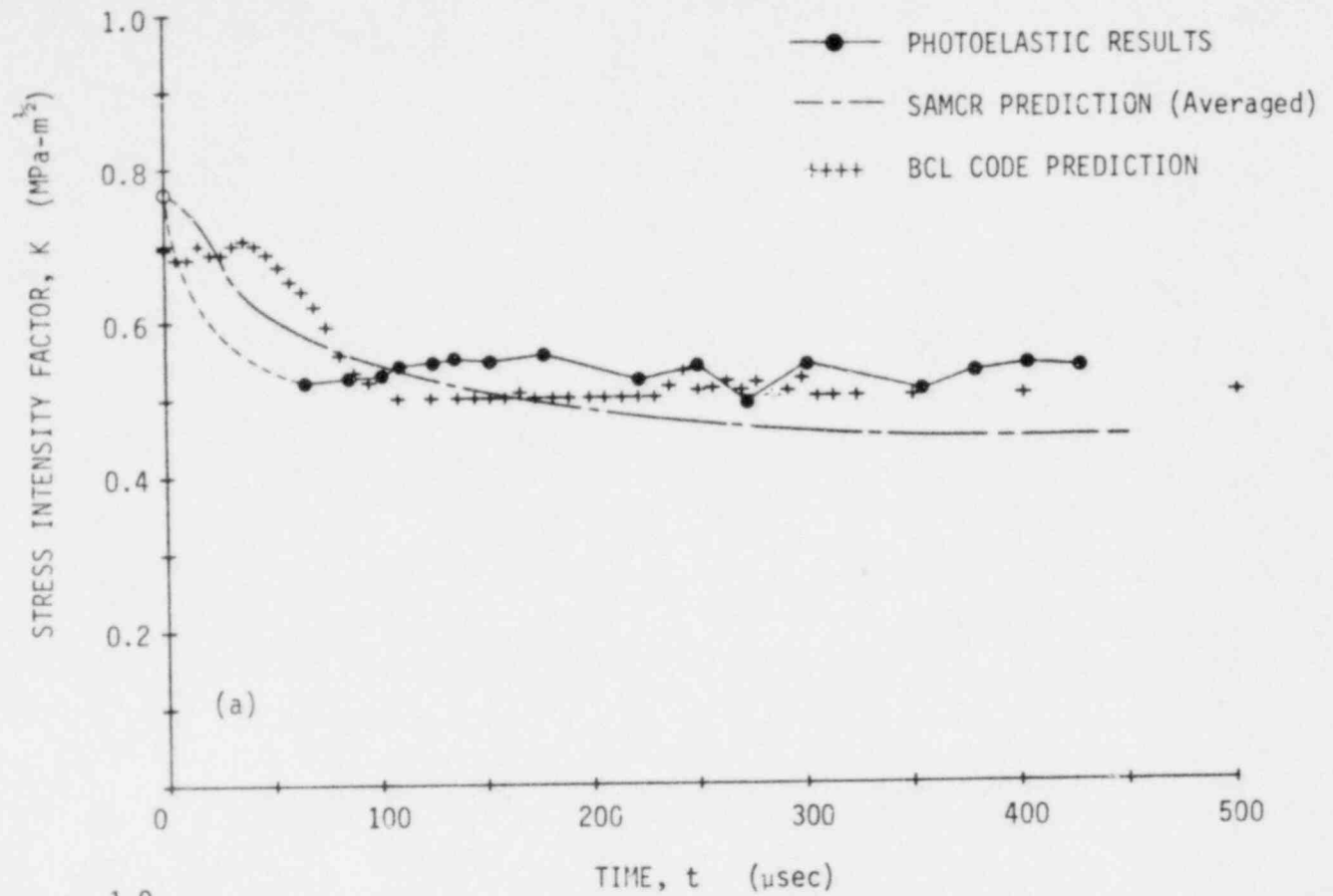
Fig. 4.10 Observed and Predicted Stress Intensity Factors for Test P-9
(a) as a Function of Time; and (b) as a Function of Crack Extension

177
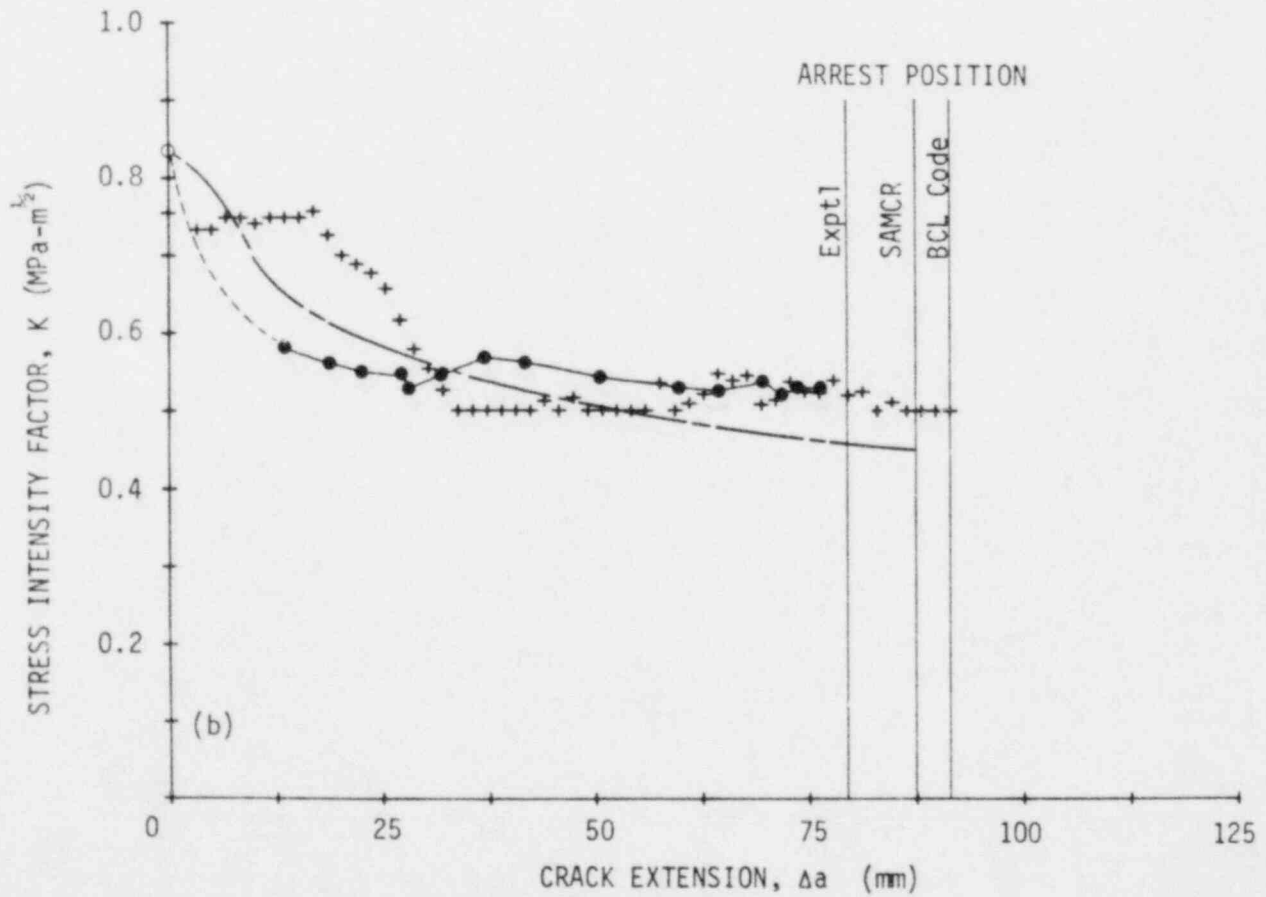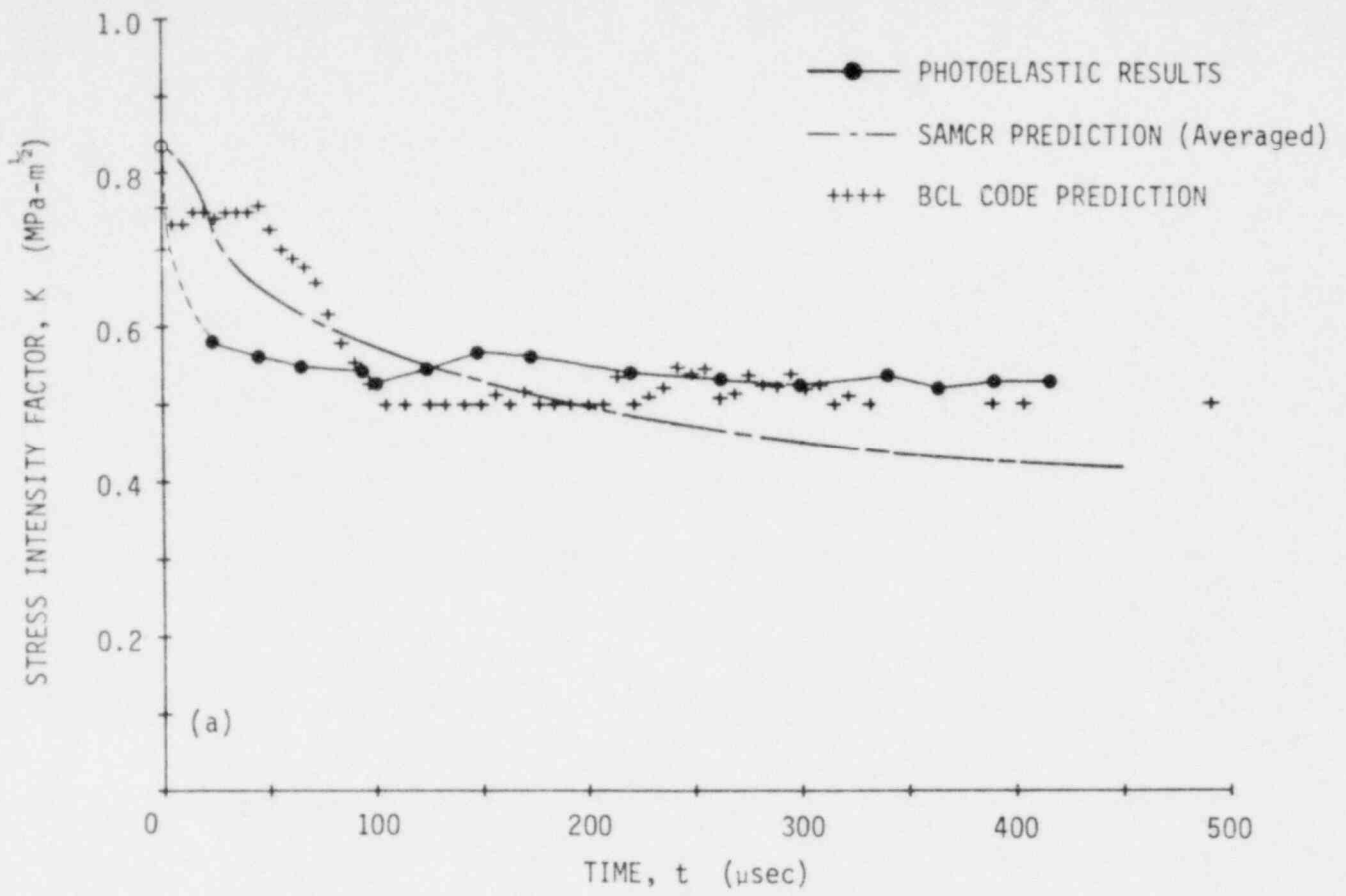
Fig. 4.11 Observed and Predicted Stress Intensity Factors for Test P-7
(a) as a Function of Time; and (b) as a Function of Crack Extension

178
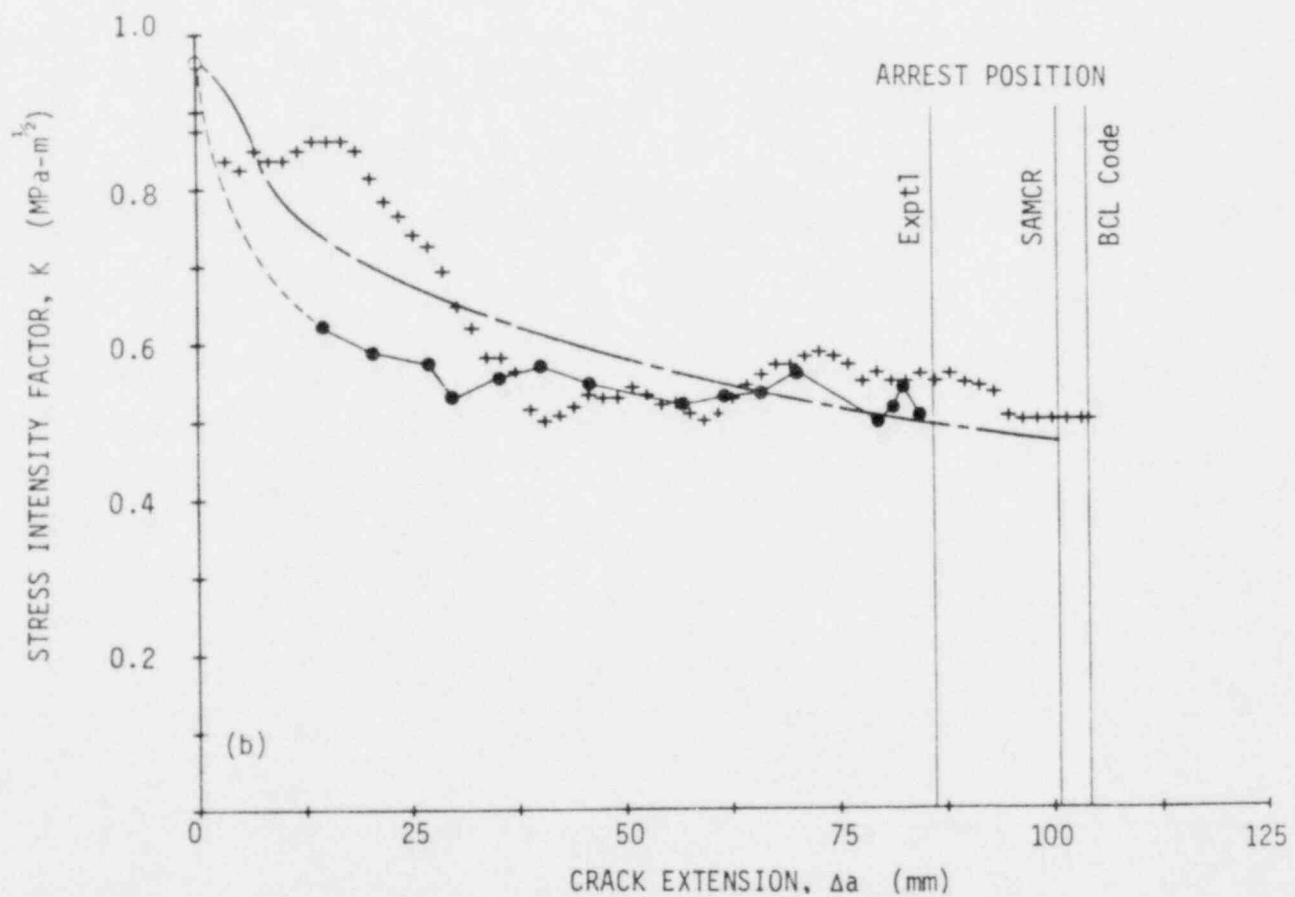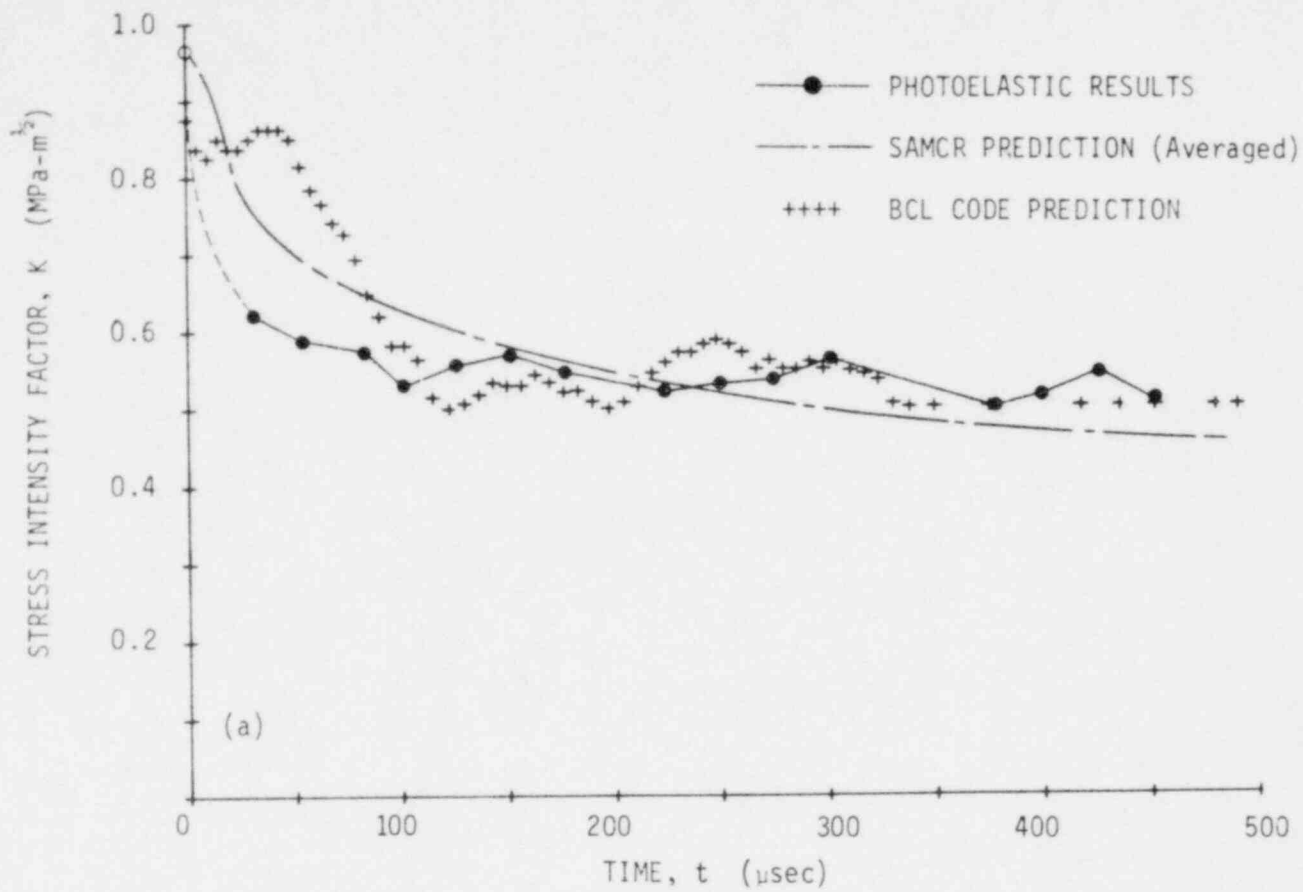
Fig. 4.12 Observed and Predicted Stress Intensity Factors for Test P-10
(a) as a Function of Time; and (b) as a Function of Crack Extension

179
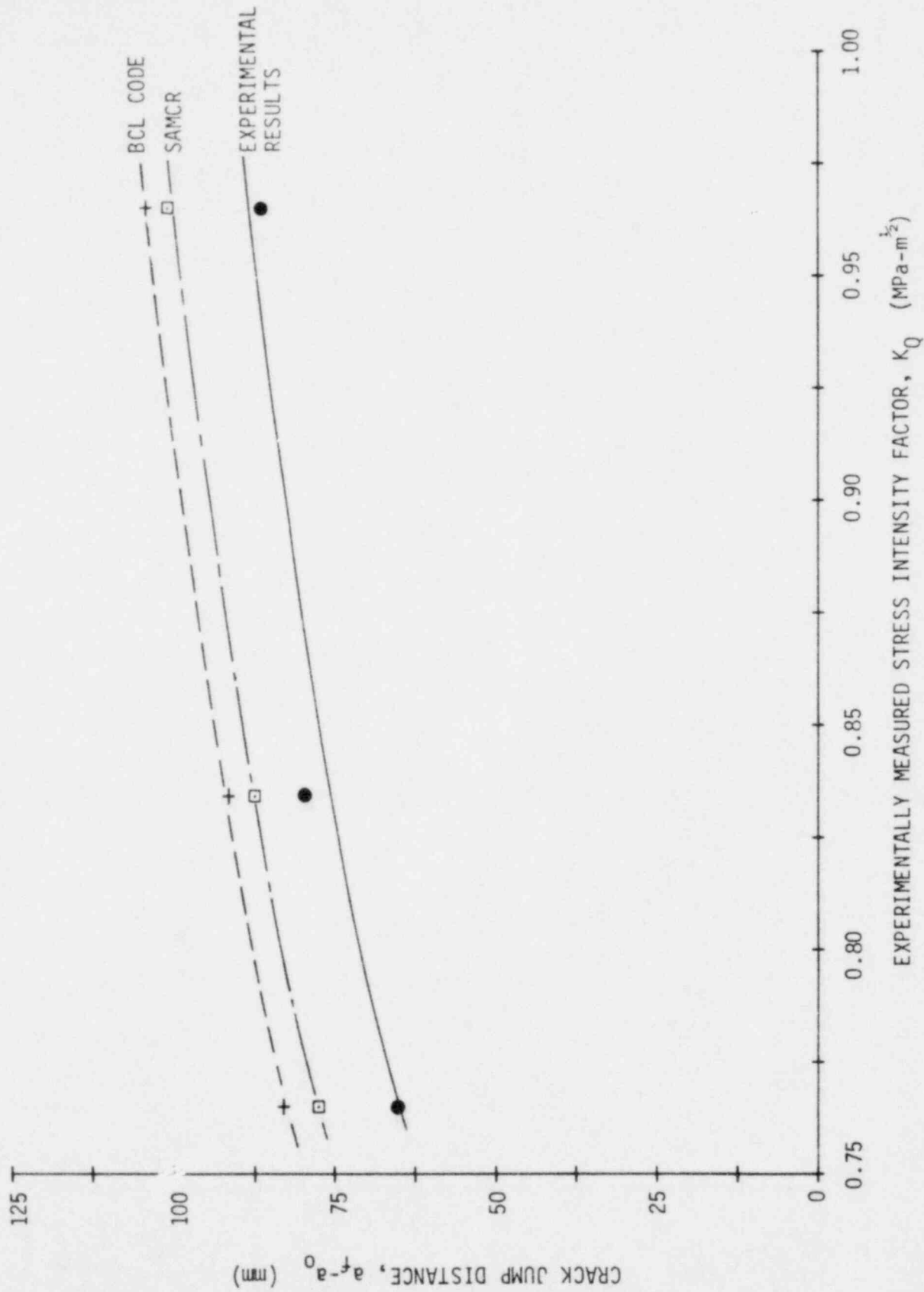
Fig. 4.13 Observed and Predicted Crack Jump Distances as a Function of the Experimentally Measured K_Q Value

180

5.   Determination of K-å Relations in 4340 Steel With Birefringent Coatings

5.1   Introduction

By using a split-birefringent coating technique coupled with high
speed photography, it was possible to record the dynamic isochromatic
fringe patterns associated with crack propagation and arrest in 4340
steel fracture specimens. From these isochromatic fringe patterns the
associated dynamic stress intensity factor, K_D, was calculated and a
K-å relation developed for three different heat treatments of aircraft
quality 4340 steel.

The use of birefringent coatings to study dynamic fracture in
opaque materials is not new, but the results of previous researchers [5.1-5.4]
have been primarily qualitative in nature. When a continuous sheet of
coating material is placed over the base material, an uncertainty arises
as to whether the observed response in the coating is dominated by the
fracture of the base material or by the plastic deformation and fracture
of the coating itself [5.5]. A split birefringent coating technique--a
separate sheet of birefringement coating bonded onto either side of the
anticipated crack path--has been developed at the University of Maryland.
This technique alleviates the uncertainty of the coating response encountered
by previous investigators.

This split birefringent coating technique has been developed [5.5] and
has been preliminarily applied to study fracture in 4340 steel [5.6, 5.7]. The
preliminary work with 4340 steel resulted in only limited information
about the K-å relation. Problems were encountered in a uniform heat treat-
ment between specimens and only a limited number of successful tests were
conducted. This chapter describes an extension of the preliminary work and
presents the K-å relation for three specific heat treatments of aircraft
quality 4340 steel.

181

5.2 Experimental Procedure

The experimental procedure involves taking high speed photos of the isochromatic fringe patterns in the birefringent coating during the fracture event. A schematic of the experimental set-up showing the fracture specimen and loading fixture, the camera, and the flash lamps is shown in Fig. 5.1.

5.2.1 Specimens and Loading Fixture

Thirty fracture specimens were made from hot rolled, annealed, aircraft quality 4340 steel. The specimen geometry is similar to the MRL proposed compact transverse wedge loaded crack arrest toughness specimen [5.8] and is shown in Fig. 5.2. Two different face groove depths were used. The shallow grooves ($B_N/B = 0.875$) were used with the harder more brittle specimens to minimize effects of the groove on the surface strains. The more normal face groove depth of $B_N/B = 0.750$ was only used on the more tempered, tougher specimens.

The required stress-intensity factor for initiation K_Q, was varied by altering the shape and sharpness of a chevron starter notch. These chevron notches were sawn into the specimens with an abrasive cut-off saw after heat treatment. Throughout the testing multiple loading cycles and pre-compression were avoided to prevent isochromatic fringes due to residual stresses.

Twenty compact specimens with the shallow face grooves were batch heat treated in lots of ten to hardness levels of $R_c 50$ and $R_c 46$. The typical heat treatment pro. 'ure entailed austenizing the specimens at 820°C for 60 minutes, oil quenching, and then tempering at a temperature dependent upon final desired hardness. Unfortunately, quench cracks

developed in the throats of the specimens. It was possible to saw out the majority of these quench cracks, but only at the expense of increasing initial crack length.

The final batch of ten specimens was originally tempered to $R_c 26$. At this level of toughness it was not possible to initiate and propagate a crack from a chevron notch even with residual stresses due to precompression. After two unsuccessful attempts, the final eight $R_c 26$ specimens were annealed and then heat treated to a hardness of $R_c 37$.

One face of the heat treated specimens was sanded and cleaned in preparation for bonding on a birefringent coating. The coating material used was nominally 2 mm thick polycarbonate sheet (PS-1) with reflective backing manufactured by Photoelastic, Inc. Two pieces 120 mm by 140 mm were bonded onto either side of the face groove with the edge of the coating along the face groove machined to have the same slope as the groove. Hysol EA 9810 structural high strength epoxy adhesive was used as the bonding agent.

The specimen was loaded by a transverse wedge and split pin in a specially designed loading fixture as seen in Fig. 5.3. The wedge was forced between the two halves of the split pin with a hydraulic cylinder until crack initiation occurred. The crack opening displacement was monitored with an eddy current displacement transducer (Kaman Model KD-2300-25) mounted at a position 0.25 W above the load line as tentatively specified in the MRL procedure. The signal from the displacement transducer was recorded from 0.235 ms before crack initiation to 10 ms after initiation with a digital memory oscilloscope (Nicolet Explorer III). The record of crack opening displacement was used to calculate the stress intensity

factor at initiation, K_Q, and the stress intensity factor at arrest, K_a, by employing the MRL procedure [5.8].

5.2.2 Camera and Data Recording

A Cordin model 330 A drum camera was used to record the dynamic fringe patterns. Typically for these experiments a framing rate of 220,000 fps was used. This was the maximum rate possible to prevent over-write with the flash lamp system used. (The camera lens remained open during the test). Faster framing rates were tried with a blast shutter, but the technique was not used due to increased complexity and only marginal gain in data quantity.

The exposure time for the camera is a function of framing rate and width of framing stop. For these experiments it is estimated that the exposure duration is about 1.5 µs. Kodak 2495 RAR high speed negative film was used with a Kodak No. 8 filter to record the images. This film is orthochromatic and sensitive to wavelengths less than about 600 nm. The No. 8 filter passes light with wavelengths greater than 500 nm. Thus the wavelength of light used to record the fringe patterns peaked at 550 nm with a bandwidth of about 100 nm.

A special high-intensity, short duration xenon flash lamp system was built to illuminate the specimen. The two lamps in parabolic reflectors were placed on either side of the specimen just out of the field of view of the camera. The initial trigger signal to fire the lamps occurred with the breaking of a conductive line placed at the tip of the machined crack starter notch. Within 15-20 µs of the trigger signal the lamps developed sufficient intensity to expose the film. Assuming a typical crack propagation velocity in the early part of the event of between 500-1,000 m/s in steel,

184

this means that the crack has traveled between 8 and 20 mm before the camera can record any pictures. The duration of this intensity was about 250 μs.

5.2.3 Determination of Stress Intensity Factor

A typical high-speed photograph of the isochromatic fringe pattern in the birefringent coated 4340 steel specimen is shown in Fig. 5.4. The crack is traveling downward at a velocity of 439 m/s. The second order fringe loops are indicated in the photograph, as is the crack tip position.

The stress intensity factor was determined from fringe loop information located further than 3 face groove depths away from the crack tip. The region close to the groove was eliminated due to the groove influence on the surface strains. Typically fringe loop information was obtained at distances from 20 to 40 mm away from the crack tip. Distances greater than 40 mm were avoided due to possible boundary influences.

Based on the work of Sanford [5.9], an overdeterministic two-parameter method was developed to directly determine the stress-intensity factor in the steel from the isochromatic fringe patterns. The method is a least squares fitting of a theoretical fringe loop of order N, for a calculated value of K, to twenty data points (r,θ) located on the experimentally determined fringe loop of the same order N.

The data processing was performed on an optical digitizer (Talos, Inc. Model BL 611-B) interfaced with a desktop computer (HP-9815A) and plotter (HP-7225). Twenty data points from a particular fringe order were read from an isochromatic photograph with the digitizer. The computer then iteratively solved for K and fit the theoretical fringe loop to the data points in a least squares manner. Then the computer plotted the shape of the theoretical loop and the location of the twenty input data points.

With this information it was possible to visibly confirm that the best fit theoretical fringe loop, for some calculated value of stress-intensity-factor K, agreed with the input data points.

The method for determining K used the static near field equations. It was a two parameter method with only K and σ_{ox} as unknowns. It was felt that the errors introduced by not employing the dynamic equations for the stress fields, or the higher order terms, were minimal compared to errors in resolution and accuracy in measuring r and θ from the high speed photographs. Typical data scatter in K from the experiments indicate that the error band is around 10% for the calculation of the stress intensity factor from the birefringent coating isochromatics.

The basic equation for calculating the stress-intensity-factor in the base material from the isochromatic fringe pattern in a birefringent coating is described in detail in References [5.5-5.7]. It is

$$K^S = \frac{E^S}{E^C} \frac{1+\nu^C}{1+\nu^S} \left(\frac{B}{B_N}\right)^{\frac{1}{2}} K^C \tag{5.1}$$

where the superscripts s and c refer to the steel and coating respectively, and   E is Young's Modulus

     ν is Poisson's Ratio

     B is the ungrooved thickness and

     B_N is the thickness B, minus the groove depths.

K is the stress intensity factor in the coating and can be related to the isochromatic pattern in the neighborhood of the crack tip by the 2 parameter (K and σ_{ox}) approximation

$$\left(\frac{Nf_\sigma}{2t}\right)^2 = \frac{K^2}{2\pi r} \sin^2\theta + \frac{2\sigma_{ox}K}{\sqrt{2\pi r}} \sin\theta \sin\frac{3\theta}{2} + \sigma_{ox}^2 \tag{5.2}$$

186

where N is fringe order number

t is thickness of coating

f_σ is the stress optic coefficient of the coating.

The crack mouth opening at 0.25 W above the load line was continually monitored during the event. From this crack mouth opening data and knowledge of the final crack position at arrest, the stress intensity factor after arrest K_a could be calculated using the MRL procedure [5.8]. This procedure was modified from that specified in reference [5.8] due to errors in the original procedure relating displacement at 0.25 above the load line to the displacement at the load line. From the MRL procedure the stress intensity factor at arrest is

$$K = \left(\frac{KW^{\frac{1}{2}}}{E\delta_L}\right)\left(\frac{\delta_L}{\delta_{0.25W}}\right)\delta_{0.25W}\ \frac{E}{W^{\frac{1}{2}}}\ \left(\frac{B}{B_N}\right)^{\frac{1}{2}} \tag{5.3}$$

where $\left(\frac{KW}{E\delta_L}\right)^{\frac{1}{2}}$ is a dimensionless stress intensity factor numerically determined for the compact specimen and obtained from reference [5.10]

δ is the crack opening displacement and the subscripts

L and 0.25W refer to the load line and 0.25W above the load line.

$\frac{\delta_L}{\delta_{0.25W}}$ is the ratio of displacements and assumed to be a constant equal to 0.77 [5.11].

5.3 Experimental Results

The experimental results for the different heat tints of the 4340 steel will be presented separately.

5.3.1 R_c50 - Specimens

All of the ten R_c50 specimens developed a severe quench crack in the specimen throat due to a sharp chevron starter notch that was machined

into the specimen before heat treating. Attempts to remove this crack by sawing out additional material and increasing the initial crack length a_o were only marginally successful. Four specimens were lost due to severe quench cracking and cracks that travelled out of the face grooved region during testing. Three specimens had short crack jumps of only about 30 mm due to initiation at quench cracks not successfully removed. These distances were too short for the lamps to come up to sufficient intensity for photos of the run. Dynamic isochromatic fringe information was obtained for two running cracks. In both of these specimens, crack arrest did not occur.

The records of stress-intensity-factor and crack tip location as a function of time for these two tests are presented in Figs. 5.5 and 5.6. Crack length in mm and stress-intensity-factor in MPa-m$^{\frac{1}{2}}$ are plotted on a common vertical axis. Relative time in microseconds is plotted horizontally. Relative time must be used because the camera lacks the ability to record a zero reference mark. The camera only knows when the flash lamps reach sufficient energy to expose the film.

In test 407, Fig. 5.5, the crack is slowing from 845 m/s to 688 m/s during the recorded event. The stress-intensity-factor is holding about constant at 90 MPa-m$^{\frac{1}{2}}$. Information gathering was terminated at a crack length of about 165 mm due to approach of the free boundary (W=255 mm) and the limited field of view of the camera. In test 408, Fig. 5.6, the crack was traveling at 639 m/s and K was again around 90 MPa-m$^{\frac{1}{2}}$.

A summary of the R_c50 specimen data used in the calculation of K_a by the MRL Procedure is presented in Table 5.1. The average arrest toughness K_a for three tests was found to be 49.5 MPa-m$^{\frac{1}{2}}$ with a standard

188

Table 5.1

R_c50 Specimen Data for Calculation of K_a

$(W = 210mm; B/B_N = 8/7; B = 26.1mm)$

Specimen No.	Δa (mm)	a_o/W	a_f/W	δ_o (mm)	δ_f (mm)	K_Q (MPa-m$^{\frac{1}{2}}$)	K_a (MPa-m$^{\frac{1}{2}}$)	Comments
403	31.0	0.355	0.510	0.508	0.533	62.9	50.9	Photos of post arrest only (multiple arrest)
404	24.9	0.367	0.485	0.511	0.514	61.8	49.6	Photos of post arrest only
405	110.9	0.367	0.896	1.001	1.237	121.7	-	Lamps failed. a_f/W too large for valid K_a test.
406	14.9	0.444	0.515	0.505	0.521	54.1	48.0	Δa too small for valid test. Photos of post arrest only.
407	-	0.433	-	1.024	-	111.6	No Arrest	Good photos of run
408	-	0.511	-	1.900	-	178.8	No Arrest	Good photos of run

Average K_a = 49.5 MPa-m$^{\frac{1}{2}}$

Standard deviation = 1.5 MPa-m$^{\frac{1}{2}}$ (2.9%)

189

deviation of less than 1.5 MPa-m$^{\frac{1}{2}}$ (3%). The displacement records for up

to 10 ms after initiation at 0.25 W above the load line are presented

in Figs. 5.7 - 5.9 for tests 403, 404, and 406. In each of these tests

the crack initiated at a relative low K_Q value, about 60 MPa-m$^{\frac{1}{2}}$, and

the crack jump distance was too short for the lamps to come up to suffi-

cient intensity for photographic records of the run phase. In all three

records the change in crack mouth opening was minor. The largest change in

crack opening displacement was 0.025 mm. Even at 10 m the opening dis-

placements had not completely stabilized with some ringing of about a kilo-

hertz frequency still present.

In comparing post arrest photos taken about 1 minute after the event

to photos taken by the high speed camera, it was discovered that the crack

in test 403 had reinitiated after the high speed camera had stopped record-

ing. In this particular test the crack first arrested before the lamps

had come up to full intensity, less than 15 μs, and then reinitiated before

post arrest photos were taken, approximately 2 minutes. This additional

crack travel was 10 mm in length and accounted for 1/3 of the total measured

crack jump Δa. This was the only test of this heat treatment that experi-

enced crack arrest and then reinitiation. The reinitiation was probably

due to an increase in load from the load fixture after the first crack

extension. This particular test also had the greatest amplitude of crack

mouth opening oscillations. These oscillations are still very much present

at 10 ms in this test whereas they had died out in the others.

5.3.2 R$_c$46 Specimens

Six successful tests were conducted with the R$_c$46 specimens. Un-

fortunately in two tests the photoelastic results were lost due to

equipment failure. For the successful tests, the plots of crack length
and stress intensity factor as a function of time are presented in Figs.
5.10 - 5.13.

Test 412, Fig. 5.10, was a run arrest event with the crack traveling
at 636 m/s just before arrest at a final crack length of 160 mm. Marked on
the plot is the actual measured crack length a_f, defined as being the average
of the two quarter-thickness positions and the mid-section position. This
value is very close to the apparent crack length indicated by the iso-
chromatic fringe loops in the birefringent coating. Throughout this test K
was slowly decreasing. From the photoelastic data, K at arrest was about
92 MPa-m$^{\frac{1}{2}}$, while K_a as determined from the MRL procedure was found to be
63 MPa-m$^{\frac{1}{2}}$. This difference of 29 MPa-m$^{\frac{1}{2}}$ between the two arrest toughnesses
was greater in this test than for any other test conducted.

Test 413, Fig. 5.11, was another run arrest event. During this
test the crack velocity approaching arrest was 228 m/s, about 1/3 that of
the previous test. There was a large amount of data scatter in the cal-
culation of K for this test. The values varied as much as ±15% between
successive frames during crack propagation. The calculated arrest tough-
ness K_a from the MRL procedure of 78 MPa-m$^{\frac{1}{2}}$ agrees quite well with the
photoelastically determined K at arrest of about 78 MPa-m$^{\frac{1}{2}}$.

Test 415, Fig. 5.12, was again a run arrest event. The data scatter
in K is not as great in this test as the last one. The arrest toughness
K_a (MRL) was 75 MPa-m$^{\frac{1}{2}}$, slightly greater than the observed K at arrest
of 70 MPa-m$^{\frac{1}{2}}$.

Test 418, Fig. 5.13, was a run event only, with a crack velocity
of 762 m/s. The mean K observed was about 85 MPa-m$^{\frac{1}{2}}$ with a scatter of
less than ±10% during the observed event.

A summary of the R_c46 specimen data is presented in Table 5.2. For the four valid arrest tests the average K_a (MRL) is 70.1 MPa-m$^{\frac{1}{2}}$ with a standard deviation of 7.5 MPa-m$^{\frac{1}{2}}$ (11%).

The crack opening displacement versus time records are presented in Figs. 5.14 - 5.18 for all the R_c46 tests except 418 which was a run event only. Some of the arrest specimens did experience a relative large change in opening displacement during propagation while others did not. Tests 412 and 413 experienced about a 0.12 mm change while tests 414 and 415 experienced less than 0.04 mm change. There was no correlation between this observation and the calculated values of K_a. Note also that in all cases arrest had occurred by 150 µs and that the displacement reading did not start oscillating about the final value until about 1 ms. The large oscillations in test 410, Fig. 5.14, are due to the fact that $a_f/W = 0.9$ and there is little material holding the two halves of the specimen together.

5.3.3 R_c37 Specimens

Five successful tests were conducted with the tougher R_c37 specimens that had the deeper face grooves. Two tests, 420 and 423, were short run-arrest tests where the flash lamps did not reach sufficient intensity soon enough to catch any crack propagation. Figs. 5.19 and 5.20 show the post arrest behavior of K in these two tests. Indicated on the figures is the final measured crack length a_f from the heat tinted specimens. In both cases the crack grew about an additional 20 mm in length between initial arrest at less than 15 µs and 1-2 minutes after initiation when static post arrest photos were taken. During this period of time the load was assumed to be constant.

Table 5.2

R_c46 Specimen Data for Calculation of K_a

(W = 210mm; B/B_N = 8/7; $B\cdot$ = 26.1mm)

Specimen No.	Δa (mm)	a_0/W	a_f/W	δ_0 (mm)	δ_f (mm)	K_Q (MPa-m$^{\frac{1}{2}}$)	K_a (MPa-m$^{\frac{1}{2}}$)	Comments
410	80.4	0.511	0.899	1.509	1.582	142.0	–	Lamps failed. a_f/W too large for valid K_a test
412	58.3	0.483	0.761	0.986	1.128	97.9	63.3	Good run-arrest photos
413	64.0	0.373	0.679	0.925	1.151	112.5	77.8	Good run-arrest photos
414	48.9	0.510	0.743	1.041	1.074	97.9	63.9	Run-arrest, lost photos
415	63.2	0.371	0.673	1.046	1.087	127.2	75.2	Good run-arrest photos
418	–	0.400	–	1.407	–	162.2	No arrest	Good run photos

Average K_a = 70.1 MPa-m$^{\frac{1}{2}}$

Standard deviation = 7.5 MPa-m$^{\frac{1}{2}}$ (10.7%)

193

The short term crack opening information for Test 423 was lost but the crack opening for Test 420 increased only ^05 mm between initiation and 10 ms later after arrest. There were no perceptible oscillations. It occurred as a steady monotonic increase in crack mouth opening. Long time behavior was monitored on a strip chart. After 1 second the change in crack opening displacement had increased to 0.05 mm and after 3 seconds, maximum change in crack opening displacement of 0.08 mm had occurred.

The stress-intensity-factor and crack tip position records are shown in Figs. 5.21 and 5.22 for the two successful run-arrest tests. In test 419, the crack first arrested at a length of about 127 mm. Final arrest was measured from the static post arrest photos and the heat tintε¹ specimen halves at 160 mm. This additional crack extension again occurred after the end of the high speed photographic recording. This same additional extension behaviour is noted in Fig. 5.22 for Test 421.

In test 419, Fig. 5.21, the observed K at first arrest was about 135 MPa-m$^{\frac{1}{2}}$. Note how K decreases to a minimum value of about 119 MPa-m$^{\frac{1}{2}}$ at a relative time into the event of 180 μs. The stress intensity factor then starts to increase. At the end of the recording period, 300 μs, the stress-intensity-factor has increased to 130 MPa-m$^{\frac{1}{2}}$ and it appears to be still increasing in value. This increase in the stress-intensity-factor must have re-initiated the crack after the high speed recording had ended.

In test 421, Fig. 5.22, the observed K at first arrest was again about 135 MPa-m$^{\frac{1}{2}}$. In this test K decreased to a minimum of about 103 MPa-m$^{\frac{1}{2}}$ before rapidly increasing in value. Observation was terminated before re-initiation. The final measured crack length indicated that this crack propagated another 15 mm.

194

In one specimen the crack failed to arrest. Fig. 5.23 presents the records of K and crack tip position for this test. When the observation was first started the crack was traveling at 687 m/s at a K of about 130 MPa-m$^{\frac{1}{2}}$. The crack subsequently increased in velocity to 868 m/s and the increased K was 138 MPa-m$^{\frac{1}{2}}$.

A summary of the R_c37 specimen crack opening displacement data is presented in Table 5.3. All run-arrest tests of this heat tint exhibited an early arrest no later than 100 μs after initiation. All specimens then reinitiated sometime after 300 μs when observation with the high speed camera terminated and before static post arrest photos were taken at about 1-2 minutes. Two crack lengths, a_f/W, are presented in the table. The number in parentheses is the arrested crack length measured from the high speed photos of the isochromatic fringe patterns. The other length is the arrested length measured from the heat tinted specimens. This second, longer length was found to agree with the static post arrest photos. The crack opening displacement at arrest δ_f was measured two ways. The number in parentheses is the value at 10 ms after initiation measured with the digital oscilloscope while the other number is that measured from a strip chart at 2-3 seconds after initiation. Two arrest toughnesses are calculated, one for the intermediate arrested crack length and crack opening displacement and one for the final longer length and larger opening displacement. The average arrest toughness K_a for four tests, as calculated from the final longer crack lengths and opening displacements, was 117.1 MPa-m$^{\frac{1}{2}}$ with a standard deviation of 13.8 MPa-m$^{\frac{1}{2}}$ (12%).

Table 5.3

R$_c$ 37 Specimen data for Calculation of K$_a$

(W = 210mm; B/B$_N$ = 4/3; B = 26.1mm)

Specimen No.	Δa (mm)	a$_o$/W	a$_f$/W	δ$_o$ (mm)	δ$_f$ (mm)	K$_Q$ (MPa-m$^{\frac{1}{2}}$)	K$_a$ (MPa-m$^{\frac{1}{2}}$)	Comments
419	(53.0)* 84.1	.363	(.614) .764	1.697	(1.842) 1.981	210.1	(153.9) 119.5	Good run-arrest photos; multiple arrests.
420	(27.0) 45.1	.378	(.505) .594	1.034	(1.039) 1.125	123.4	(106.4) 98.1	Post arrest photos only; multiple arrest.
421	(59.0) 74.2	.358	(.638) .712	1.577	(1.887) 1.910	195.3	(150.1) 131.2	Good run-arrest photos; multiple arrest.
423	46.6	.357	.579	-	1.346		119.5	Post arrest photos only; multiple arrest.
424	-	.334	-	1.956	-	275.0	No arrest	Good run photos.

Average K$_a$ = 117.1 MPa-m$^{\frac{1}{2}}$

Standard deviation = 13.8 MPa-m$^{\frac{1}{2}}$

*--( ) denotes intermediate arrest values.

196

5.4   Discussion of Birefringent Coating Results

The overall accuracy of the split birefringent coating technique must be understood before discussing the implications of the test results. To obtain a number for this accuracy is difficult. The greatest problem with the technique is obtaining a distinct isochromatic fringe pattern. To avoid problems associated with the delayed time response of the coating during crack propagation, thin coatings were employed. Thin coatings also prevented edge problems encountered with thick coatings where data can not be taken near coating boundaries. By using thin coatings, the maximum useable fringe order was 1.5 to 2. These low order fringes always appear in photographs as very broad fringes. It is difficult to locate the fringe maximum. The use of a 20 data point technique hopefully averages out some of the error associated with locating the fringe maximum.

Location of crack tip position was difficult due to the presence of the groove and absence of birefringement material. In the R_c50 and R_c46 specimens the crack tip was assumed to be located where an extension of the loops intersected the crack line or where a loop became tangent to the crack line. In the R_c37 specimens there was an appreciable fringe disturbance due to a deeper groove and plastic zone near the crack tip. The crack tip was located by a distinct zero order fringe in this fringe disturbance. These crack tip location techniques were checked by measuring crack lengths from the static post arrest photos and then comparing to the measured crack lengths from the heat tinted specimen halves. As could be seen in the figures showing the crack tip location for the various tests, the location accuracy of the crack tip was only on the order of ±1-2 mm. This was

reasonable since the camera resolution was only 1 line pair/mm.

In an attempt to determine errors associated with an erroneous crack tip location, several typical high speed photographs were analyzed while shifting the assumed crack tip 2 mm. For the same sets of 20 data points, K varied less than 3%. Thus for the typical fringe patterns encountered K was relatively insensitive to crack tip location. The source of major error was in locating the fringe contour and the 20 data points required.

From the various figures showing K as a function of time, general trends are very definite. The variation in K between adjacent frames, taken typically 4.63 µs apart, is rarely greater than 10%. Thus as a first approximation for the accuracy of this technique, 10% is a resonable answer.

5.4.1 Stress Intensity Factor at Arrest

In the R_c50 specimens all the cracks arrested before the camera could start taking pictures. Thus all the high speed photos were either post arrest or of a propagating crack that did not arrest. Table 5.4 summarizes again the calculated values of K_a by the MRL procedure. The average K_a was found to be 49.5 MPa-m$^{\frac{1}{2}}$. Test 403 was the only test of this heat tint that experienced an intermediate arrest at a length 10 mm less than the final length. Using this intermediate crack length and the same crack opening displacement taken at 10 ms, the K_a equals 55.4 MPa-m$^{\frac{1}{2}}$. The same crack opening displacement at 10 ms was used for both calculations since it was not known nor was it apparent in the displacement record when the crack jumped the final 10 mm.

In the R_c46 heat tint, there are three photoelastic tests to compare with the K_a values from the MRL procedure. The average K at arrest from

198

Table 5.4

Stress-Intensity Factor, K_a, at Arrest (MPa-m$^{\frac{1}{2}}$)

	Photoelastic data	MRL (Intermediate Arrest)	MRL (Final Arrest)
R_c50 Specimens			
Test 403	-	55.4	50.9
404	-	-	49.6
406	-	-	48.8
Average	-	55.4	49.5
Standard Deviation	-	-	1.5 (2.9%)
R_c46 Specimens			
Test 412	92	-	63.3
413	78	-	77.8
414	(lost)	-	63.9
415	70	-	75.2
Average	80	-	70.1
Standard Deviation	11 (14%)		7.5 (10.7%)
R_c37 Specimens			
Test 419	135	153.9	119.5
420	-	106.4	98.1
421	136	150.1	131.2
423	-	(lost)	119.5
Average	136	137.0	117.1
Standard Deviation	0.7 (0.5%)	26 (19%)	13.8 (11.8%)

199

the birefringent analysis was 80 MPa-m$^{\frac{1}{2}}$ while the average K_a (MRL) for 4 tests was 70 MPa-m $^{\frac{1}{2}}$. This is a difference of 14%. Table 5.4 lists the exact test values. This 14% difference is just barely a true difference when it is realized that both the photoelastic determined and MRL determined K at arrest have a standard deviation of 14% and 10% respectively. There were no intermediate arrests with the specimens of this heat tint.

In the R_c37 specimens, every test experienced an intermediate arrest. Thus there are two values of K_a (MRL) calculated as explained in section 5.3.3 and summarized in Table 5.4. Two photoelastic tests yielded the same arrest toughness of 136 MPa-m$^{\frac{1}{2}}$. The arrest toughness as calculated by the MRL procedure for the final arrested length was 117 MPa-m$^{\frac{1}{2}}$ for 4 tests with a standard deviation of 12%. This value for the arrest toughness is 16% lower than the photoelastic value. Again considering the size of the standard deviation this difference is not that significant. If Test 420 is ignored due to its low values for K_a, the average MRL K_a for three tests becomes 123 MPa-m$^{\frac{1}{2}}$. The difference between the photoelastic and the MRL K_a is then only 10%.

The average for the intermediate arrest K_a value by the MRL procedure is equal to the photoelastic determined value, but the low value of Test 420 is biasing the results. Eliminating Test 420 gives an MRL calculated value of K_a 12% larger than the photoelastic data. This intermediate K_a value calculated by the MRL procedure is questioned due to the uncertainty of measuring the crack opening displacement due only to the intermediate crack length. This intermediate COD was measured 10 ms after initiation and according to the K records, re-initiation probably occurred around 350 µs. A COD could not be measured earlier than 10 ms after initiation due to ringing or oscillations in the specimen. Averaging

200

these oscillations yielded a COD almost constant in value from 1 ms until they were almost damped out at 10 ms.

All four $R_c 37$ arrest specimens experienced an intermediate arrest while only one out of a total of ten $R_c 50$ and $R_c 46$ arrest specimens (including some bad tests where cracks propagated out of the groove) experienced an intermediate arrest. If the reinitiation was caused by continual loading or an increase in the load on the specimen by the load fixture, it would be expected that a higher percentage of the brittle specimens would have also reinitiated. This did not occur.

A possible explanation for the reinitiation of the tougher $R_c 37$ specimens can be found by comparing the fracture surfaces of the $R_c 37$ specimens to those of the $R_c 50$ and $R_c 46$ specimens. A typical $R_c 37$ fracture surface is shown in Fig. 5.24. Note the woody texture and the presence of various ligaments that linked the two specimen halves together at some time during the fracture event. The $R_c 50$ and $R_c 46$ fractures surfaces seen in Figs. 5.25 and 5.26 are very smooth with almost a complete absence of any ligament remains. During crack propagation in the tougher $R_c 37$ specimen, the brittle cleavage crack tip is further advanced than the more ductile tearing of the ligaments. The cleavage crack will eventually arrest when K decreases to some value. When this crack arrests, some ligaments behind the crack tip are still unbroken. If the more ductile breaking of the ligaments is strain rate sensitive, some ligaments will break after the cleavage crack tip has arrested. This late breaking or relaxation of the ligaments behind the crack tip will increase the K at the crack tip. If K is increased enough, the crack will reinitiate. The increase in K at the crack tip as seen in Figs. 5.21 and 5.22 may be due to this

delayed action of ligaments. A future experiment is planned to try and determine whether this is a load frame action or whether it is due to the ligaments. If it is due to a strain rate effect of the ligaments, this could have important implications in quasi-static crack arrest experiments.

5.4.2 K-à Relation for 4340 Steel

A compilation of the stress-intensity-factor as a function of crack velocity data for all the tests of the three different heat treatments is shown in Fig. 5.27. For non-zero velocity, a mean value of the stress-intensity-factor is plotted for each observed crack velocity. The error bars indicate the typical data scatter in K at that velocity. Normally this scatter was on the order of $\pm 5\%$. Two different crack arrest toughness values are shown. The solid data points indicate the values calculated by the MRL procedure and are so noted. The open data points are the photo-elastically determined values.

Two straight lines were fit in a least squares manner to the photo-elastic data for the $R_c 46$ and $R_c 37$ specimens. The slope of the K-à best fit line for the $R_c 37$ material is steeper than for the harder, more brittle $R_c 46$ material, as can be seen in Fig. 5.27a.

A straight line was found to be the best fit to the data even though it is expected that at higher velocities the slope would start to decrease. Unfortunately due to the inherent delay in the flash lamps, it was not possible to photographically record the high initial crack velocities in the compact specimens. From crack tip position records it is estimated that early crack velocities exceeded 2,000 m/s. The maximum photographically recorded velocities were less than 1,000 m/s, and from the data it appears that the roll-over in the K-à curve for the $R_c 46$ and $R_c 37$ material has not yet

been reached.

No attempt was made to draw a line through the R_c50 points due to the limited amount of data. The only data obtained was for two specimens with cracks that did not arrest. These points are shown as solid circles and should not be grouped with the open squares which are for the R_c46 specimens. The R_c50 specimens showed a distinctly different fracture surface appearance and a distinctly different arrest toughness as computed by the MRL procedure.

Kobayashi [5.6] had previously obtained some K-à data for 4340 steel of hardness R_c50 using the split birefringent coating technique. His original raw data was re-examined and is shown in Fig. 5.27b along with the R_c50 data from the current series of tests. Due to the grouping of the data points between 600 and 800 m/s, it appears that this particular heat treatment is reaching the plateau of the K-à curve. A parabolic curve was the best fit to the combined data and is shown in the figure. Also included in this figure are the linear best fits to the R_c46 and R_c 7 data for comparison.

5.5 Conclusions

Three different heat treatments of aircraft quality 4340 steel crack arrest specimens were tested using a split birefringent coating technique. A high speed camera recorded the isochromatic fringe pattern in the coating material and from this pattern the dynamic stress-intensity-factor in the specimen was calculated.

It was found that each heat treatment exhibited a unique K_a and a unique K-à relation for velocities less than 1,000 m/s. It appears that the tougher the specimen, the more drastically the crack velocity drops for a given decrease in K as the crack approaches arrest. Taking into account data

scatter within individual experiments and between experiments, the difference in K_a measured by the MRL procedure and from the photoelastic data was almost insignificant. In each case though, the MRL calculated value was always less than the photoelastically determined value.

Crack arrest and then re-initiation was observed in all four arrest tests in the toughest specimens ($R_c 37$). It was observed in only one out of ten tests in the more brittle specimens. This arrest and re-initiation could have been caused by late breaking or relaxing of ligaments. This would have important implications on quasi-static crack arrest experiments. Future experiments are planned to check whether this re-initiation was caused by loading system interactions unique to the experimental set up.

References

5.1 Van Elst, H.C., "The Intermittent Propagation of Brittle Fracture in Steel", Trans. of American Inst. Mechn. Engrs., Vol 230, 1964, p. 460.

5.2 Pratt, P.L. and Stock, T., "The Distribution of Strain About a Running Crack", Conf. Proc. of Royal Society (London), Series A, Vol. 285, 1965, pp. 73-82.

5.3. Daniel, I.M. and Rowlands, R.E., "On Wave and Fracture Propagation in Rock", Experimental Mechanics, Vol. 15, Dec. 1975, pp. 449-457.

5.4 Gleen, L.A. and Jaun, H. "Crack Propagation in Rock Plates Loaded by Projectile Impact", Experimental Mechanics, Vol. 18, January 1978, pp. 35-40.

5.5 Der, V.K., Barker, D.B., and Holloway, D.C., "A Split Birefringement Coating Technique to Determine Dynamic Stress Intensity Factors", Mechanics Research Communications, Vol. 5, No. 6, 1978, pp. 313-318.

5.6 Kobayashi, T. and Dally, J.W., "Dynamic Photoelastic Determination of the $\dot{a}$-K Relation for 4340 Alloy Steel", to appear in ASTM STP (1979).

5.7 Irwin, G.R., et al., "Photoelastic Studies of Crack Propagation and Arrest in Polymers and 4340 Steel", Report for Nuclear Regulatory Commission by the University of Maryland Photomechanics Laboratory, November 1978, NUREG/CRO542.*

5.8 Crosley, P.B. and Ripling, E.J., "Guidelines for Measuring K_{Ia} with a Compact Specimen", Prospectus for a Cooperative Test Program on Crack Arrest Toughness Measurement order the auspices of ASTM E24.03.04, July 1977.

5.9 Sanford, R.J., "Application of the Least-Squares Method to Photoelastic Analysis", Presented at 1979 SESA Spring Meeting, San Francisco, May 1979, to be published in Experimental Mechanics, 1979.

5.10 Hoagland, R.G., et al., "Proposed Tentative Method of Test for Fast Fracture Toughness and Crack Arrest Toughness", Submitted to ASTM E24.03.04, July 1977.

5.11 Rosenfield, A.R., et al, "Critical Experiments, Measurements and Analysis to Establish a Crack Arrest Methodology for Nuclear Pressure Vessel Steels", Battelle Columbus Laboratories Progress Report, January to June 1979, NUREG/CRO991, BMI-2036.*

---

*Available for purchase from the NRC/GPO Sales Program, U.S. Nuclear Regulatory Commission, Washington, D.C. 20555, and the National Technical Information Service, Springfield, Virginia 22161.
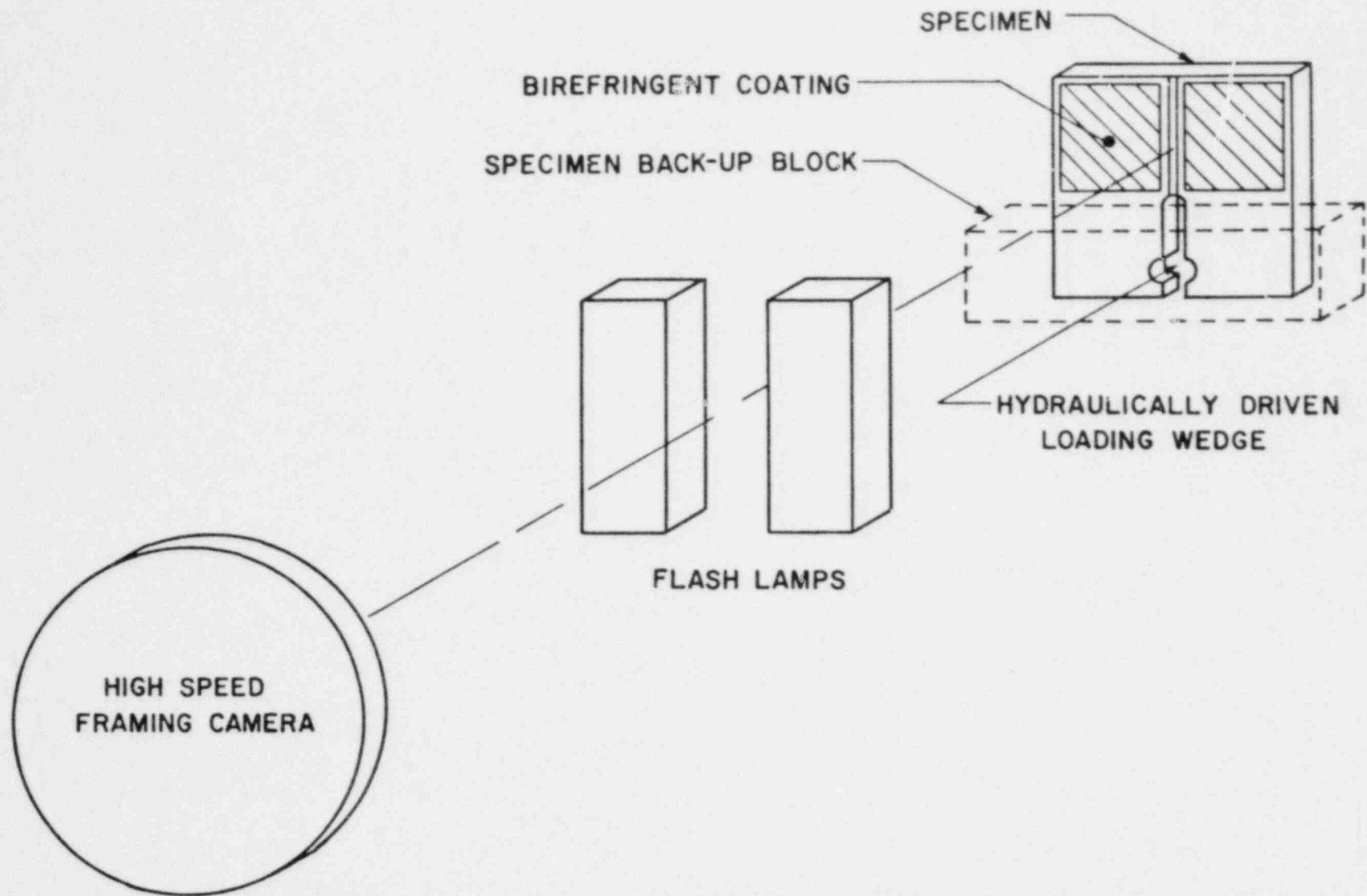
Fig. 5.1   Schematic of Experimental Set-Up.
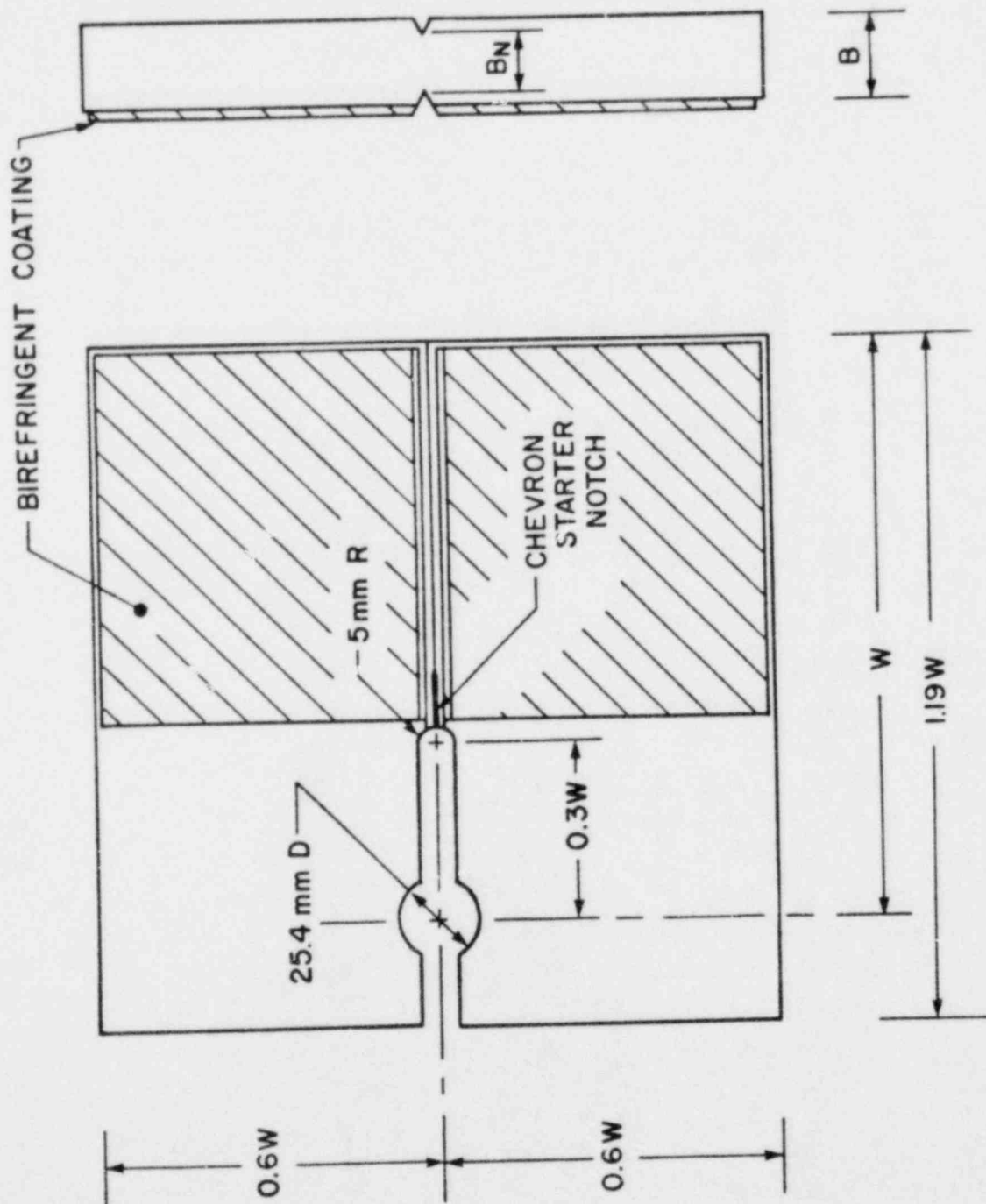
COMPACT TENSION FRACTURE SPECIMEN

W = 210 mm   B = 25.4 mm B/B_N = 8/7 or 4/3

Fig. 5.2 Specimen Geometry.

BIREFRINGENT COATING

B_N

B

5 mm R

CHEVRON STARTER NOTCH

25.4 mm D

0.3W

W

1.19W

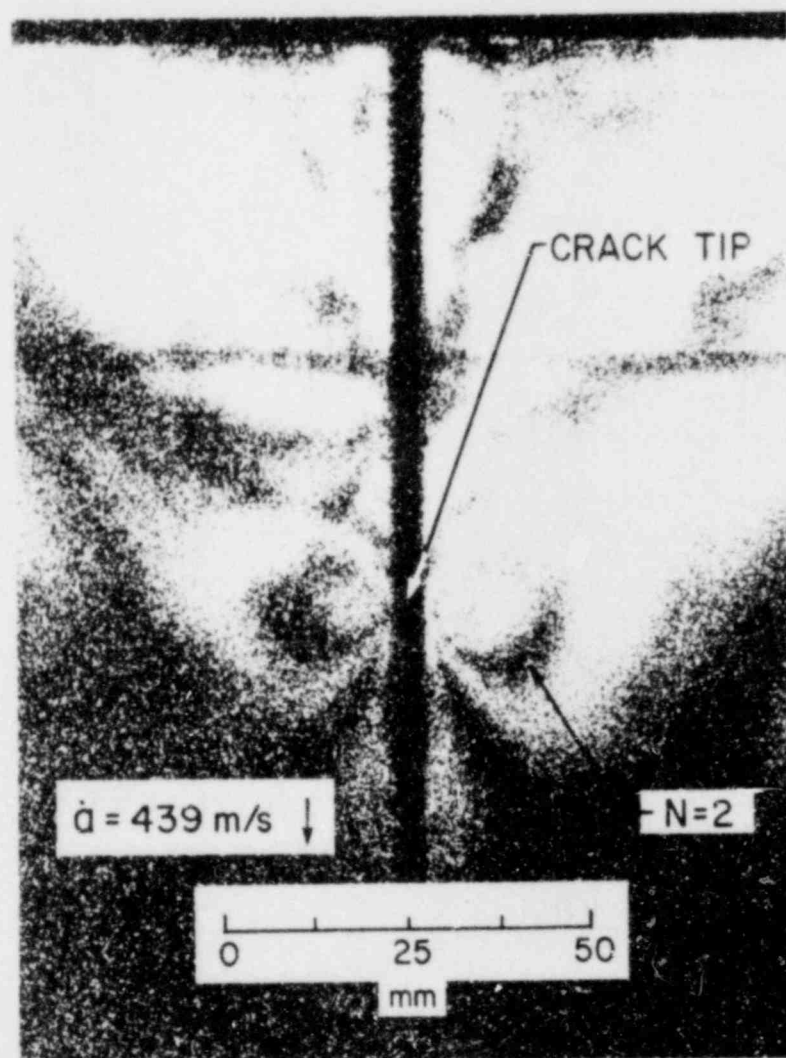0.6W

0.6W

207

Fig. 5.3 Specimen Mounted in Loading Fixture.

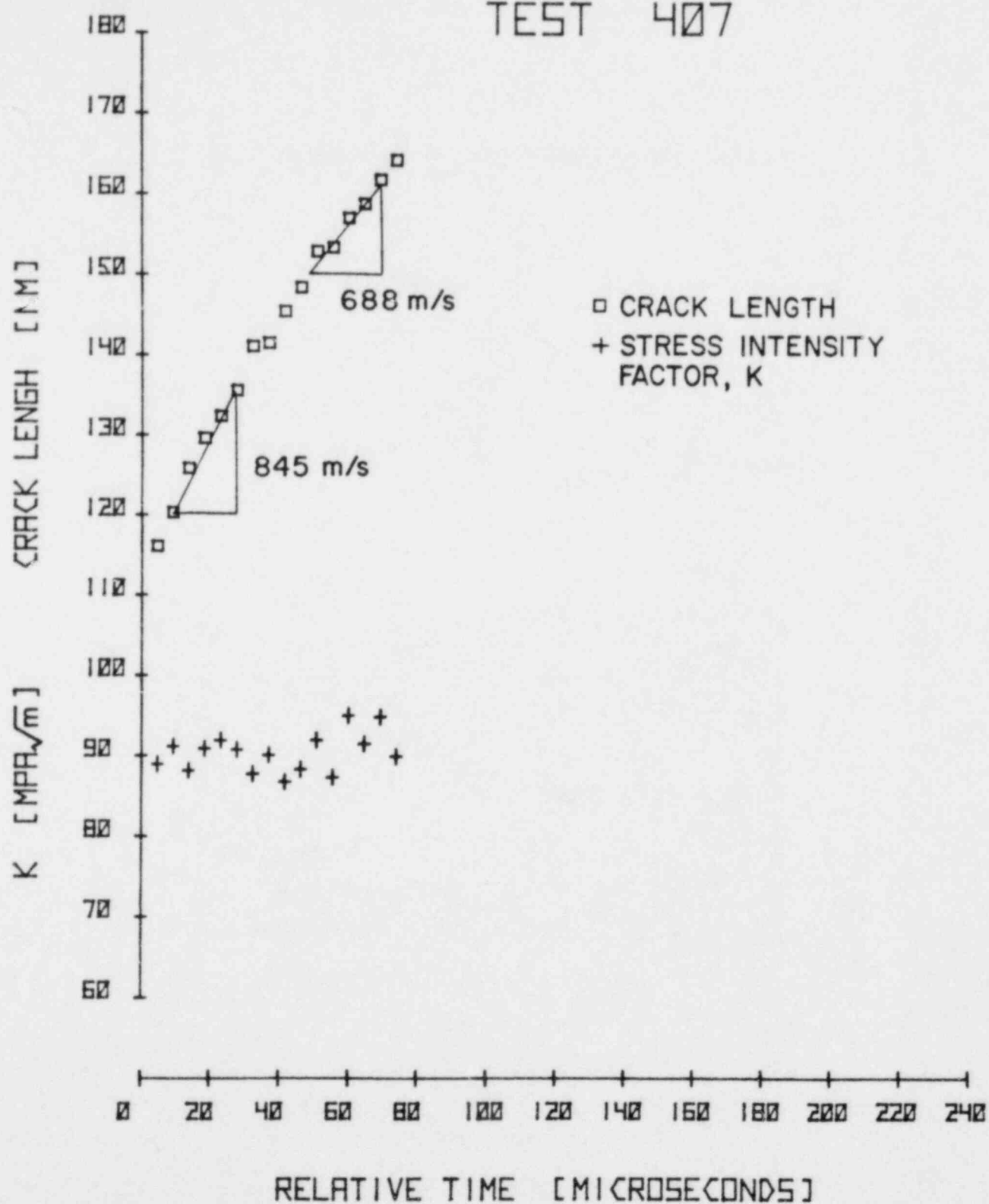Fig. 5.4 Typical Isochromatic Fringe Pattern in Birefringent Coating

209

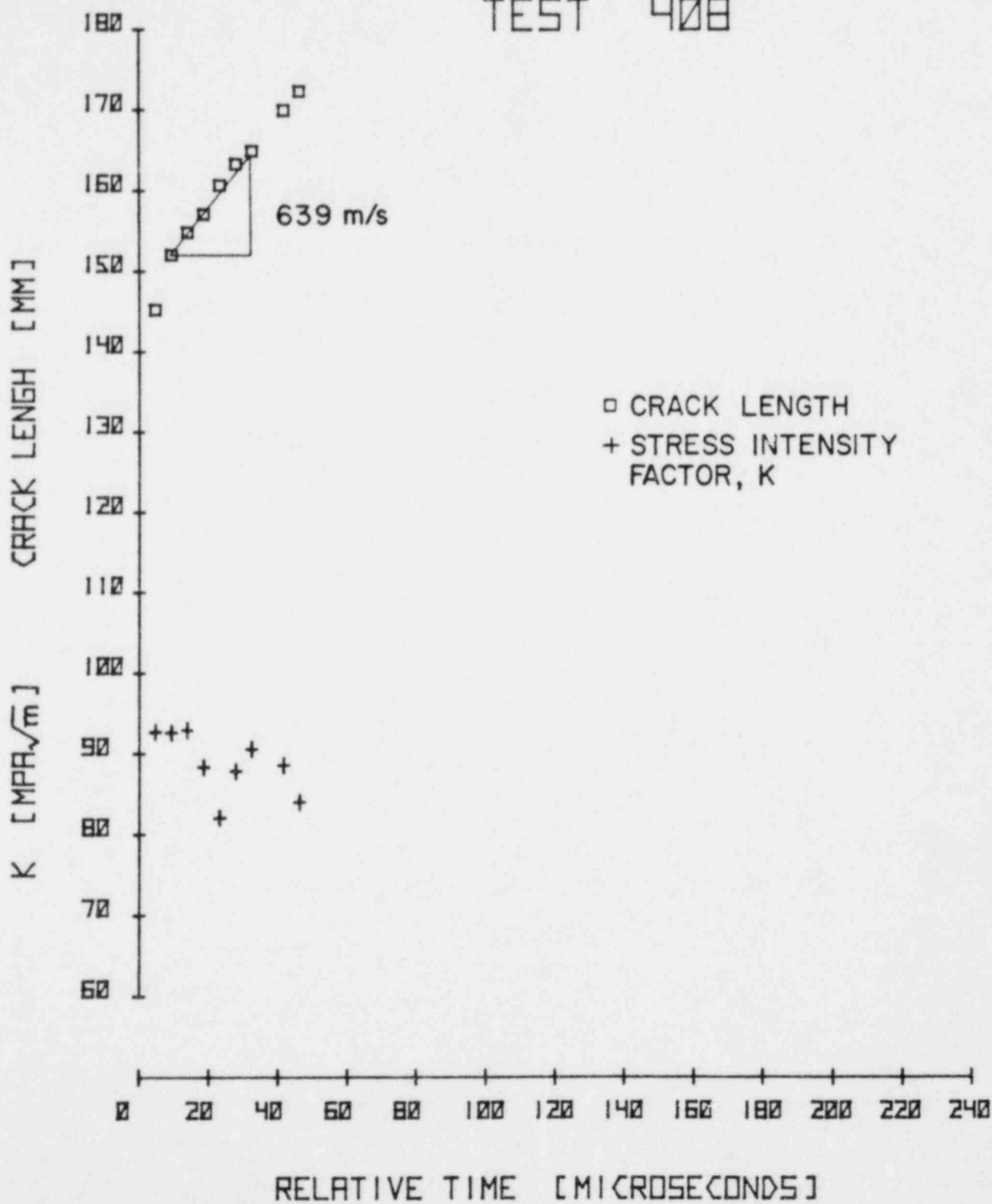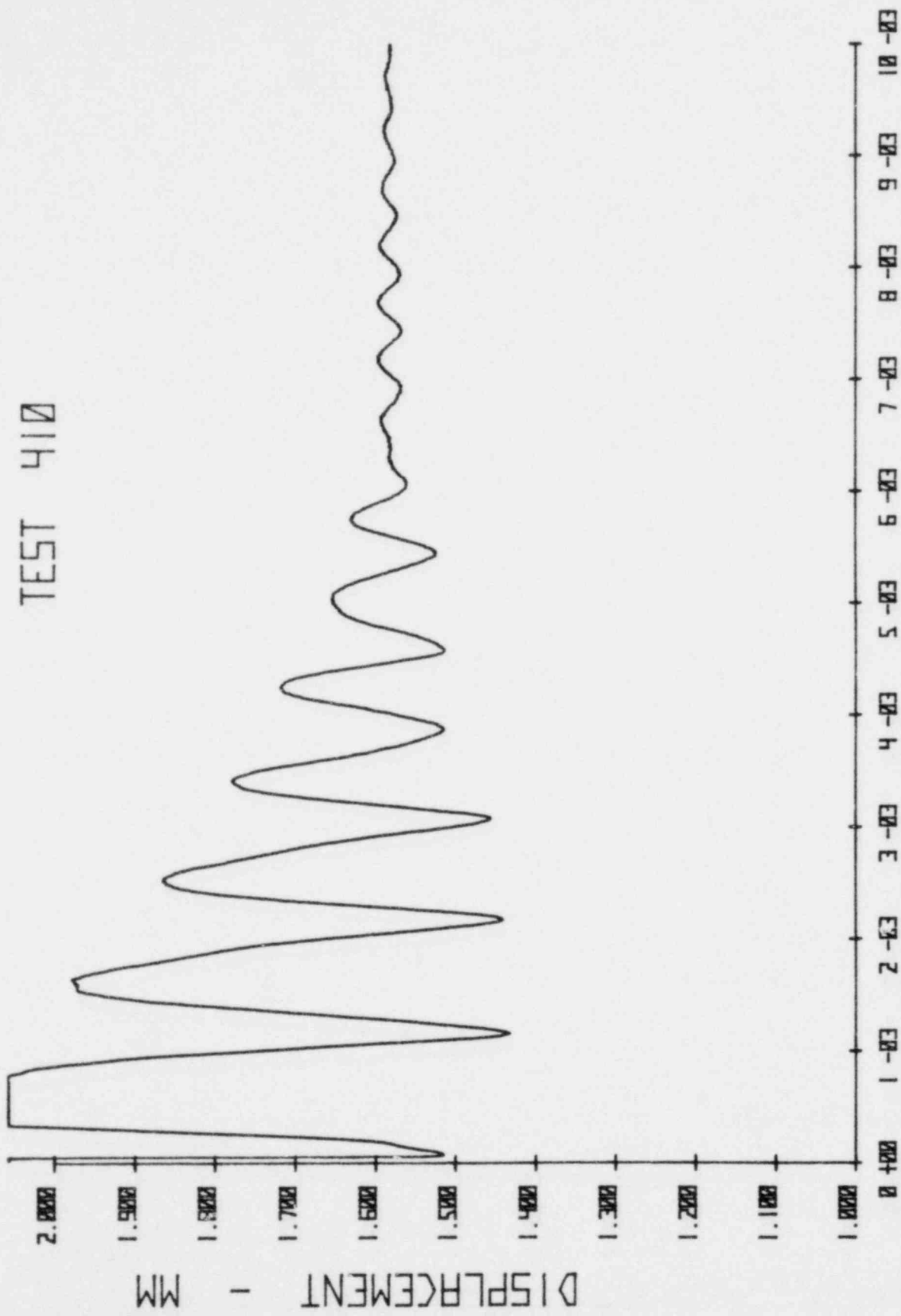Fig. 5.5 Stress-Intensity-Factor and Crack Tip Position, Test 407.

210

Fig. 5.6 Stress-Intensity-Factor and Crack Tip Position, Test 408.

211
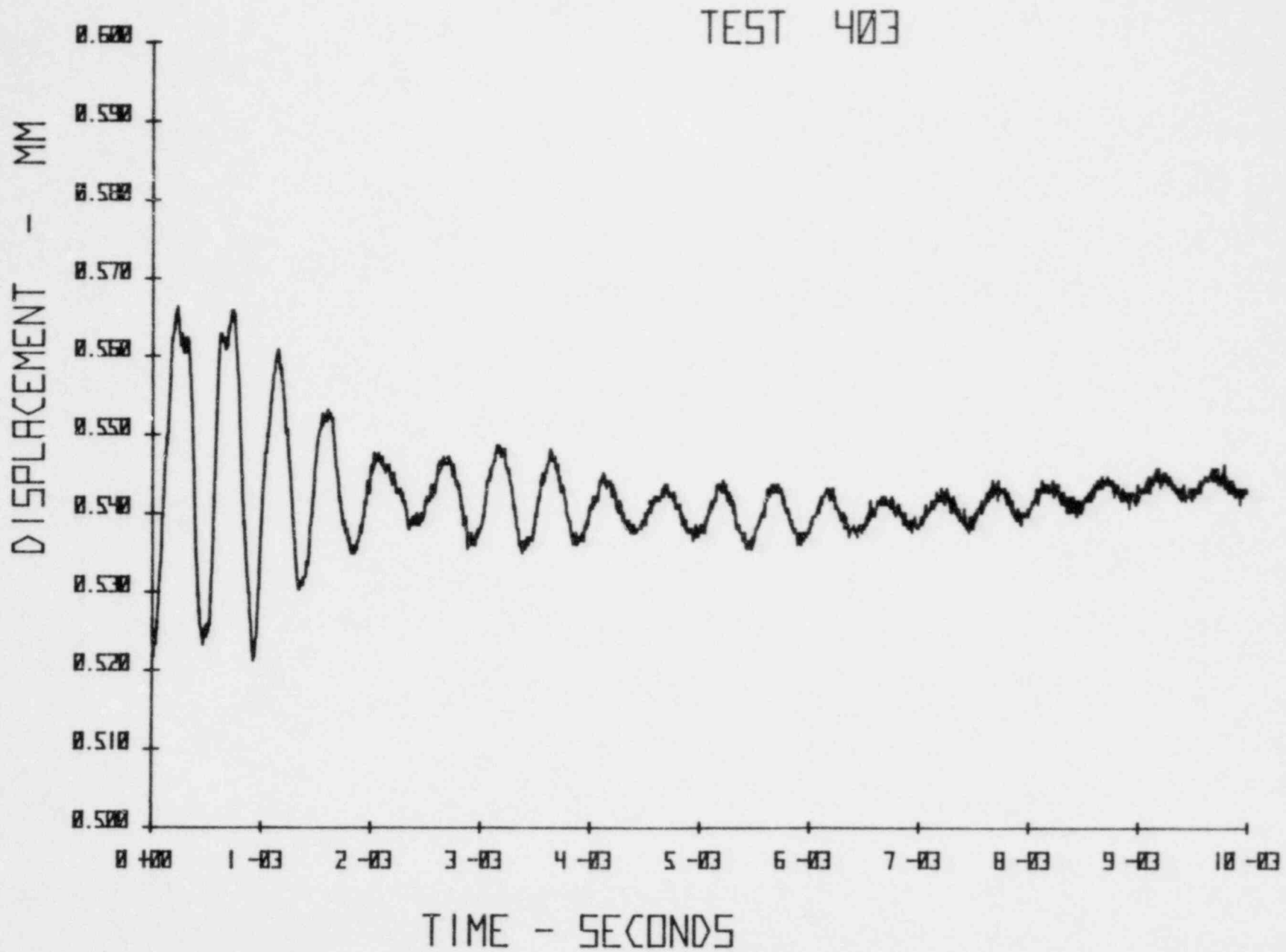
Fig. 5.7 Displacement Record Measured 0.25W Above Load Line, Test 403.

212
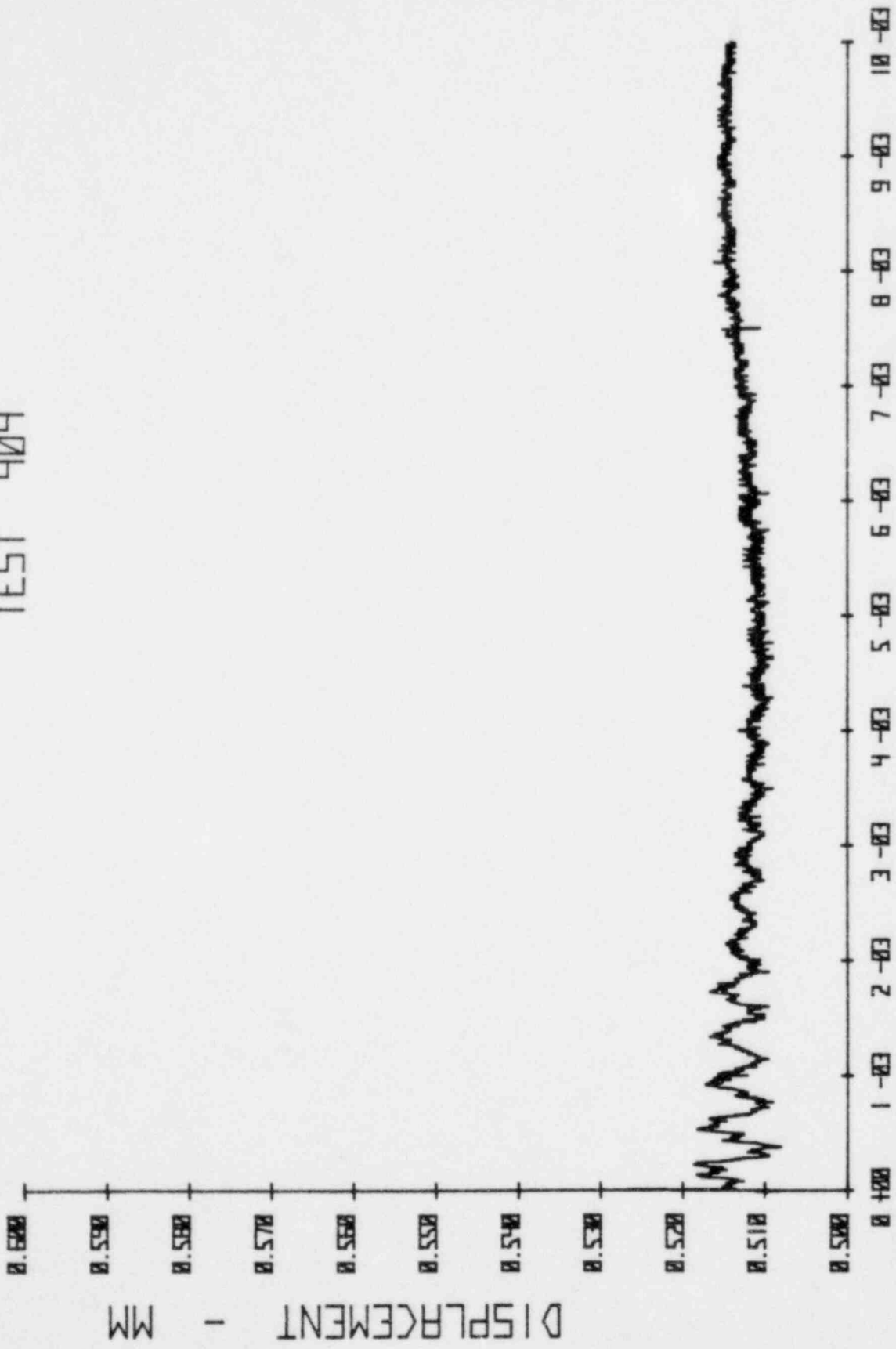
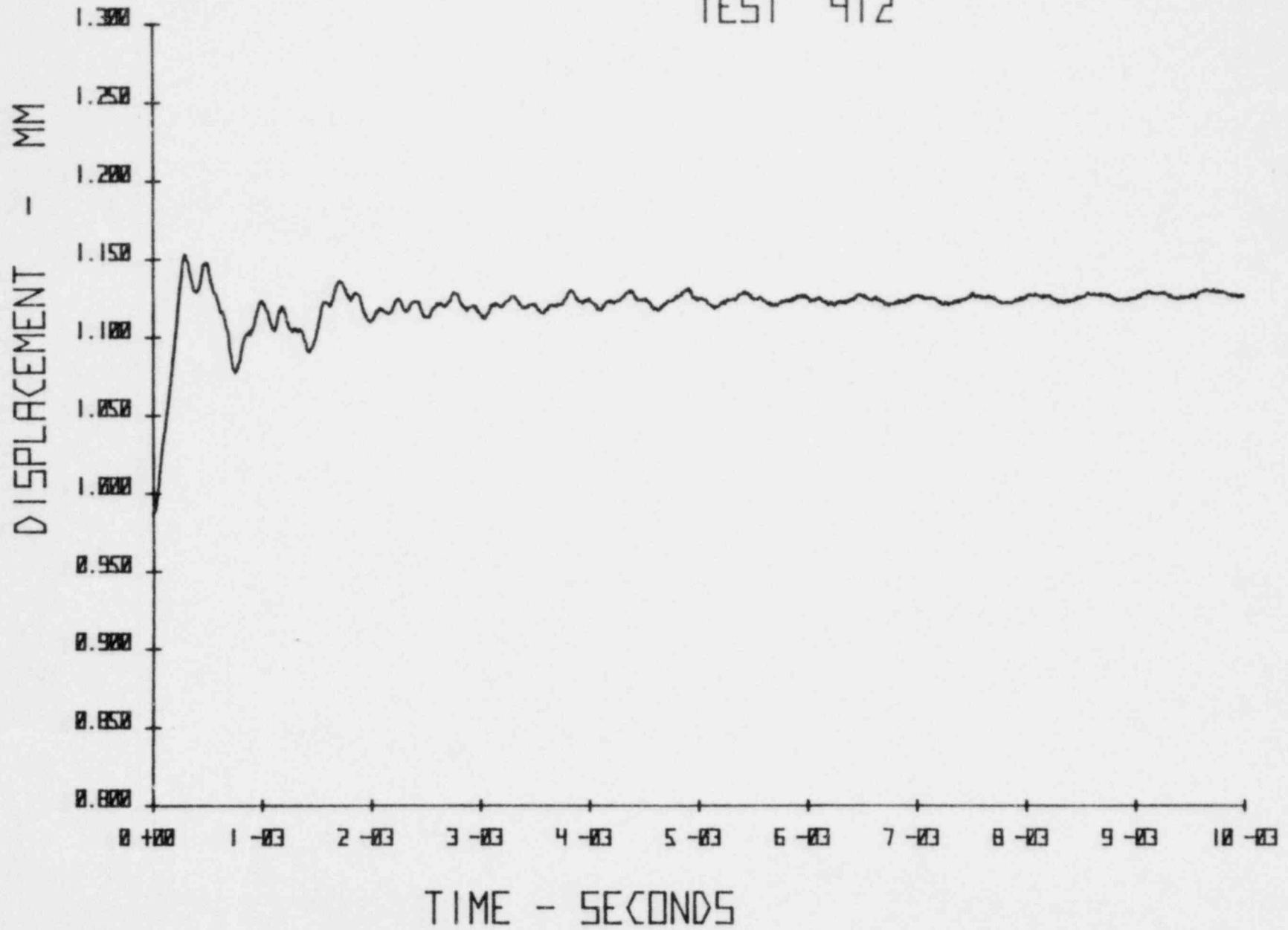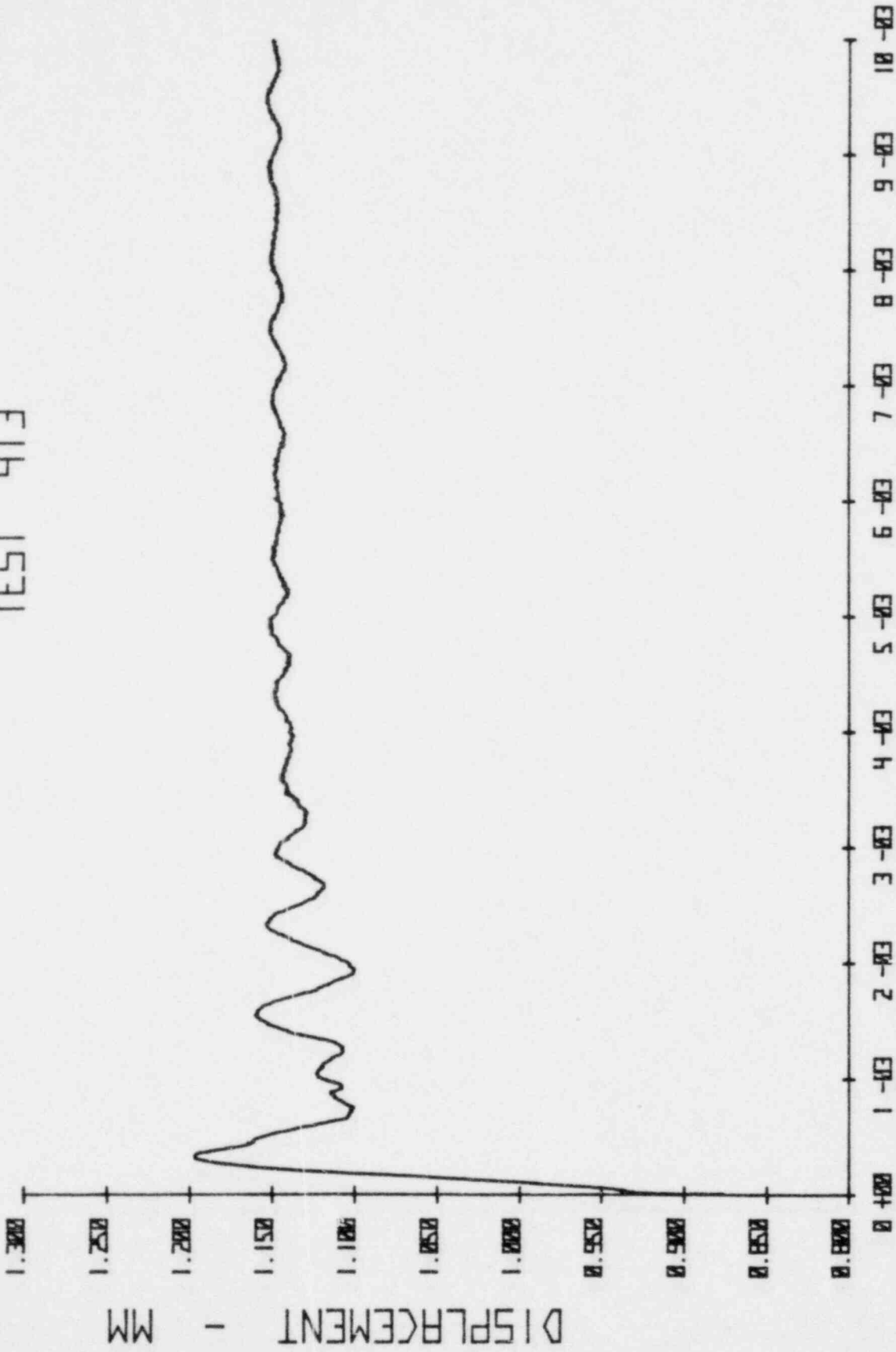Fig. 5.8 Displacement Record Measured 0.25W Above Load Line, Test 404.
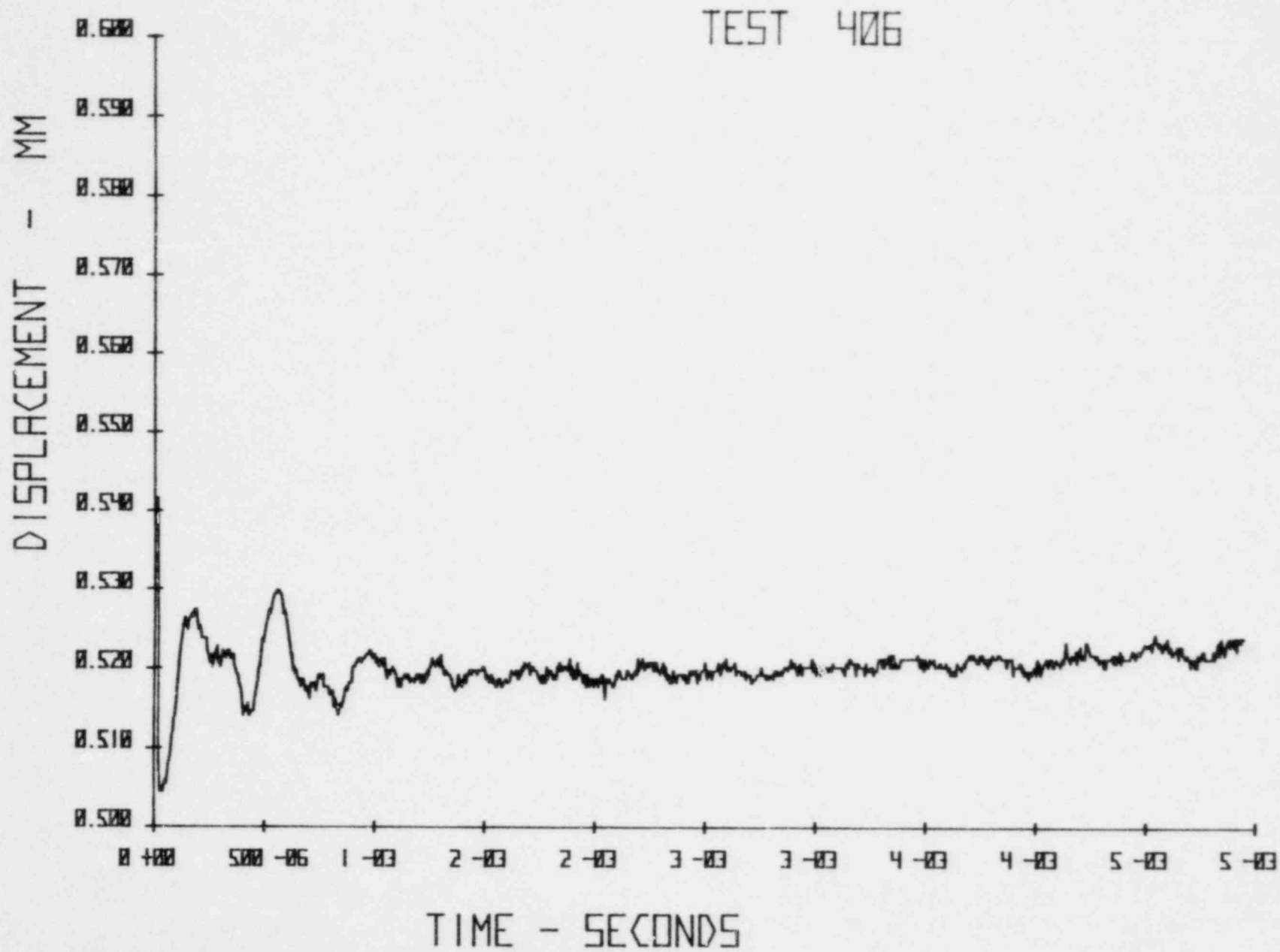
Fig. 5.9 Displacement Record Measured 0.25W Above Load Line, Test 406.
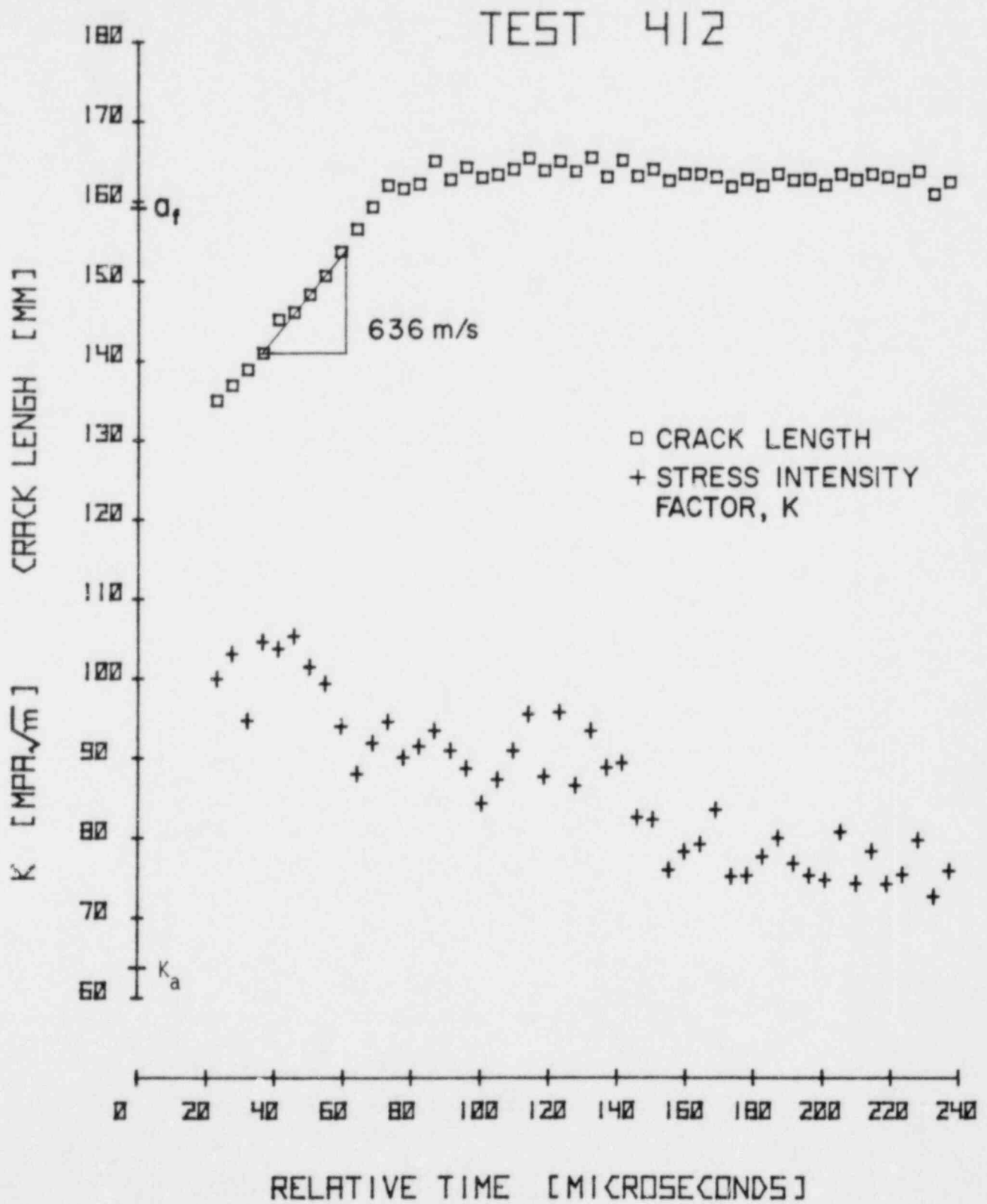
Fig. 5.10 Stress-Intensity-Factor and Crack Tip Position, Test 412.
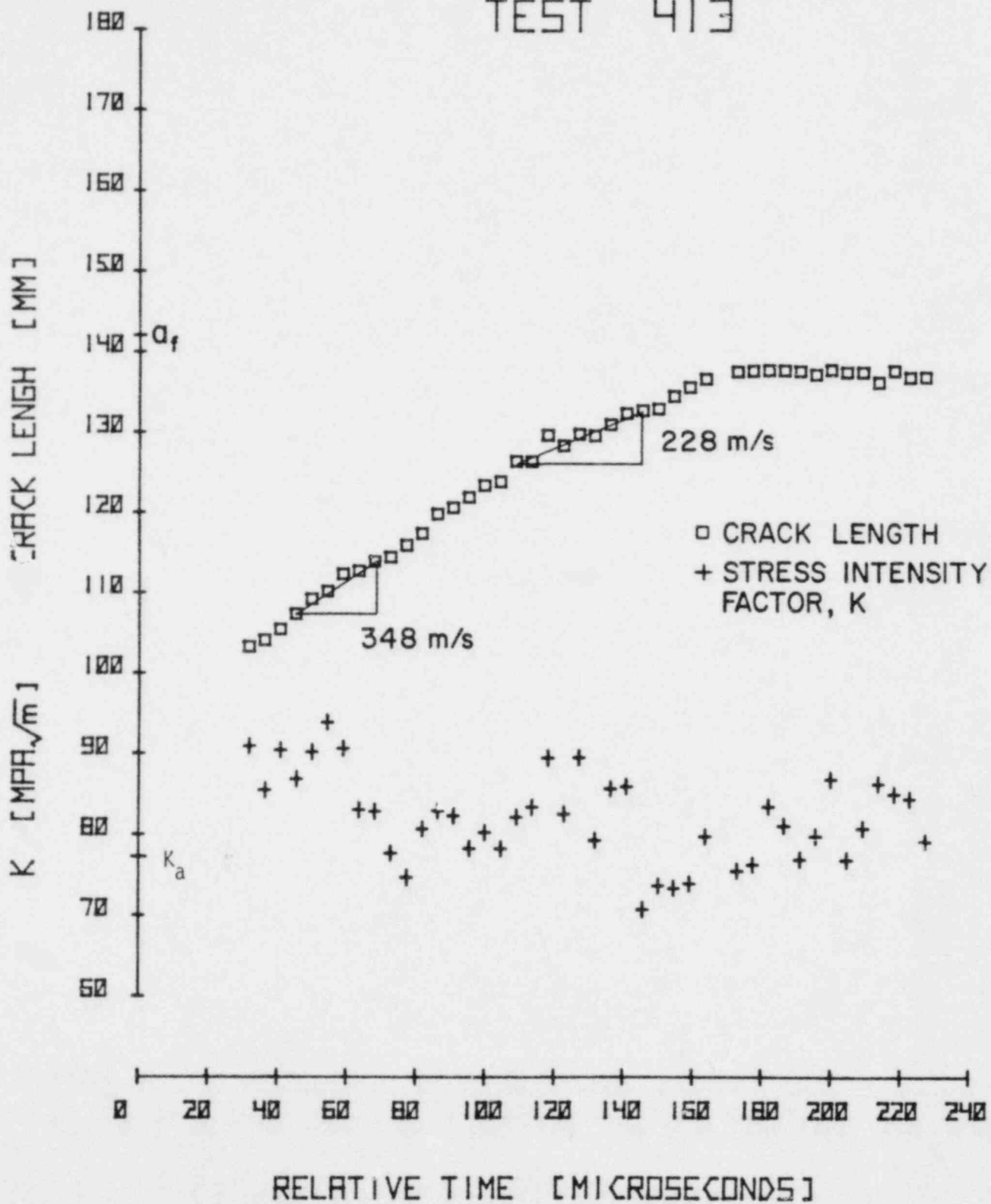
Fig. 5.11 Stress-Intensity-Factor and Crack Tip Position, Test 413.

TEST 415
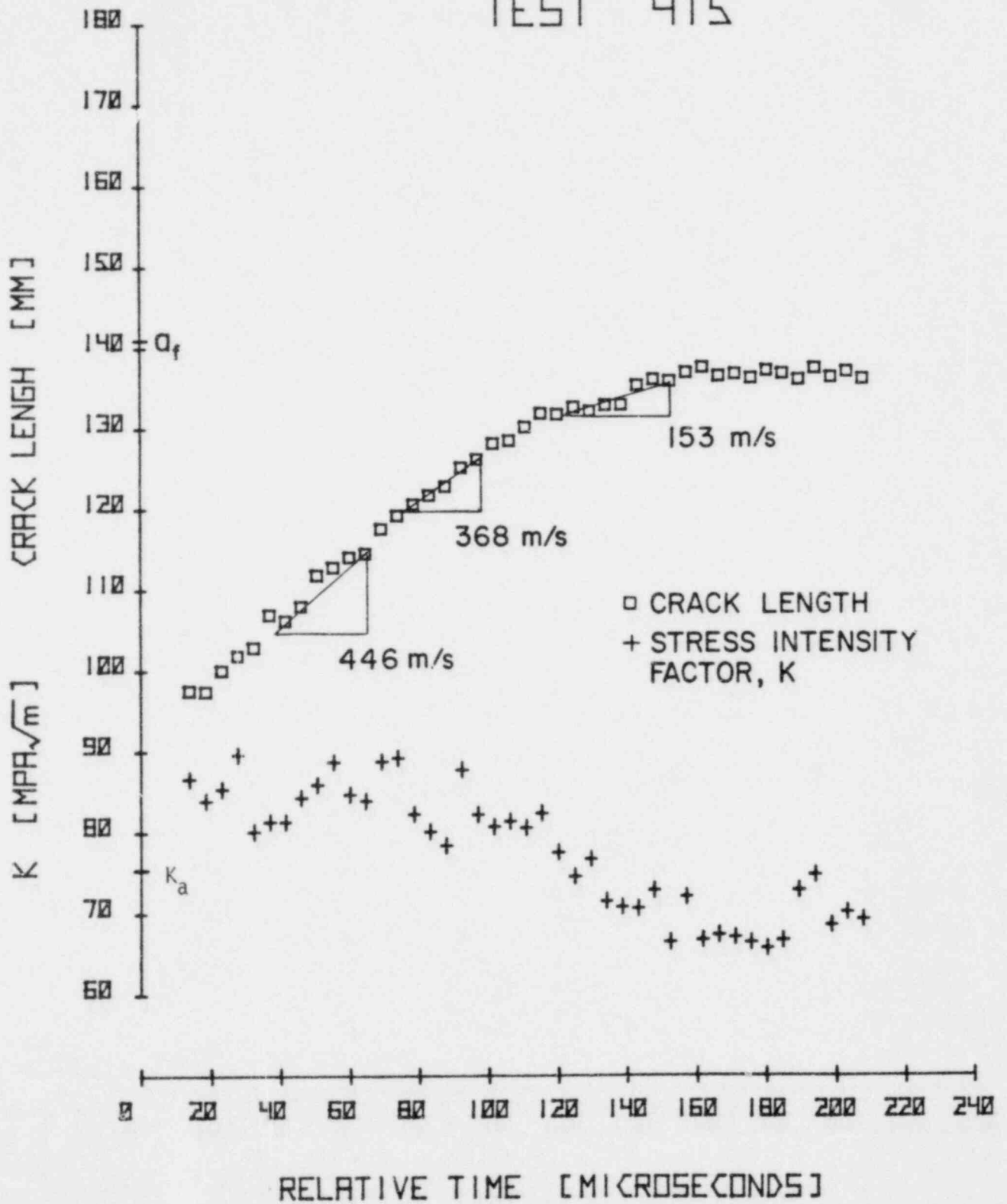
Fig. 5.12 Stress-Intensity-Factor and Crack Tip Position, Test 415.

217
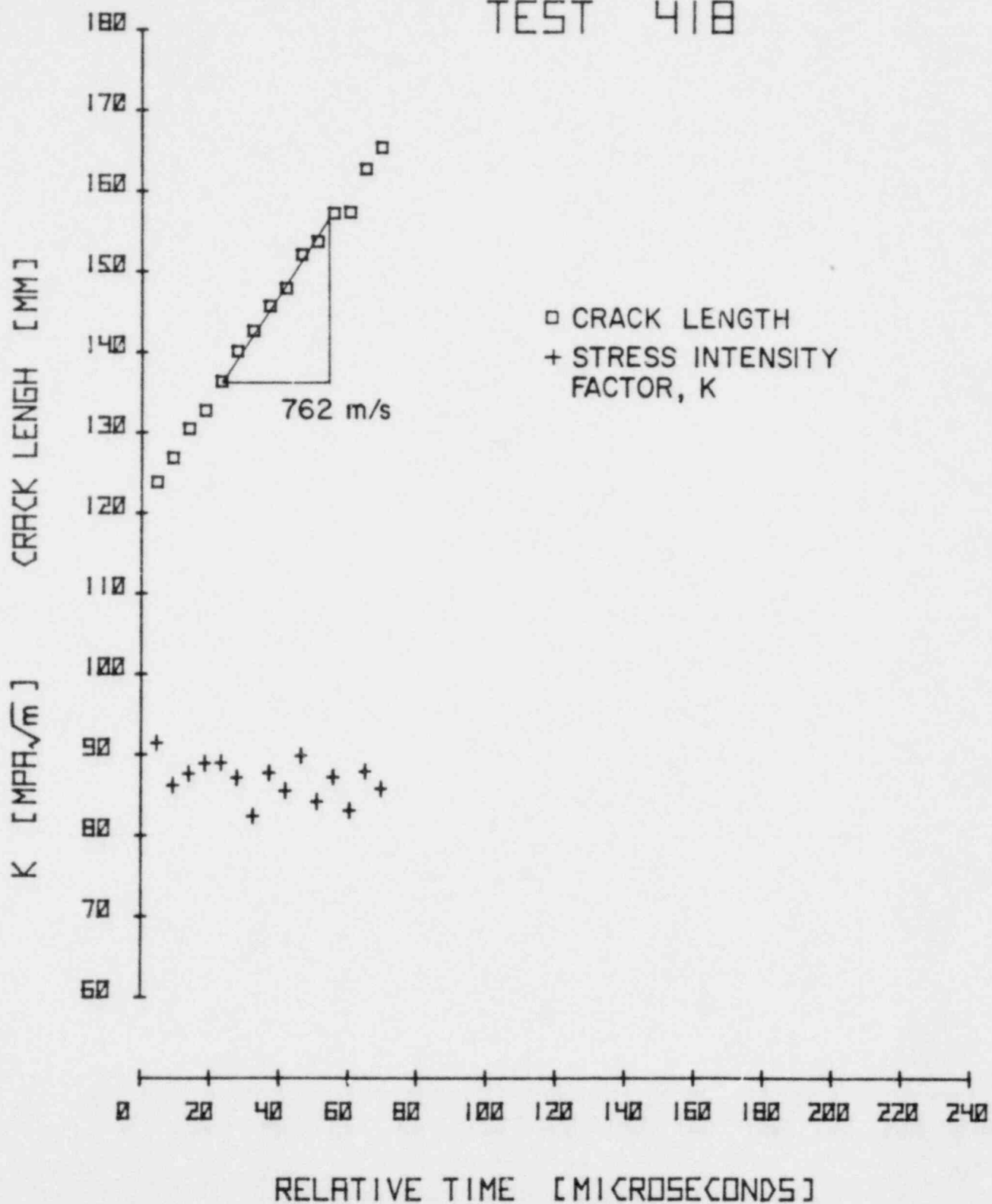
Fig. 5.13 Stress-Intensity-Factor and Crack Tip Position, Test 418.
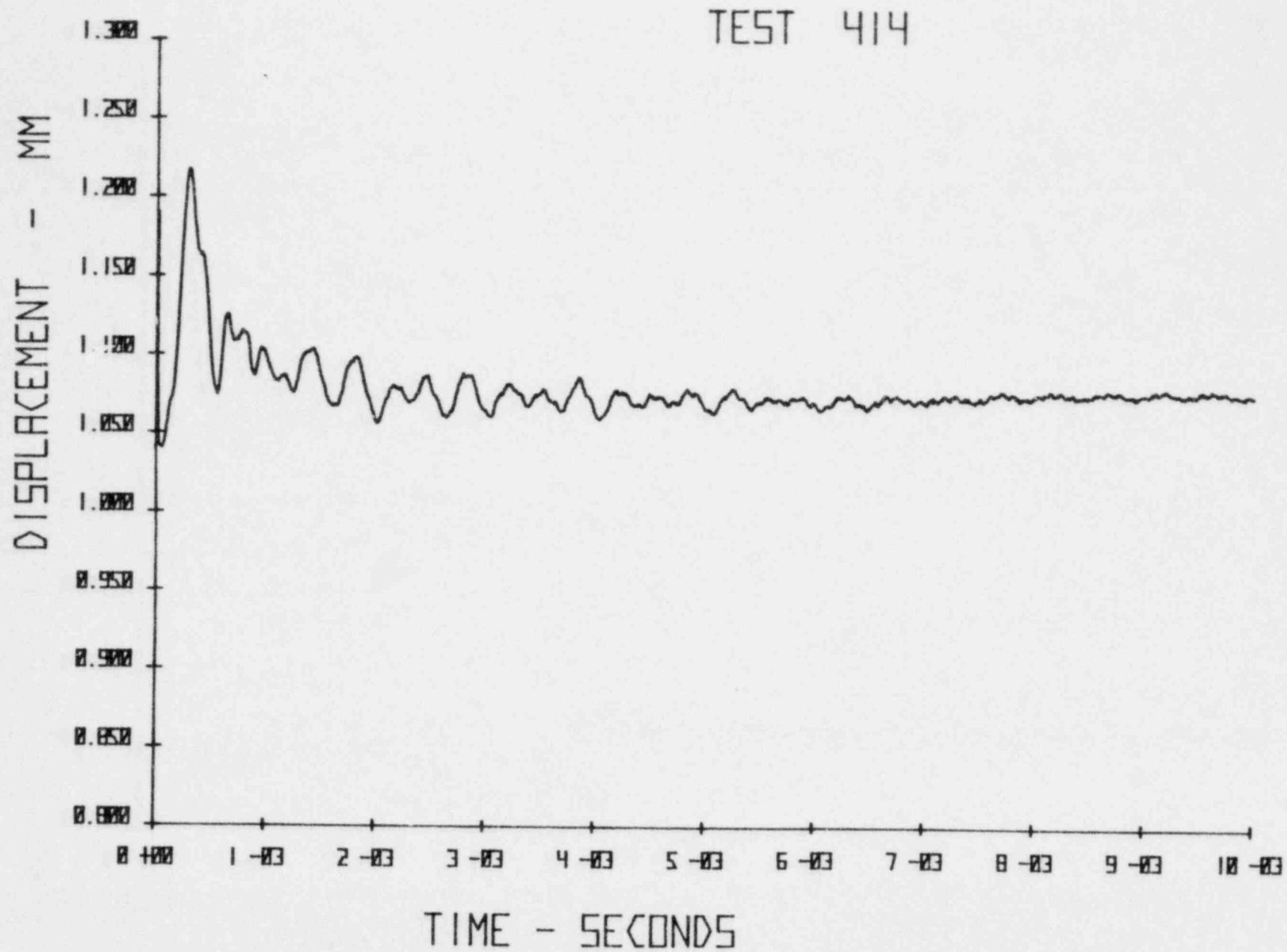
218

Fig. 5.14 Displacement Record Measured 0.25W Above Load Line, Test 410.

Fig. 5.15 Displacement Record Measured 0.25W Above Load Line, Test 412.

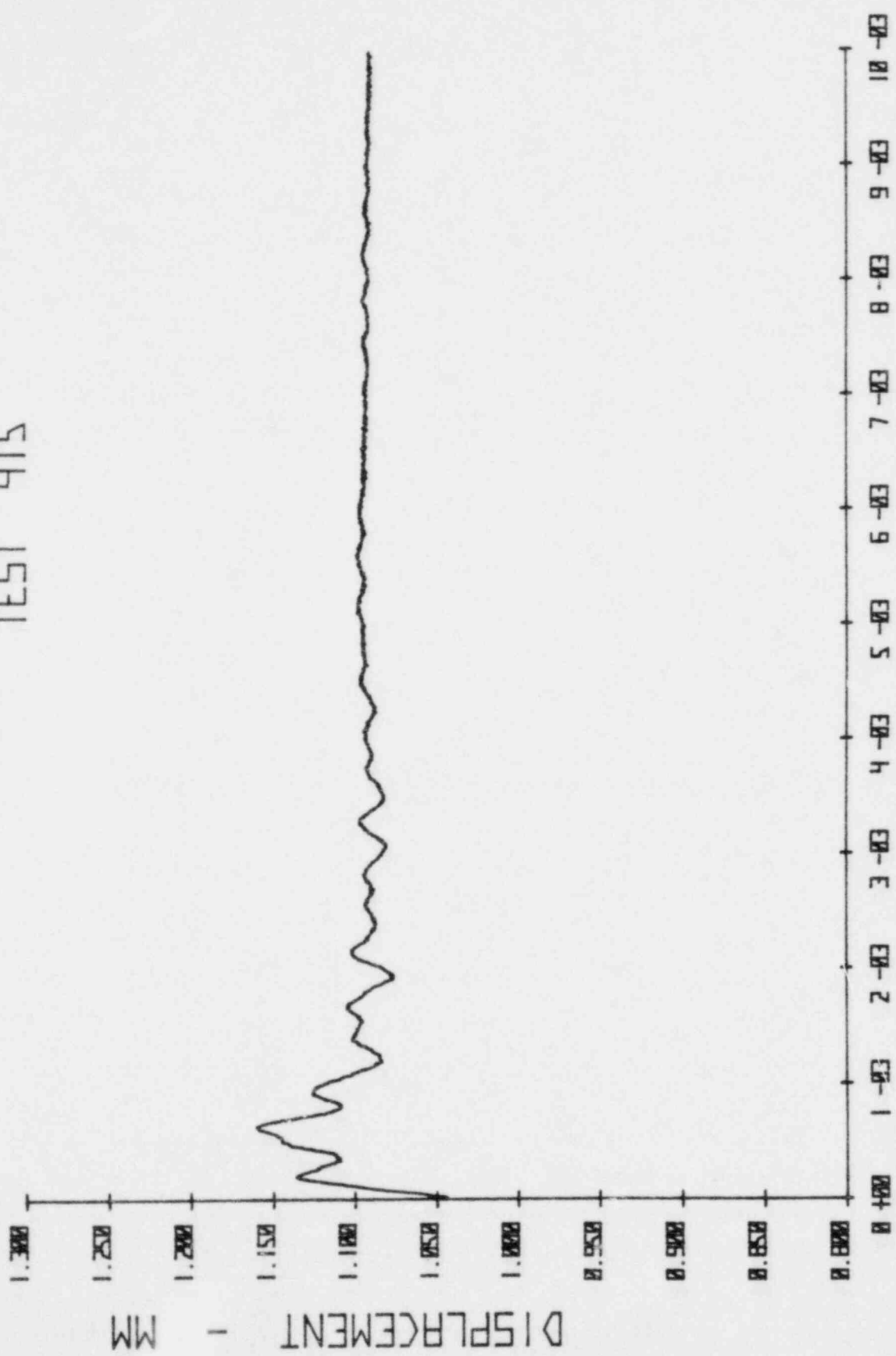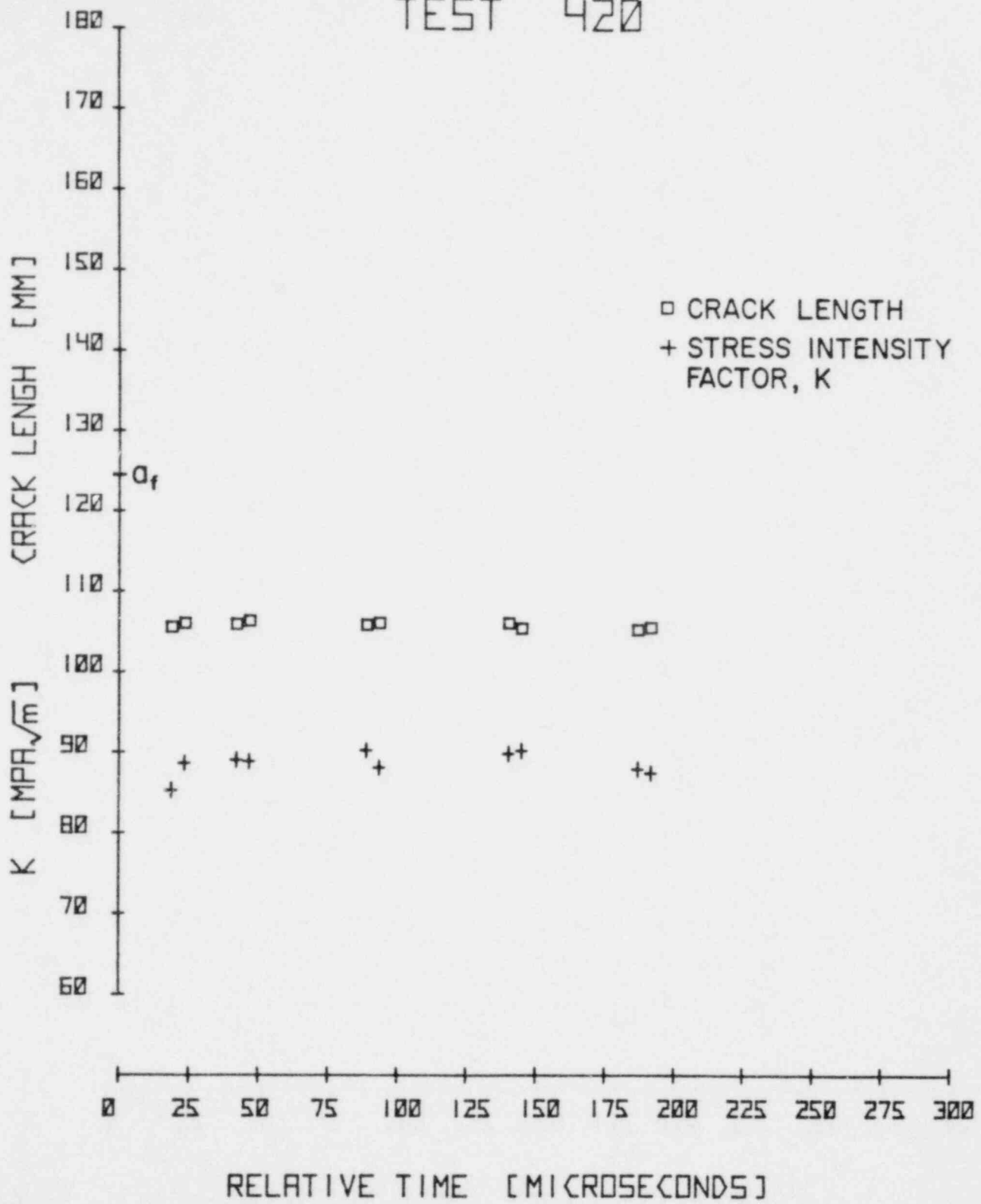Fig. 5.16 Displacement Record Measured 0.25W Above Load Line, Test 413.

Fig. 5.17 Displacement Record Measured 0.25W Above Load Line, Test 414.

Fig. 5.18 Displacement Record Measured 0.25W Above Load Line, Test 415.

TEST 420

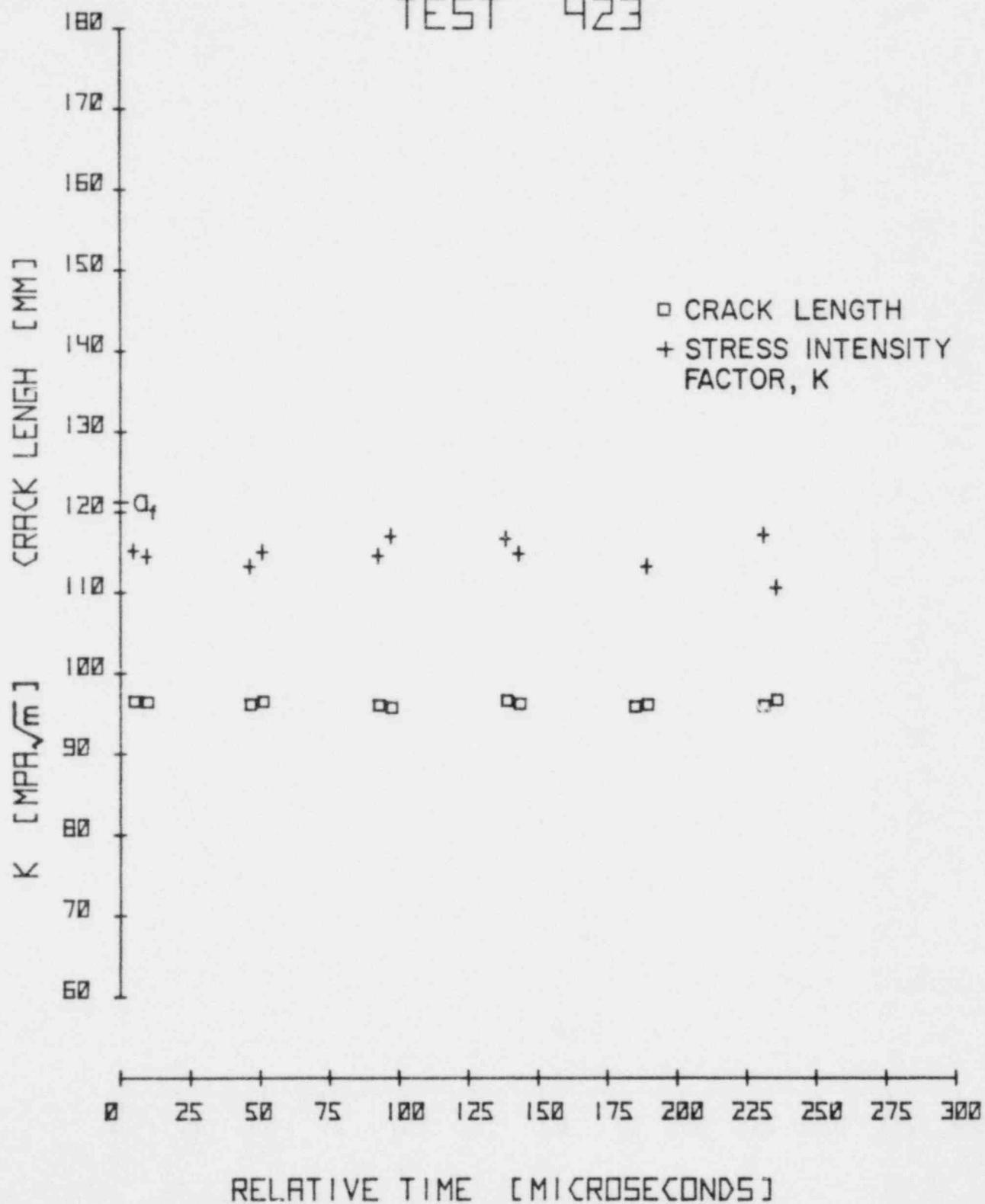Fig. 5.19 Stress-Intensity-Factor and Crack Tip Position, Test 420.

224

TEST 423

CRACK LENGH [MM]

K [MPA√m]

180
170
160
150
140
130
120 — a_f
110
100
90
80
70
60

□ CRACK LENGTH
+ STRESS INTENSITY
  FACTOR, K

0   25   50   75   100   125   150   175   200   225   250   275   300

RELATIVE TIME [MICROSECONDS]

Fig. 5.20 Stress-Intensity-Factor and Crack Tip Position, Test 423.
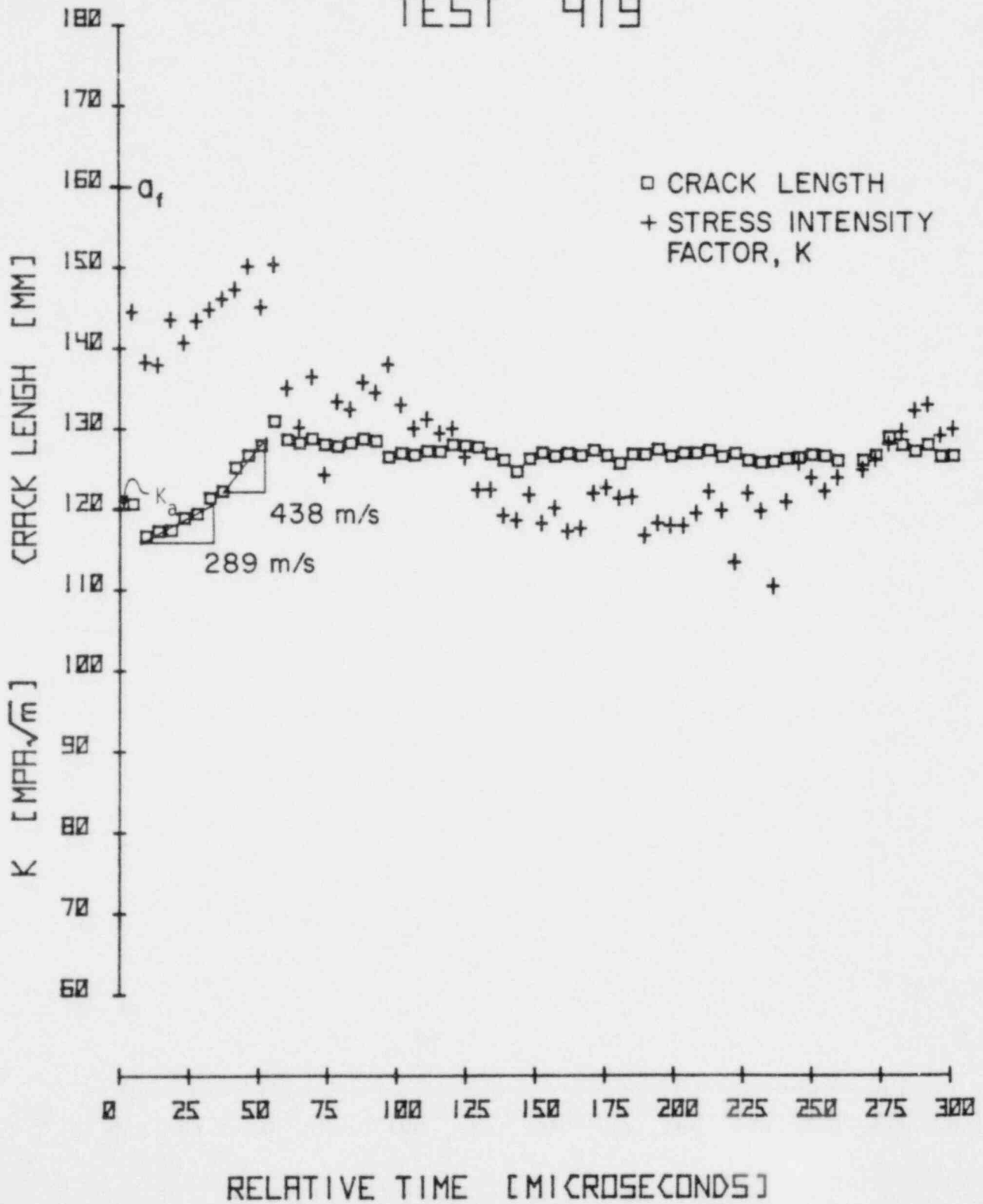
Fig. 5.21 Stress-Intensity-Factor and Crack Tip Position, Test 419.

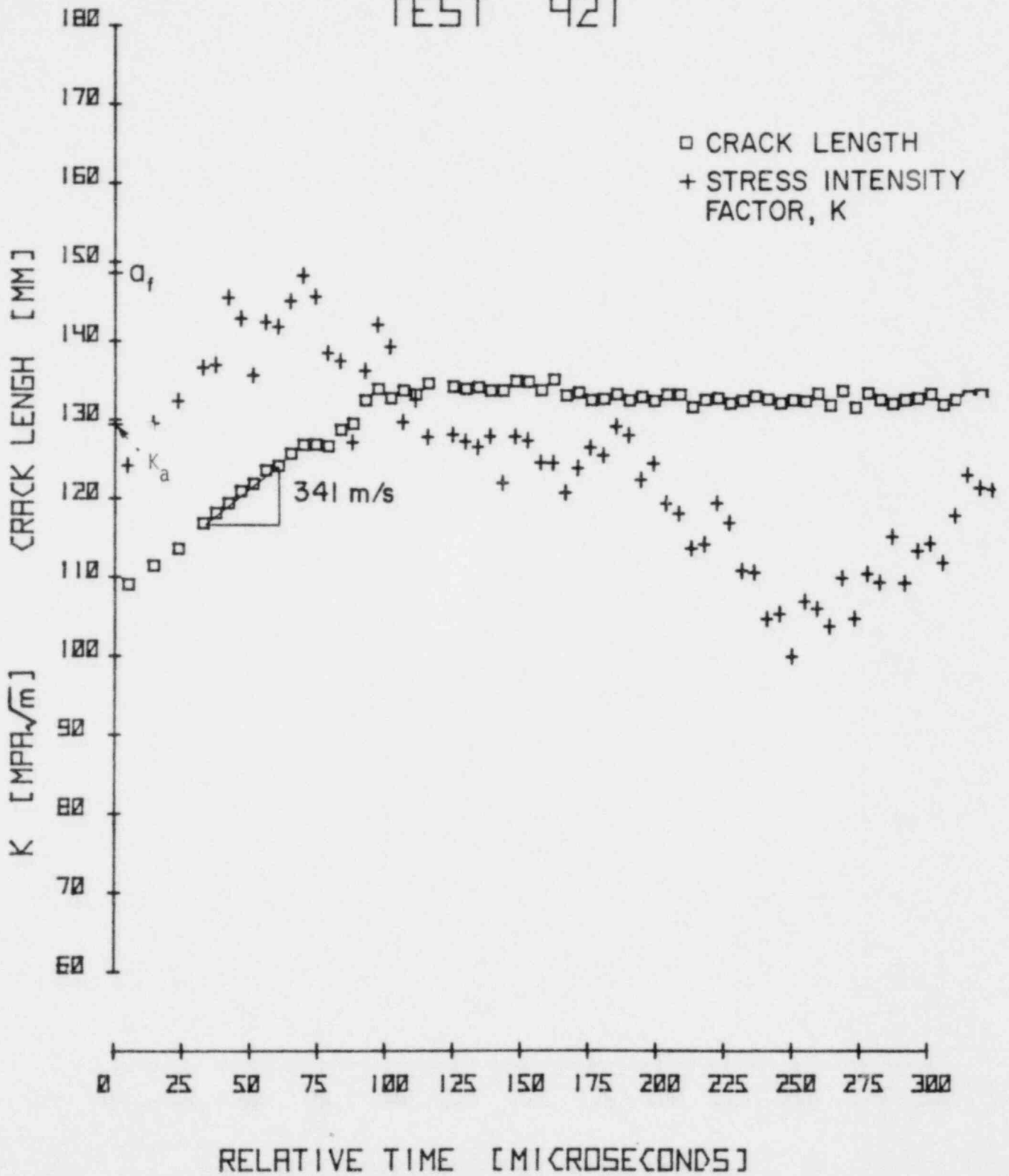Fig. 5.22 Stress-Intensity-Factor and Crack Tip Position, Test 421.
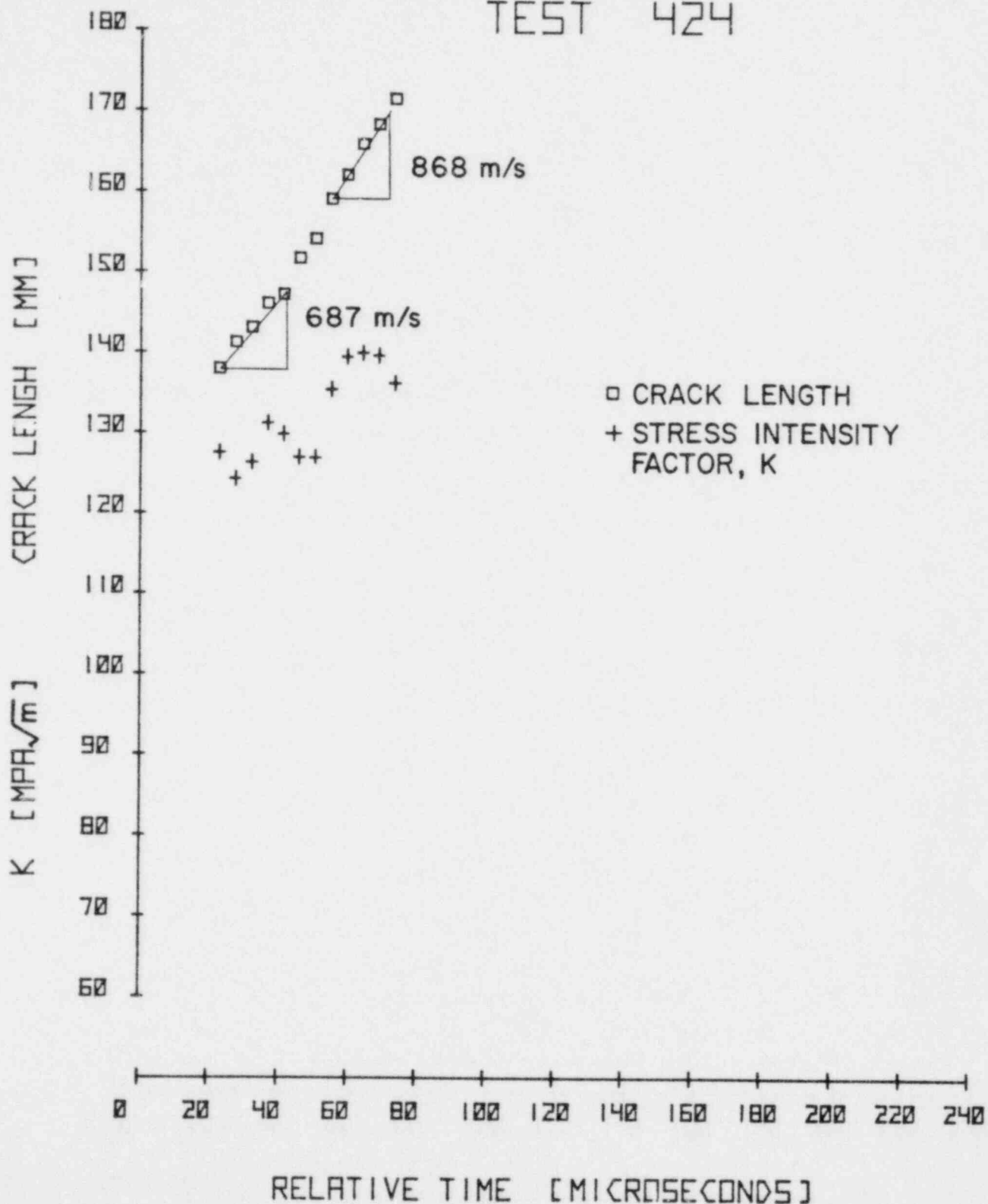
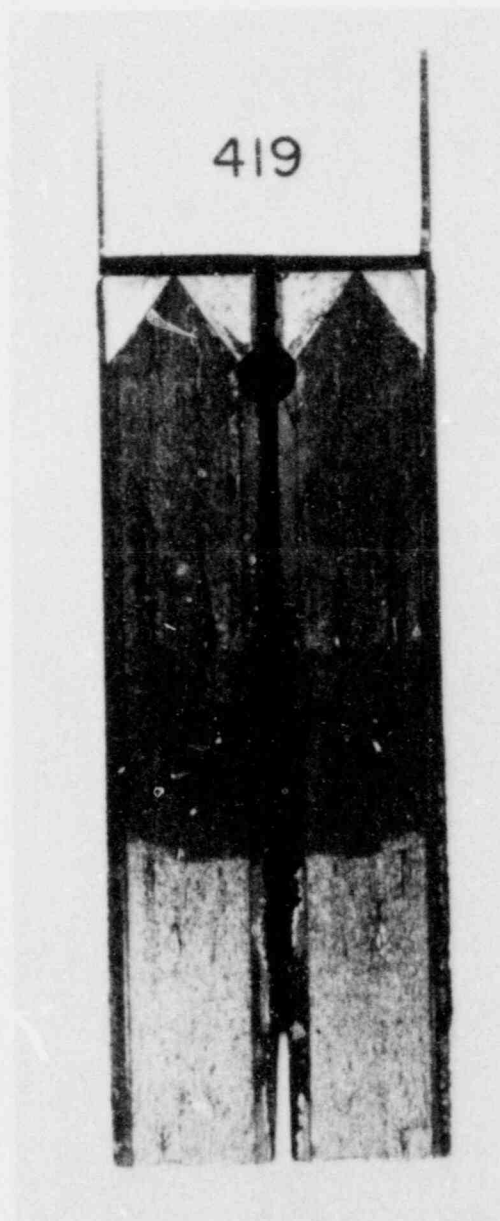Fig. 5.23 Stress-Intensity-Factor and Crack Tip Position, Test 424.

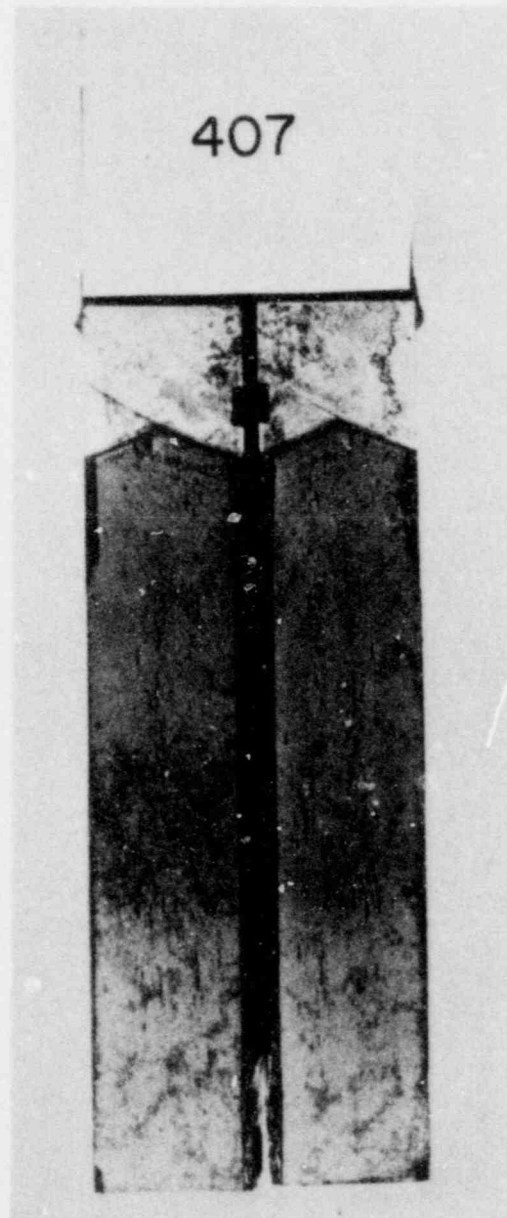Fig. 5.24 Typical Fracture Surface in R_c 37 Specimens.

Fig. 5.25 Typical Fracture Surface in R_c 50 Specimens.

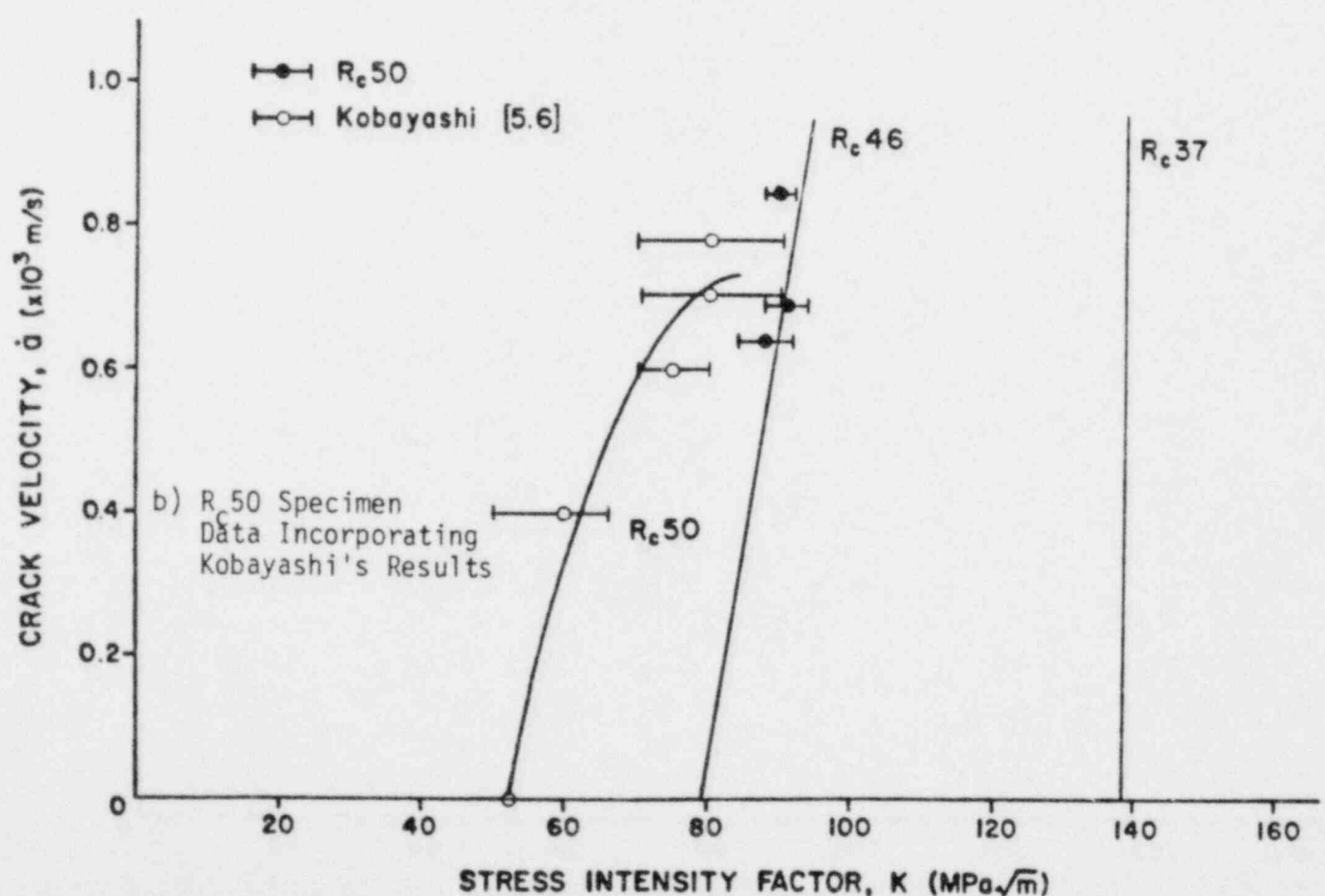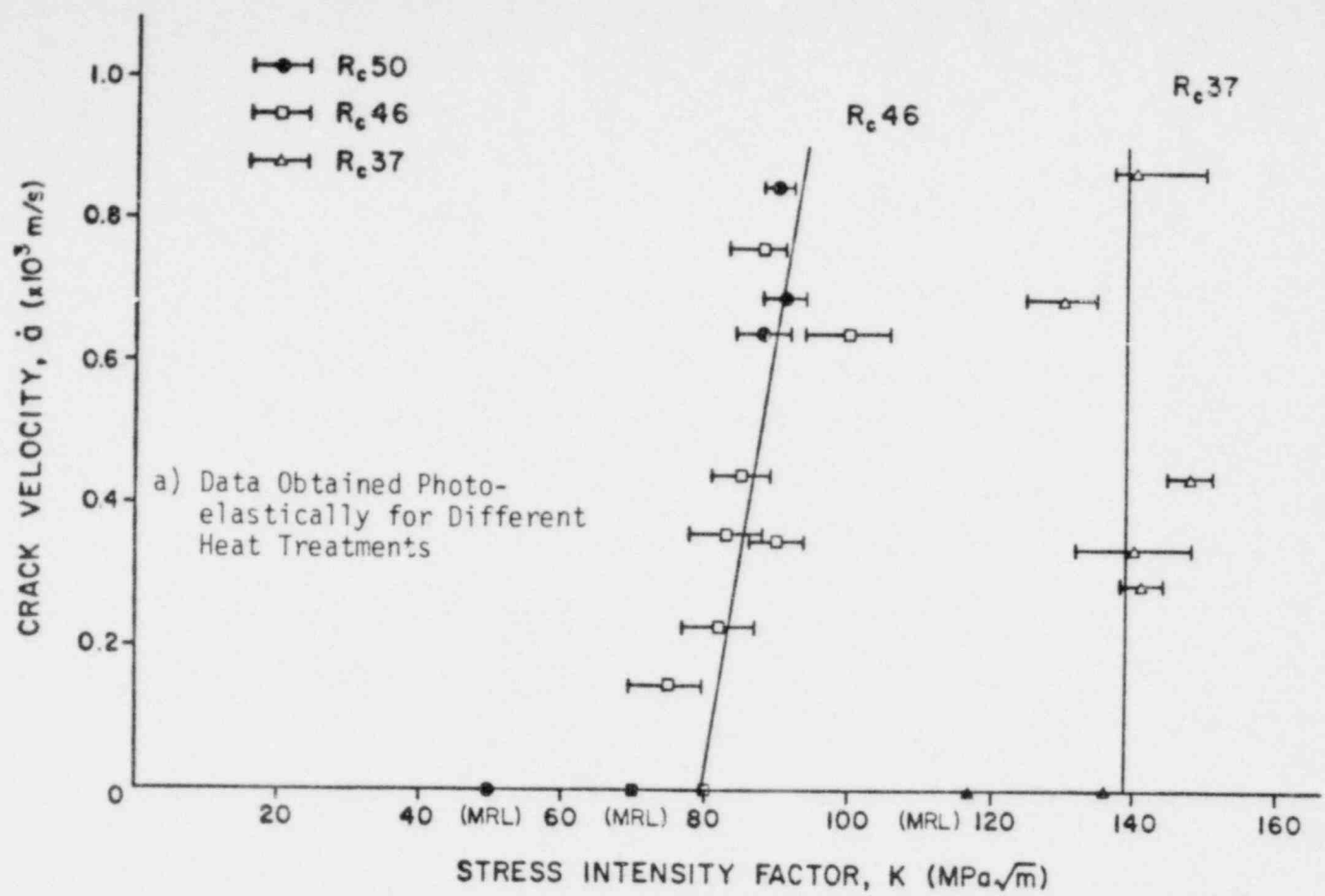Fig. 5.26 Typical Fracture Surface in R$_c$46 Specimens.

231

Fig. 5.27 Stress-Intensity-Factor as a Function of Crack Velocity for 4340 Steel

Appendix - Participation in Crack Arrest Co-operative Test Program

The University of Maryland Photomechanics Laboratory was one of
the participants in the crack arrest cooperative test program.
While participating in the program we attempted to use the split
birefringent coating technique described in Chapter 5 to evaluate
a dynamic K during propagation and arrest. The attempt was not
successful. The technique was first tried on the MRL weld embrittled
specimens and failed because of small specimen size. The deep face
grooves too severely restricted the isochromatics suitable for analysis.
The isochromatics that could be analyzed were located too close to the
specimen boundaries.

Due to the small specimen size and associated crack jump, all but
two of the six specimens arrested in less than 20 µs, before the camera
light source could reach sufficient intensity to expose the camera film.
Figure A-1 shows the results of the only successful photelastic test.
This particular specimen had the longest crack jump, 65 mm. The crack
was traveling at about 320 m/s until it arrested. The K appeared to
be dropping until arrest at about 90 MPa-m$^{\frac{1}{2}}$. This photoelastically
determined value of K was very close to that determined by the MRL
and BCL procedures.

Due to the very limited success with the split birefringent coating
technique and the MRL specimens, the technique was not tried on the BCL
specimens.

The results of our participation and our comments as sent to Dr.
George Hahn at BCL and Dr. E. J. Ripling at MRL are given on the
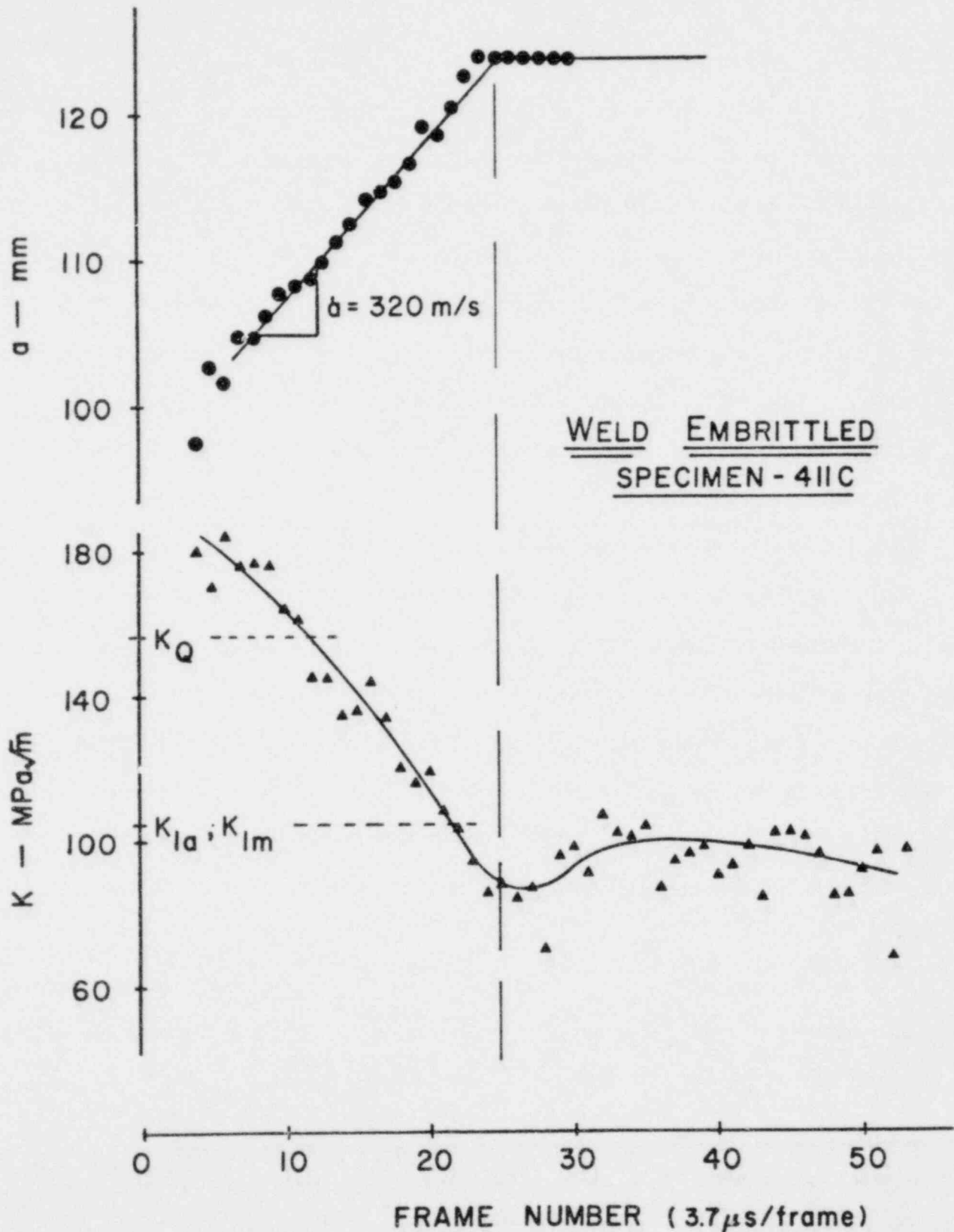following pages.

Fig. A-1   Photoelastic Results for Specimen 411C

COLLEGE OF ENGINEERING
GLENN L. MARTIN INSTITUTE OF TECHNOLOGY
DEPARTMENT OF MECHANICAL ENGINEERING

January 25, 1979

Dr. George T. Hahn
Battelle Columbus Laboratories
505 King Avenue
Columbus, Ohio 43201

Dear Dr. Hahn,

Here are our findings and comments with respect to our participation in the crack arrest cooperative test program.

The completed test records using the forms supplied by MRL and Battelle have been filled out. Also enclosed with the test forms are copies of the crack opening displacement plots and photos showing the fracture surface and any unbroken ligaments. A brief description precedes each set of test forms describing any variation from recommended procedure and any additional measurements that were taken.

The supplementary measurements taken by S. Salonen and K. Rahle at the Technical Research Center of Finland were of special interest to the Univ. of Maryland group. The influence of the unbroken ligaments is of concern to us. We would be willing to repeat measurements of this kind on additional specimens if any are available.

The roughness and occasional unbroken segment introduced at the electron beam weld of the Battelle duplex specimen seem undesirable. We believe some improvement in uniformity and smallness of the weld region will be necessary in both specimens.

Greater care with the pre-compression feature of the MRL specimen may be required. On the other hand, our results show no special evidence for a large residual stress zone as has been implied.

Sincerely,

D B Barker

D. B. Barker
Assistant Professor
Mechanical Engineering Department

DBB:daz

cc: E. J. Ripling, MRL
    P. Albrecht, NRC
    T. Marston, EPRI

235

MRL Weld Embrittled Specimens

The two AISI 1018 and the four A533B weld embrittled specimens were tested as per Crosley's letter of July 18, 1978 and August 3, 1978 except for minor departures in procedure. These departures were necessary to accomodate a simultaneous dynamic analysis of the specimen using a split birefringent coating technique. Using an ultra-high speed camera, the isochromatic fringe pattern was photographed during crack propagation and arrest. The following departures in the requested procedure were necessary:

1. The furnished back-up block was not used. The birefringent coating was bonded to the specimen on the side opposite the entrance of the loading wedge. The back-up block in the loading frame used for these tests measured 127 mm x 279 mm x 51 mm thick with a 25 mm diameter hole centrally located for clearance of the wedge. This back-up block was firmly clamped at the two long ends. As can be seen in the photos of the specimens fracture surfaces, longer crack growth occured on the specimen side in contact with the back-up block. This implies that the back-up block significally deformed under the application of the load.

2. A 14 mm long groove was cut across the specimens face groove 2 mm ahead of the starter notch with a 6.4 mm diameter ball end mill. This groove was cut approximately 0.1 mm deeper than the face groove on the side of the specimen that the loading wedge entered. A conductive trip line was then placed across the face groove in the bottom of this groove. This started our instrumentation and light source for the high speed camera.

3. On all specimens two pieces of 95 mm x 108 mm birefringent coating were bonded on either side of the face groove on the side opposite the entrance of the loading wedge. The thickest

coating used was 2.0 mm polycarbonate bonded with a thin layer
of Hysol EA 9810 structural high strength epoxy adhesive. The
bonded coating should have negligible influence on the specimens
behavior.

4. All the specimens were tested at room temperature so that the
   split birefringent coating technique could be used.

5. The loading wedge did not always enter the specimen on the
   numbered side. This exception is noted on the test report forms.
   The surface with the fewest dings and other imperfections was
   always choosen for the birefringent coating.

The crack opening displacement was monitored with an eddy current displacement transducer (Kaman Model KD-2300-2S) mounted in the furnished blocks.
The displacement signal was recorded with a digital memory oscilloscope
(Nicolets, Inc. Model Explorer III) which was triggered with the breaking
of the conductive trip line. The crack opening displacements used in the
calculations and the included plots of opening versus time with the test
report forms are from this oscilloscope. A back-up record of the crack opening
was recorded on a strip chart. These measurements are not included on the
report forms because there was a negligible difference between the arrest and
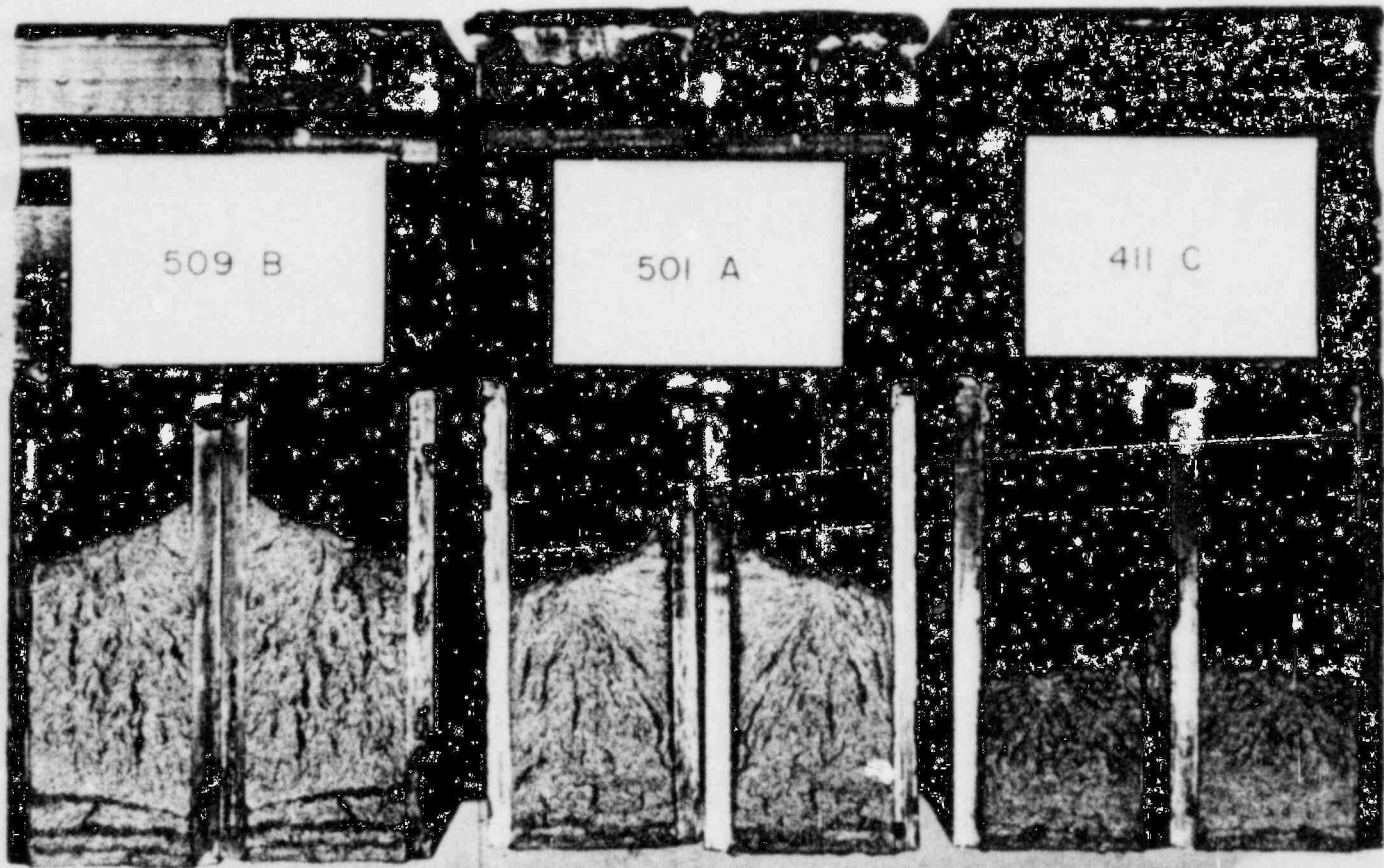initiation measurements from the two recording systems.

The completed report forms, a plot of the crack opening displacement
versus time, and photos of the fracture surfaces follow.

202 B

6341/51

6341/13

509 B 501 A 411 C

239
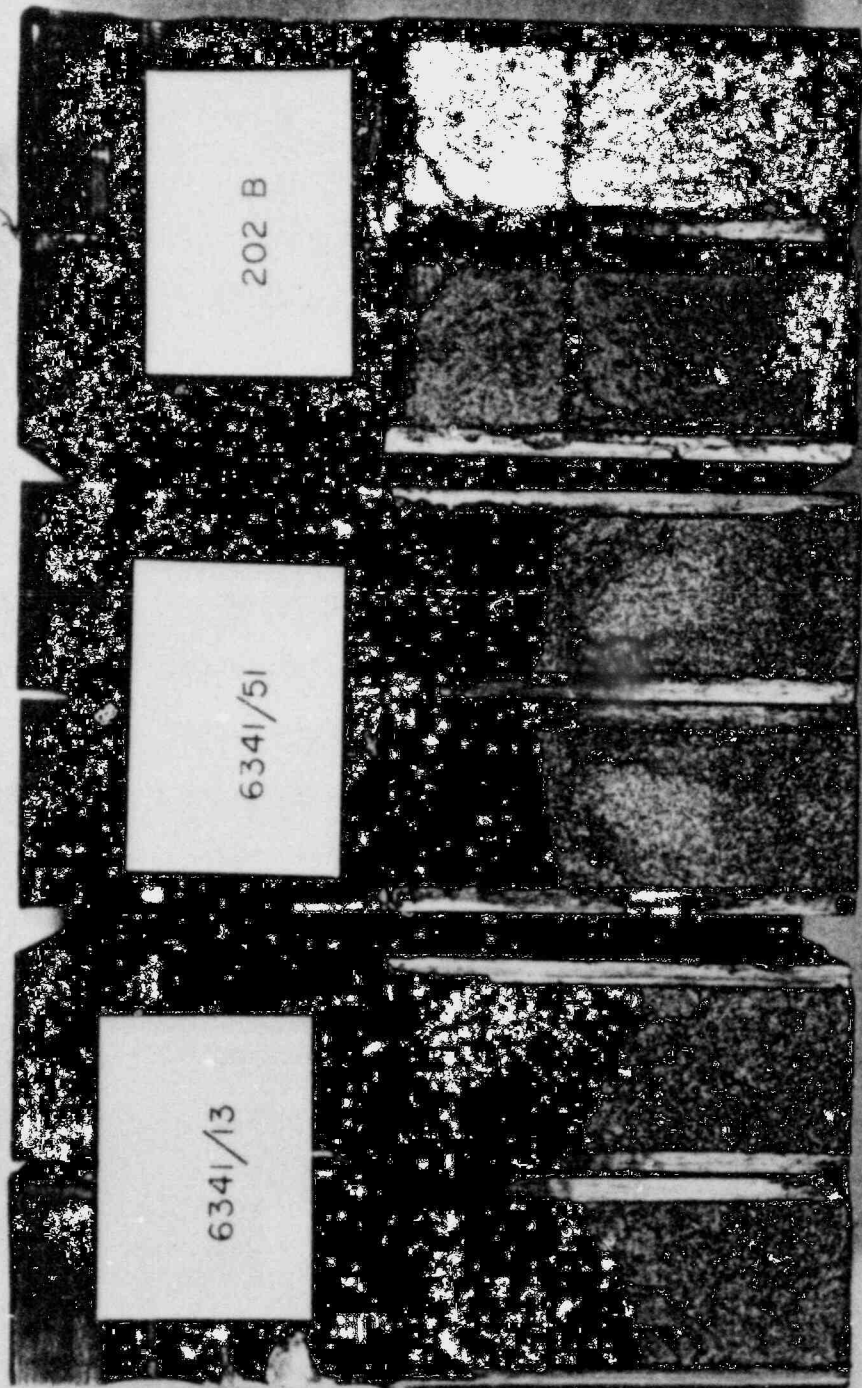
COMPACT SPECIMEN K_{Ia} TEST REPORT

Materials
Research
L~'~ratory,
Inc.

Laboratory: Date: 9/27/78   Material: AISI 1018 CO·OP

UNIV - MD.   Specimen: 6341/13

                                            Temperature: 23 C

                                            K_{Ia}: 102 MPa-m$^{\frac{1}{2}}$

Specimen Dimensions:

B = 50.3 mm, B_N = 39.4 mm, W = 169.3 mm,

Machined notch depth, a_o = 58.5 mm.

Precompression:

Total Δ = 1.524 mm, permanent Δ = 0.295 mm.

Precompression load = 393 kN.

Crack Length:

Surfaces, a_1 = 118.4 mm, a_5 = 105.4 mm,

Quarter points, a_2 = 115.4 mm, a_4 = 106.7 mm,

Center, a_3 = 112.5 mm,

$$\frac{1}{3}(a_2 + a_3 + a_4) = a_f = 111.5 \text{ mm.}$$

Test Results:

Initiation, Δ = 1.10 mm, K_Q = 134 MPa-m$^{\frac{1}{2}}$.

Arrest Δ = 1.26 mm, K_{Ia} = 102 MPa-m$^{\frac{1}{2}}$.

Comments:

a_5 - side towards wedge

a_1 - number side

Fracture Appearance:

(Attach photo)
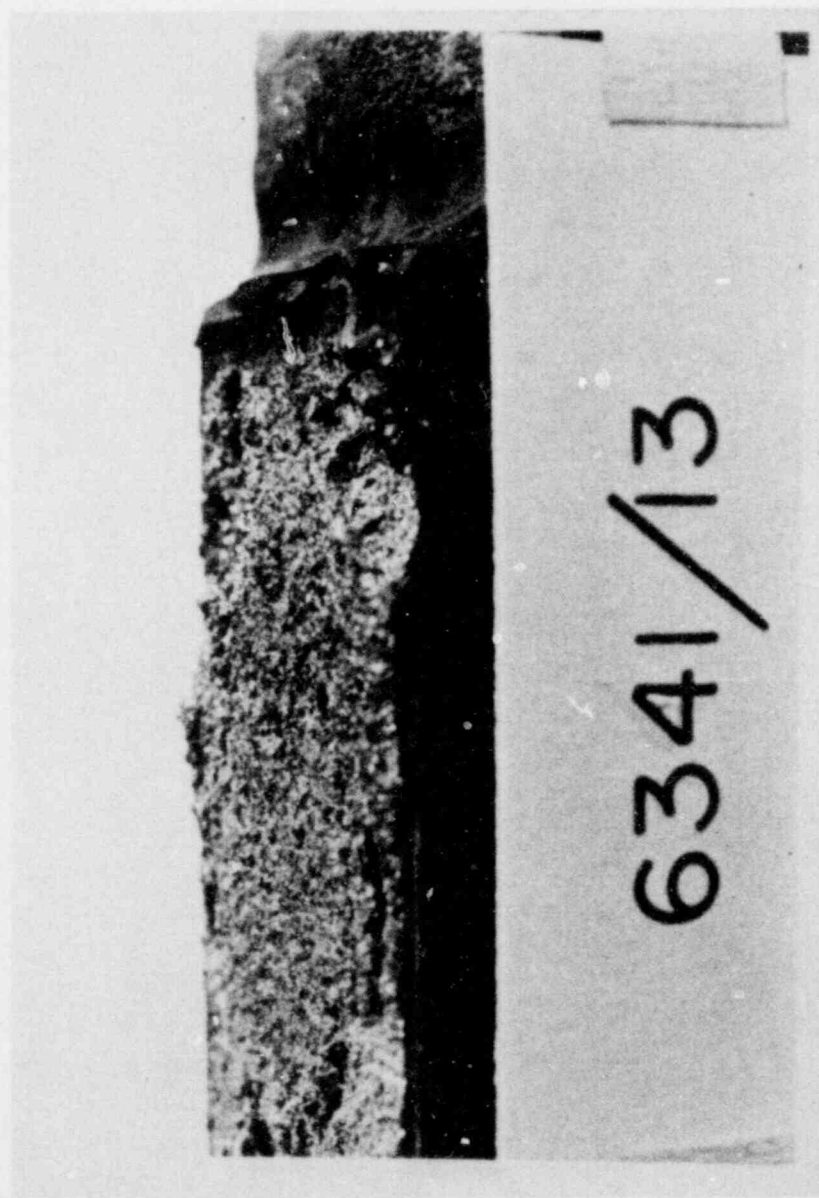
G3341/t3
-75°C
9/27/78

ARREST 0.0496

INITIAL DAMAGE 0.0482

Crack Opening @ 0.25W — inches

0.050

0.046

0.040

TIME — m sec

0.2   0.4   0.6   0.8   1.0

1 m s

Materials
Research
L oratory,
Inc.

Laboratory: Date: 10/5/78   Material: AISI 1018 CO-OP

Univ. Md.   Specimen: 6341/51

        Temperature: 23 C

        K_{Ia}:   70 MPa-m$^{\frac{1}{2}}$

Specimen Dimensions:

B = 50.3 mm, B_N = 37.5 mm, W = 169.5 mm,
Machined notch depth, a_o = 58.8 mm.

Precompression:

Total Δ = 1.524 mm, permanent Δ = 0.330 mm.
Precompression load = 403 kN.

Crack Length:

Surfaces, a_1 = 95.6 mm, a_5 = 91.1 mm,
Quarter points, a_2 = 96.4 mm, a_4 = 93.2 mm,
Center, a_3 = 94.2 mm,
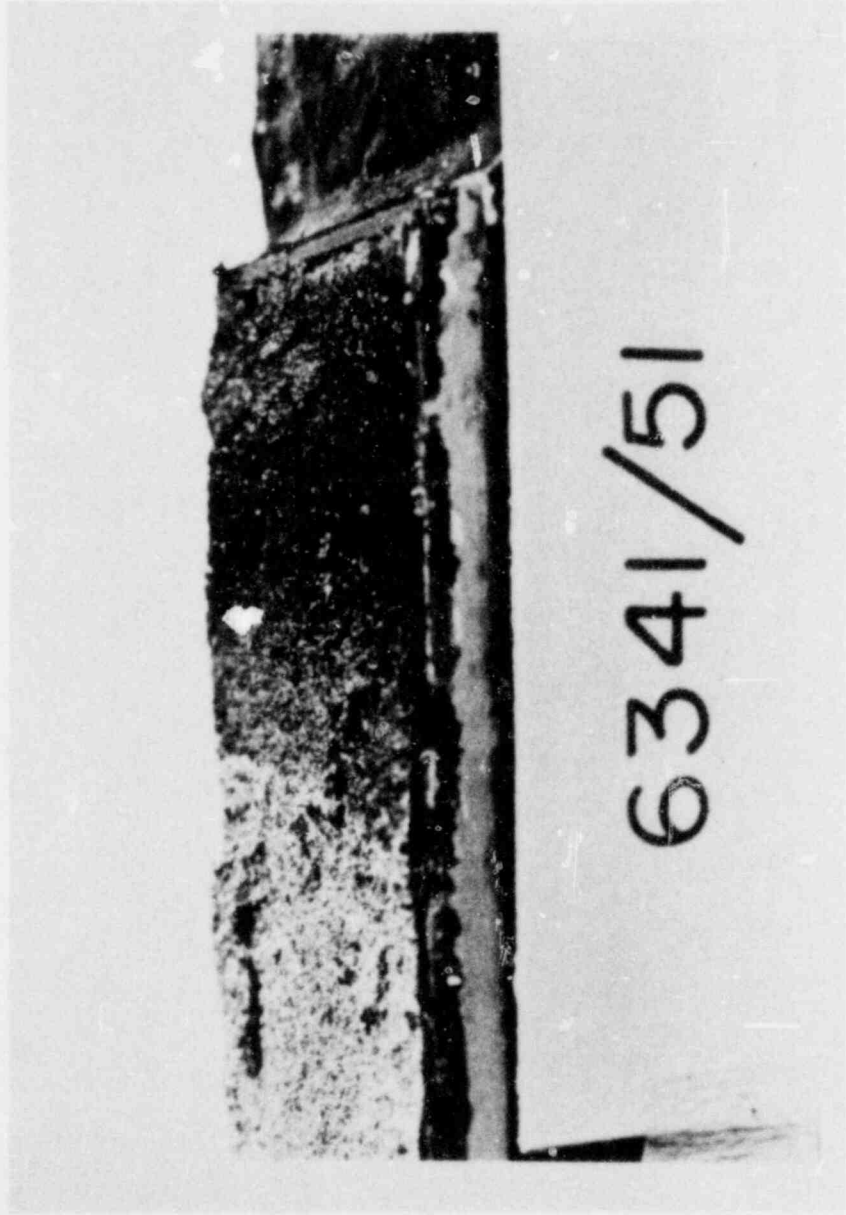
$$\frac{1}{3}(a_2 + a_3 + a_4) = a_f = 94.6 \text{ mm.}$$

Test Results:

Initiation, Δ = 0.79 mm, K_Q = 98 MPa-m$^{\frac{1}{2}}$.
Arrest Δ = 0.72 mm, K_{Ia} = 70 MPa-m$^{\frac{1}{2}}$.

Comments:

a_5- side towards wedge
a_1- number side

Fracture Appearance:

(Attach photo)

6341/51

244

TIME - MSEC

1.0   0.8   0.6   0.4   0.2

GAS W OPENING - INCHES

0.025

ARREST 0.0282

0.030

INITIATE 0.0311

0.035

G341/51
23°C
10/5/78

245
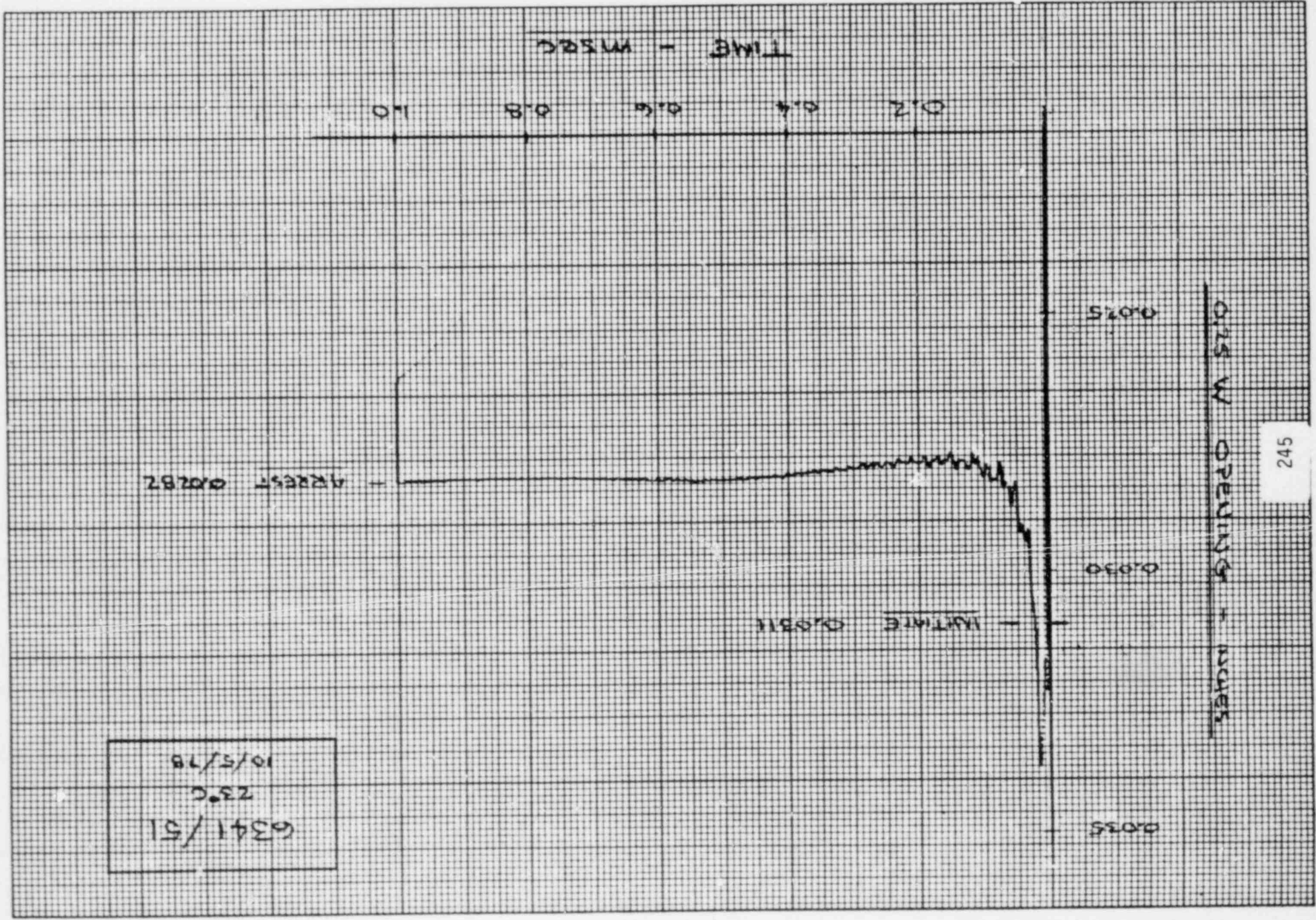
COMPACT SPECIMEN K_{Ia} TEST REPORT

Laboratory: Date: 11/2/78   Material: A 533 B

Univ-Md.   Specimen: 202 B

                                   Temperature: 23 C

                                   K_{Ia}: 117 MPa-m$^{\frac{1}{2}}$

Specimen Dimensions:

B = 50.5 mm, B_N = 38.5 mm, W = 169.2 mm,
Machined notch depth, a_o = 58.4 mm.

Precompression:

Total Δ = 1.527 mm, permanent Δ = 0.132 mm.
Precompression load = 485 kN.

Crack Length:

Surfaces, a_1 = 63.15 mm, a_5 = 63.65 mm,
Quarter points, a_2 = 63.45 mm, a_4 = 63.65 mm,
Center, a_3 = 63.75 mm,

$$\frac{1}{3} (a_2 + a_3 + a_4) = a_f = 63.62 \text{ mm.}$$

Test Results:

Initiation, Δ = 0.971 mm, K_Q = 120 MPa-m$^{\frac{1}{2}}$.
Arrest Δ = 0.971 mm, K_{Ia} = 117 MPa-m$^{\frac{1}{2}}$.

Comments:

crack did not propagate past weld zone

Fracture Appearance:
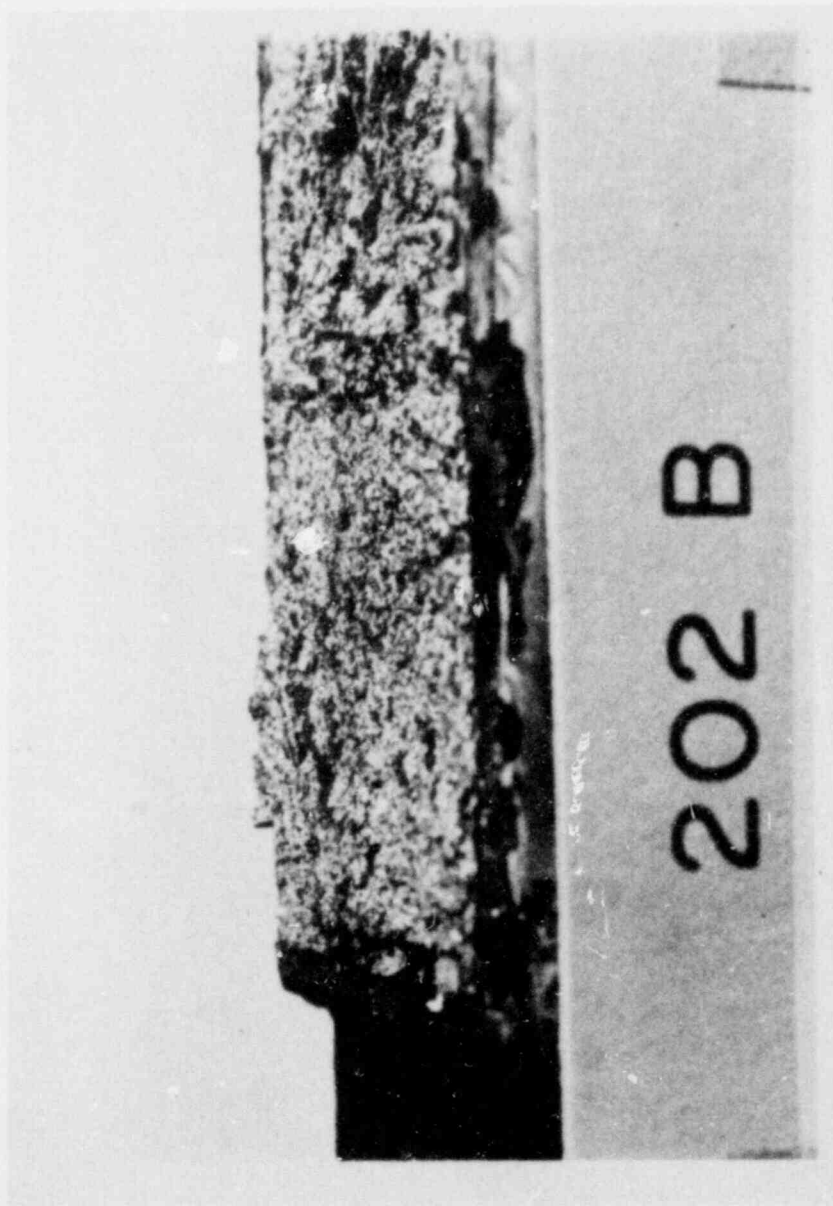
(Attach photo)

202 B

247

TIME — mSEC

1.0   0.8   0.6   0.4   0.2

CRACK OPENING @ 0.25 W — INCHES

0.0350

ARREST 0.0382   ARREST 0.0382

0.0382 —
INITIATE

0.040

0.045

202 B
23°C
11/2/78

248
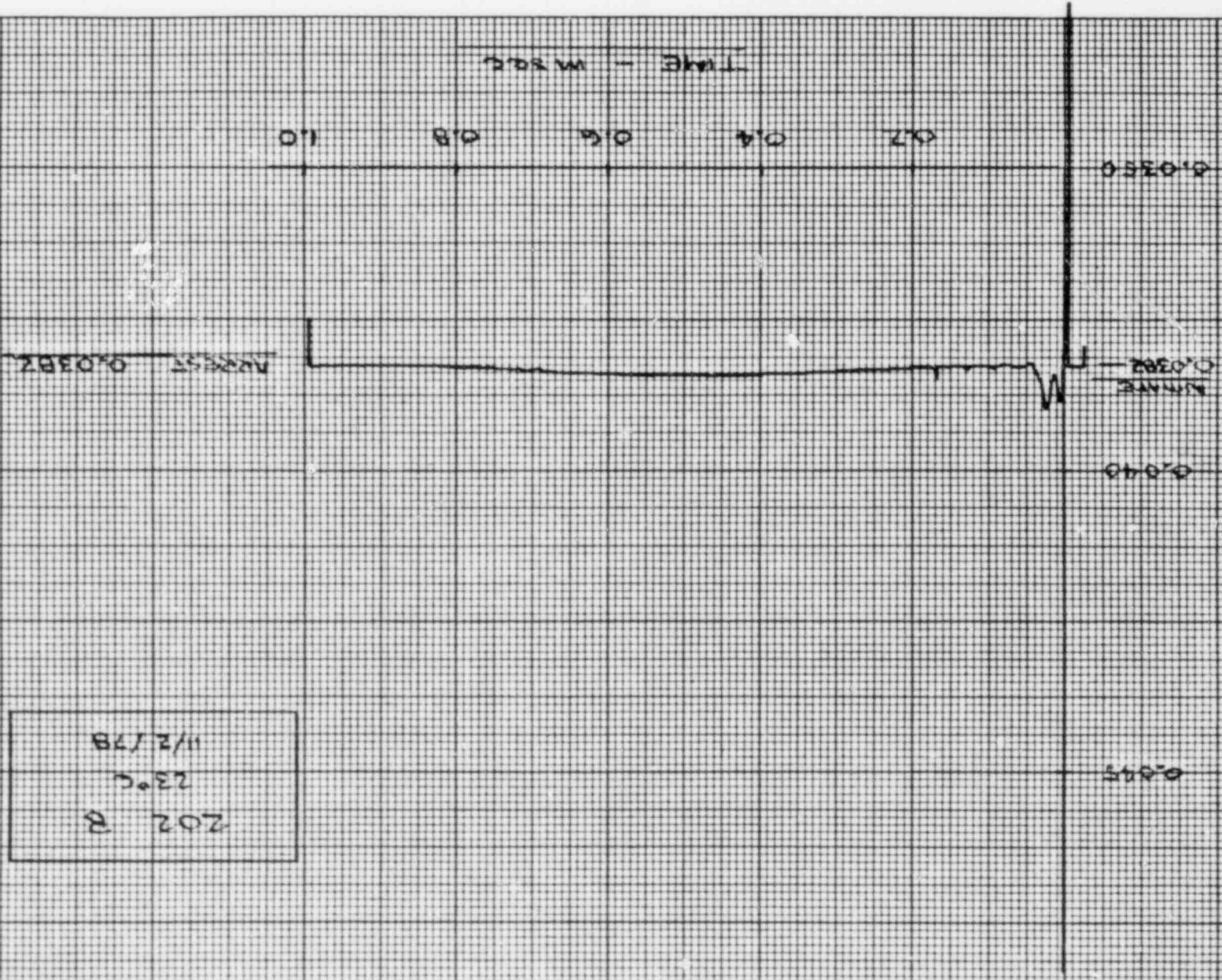
Materials
Research
oratory,
Inc.

Laboratory: Date: 10/19/78   Material: __A 533 B__

UNIV. MD   Specimen: __501 A__

_____   Temperature: _____ 23 C

K_{Ia}: _____ MPa-m$^{\frac{1}{2}}$

Specimen Dimensions:

B = __50.7__ mm, B_N = __38.4__ mm, W = __169.3__ mm,

Machined notch depth, a_o = __58.5__ mm.

Precompression:

Total Δ = __1.521__ mm, permanent Δ = __0.127__ mm.

Precompression load = __476__ kN.

Crack Length:

Surfaces, a_1 = __106.5__ mm, a_5 = __70.5__ mm,

Quarter points, a_2 = __103.2__ mm, a_4 = __99.8__ mm,

Center, a_3 = __102.4__ mm,

$$\frac{1}{3}(a_2 + a_3 + a_4) = a_f = \underline{101.8}\,mm.$$

Test Results:

Initiation, Δ = _____ mm, K_Q = _____ MPa-m$^{\frac{1}{2}}$.

Arrest Δ = _____ mm, K_{Ia} = _____ MPa-m$^{\frac{1}{2}}$.
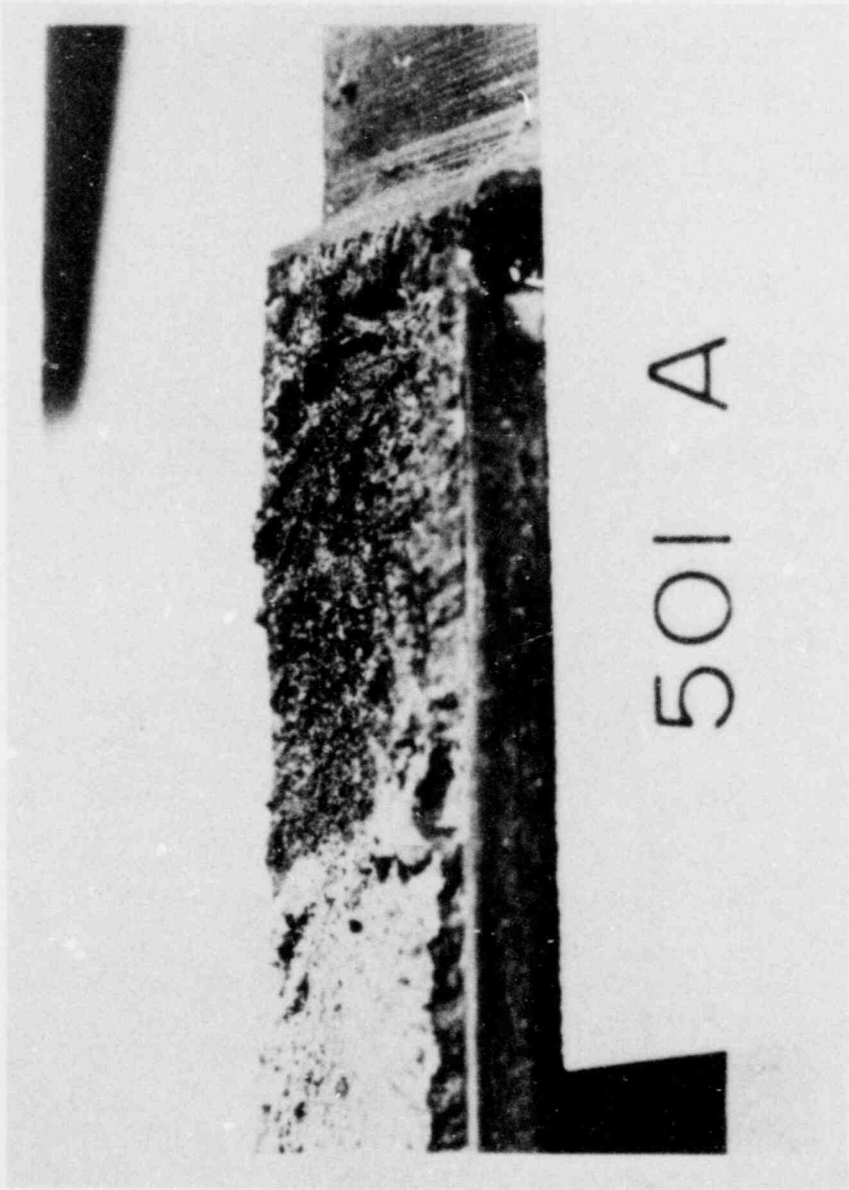
Comments:

Instrumentation malfunction - lost initiation & arrest data

a_5- side towards wedge

a_1- number side

Fracture Appearance:

note large ligaments in following photo

(Attach photo)

501 A

Materials
Research
L ratory,
Inc.

Laboratory: Date: 11/9/78   **Material:** A533B

Univ. Md.   **Specimen:** 509 B

       Temperature: 23 C

K_{Ia}: 106 MPa-m$^{\frac{1}{2}}$

Specimen Dimensions:

B = 50.8 mm, B_N = 38.2 mm, W = 169.5 mm,
Machined notch depth, a_o = 58.5 mm.

Precompression:

Total Δ = 1.529 mm, permanent Δ = 0.145 mm.
Precompression load = 505 kN.

Crack Length:

Surfaces, a_1 = 70.5 mm, a_5 = 96.7 mm,
Quarter points, a_2 = 86.7 mm, a_4 = 94.7 mm,
Center, a_3 = 90.5 mm,

$$\frac{1}{3}(a_2 + a_3 + a_4) = a_f = 90.6 \text{ mm.}$$

Test Results:

Initiation, Δ = 1.008 mm, K_Q = 126 MPa-m$^{\frac{1}{2}}$.
Arrest Δ = 1.057 mm, K_{Ia} = 106 MPa-m$^{\frac{1}{2}}$.

Comments:

Fracture Appearance:

(Attach photo)

509 B

509 R
23°C
11/9/78
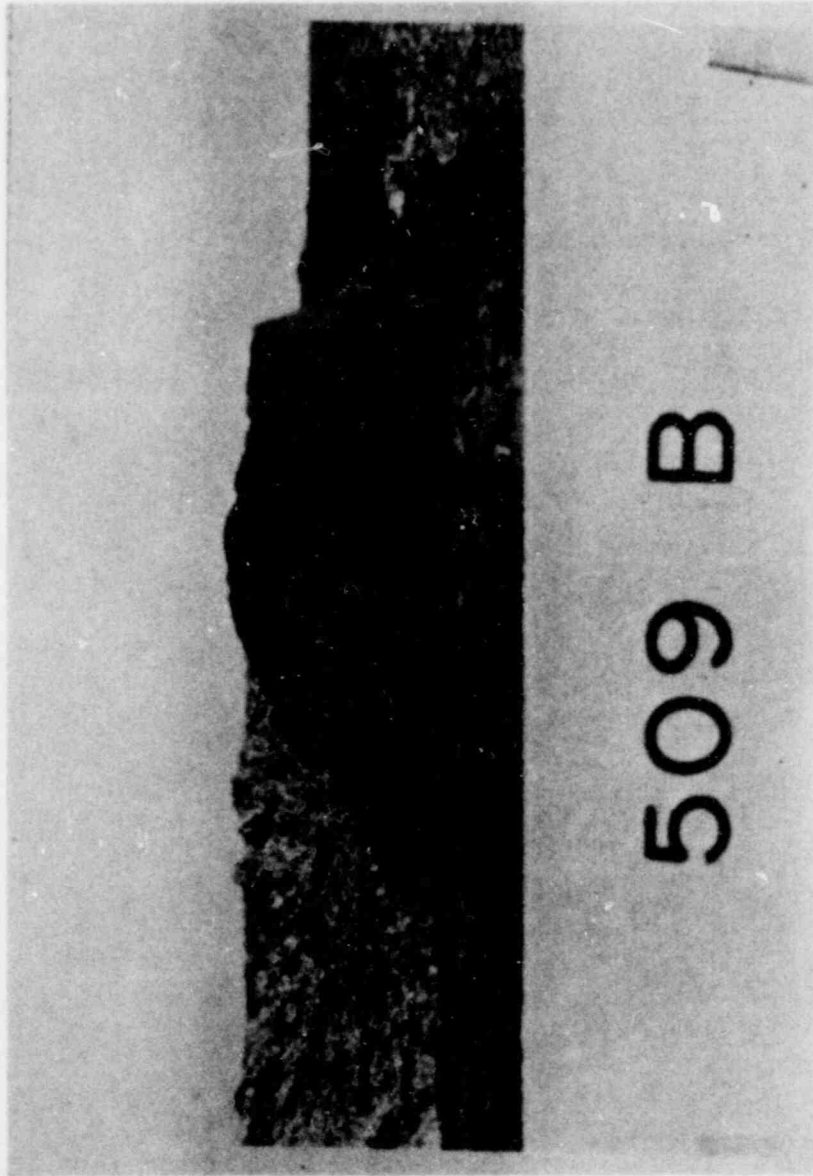
CRACK OPENING @ 0.75W — inches

ARREST 0.0418

INITIATE 0.0397

0.045

0.040

0.035

TIME m/secs

0.2   0.4   0.6   0.8   1.0

COMPACT SPECIMEN K_{Ia} TEST REPORT

Laboratory: Date: 11/16/78   **Material:** _A 533 B_

UNIV. MD.   **Specimen:** _411 C_

Temperature: _22_ C

K_{Ia}: _157_ MPa-m$^{\frac{1}{2}}$

Specimen Dimensions:

B = _50.7_ mm, B_N = _38.0_ mm, W = _169.2_ mm,

Machined notch depth, a_o = _58.85_ mm.

Precompression:

Total Δ = _1.524_ mm, permanent Δ = _0.130_ mm.

Precompression load = _501_ kN.

Crack Length:

Surfaces, a_1 = _103.35_ mm, a_5 = _120.05_ mm,

Quarter points, a_2 = _122.95_ mm, a_4 = _125.05_ mm,

Center, a_3 = _124.95_ mm,

$$\frac{1}{3}(a_2 + a_3 + a_4) = a_f = \text{\_124.05\_ mm.}$$

Test Results:

Initiation, Δ = _1.264_ mm, K_Q = _157_ MPa-m$^{\frac{1}{2}}$.

Arrest Δ = _1.442_ mm, K_{Ia} = _104_ MPa-m$^{\frac{1}{2}}$.

Comments:

unbroken ligaments small in size, but very numerous

Fracture Appearance:

(Attach photo)

411 C

ARREST 0.0572

41 C
22°C
11/16/78

INITIATE 0.0502

TIME - SECONDS

0.2   0.4   0.6   0.8   1.0

CRACK OPENING @ .025W - INCHES

0.060

0.055

0.050

0.045

256
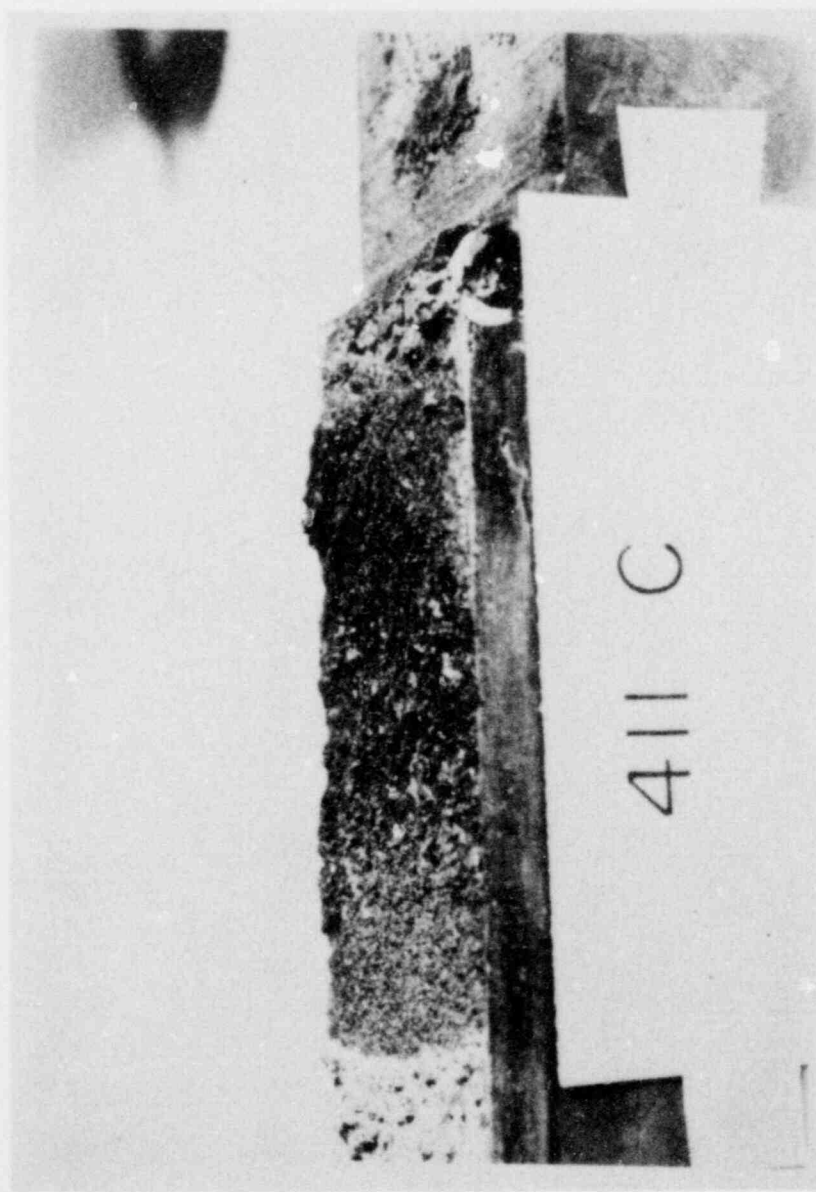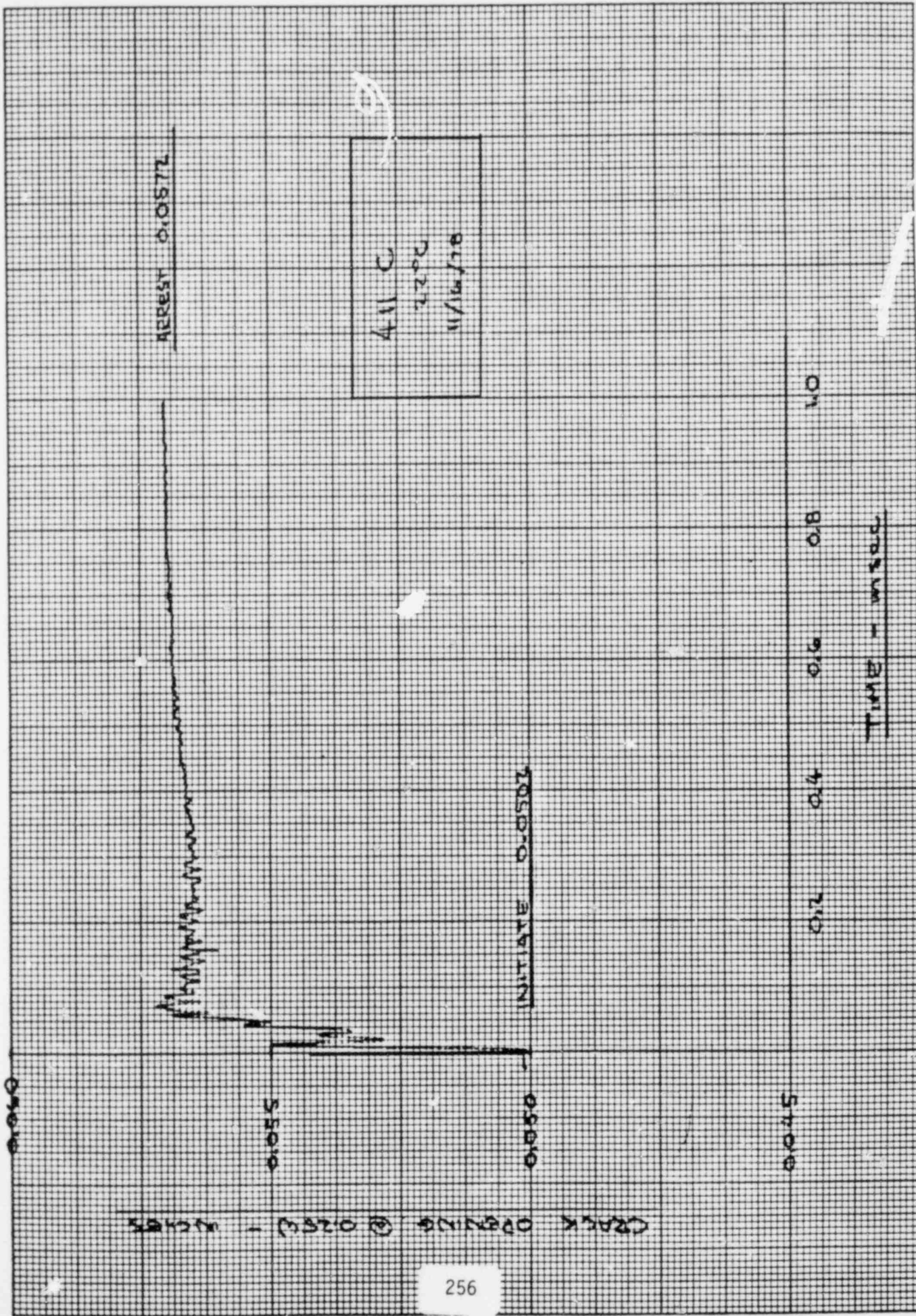
Battelle Duplex

The four duplex specimens were tested as per "Supplementary Information on the Battelle Test Method" by Hahn, et al dated August 4, 1978. The load line displacement was measured with a E-399 type double beam clip gage as recommended. The test report forms and photos of the fracture surfaces follow. Photos are also included showing any unfractured ligaments and shear lips.

The only additional measurement not originally asked for was the crack opening displacement at 0.25W above the load line. This measurement was only taken for the two 0°C test specimens and is included on the test report forms. This measurement was taken with a eddy current type displacement transducer and recorded on a strip chart.
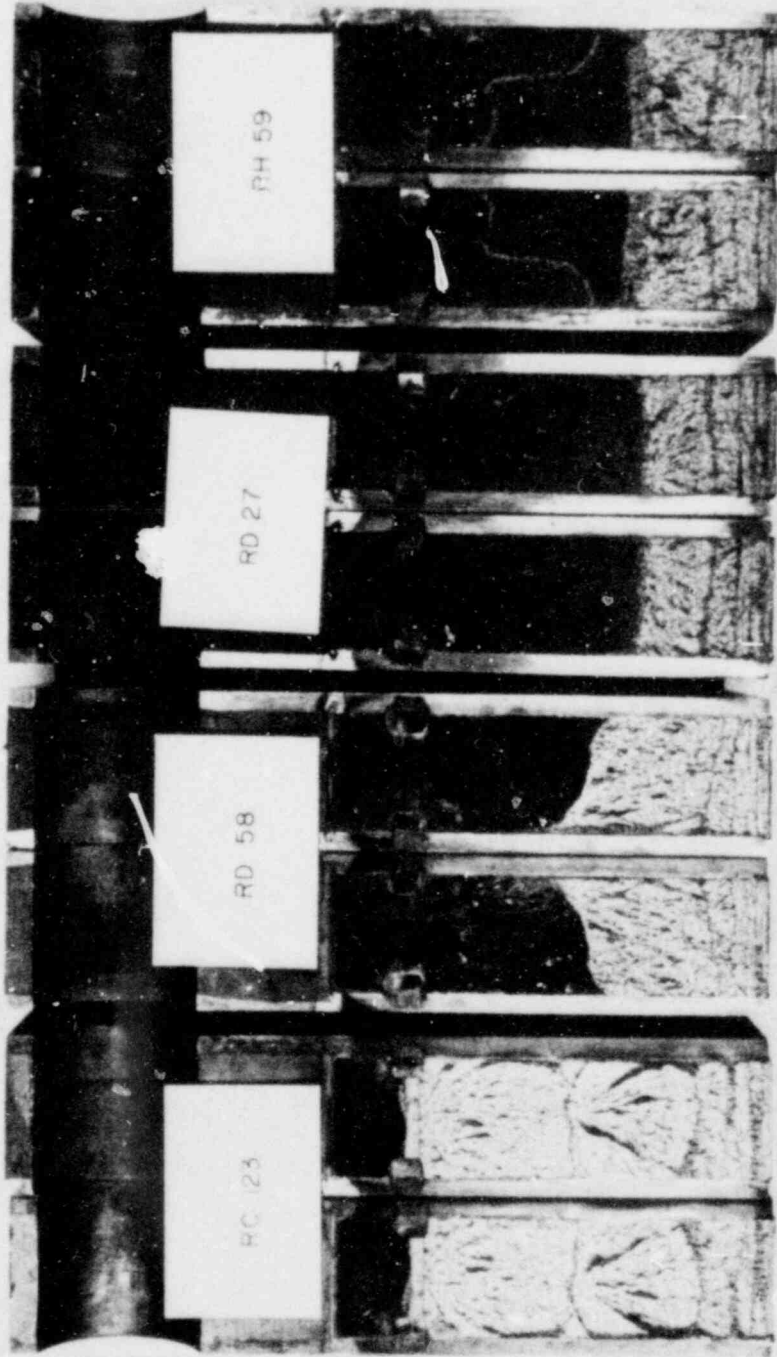
Specimen Number ___ RC 123 ___   Material ___ A533B-1 COOP ___

Page __1__ of _____   Laboratory ___ Univ. Md. ___

Temperature _____ 16 °C   Test Performed by ___ D. B. Barker ___

Thickness (B) __50.4__ mm

Thickness at Roots of Side Grooves (B_N) __37.8__ mm

Width (W) __208.0__ mm

Notch Diameter __2.0__ mm

Starting Notch Depth __0.5__ mm

*Arrested Crack Length __91.1__ mm

Thickness of Fracture Surface (B_f) __37.8__ mm

Load-Line Displacement

   Initiation (y_0) __1.041__ mm

   Arrest (y_f) __1.054__ mm

Fracture Load

   Initiation __55__ kN

   Arrest __33__ kN

Number of Load Cycles Required to Initiate Fracture __1__

Comments:
   Crack did not penetrate weld zone

$^*K_Q$ __190__	MPam$^{1/2}$	
$^*K_a$ _____	MPam$^{1/2}$	
$^*K_{ID}$ _____	MPam$^{1/2}$	

---

*From calculation sheet, page 2.

Specimen Number _____ RC 123 _____

Page __2__ of _____

Calculations

1. Arrested Crack Length (a_f)

   Edges a_1 = ___91.5___ mm a_5 = ___90.5___ mm

   Quarter Points a_2 = ___92.2___ mm a_4 = ___89.9___ mm

   Midpoint a_3 = ___91.2___ mm

   $$a_f = \frac{1}{3}(a_2 + a_3 + a_4) \quad \underline{91.1} \text{ mm}$$

2. Crack Penetration into Test Section (Δa_T)

   a_o = ___69.4___ mm

   Distance from notch tip to weld line (Δa_S) ___25.2___ mm

   $\Delta a_T = (a_f - \Delta a_S - a_o)$ ___-3.5___ mm

3. Stress Intensity at Initiation (K_Q)

   $$\frac{a_o}{w} = \underline{0.334} \; ; \quad f_o = \frac{Kw^{1/2}}{Ey_{pin}} \; \underline{0.3485} \; ; \quad \sqrt{\frac{B}{Bn}} = \underline{1.155}$$

   $$K_Q = \frac{Ey_o f_o}{w^{1/2}} \sqrt{\frac{B}{Bn}} \quad \underline{190.0} \text{ MPam}^{1/2}$$

4. Propagating Crack Toughness (K_{ID})

   $$\frac{\Delta a_T}{w} \underline{\quad\quad} \quad \frac{K_{ID}}{K_Q} \underline{\quad\quad} \quad \text{(from Figure 8a)}$$

5. Stress Intensity at Arrest (K_a)

   $$\frac{a_f}{w} = \underline{\quad\quad} \; ; \quad f_f = \frac{Kw^{1/2}}{Ey_{pin}} \underline{\quad\quad} \; ; \quad \sqrt{\frac{B}{Bn}} = \underline{\quad\quad}$$

   $$K_a = \frac{Ey_f f_f}{w^{1/2}} \sqrt{\frac{B}{Bn}} \underline{\quad\quad} \text{ MPam}^{1/2}$$

260

RC 123
run-1, 10⁵C
12/20/78

LOAD LINE DISPLACEMENT — INCHES

LOAD — 10³ lbs

261
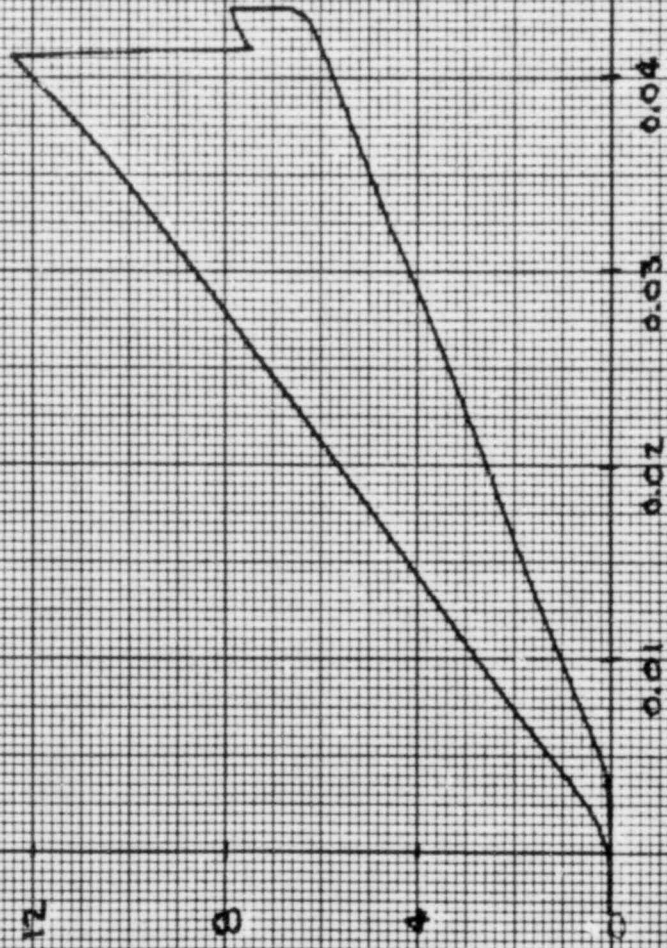
Specimen Number __RD 58__   Material _____A533B-1 COOP_____

Page _1_ of _____   Laboratory __UNIV. MD.__

Temperature _____16_ °C   Test Performed by __DB BARKER__

Thickness (B) __50.6__ mm

Thickness at Roots of Side Grooves (B_N) __38.0__ mm

Width (W) __208.0__ mm

Notch Diameter __7.4__ mm

Starting Notch Depth __0.6__ mm

*Arrested Crack Length __148.8__ mm

Thickness of Fracture Surface (B_f) __38.0__ mm

Load-Line Displacement

   Initiation (y_o) __1.257__ mm

   Arrest (y_f) __1.245__ mm

Fracture Load

   Initiation __68__ kN

   Arrest __12__ kN

Number of Load Cycles Required to Initiate Fracture __1__

Comments:
   note ligaments that formed from weld zone

*K_Q __230__ MPam$^{1/2}$
*K_a __110__ MPam$^{1/2}$
*K_{ID} __189__ MPam$^{1/2}$

---

*From calculation sheet, page 2.

Specimen Number __RD 58__

Calculations

1. Arrested Crack Length (a_f)

   Edges a_1 = __113.4__ mm a_5 = __156.0__ mm

   Quarter Points a_2 = __145.7__ mm a_4 = __150.9__ mm

   Midpoint a_3 = __149.8__ mm

   $$a_f = \frac{1}{3}(a_2 + a_3 + a_4) \quad \underline{148.8} \text{ mm}$$

2. Crack Penetration into Test Section (Δa_T)

   a_o = __69.4__ mm

   Distance from notch tip to weld line (Δa_S) __25.1__ mm

   $\Delta a_T = (a_f - \Delta a_S - a_o)$ __54.3__ mm

3. Stress Intensity at Initiation (K_Q)

   $$\frac{a_o}{w} = \underline{0.333} \; ; \quad f_o = \frac{KW^{1/2}}{Ey_{pin}} \; \underline{0.3491} \; ; \quad \sqrt{\frac{B}{Bn}} = \underline{1.154}$$

   $$K_Q = \frac{Ey_o f_o}{w^{1/2}} \sqrt{\frac{B}{Bn}} \quad \underline{229.7} \text{ MPam}^{1/2}$$
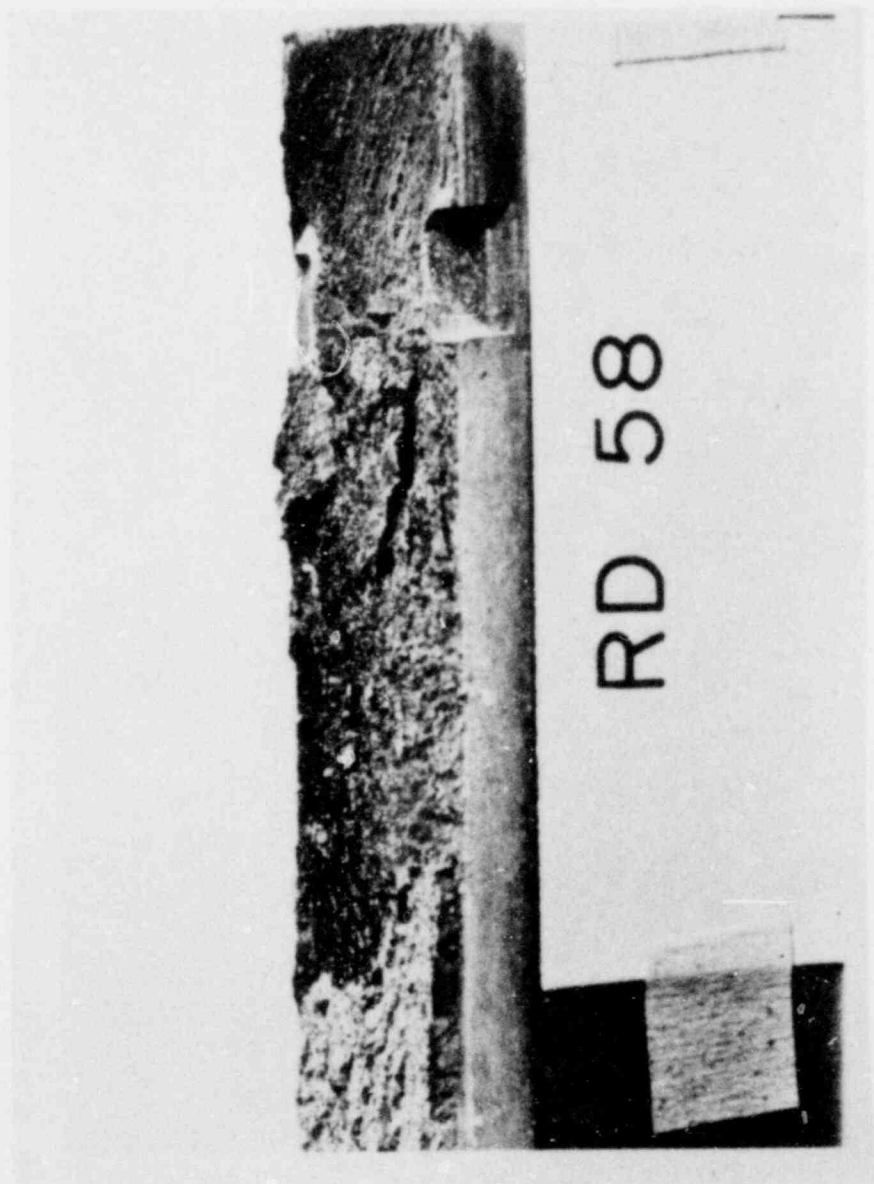
4. Propagating Crack Toughness (K_{ID})

   $$\frac{\Delta a_T}{w} \; \underline{0.261} \qquad \frac{K_{ID}}{K_Q} \; \underline{0.82} \quad \text{(from Figure 8a)}$$

5. Stress Intensity at Arrest (K_a)

   $$\frac{a_f}{w} = \underline{0.715} \; ; \quad f_f = \frac{Kw^{1/2}}{Ey_{pin}} \; \underline{0.1695} \; ; \quad \sqrt{\frac{B}{Bn}} = \underline{1.154}$$

   $$K_a = \frac{Ey_f f_f}{w^{1/2}} \sqrt{\frac{B}{Bn}} \quad \underline{110.4} \text{ MPam}^{1/2}$$

263

RD 58
run-1, 16°C
12/20/78

LOAD LINE DISPLACEMENT - INCHES

LOAD - 10^3 lbs

RD 58
60.8°F

265

Specimen Number __RH 59__   Material __A533B-1 COOP__

Page __1__ of _____   Laboratory __Univ. - Md.__

Temperature __0__ °C   Test Performed by __D. B. Barker__

Thickness (B) __50.0__ mm

Thickness at Roots of Side Grooves (B_N) __37.3__ mm

Width (W) __208.0__ mm

Notch Diameter __7.0__ mm

Starting Notch Depth __0.5__ mm

*Arrested Crack Length __159.7__ mm

Thickness of Fracture Surface (B_f) __37.3__ mm

Load-Line Displacement

   Initiation (y_o) __0.998__ mm

   Arrest (y_f) __1.016__ mm

Fracture Load

   Initiation __67__ kN

   Arrest __7__ kN

Number of Load Cycles Required to Initiate Fracture __1__

Comments:

   — at 0.25 W above load line : y_o = 1.262 mm , y_f = 1.331 mm

   — void along weld line

$^*K_Q$	__184__	$MPam^{1/2}$
$^*K_a$	__79__	$MPam^{1/2}$
$^*K_{ID}$	__140__	$MPam^{1/2}$

---

*From calculation sheet, page 2.

Specimen Number ___RH 59___

Page ___2___ of _____

Calculations

1. Arrested Crack Length (a_f)

   Edges a_1 = ___160.2___ mm a_5 = ___150.4___ mm

   Quarter Points a_2 = ___160.6___ mm a_4 = ___159.3___ mm

   Midpoint a_3 = ___159.1___ mm

$$a_f = \frac{1}{3}(a_2 + a_3 + a_4) \quad \underline{159.7} \text{ mm}$$

2. Crack Penetration into Test Section (Δa_T)

   a_o = ___68.5___ mm

   Distance from notch tip to weld line (Δa_S) ___25.1___ mm

   $\Delta a_T = (a_f - \Delta a_S - a_o)$ ___66.1___ mm

3. Stress Intensity at Initiation (K_Q)

   $\frac{a_o}{w}$ = ___0.329___ ; $f_o = \frac{Kw^{1/2}}{Ey_{pin}}$ ___0.3515___ ; $\sqrt{\frac{B}{Bn}}$ = ___1.158___

$$K_Q = \frac{Ey_o f_o}{w^{1/2}}\sqrt{\frac{B}{Bn}} \quad \underline{184.2} \text{ MPam}^{1/2}$$

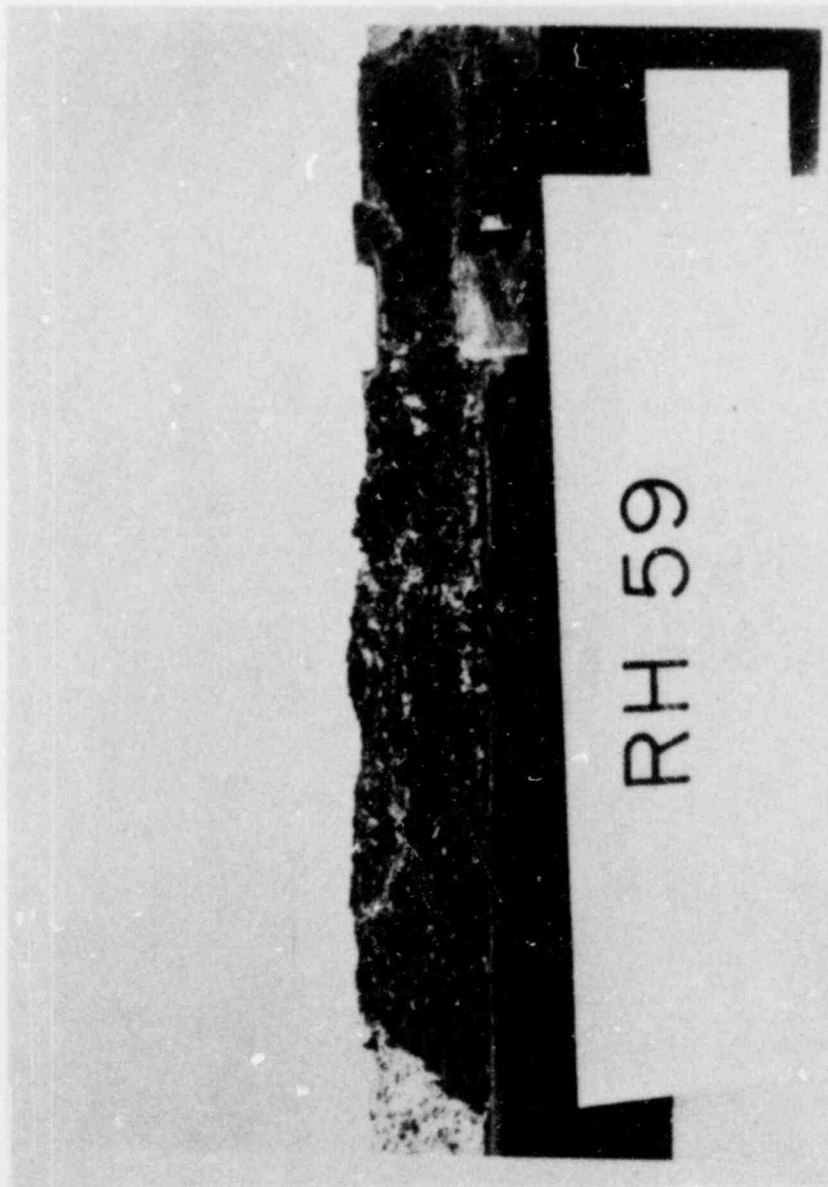4. Propagating Crack Toughness (K_{ID})

   $\frac{\Delta a_T}{w}$ ___0.318___ $\frac{K_{ID}}{K_Q}$ ___0.76___ (from Figure 8a)

5. Stress Intensity at Arrest (K_a)

   $\frac{a_f}{w}$ = ___0.768___ ; $f_f = \frac{Kw^{1/2}}{Ey_{pin}}$ ___0.1477___ ; $\sqrt{\frac{B}{Bn}}$ = ___1.158___

$$K_a = \frac{Ey_f f_f}{w^{1/2}}\sqrt{\frac{B}{Bn}} \quad \underline{78.8} \text{ MPam}^{1/2}$$

RH 59

RH 59
run 1, 0°C
1/8/79

LOAD LINE DISPLACEMENT - INCHES

LOAD - 10³ lbs
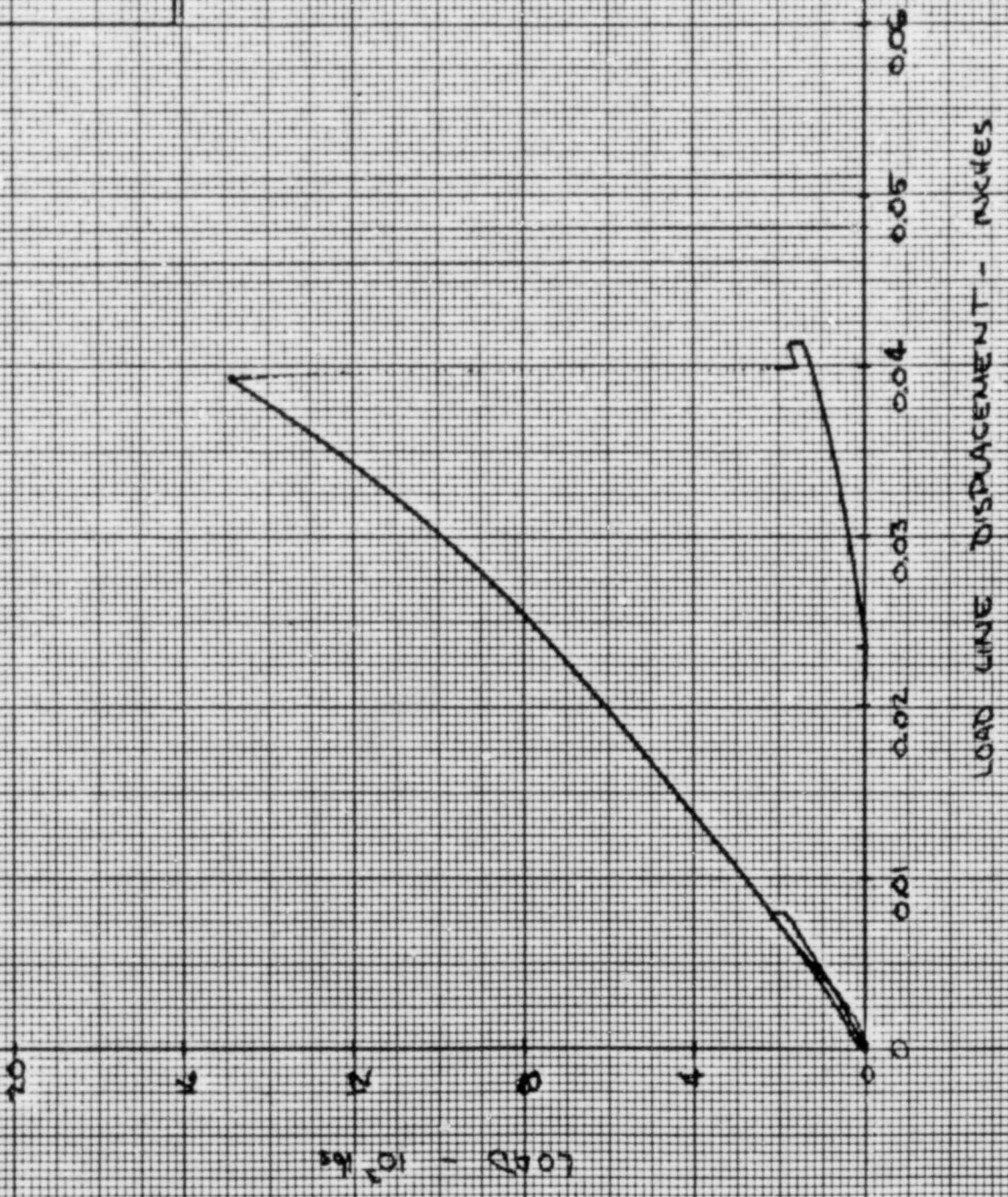
COOPERATIVE CRACK ARREST TEST PROGRAM
DUPLEX SPECIMEN TEST RECORD

Specimen Number ___RD 27___   Material ___A533B-1 COOP___

Page ___1___ of _____   Laboratory ___Univ. Md___

Temperature ___1___ °C   Test Performed by ___D.B.Barker___

Thickness (B) ___50.2___ mm

Thickness at Roots of Side Grooves (B_N) ___37.7___ mm

Width (W) ___208.0___ mm

Notch Diameter ___2.0___ mm

Starting Notch Depth ___0.5___ mm

*Arrested Crack Length ___165.4___ mm

Thickness of Fracture Surface (B_f) ___37.7___ mm

Load-Line Displacement

  Initiation (y_0) ___1.168___ mm

  Arrest (y_f) ___1.199___ mm

Fracture Load

  Initiation ___82___ kN

  Arrest ___8___ kN

Number of Load Cycles Required to Initiate Fracture ___2___

Comments:

    at 0.25 W above load line : y_0 = 1.506 mm , y_f - lost data

    large ligaments formed

*K_Q	___214___ MPam$^{1/2}$
*K_a	___85___ MPam$^{1/2}$
*K_{ID}	___150___ MPam$^{1/2}$

---
*From calculation sheet, page 2.

Specimen Number __RD 27__

Page __2__ of _____

Calculations

1. Arrested Crack Length (a_f)

   Edges a_1 = __165.8__ mm a_5 = __152.5__ mm

   Quarter Points a_2 = __165.2__ mm a_4 = __165.2__ mm

   Midpoint a_3 = __165.8__ mm

   $$a_f = \frac{1}{3}(a_2 + a_3 + a_4) \quad \underline{165.4} \text{ mm}$$

2. Crack Penetration into Test Section (Δa_T)

   a_o = __69.5__ mm

   Distance from notch tip to weld line (Δa_S) __25.3__ mm

   $\Delta a_T = (a_f - \Delta a_S - a_o)$ __70.6__ mm

3. Stress Intensity at Initiation (K_Q)

   $$\frac{a_o}{w} = \underline{0.334}; \quad f_o = \frac{Kw^{1/2}}{Ey_{pin}} \underline{0.3485}; \quad \sqrt{\frac{B}{Bn}} = \underline{1.154}$$

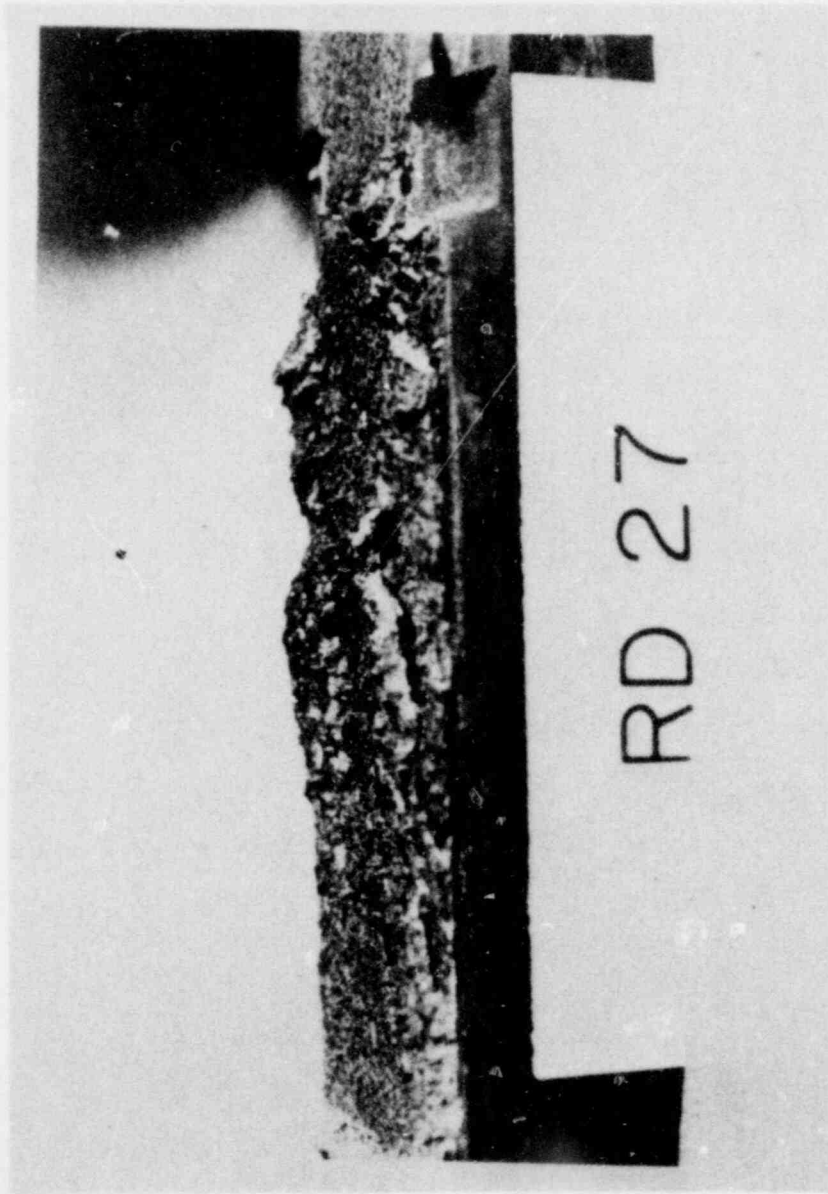 $$K_Q = \frac{Ey_o f_o}{w^{1/2}} \sqrt{\frac{B}{Bn}} \quad \underline{213.6} \text{ MPam}^{1/2}$$

4. Propagating Crack Toughness (K_{ID})

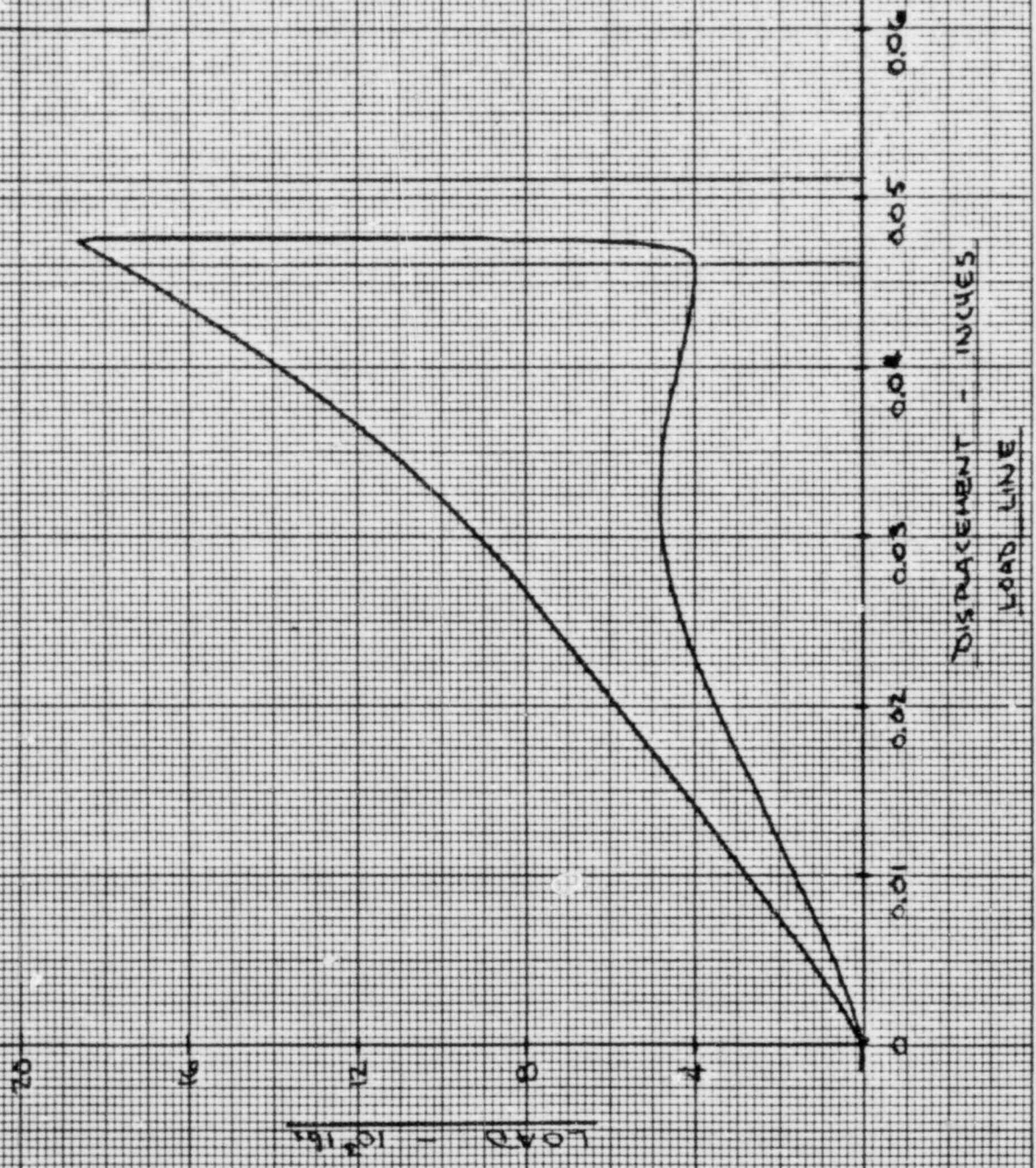 $$\frac{\Delta a_T}{w} \underline{0.339} \quad \frac{K_{ID}}{K_Q} \underline{0.70} \quad \text{(from Figure 8a)}$$

5. Stress Intensity at Arrest (K_a)

   $$\frac{a_f}{w} = \underline{0.795}; \quad f_f = \frac{Kw^{1/2}}{Ey_{pin}} \underline{.1350}; \quad \sqrt{\frac{B}{Bn}} = \underline{1.154}$$

   $$K_a = \frac{Ey_f f_f}{w^{1/2}} \sqrt{\frac{B}{Bn}} \quad \underline{84.7} \text{ MPam}^{1/2}$$

271

RD 27

RD 27
Run #1 - 1"
4/3/79

LOAD - 10³ lbf.

DISPLACEMENT - INCHES
LOAD LINE

RD 27

row • 2 - 1"
1/8/79
2" - 1"

LOAD - 10³lbs
20
16
12
8
4

LOAD LINE DISPLACEMENT - INCHES
0   0.01   0.02   0.03   0.04   0.05   0.06

1. REPORT NUMBER (Assigned by DDC) NUREG/CR-1455	

4. TITLE AND SUBTITLE (Add Volume No., if appropriate) Photoelastic Studies of Damping, Crack Propagation, and Crack Arrest in Polymers and 4340 Steel	2. (Leave blank)
	3. RECIPIENT'S ACCESSION NO.

7. AUTHOR(S) G. R. Irwin and others	5. DATE REPORT COMPLETED

MONTH November	YEAR 1979

9. PERFORMING ORGANIZATION NAME AND MAILING ADDRESS (Include Zip Code) University of Maryland Department of Mechanical Engineering College Park, MD 20742	DATE REPORT ISSUED

MONTH May	YEAR 1980
6. (Leave blank)	
8. (Leave blank)	

12. SPONSORING ORGANIZATION NAME AND MAILING ADDRESS (Include Zip Code) Division of Reactor Safety Research U.S. Nuclear Regulatory Commission Mail Stop 1130 SS Washington, DC 20555	10. PROJECT/TASK/WORK UNIT NO.
	11. CONTRACT NO. FIN No. A9026

13. TYPE OF REPORT Annual Report	PERIOD COVERED (Inclusive dates)
15. SUPPLEMENTARY NOTES	14. (Leave blank)

16. ABSTRACT (200 words or less)

This report describes the progress made during the fifth year on a research program dealing with the dynamic characterization of fracture.

17. KEY WORDS AND DOCUMENT ANALYSIS   17a. DESCRIPTORS

17b. IDENTIFIERS/OPEN-ENDED TERMS

18. AVAILABILITY STATEMENT	19. SECURITY CLASS (This report) Unclassified	21. NO. OF PAGES
Unlimited	20. SECURITY CLASS (This page) Unclassified	22. PRICE $